The impact of DNA damage repair inhibitors on the therapeutic window of thoracic radiation

Jennifer Martin

St Peter's College

Thesis submitted to the University of Oxford in accordance with the requirements for the degree of Doctor of Philosophy

Michaelmas Term 2020
University of Oxford

Word Count: 36000 words

Acknowledgments

I would like to first thank my supervisor Andy Ryan for his expert guidance over the past 4 years. I have learned so much from you beyond the lab too, and I appreciate all of the life advice.

Thank you to the Department of Oncology, especially the BMS staff, Imaging group, Graduate Studies team, Biophysics (Jamie and Amy for all the SARRP support), Facilities (Caroline, Andy, Mari-Lenna), Finance (Jackie, Sheji, Alaine), and Pash and Ihor (always bringing the positive vibes).

I'd like to thank the team at AstraZeneca (Barry Davies, Alan Lau, Elaine Cadogan, Stephen Durant, Jen Barnes, and Anna Cronin) for their collaboration and support and the current and previous Ryan lab members: Yanyan and Steve for their experimental data included in this work, Neele, Letitia, Fiona, Maryam, Agnes, Yasmin, Sureyya, Callum, and especially John and Kay for their support with the *in vivo* work.

Luiza, my mentor, thank you for teaching me how to be a better scientist and for our friendship and chats both in lab and beyond. I am so grateful for your hard work in developing this model and trust in me to carry it further. Agata, thank you for always being a source of sanity and fun, especially on the hardest days.

To all my friends from college and the department, I could not imagine the past 4 years without your support and advice: Luana, Jamie Green, Timo, Sam, Ania, Sovan, Sophie, Bruno, Simone, Siobhan, Shaliny, Asmita, Eva, Tiffany, Guillaume, Salome, Ishna, Kasia, Lisa, Alix, Joe, and Liz. Greg Blow, as the departmental computer wizard, thank you for the IT help but, more importantly, for your friendship.

Thank you to my friends across the UK and USA: Surya, Ben, Ellie, Adam, Grace, Lance, Annique, Shaan, Siân, Hanna, Cliff, Fran, and Henrietta. Ferne, you have been a pillar of support, always just a phone call away. Megan, I will be forever grateful for you dragging me across the pond all those years ago. Your friendship and encouragement (sour s'ghetti) have been so important in helping get me this far. Marissa, Andy, Thilini, and Charlie, thank you for making 5000 miles and the years we've been apart feel like nothing. To Annie, Richard, and Wendy – thank you for always checking on me and making me feel like I wasn't alone in the village.

Larry and Lynnette – thank you for welcoming me into your family with open arms. This year has been one of the hardest, but your support (food care packages) and kindness have made it so much easier.

Natalie, my better(er) half, I am so lucky to have met you during this DPhil. It feels like we've been through so much in our 3 years together, and I could not have made it without your love and encouragement.

And finally, to my wonderful parents, brother, and family – thank you for always believing in me and cheering me on through my toughest moments and celebrating my achievements.

Abstract

Background: Lung cancer is the leading cause of cancer death worldwide. A mainstay of treatment is radiotherapy, although its efficacy is limited by toxicity to surrounding normal tissue. New combination treatments are being proposed to increase the radiotherapy anti-tumour effect, but there has been a lack of preclinical studies looking at normal tissue effects simultaneously.

Aim: To address the need for a mouse model of anti-tumour and normal tissue responses concurrently over an appropriate time-course for early and late tissue effects, we evaluated the A/J model of chemically-induced lung carcinoma.

Methods: Autochthonous lung tumours were induced by urethane treatment of A/J mice. Tumour bearing animals were treated with whole thorax, hemithorax, or CT-guided left lung ionising radiation (IR, 10 Gy, 13 Gy, or 15 Gy single dose or 5 x 5 Gy fractionated dose) alone or in combination with DNA damage response (DDR) inhibitors (AZD6738, AZD7648, AZD1390) at different time points during tumour development. Tumour and normal tissue responses were followed for up to 26 weeks. Lungs were collected and processed for histology, and Masson's trichrome staining was performed to evaluate collagen deposition in irradiated lungs. Magnetic resonance images of lung and tumours were obtained during the course of the experiments.

Results: Whole thorax IR combined with DDR inhibitors resulted in oesophageal inflammation and immune cell infiltration, so hemithorax fractionated and single dose IR protocols were developed. Hemithorax IR combined with an ATR inhibitor (AZD6738) had limited anti-tumour effects but also few normal tissue responses. In contrast, hemithorax IR combined with a DNA-PK inhibitor (AZD7648) led to significant anti-tumour effects but also was associated with increased skin and lung normal tissue damage. Furthermore, hemithorax IR combined with an ATM inhibitor (AZD1390) resulted in limited anti-tumour effects and also skin and lung normal tissue damage. Early oesophageal modelling of fractionated whole thorax IR with AZD7648 revealed subclinical histological changes.

Conclusions: A/J mice provide a model for the concurrent evaluation of anti-tumour and normal tissue effects and may be useful in assessing the therapeutic window of novel therapies in combination with IR. The value of the model in assessing therapeutic window will need to be confirmed by clinical studies.

Table of Contents

Acknowledgments I

Abstract II

Table of Contents III

Abbreviations VII

List of Presentations and Publications IX

Presentations ..... *IX*

Publications ..... *IX*

List of Figures X

List of Tables XVI

1. General Introduction 1

1.1. Lung cancer diagnosis and staging *1*

1.2. NSCLC treatment *3*

1.3. Principles of radiotherapy *7*

1.4. Radiotherapy and targeting the DDR pathway *9*

1.5. The therapeutic window of response to IR *16*

1.6. Preclinical mouse models *20*

1.7. Aims *25*

2. Materials and Methods 26

2.1. Reagents *26*

2.2. In vivo experiments *26*

2.3. Subcutaneous xenograft tumour induction *26*

2.4. Urethane induction of tumours *27*

2.5. Animal welfare *27*

2.6. Irradiation ***28***
2.6.1. Xenograft, whole thorax, or hemithorax IR 28
2.6.2. Image-guided IR of the left lung 31
2.7. Cardio-respiratory gated magnetic resonance imaging ***32***
2.8. Drug formulation and dosing ***33***
2.9. Euthanasia and sample processing ***34***
2.10. Slide preparation ***34***
2.11. Dewaxing and hydration ***34***
2.12. Immunohistochemistry ***34***
2.13. Chromogenic detection and counterstaining ***36***
2.14. Haematoxylin and eosin ***37***
2.15. Masson's trichrome ***37***
2.16. Slide scanning and image analysis ***38***
2.17. Statistical analysis ***40***
3. Results **41**
3.1. A/J mouse model of therapeutic intervention ***41***
3.1.1. Introduction 41
3.1.2. A/J urethane-induced tumour characterisation 46
3.1.3. Urethane induction of A/J lung tumours is dose dependent and can be assessed by magnetic resonance imaging 50
3.1.4. Single fraction whole thorax IR of A/J mice leads to collagen accumulation in lungs and increased fibrosis score 55
3.1.5. CT-guided left lung IR of A/J mice leads to limited collagen accumulation and fibrosis score 59
3.1.6. Discussion 62
3.2. Therapeutic window of AZD6738 and IR in A/J mouse model ***67***
3.2.1. Introduction 67
3.2.2. AZD6738 radiosensitises Calu6 xenograft tumours in CD-1 nude mice 72
3.2.3. AZD6738 and fractionated whole thorax IR leads to oesophageal inflammation in the A/J early intervention therapeutic window study 74

3.2.4. AZD6738 combined with hemithorax fractionated IR is well tolerated but shows limited efficacy in A/J early intervention therapeutic window study78
3.2.5. AZD6738 and CT-guided left lung IR is well tolerated but shows limited efficacy in A/J late intervention therapeutic window study 84
3.2.6. Pharmacodynamics of AZD6738 at 50 mg/kg combined with IR does not significantly affect pan-nuclear γH2AX levels in lung tumours or the bronchial or oesophageal epithelium 90
3.2.7. Pharmacodynamics of AZD6738 at 50 mg/kg combined with IR decreases pKAP1 in tumours but not in bronchial or oesophageal epithelial cells..... 95
3.2.8. Discussion..... 99

3.3. Therapeutic window of DNA-PK and IR in A/J mouse model 103

3.3.1 Introduction..... 103
3.3.2. AZD7648 radiosensitises Calu6 xenograft tumours in CD-1 nude mice106
3.3.3. AZD7648 and fractionated whole thorax IR leads to oesophageal inflammation in A/J early intervention therapeutic window study 108
3.3.4. Oesophageal tolerability of AZD7648 combined with IR disrupts tissue layers and leads to increased nuclear condensation 112
3.3.5. AZD7648 and fractionated hemithorax IR is efficacious but damages normal tissue in A/J early intervention therapeutic window study 113
3.3.6. AZD7648 and CT-guided left lung IR is tolerated but shows limited efficacy in A/J late intervention therapeutic window study 120
3.3.7. Pharmacodynamics of AZD7648 at 50 mg/kg combined with IR does not significantly affect γH2AX levels in lung tumours or the bronchial or oesophageal epithelium..... 126
3.3.8. Pharmacodynamics of AZD7648 at 50 mg/kg combined with IR decreases pKAP1 in tumours but not in bronchial or oesophageal epithelial cells..... 131
3.3.9. Discussion..... 135

3.4. Therapeutic window of ATM and IR in A/J mouse model 138

3.4.1. Introduction..... 138
3.4.2. AZD1390 radiosensitises Calu6 xenograft tumours in CD-1 nude mice141
3.4.3. AZD1390 and fractionated whole thorax IR leads to oesophageal inflammation in A/J mice..... 142

3.4.4. AZD1390 and fractionated hemithorax IR shows limited efficacy and damages normal tissue in A/J early intervention therapeutic window study 147
3.4.5. AZD1390 and CT-guided left lung IR is tolerated but shows limited efficacy in A/J late intervention therapeutic window study 152
3.4.6. Pharmacodynamics of AZD1390 at 10 mg/kg combined with IR significantly decreases γH2AX levels in bronchial epithelial cells but not lung tumours or oesophageal epithelium 158
3.4.7. Pharmacodynamics of AZD1390 at 10 mg/kg combined with IR decreases pKAP1 in tumours but not in bronchial or oesophageal epithelial cells..... 163
3.4.8. Discussion 167

4. General Discussion and Conclusions..... 171

5. References 179

6. Appendix 202

Abbreviations

°C: °Celcius
53BP1: tumour protein p53 binding protein 1
ALK: anaplastic lymphoma kinase
ANOVA: analysis of variance
A-T: ataxia-telangiectasia
ATM: ataxia-telangiectasia mutated
ATR: ataxia-telangiectasia and Rad3-related
ATRIP: ATR-interacting protein
BED: biologically effective dose
BER: base excision repair
BRCA1/2: breast cancer type susceptibility gene 1/2
BrdU: bromodeoxyuridine
CDC25: cell division cycle 25
CDK1/2: cyclin dependent kinase 1/2
CHART: continuous hyperfractionated, accelerated radiotherapy
CHK1: checkpoint kinase 1
CHK2: checkpoint kinase 2
CT: computed tomography
CTCAE: Common terminology criteria for adverse events
CYP2E1: cytochrome P450 2E1
DAB: 3,3'-diaminobenzidine
DAMP: damage associated molecular pattern
DDR: DNA damage response
DMSO: dimethyl sulfoxide
DNA: deoxyribonucleic acid
DNA-PKcs: DNA-dependent protein kinase catalytic subunit
DNA-PK: DNA-dependent protein kinase
DSB: double strand break
dsDNA: double stranded DNA
EGFR: epidermal growth factor receptor
ETAA1: Ewing's tumour-associated antigen 1
H2AX: histone H2AX
H&E: haematoxylin and eosin
HR: homologous recombination
IC_{50}: 50% inhibitory concentration
IHC: immunohistochemistry
i.p.: intraperitoneal
IR: ionising radiation
K-ras: Kirsten rat sarcoma viral oncogene homologue
KAP1: KRAB-associated protein 1
LDCT: low-dose computed tomography
LET: linear energy transfer
Ly6G/C: lymphocyte antigen 6 GC

MAPK: mitogen-activated protein kinase
mm Hg: millimetres of mercury
MRI: magnetic resonance imaging
MRN: protein complex of MRE11, RAD50 and NBS1
mRNA: messenger ribonucleic acid
mTOR: mechanistic target of rapamycin
NC3R: National Centre for the Replacement, Refinement & Reduction of Animals in Research
NER: nucleotide excision repair
NHEJ: non-homologous end joining
NHS: National Health Service
NSCLC: non-small cell lung cancer
OAR: organ at risk
p.o.: *per os*, orally
p53: tumour protein 53
Pas1: pulmonary adenoma susceptibility locus 1
PBS: phosphate buffered saline
PD: pharmacodynamic
PD-L1: programmed death-ligand 1
PDX: patient-derived xenograft
PET: positron emission tomography
PI3K: phosphatidylinositol 3-kinase
PIKK: phosphatidylinositol 3-kinase-related kinase
RHINO: RAD9-HUS1-RAD-1-interacting nuclear orphan
ROI: region of interest
ROS: reactive oxygen species
RPA: replication protein A
SABR: stereotactic ablative body radiotherapy
SARRP: small animal radiation research platform
SASP: senescence-associated secretory phenotype
SCID: severe combined immunodeficiency
SEM: standard error of the mean
SSB: single strand break
ssDNA: single-stranded DNA
TNM: Tumour-node-metastasis
TOPBP1: topoisomerase (DNA) II binding protein 1
V_{20Gy}: the limit of the volume of lung that receives 20 Gy
XLF: XRCC4-like factor

List of Presentations and Publications

Presentations

Radiation Research Society Conference, San Diego USA, 2019
"A mouse model for evaluating the therapeutic window of novel lung cancer therapies combined with radiation"

International Congress of Radiation Research Conference, Manchester UK, 2019
"A mouse model for evaluating the therapeutic window of novel lung cancer therapies combined with radiation"

Oxford Institute for Radiation Oncology Symposium, Oxford UK, 2018
"A mouse model for evaluating the therapeutic window of novel lung cancer therapies combined with radiation"

AstraZeneca-Oxford Cancer Symposium, Oxford UK, 2018
"A mouse model for evaluating the therapeutic window of novel lung cancer therapies combined with radiation"

Oxford Oncology Student Symposium, Oxford UK, 2017
"Targeting DNA Damage Responses to Improve the Treatment of Lung Cancer"

Publications

Jiang Y, **Martin J**, Alkadhimi M, Shigemori K, Kinchesh P, Gilchrist S, Kersemans V, Smart S, Thompson J, Hill M, O'Connor M, Davies B, Ryan A (2021). "Olaparib increases the therapeutic index of hemithoracic irradiation compared with hemithoracic irradiation alone in a mouse lung cancer model." *British Journal of Cancer*. 10.1038/s41416-021-01296-y.

List of Figures

Figure 1.1.1. Common oncogenic drivers of NSCLC. 6
Figure 1.1.2. Different types of IR-induced DNA damage. 7
Figure 1.1.3. Therapeutic window of IR dose, tumour response, and normal tissue toxicities. 9
Figure 1.1.4. Radiotherapy and drug combination strategies to target cancer characteristics. 11
Figure 1.1.5. IR-induced DNA damage and repair pathways. 12
Figure 1.1.6. DSB repair through NHEJ or HR. 13
Figure 1.1.7. DDR pathways and clinical compounds 14
Figure 1.1.8. The CONCORDE platform summary. 15
Figure 1.1.9. IR-induced tissue response timeline. 16
Figure 1.1.10. IR-induced lung damage progression. 19
Figure 1.1.11. IR-induced lung damage mouse strains by paper numbers and year published. 23
Figure 2.6.1.1. Xenograft irradiation rig. 29
Figure 2.6.1.2. Whole thorax irradiation rig. 30
Figure 2.6.1.3. Hemithorax irradiation rig. 31
Figure 2.6.2.4. CT-guided left lung irradiation rig. 32
Figure 2.16.1. Immunohistochemistry of γH2AX categories 39
Figure 2.16.2. Fibrosis scoring comparison. 40
Figure 3.1.1. Ethyl carbamate (urethane) metabolism by CYP2E1 43
Figure 3.1.2. Fractionated whole thorax IR induces collagen deposition in A/J mice. 45
Figure 3.1.3. Main aims and experimental arms. 46
Figure 3.1.4. A/J urethane-induced tumours can be visually and histologically assessed. 47
Figure 3.1.5. A/J urethane-induced tumours show few BrdU-positive cells and few pimonidazole-positive regions. 49
Figure 3.1.6. Superficial tumour numbers and total tumour area burden are urethane dose dependent 52
Figure 3.1.7. Tumour numbers, total volume, and total volume change are urethane dose dependent and can be measured by MRI. 54
Figure 3.1.8. Whole thorax IR with 13 or 15 Gy induces body weight loss. 57

Figure 3.1.9. Fibrosis scoring of whole thorax IR. 58
Figure 3.1.10. CT-guided left lung IR did not induce body weight loss. 60
Figure 3.1.11. Fibrosis scoring of CT-guided hemithoracic left lung IR. 61
Figure 3.1.12. Experimental design for early intervention whole thorax or hemithorax IR therapeutic window studies. 62
Figure 3.1.13. Experimental design for late intervention CT-guided IR therapeutic window study. 63
Figure 3.1.14. Experimental design for pharmacodynamic studies. 63
Figure 3.2.1. ATR signalling pathway after activation by DNA damage or replication stress. 68
Figure 3.2.2. Main aims and experimental arms. 72
Figure 3.2.3. AZD6738 in combination with IR increased tumour growth inhibition in Calu6 xenografts. 73
Figure 3.2.4. Early intervention with whole thorax IR combined with AZD6738 induced sustained body weight loss in A/J mice. 75
Figure 3.2.5. AZD6738 combined with whole thorax IR results in oesophageal inflammation. 77
Figure 3.2.6. AZD6738 in combination with hemithorax IR did not induce body weight loss. 79
Figure 3.2.7. AZD6738 in combination with hemithorax IR did not reduce superficial tumour counts or ratio compared with hemithorax IR alone. 81
Figure 3.2.8. AZD6738 in combination with hemithorax IR did not reduce tumour number or area per lung slice compared with hemithorax IR alone. 82
Figure 3.2.9. AZD6738 in combination with hemithorax IR did not affect lung weights or fibrosis scores compared with hemithorax IR alone. 83
Figure 3.2.10. AZD6738 in combination with CT-guided left lung IR did not induce body weight loss. 85
Figure 3.2.11. AZD6738 in combination with CT-guided left lung IR did not reduce superficial tumour counts or ratio. 86
Figure 3.2.12. AZD6738 in combination with CT-guided left lung IR did not reduce tumour numbers or area per lung slice. 86
Figure 3.2.13. AZD6738 in combination with CT-guided left lung IR did not affect MRI tumour volume change compared with IR alone. 88
Figure 3.2.14. AZD6738 in combination with CT-guided left lung IR did not affect lung weight or histology. 89

Figure 3.2.15. AZD6738 in combination with IR did not affect pan-nuclear γH2AX levels in tumours. 91
Figure 3.2.16. AZD6738 in combination with IR did not affect pan-nuclear γH2AX levels in bronchial epithelial cells..... 93
Figure 3.2.17. AZD6738 in combination with IR did not affect pan-nuclear γH2AX in oesophageal epithelial cells..... 94
Figure 3.2.18. AZD6738 in combination with IR decreased pKAP1 levels in tumours. 96
Figure 3.2.19. AZD6738 in combination with IR did not affect pKAP1 levels in bronchial epithelial cells. 97
Figure 3.2.20. AZD6738 in combination with IR did not affect pKAP1 levels in oesophageal epithelial cells..... 98
Figure 3.3.1. Non-homologous end joining. 104
Figure 3.3.2. Main aims and experimental arms. 106
Figure 3.3.3. AZD7648 in combination with IR results in increased tumour growth inhibition in Calu6 xenografts. 107
Figure 3.3.4. Whole thorax early intervention treatment with AZD7648 combined with IR induced sustained body weight loss in A/J mice. 109
Figure 3.3.5. AZD7648 combined with whole thorax IR results in oesophageal inflammation. 111
Figure 3.3.6. AZD7648 in combination with whole thorax IR did not induce body weight loss..... 112
Figure 3.3.7. AZD7648 in combination with whole thorax IR shows subclinical histological evidence of oesophageal epithelium damage..... 113
Figure 3.3.8. AZD7648 in combination with hemithorax IR induces mild body weight loss and skin effects. 115
Figure 3.3.9. AZD7648 in combination with hemithorax IR reduced superficial tumour counts and ratio compared with hemithorax IR alone..... 117
Figure 3.3.10. AZD7648 in combination with hemithorax IR reduced tumour numbers and area per lung slice compared with hemithorax IR alone. 118
Figure 3.3.11. AZD7648 in combination with hemithorax IR significantly altered lung weights and fibrosis scores compared with hemithorax IR alone. 119
Figure 3.3.12. AZD7648 in combination with CT-guided left lung IR did not induce body weight loss. 121

Figure 3.3.13. AZD7648 in combination with CT-guided left lung IR did not reduce superficial tumour counts or ratio. 122
Figure 3.3.14. AZD7648 in combination with CT-guided left lung IR did not reduce tumour numbers or area per lung slice. 123
Figure 3.3.15. AZD7648 in combination with CT-guided left lung IR significantly reduced tumour volume change compared with IR alone. 124
Figure 3.3.16. AZD7648 in combination with CT-guided left lung IR did not alter lung weight or histology 125
Figure 3.3.17. AZD7648 in combination with IR did not affect γH2AX levels in tumours. 127
Figure 3.3.18. AZD7648 in combination with IR did not affect γH2AX levels in bronchial epithelial cells. 129
Figure 3.3.19. AZD7648 in combination with IR did not affect γH2AX in oesophageal epithelial cells. 130
Figure 3.3.20. AZD7648 in combination with IR decreased pKAP1 levels in tumours. 132
Figure 3.3.21. AZD7648 in combination with IR did not affect pKAP1 levels in bronchial epithelial cells. 133
Figure 3.3.22. AZD7648 in combination with IR did not affect pKAP1 levels in oesophageal epithelial cells 134
Figure 3.4.1. ATM phosphorylation and induction of DSB response 139
Figure 3.4.2. Main aims and experimental arms. 141
Figure 3.4.3. AZD1390 in combination with IR results in increased tumour growth inhibition in Calu6 xenografts. 142
Figure 3.4.4. Whole thorax IR and AZD1390 induced significant body weight loss in A/J mice. 144
Figure 3.4.5. AZD1390 combined with whole thorax IR results in oesophageal inflammation. 146
Figure 3.4.6. AZD1390 in combination with hemithorax IR induces body weight loss and skin effects. 148
Figure 3.4.7. AZD1390 in combination with hemithorax IR did not reduce superficial tumour counts or ratio compared with hemithorax IR alone. 149
Figure 3.4.8. AZ1390 in combination with hemithorax IR did not reduce tumour numbers or burden compared with hemithorax IR alone. 150

Figure 3.4.9. AZD1390 in combination with hemithorax IR did not alter lung weights but significantly increased fibrosis scores compared with hemithorax IR alone. 151
Figure 3.4.10. AZD1390 in combination with CT-guided left lung IR did not induce body weight loss. 153
Figure 3.4.11. AZD1390 in combination with CT-guided left lung IR did not reduce superficial tumour counts and increased tumour ratio. 154
Figure 3.4.12. AZD1390 in combination with CT-guided left lung IR did not reduce tumour numbers or area per lung slice. 155
Figure 3.4.13. AZD1390 in combination with CT-guided left lung IR did not affect MRI tumour volume change compared with IR alone. 156
Figure 3.4.14. AZ1390 in combination with CT-guided left lung IR did not affect lung weight or histology 157
Figure 3.4.15. AZD1390 in combination with IR did not affect γH2AX levels compared with IR alone in tumours. 159
Figure 3.4.16. AZD1390 altered IR-induced γH2AX levels in bronchial epithelial cells. 161
Figure 3.4.17. AZD1390 in combination with IR did not affect γH2AX levels in oesophageal epithelial cells 162
Figure 3.4.18. AZD1390 in combination with IR decreased the percentage of pKAP1-positive cells in tumours. 164
Figure 3.4.19. AZD1390 in combination with IR did not affect pKAP1 levels in bronchial epithelial cells. 165
Figure 3.4.20. AZD1390 in combination with IR did not affect pKAP1 levels in oesophageal epithelial cells 166
Figure 4.1.1. Timelines of therapeutic window treatments and IR-induced normal tissue effects. 174
Appendix Figure 6.1. Experimental design of Gulmay 320 dosimetry using mouse phantoms in whole thorax and hemithorax lung irradiation rig. 207
Appendix Figure 6.2. Hemithorax irradiation rig led placement 208
Appendix Figure 6.3. A/J oesophageal epithelial cells are BrdU-positive. 209
Appendix Figure 6.4. Early intervention schedule for A/J treated with AZD6738. 210
Appendix Figure 6.5. AZD6738 did not induce body weight loss. 210
Appendix Figure 6.6. AZD6738 treatment did not reduce superficial tumour counts. 211

Appendix Figure 6.7. Early intervention schedule for A/J treated with AZD7648. ... 212
Appendix Figure 6.8. AZD7648 did not induce body weight loss. 212
Appendix Figure 6.9. AZD7648 treatment did not reduce superficial tumour counts. 213

List of Tables

Table 1.1.1. Staging and lung cancer incidence and 5-year survival in England. 1
Table 1.1.2. Stages of NSCLC and standard treatment options. 4
Table 1.1.3. Side effects from conventional radiotherapy. 17
Table 2.12.1. Antibodies used for immunohistochemistry. 36
Table 2.15.1. Masson's trichrome staining procedure modified for lung tissues. 37
Table 3.1.1. α/β ratio and biological effective dose evaluation for fractionated and single dose thoracic IR. 56
Table 3.2.1. ATR inhibitors currently in clinical trials. 71
Table 3.3.1. DNA-PK inhibitors currently in clinical trials. 105
Table 3.4.1. ATM inhibitors currently in clinical trials. 140
Table 4.1.1. Summary of anti-tumour and normal tissue effects of AZD6738, AZD7648, and AZD1390. 175
Appendix Table 6.1. Definitions of TNM staging. 203
Appendix Table 6.2. TNM Staging within each prognostic stage. 204
Appendix Table 6.3. Reagents. 205
Appendix Table 6.4. Dosimetry variation of whole thorax and hemithorax lung rig at each position and depth into phantom mouse. 206

1. General Introduction

1.1. Lung cancer diagnosis and staging

Lung cancer is the leading cause of cancer-related deaths worldwide (Bray et al., 2018). Approximately 1.8 million deaths each year are attributed to lung cancer, which is 18.4% of all cancer-related deaths (Bray et al., 2018). Smoking tobacco is a major risk factor in developing lung cancer and has been linked with more than 70% of cases in the UK (Brown et al., 2018). The most common route to patient diagnosis with lung cancer is by emergency presentation of symptoms, and a majority of these cases are either stage III or IV at diagnosis (**Table 1.1.1**) (Cancer Research UK, 2016). These stages can be further broken down using the tumour-node-metastasis (TNM) scoring based on clinical or pathological assessment of the patient (**Appendix Tables 6.1 & 6.2**). Due to the late stage at which the disease is identified, 5- and 10-year overall survival rates are low (16.2% and 9.5%, respectively) and have remained low for over 40 years (Cancer Research UK, 2020).

Stage at diagnosis	General description[1]	Incidence at diagnosis (%)[2]	Five-year survival (%)[3]
I	Tumour is ≤ 5 cm; no metastases	15	56.6
II	Tumour of any size; direct metastasis extension in ipsilateral peribronchial or hilar lymph nodes and intrapulmonary nodes	7	34.1
III	Tumour(s) of any size within lobes of one lung or spread into main non-lung thoracic structures; metastases into thoracic lymph nodes	19	12.6
IV	Tumour(s) of any size and any lymph node invasion with separate distant lung and/or other organ metastasis	48	2.9
Unknown	Tumour stage not determined	10	---

Table 1.1.1. Staging and lung cancer incidence and 5-year survival in England. See **Appendix Tables 6.1 & 6.2** for TMN definitions and detailed staging.
[1]AJCC Cancer Staging Manual, 2017 (Amin and American Joint Committee on Cancer., 2017)
[2]Lung cancer incidence by stage at diagnosis, 2017 (Cancer Research UK, 2017)
[3]Lung cancer survival by stage at diagnosis, 2013-2017 (Cancer Research UK, 2019b)

Lung cancer is made up of two major groups that are identified by their histological subtype, approximately 15% of which are small cell lung cancer, and the remaining 85% are classed as non-small cell lung cancer (NSCLC) (PDQ® Adult Treatment Editorial Board, 2020; Wood et al., 2015). NSCLC can be further categorised into adenocarcinoma (40%), squamous cell carcinoma (25-30%), and large cell carcinoma (10-15%), but they are diagnosed, staged, and treated similarly with a similar prognosis (PDQ® Adult Treatment Editorial Board, 2020; Wood et al., 2015).

In the UK National Health Service (NHS), the guidelines from the National Institute for Health and Care Excellence recommend a chest X-ray if lung cancer is suspected from a display of symptoms (National Institute for Health and Care Excellence, 2020). This exam is typically followed by computed tomography (CT) to confirm the presence of a tumour (National Health Service, 2019; National Institute for Health and Care Excellence, 2020). Additional testing can include a positron emission tomography (PET) scan, a bronchoscopy, or an endobronchial ultrasound along with a biopsy of the primary tumour and suspected lymph nodes (National Health Service, 2019). If the tumour is suspected to have metastasised, a magnetic resonance imaging (MRI) scan, bone scan, or abdominal ultrasound can also be used (Cancer Research UK, 2019a).

In contrast to the UK, the US Preventative Services Task Force and Centers for Disease Control and Prevention recommend that a subset of at-risk individuals in the US be screened yearly for lung cancer; these guidelines include an age range (≥ 55 to 80 years old), a heavy smoking history (≥ 30 pack years[1]), and smoking cessation of less than 15 years prior (CDC, 2019; Richards et al., 2014; U.S. Preventive Services Task Force, 2013). The National Lung Screening Trial, which investigated using low-

[1]Pack year: smoking an average of one cigarette pack per day for one year.

dose CT (LDCT) instead of chest X-rays to screen for lung cancer, found that LDCT improves mortality rates and has become a standard of care in the US (Hoffman and Sanchez, 2017; Mazzone et al., 2018; National Lung Screening Trial Research Team et al., 2011). While LDCT screening does increase the rate of false positives, there are further guidelines in place to either continue annual screening on benign nodules or follow-up on suspected lesions with a chest CT, PET/CT, or biopsy/excision (Eggert et al., 2017).

1.2. NSCLC treatment

Once the NSCLC stage has been determined, the appropriate treatment is planned and personalised for the patient by an interdisciplinary team. Broadly, NSCLC treatment options include surgery, chemotherapy, and radiotherapy, which can be combined together along with additional, tumour characteristic specific targeted treatments (**Table 1.1.2**) (PDQ® Adult Treatment Editorial Board, 2020). Notably, at each stage of the disease, a subset of patients will require radiotherapy in the treatment of their disease; this amounts to more than a quarter of all NSCLC patients receiving either curative or palliative radiotherapy as part of their treatment (Cheng et al., 2019; National Cancer Registration and Analysis Service, 2015).

Stage of NSCLC		Standard Treatment Options
Occult		• Surgery
Stage 0		• Surgery • Endobronchial therapies
Stages IA and IB		• Surgery • Radiotherapy
Stages IIA and IIB		• Surgery • Adjuvant chemotherapy • Neoadjuvant chemotherapy • Radiotherapy
Stage IIIA	Resected or resectable disease	• Surgery • Adjuvant chemotherapy • Neoadjuvant chemotherapy
	Unresectable disease	• Radiation therapy • Chemoradiation therapy
	Superior sulcus tumours	• Radiotherapy • Surgery • Chemoradiation therapy followed by surgery
	Tumours that invade the chest wall	• Surgery • Surgery and radiotherapy • Radiotherapy • Chemotherapy combined with radiation therapy and/or surgery
Stages IIIB and IIIC		• Sequential or concurrent chemotherapy and radiotherapy • Radiotherapy dose escalation for concurrent chemoradiation • Additional systemic therapy before or after concurrent chemotherapy and radiotherapy
Newly Diagnosed Stage IV, Relapsed, and Recurrent		• Cytotoxic combination chemotherapy • Combination chemotherapy with monoclonal antibodies • Maintenance therapy after first-line chemotherapy • Targeted therapies with inhibitors • Immune checkpoint inhibitor with or without chemotherapy
Progressive Stage IV, Relapsed, and Recurrent		• Chemotherapy • Targeted therapies • Immunotherapy

Table 1.1.2. Stages of NSCLC and standard treatment options. (Reproduced from PDQ® Adult Treatment Editorial Board, 2020).

The standard treatment for stage I and II NSCLC is surgical resection of tumours, and a possible addition of radiotherapy if positive margins remain post-surgery (Tyldesley et al., 2001). Patients with inoperable stage I and II NSCLC who receive radiotherapy with curative intent are treated with either stereotactic ablative radiotherapy (SABR, 54-60 Gy in 3 to 8 fractions spread over one to two weeks), continuous hyperfractionated, accelerated radiotherapy (CHART, 54 Gy delivered in 36 fractions over 12 continuous days), or conventional fractionation (either 64-66 Gy in 32-33 fractions or 55 Gy in 20 fractions) (Prewett et al., 2012; The Royal College of Radiologists, 2019).

In stage III locally advanced NSCLC, while surgery is possible for a subset of patients, a majority of patients (54.9%) will receive radiotherapy as part of their treatment with either curative or palliative intent (Evison and AstraZeneca, 2020). The current standard of care for local tumour control is concurrent chemoradiotherapy, but many patients (59%) are unfit for this treatment plan due to poor performance status and comorbidities (De Ruysscher et al., 2009). For these patients, radiotherapy is the only treatment. To improve patient outcomes, dose escalation or acceleration of radiotherapy treatments have shown promise in recent studies (Ramroth et al., 2016; Robinson et al., 2020). These methods are currently in phase 2 of a multi-arm clinical trial investigating how to effectively increase the radiotherapy dose in patients and have reported encouraging 2-year survival rates without dose limiting toxicities (ISRCTN47674500) (Robinson et al., 2020). This suggests that local control of stage III tumours using radiotherapy could be improved, either by altering the radiotherapy treatment method itself or by finding ways to increase the biological effect of radiation on tumour tissues.

For patients with stage IV NSCLC, tumours are tested for specific mutations that may allow the use of targeted therapies (Hirsch et al., 2017). Several inhibitors have

been developed to target common driver mutations found in NSCLC such as those in the epidermal growth factor (EGFR) or anaplastic lymphoma kinase (ALK) genes (**Fig. 1.1.1**) (Hirsch et al., 2017; PDQ® Adult Treatment Editorial Board, 2020). For some patients, aggressive treatment with targeted EGFR or ALK therapies can lead to increased progression-free survival (Gomez et al., 2016). An emerging area of NSCLC treatment includes promising immunotherapies that can be used against tumours with a high expression of programmed death-ligand 1 (PD-L1) such as durvalumab or pembrolizumab in combination with chemoradiotherapy or chemotherapy (Antonia et al., 2018; Gandhi et al., 2018; Gray et al., 2020; Ko et al., 2018).

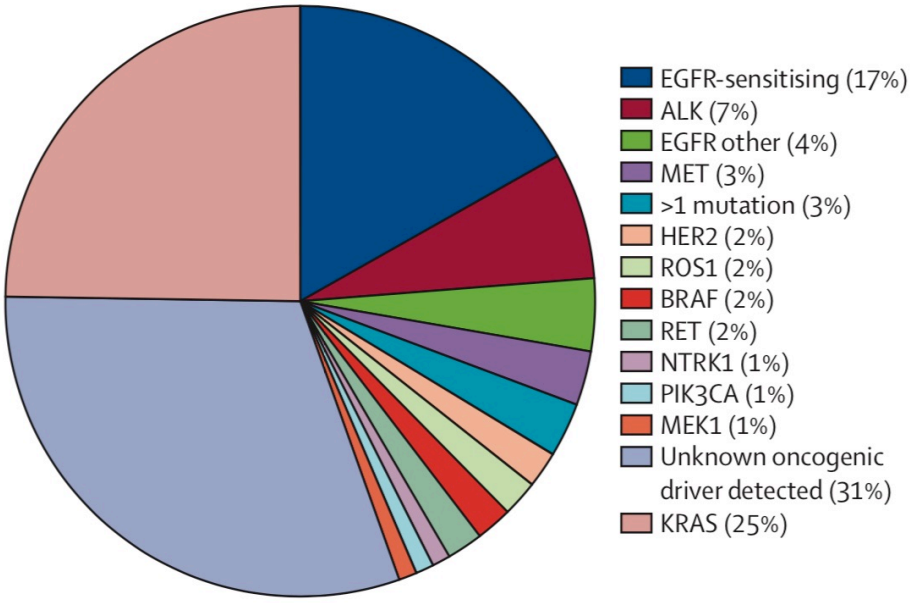

Figure 1.1.1. Common oncogenic drivers of NSCLC. (Reproduced from Hirsch et al., 2017).

However, for patients without a targetable oncogenic mutation or low PD-L1 expression in their tumours, treatment is limited to chemotherapy with additional palliative radiotherapy or other symptom management treatments (D'Antonio et al., 2014; PDQ® Adult Treatment Editorial Board, 2020). There are a number of clinical trials ongoing with inhibitors of other cellular pathways that will be discussed in later chapters (**Chapters 1.4**).

1.3. Principles of radiotherapy

Radiotherapy uses the energy emitted by ionising radiation (IR) to damage tumour cells through direct or indirect effects (Hall and Giaccia, 2012). IR can cause direct damage to deoxyribonucleic acid (DNA) structures or indirect damage through the creation of free radicals such as reactive oxygen species (ROS) that interact with DNA molecules (Santivasi and Xia, 2014). The three main types of IR-induced DNA damage are base damage, single strand breaks (SSBs), and DNA double strand breaks (DSBs), considered the more lethal of the two (**Fig. 1.1.2**) (Lomax et al., 2013; Santivasi and Xia, 2014). While base damage and SSBs are mostly caused by low linear energy transfer (LET), DSBs are the result of high LET (Lomax et al., 2013).

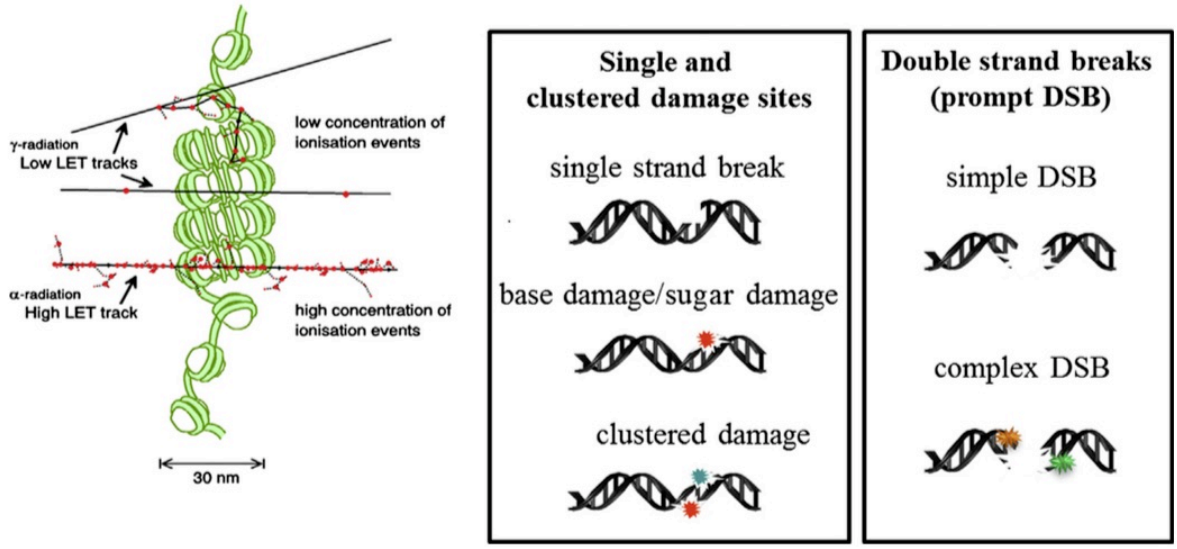

Figure 1.1.2. Different types of IR-induced DNA damage. Low LET tracks cause SSBs, base damage, and clustered damage, while high LET tracks causes DSBs (Reproduced from Lomax et al., 2013).

If DNA damage is unrepaired or improperly repaired, it can lead to cell death. This occurs more readily in rapidly proliferating cells that are frequently undergoing mitosis as chromosome aberrations can cause defective cell division (Hall and Giaccia, 2012). Importantly, sustained proliferative signalling is one of a set of traits that differentiate cancer cells from normal cells known as the enabling characteristics and hallmarks of cancer (Hanahan and Weinberg, 2000; Hanahan and Weinberg, 2011). These hallmarks and characteristics also include enabling replicative immortality,

evading growth suppression, resisting cell death, inducing angiogenesis, activating metastasis, avoiding immune destruction, deregulating cellular energetics, genome instability, and tumour promoting inflammation (Hanahan and Weinberg, 2000; Hanahan and Weinberg, 2011).

Sustained chronic proliferation, avoidance of growth suppression, and resistance of cell death allows cancer cells to rapidly divide and grow without regulation, and genomic instability contributes to the dysregulation of normal cellular processes including the DNA damage response (DDR) pathways (Hanahan and Weinberg, 2011; Jackson and Bartek, 2009). However, these characteristics also can make tumour cells vulnerable to radiotherapy; as tumours proliferate without normal regulatory or repair processes, unrepaired DNA damage can accumulate, making tumours more susceptible to further damage, which can be exploited by using IR as an anti-cancer therapy (Boss et al., 2014; Jackson and Bartek, 2009; Santivasi and Xia, 2014). Additionally, the induction of angiogenesis can increase the tumour oxygen concentration, which is necessary for the indirect damage from the generation of ROS by IR (Boss et al., 2014; Lomax et al., 2013).

The intrinsic radiosensitivity of tumour cells is one of the 5 Rs of radiobiology, the others being repair of IR-induced damage, repopulation, redistribution of cells within the cell cycle, and reoxygenation (Good and Harrington, 2013; Hall and Giaccia, 2012; Steel et al., 1989). Normal cells treated with standard fractionated radiotherapy are able to repair sublethal damage and repopulate tissues during the time between fractions, minimising normal tissue effects (Good and Harrington, 2013; Hall and Giaccia, 2012). Meanwhile, tumours undergo a redistribution of cells into more radiosensitive phases of the cell cycle and reoxygenation, allowing for more ROS generation upon IR treatment and further damage (Good and Harrington, 2013; Hall and Giaccia, 2012; McBride and Schaue, 2020). This difference between the tumour

and normal tissue responses to IR, called the therapeutic window, is critical to optimise treatment planning and minimise toxicities (**Fig. 1.1.3**).

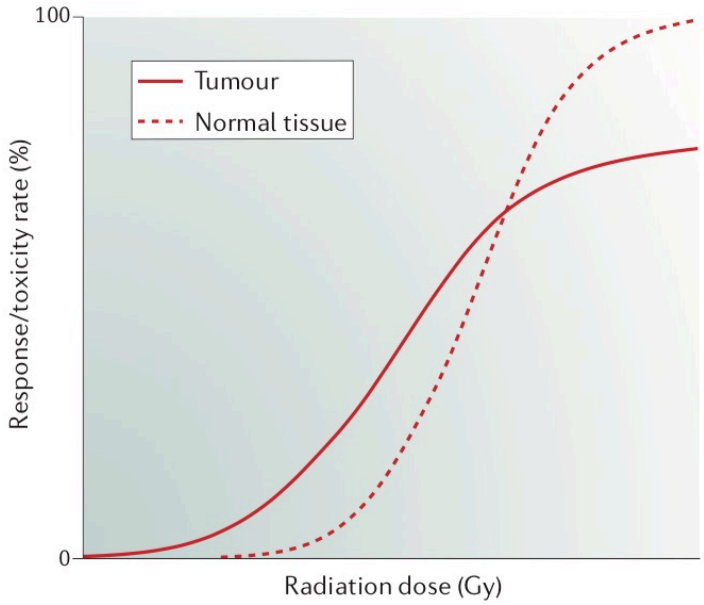

Figure 1.1.3. Therapeutic window of IR dose, tumour response, and normal tissue toxicities. As the radiation treatment dose increases, tumour response is increased, but normal tissue toxicities can also increase. The therapeutic window is the range, if any, between the tissue responses that allows for the best tumour control and least normal tissue damage (Reproduced from Sharma et al., 2016).

1.4. Radiotherapy and targeting the DDR pathway

A major limitation of radiotherapy in the treatment of cancer is the damage it also does to normal tissues. While advancements in imaging and delivery technologies have been made to improve targeting, radiotherapy also affects surrounding normal tissues, and any organs at risk (OAR) are important factors that must be considered during treatment planning (Bar-Ad et al., 2012; Berkey, 2010; Fleming et al., 2016; Kasmann et al., 2020; McBride and Schaue, 2020; Senan et al., 2004). Current NSCLC treatment guidelines use organ volume percentages and dose limitations to control the potential for toxicities. For example, in conventional fractionation, the total volume of the lung treated with 20 Gy is limited to below 35%, known as V_{20Gy} < 30-35% limit (Fleming et al., 2016). An atlas has been created to delineate thoracic OAR in radiotherapy and provide consistency between physicians and treatment schedules,

but there is still a need for consensus on the volume and dose limits of OAR (Fleming et al., 2016; Kong et al., 2011).

Despite precision targeting of tumours continuing to increase anti-tumour efficacy and reduce normal tissue side effects, local disease recurrence is still common (Robinson et al., 2020). Dose escalation is a proposed solution to improve tumour control supported by Ramroth *et al.* (2016); however, in their meta-analysis, the authors were unable to assess the toxicities arising from dose due to reporting inconsistencies (Ramroth et al., 2016). Additionally, treatment of centrally located tumours with stereotactic ablative body radiotherapy (SABR) has a high risk of Grade 3+ toxicities (Tekatli et al., 2016; Timmerman et al., 2006). Therefore, any approaches that involve increasing the IR dose must avoid also increasing the risk of severe toxicities.

With the improvements in treatment modalities, radiotherapy can target numerous inherent qualities of tumours and spare normal tissues; however, there are several characteristics that IR alone cannot overcome and must be addressed through the use of additional therapies (Boss et al., 2014; Sharma et al., 2016). The combination of radiotherapy with compounds that target these characteristics can increase the effectiveness of radiotherapy as a cancer treatment (**Fig. 1.1.4**).

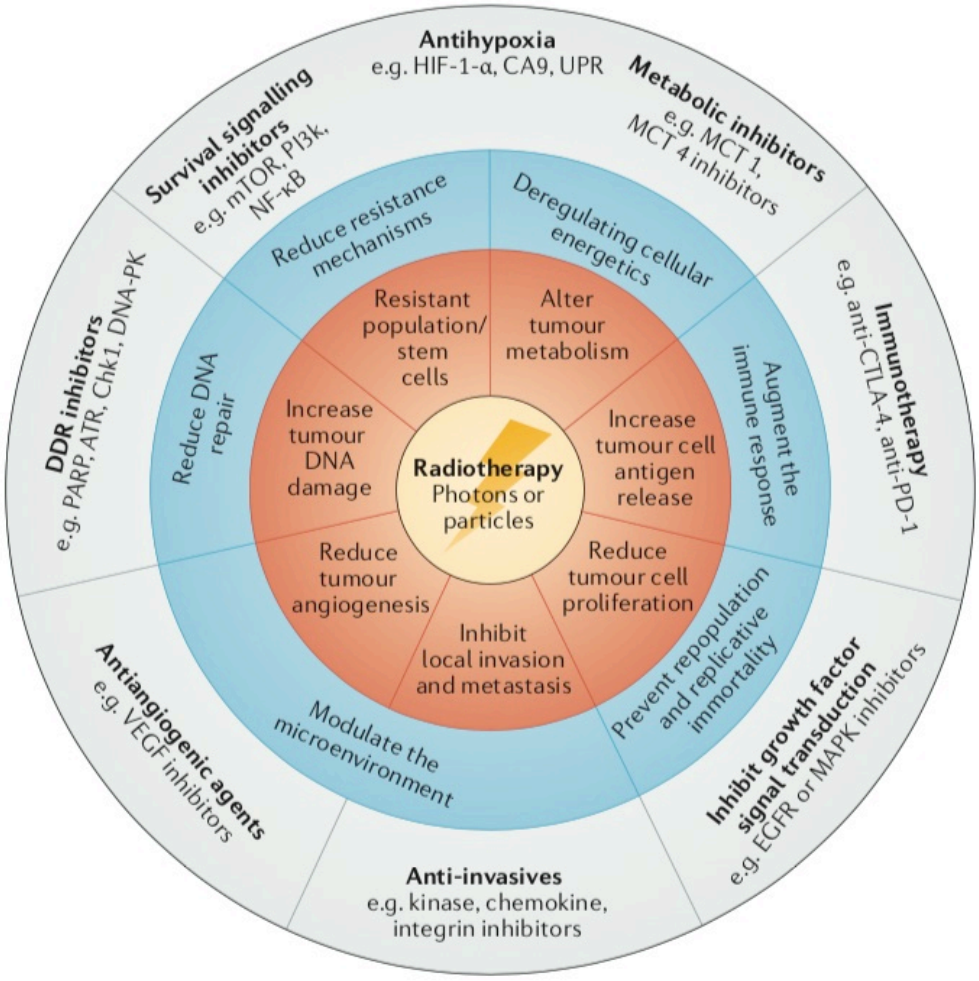

Figure 1.1.4. Radiotherapy and drug combination strategies to target cancer characteristics. (Reproduced from Sharma et al., 2016).

One such strategy involves inhibiting DDR pathways. Importantly for cell survival, DNA damage triggers different mechanisms within DDR pathways depending on the type of the lesion and location of the cell within the cell cycle, although these pathways do have overlapping compensatory functions (Pilie et al., 2019; Weber and Ryan, 2015). The DDR pathways allow cells to repair DNA damage through base excision repair (BER), nucleotide excision repair (NER), homologous recombination (HR), or non-homologous end joining (NHEJ). IR can induce base damage, single strand breaks (SSBs), or double strand breaks (DSBs), and cells respond by triggering the appropriate repair pathway (**Fig. 1.1.5**) (Blackford and Jackson, 2017; Pilie et al., 2019; Weber and Ryan, 2015).

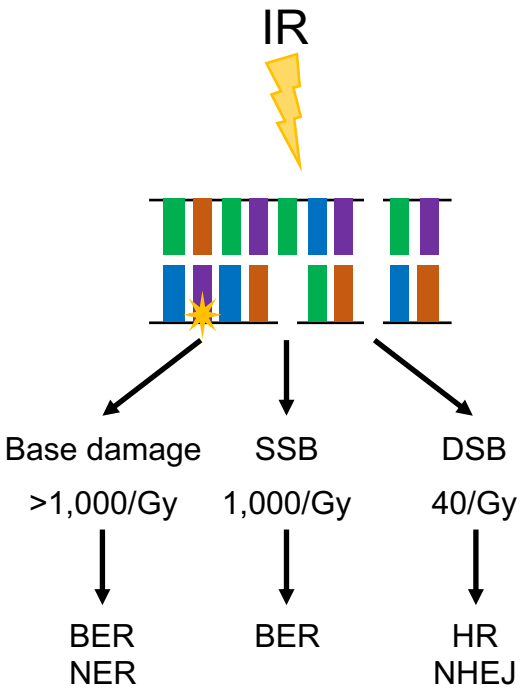

Figure 1.1.5. IR-induced DNA damage and repair pathways. IR induces three main types of DNA damage: base damage, SSB and DSB. Base damage is repaired by excision repair (BER) or nucleotide excision repair (NER). SSBs are repaired by BER, and DSBs can be repaired by homologous recombination (HR) or non-homologous end joining (NHEJ) (Hall and Giaccia, 2012).

NER and BER are two processes that are triggered upon detection of DNA base damage, bulky adducts or SSBs; following detection, the damaged region is excised and the DNA ends are processed and repaired through normal DNA replication machinery that re-ligates the ends together (Caldecott, 2008; Hosoya and Miyagawa, 2014; Lord and Ashworth, 2012). HR and NHEJ are the predominant pathways that repair DSBs and are selected based on the cell cycle phase and amount of resection necessary; NHEJ can be activated throughout the cell cycle while HR is restricted to S or G2 phase (Brandsma and Gent, 2012; Huhn et al., 2013). NHEJ relies on the direct re-ligation of the DNA ends to repair the damage and is considered error-prone (Huhn et al., 2013; Lord and Ashworth, 2012). HR requires resection and the use of a template strand from a homologous sister chromatid in order to synthesise the missing DNA sequence and is considered error-free (**Fig. 1.1.6**) (Huhn et al., 2013; Lord and Ashworth, 2012).

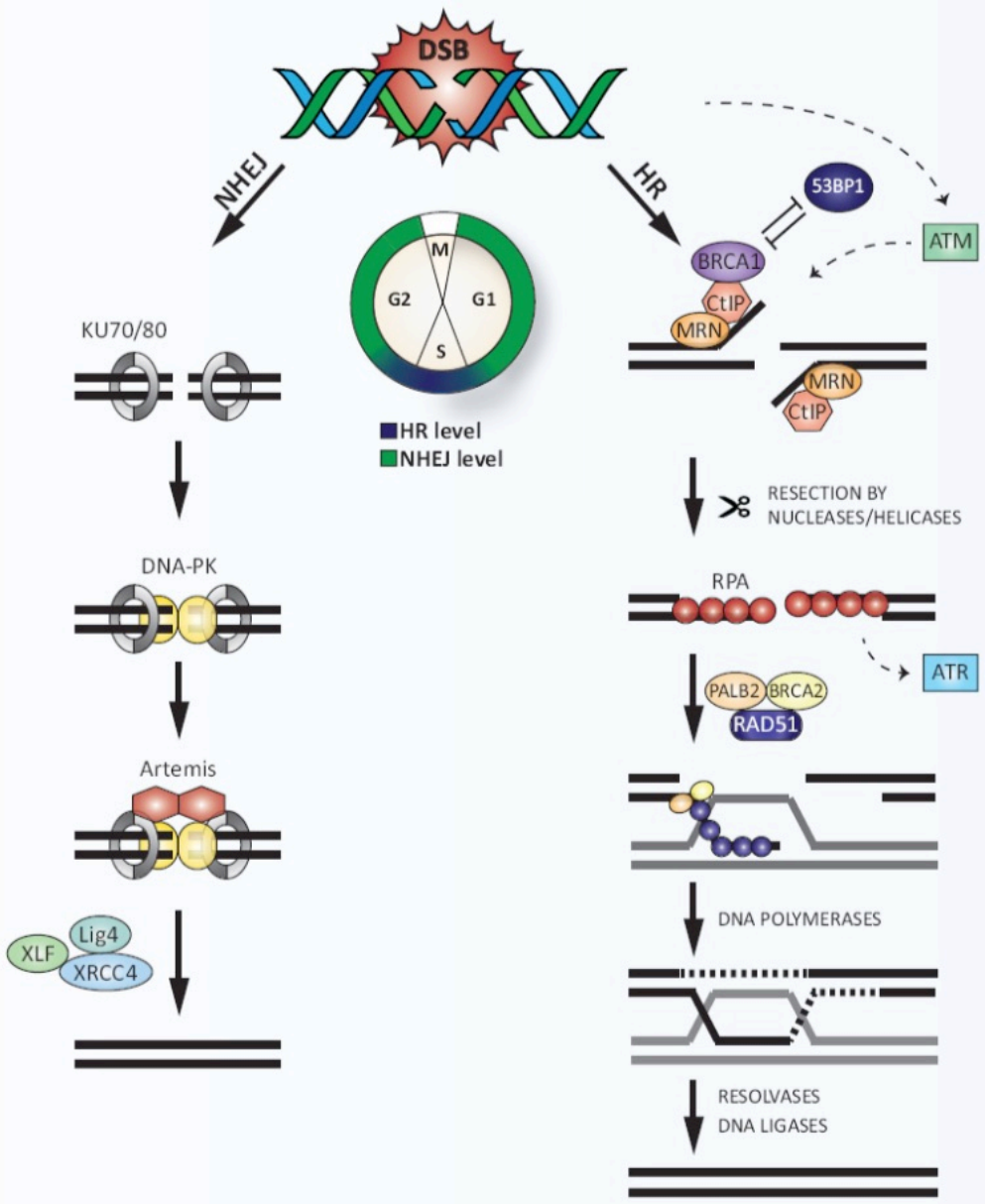

Figure 1.1.6. DSB repair through NHEJ or HR. In NHEJ, proteins bind to protect the ends of the DNA, which are then processed and directly re-ligated together. HR proteins first bind to and remove broken DNA ends and then use a homologous sister chromatid as a template strand to synthesise DNA. Once the copy is complete, the strands are separated and re-joined together (Reproduced from Huhn et al., 2013).

Current clinical strategies to modulate DDR pathways to increase the efficacy of radiotherapy and prevent cell repair processes involve many different compounds and targets, which are presently being investigated in clinical trials (**Fig. 1.1.7**). Three major DDR proteins, DNA-PK, ATR, and ATM, and their respective inhibitor compounds in development are presented in later chapters (**Table 3.2.1, 3.3.1, & 3.4.1**). Another major target involved in the repair of SSBs, poly(ADP-ribose) polymerase 1 (PARP1),

already has several approved inhibitors such as olaparib for use as monotherapies in multiple cancers (Lord and Ashworth, 2012; Rose et al., 2020).

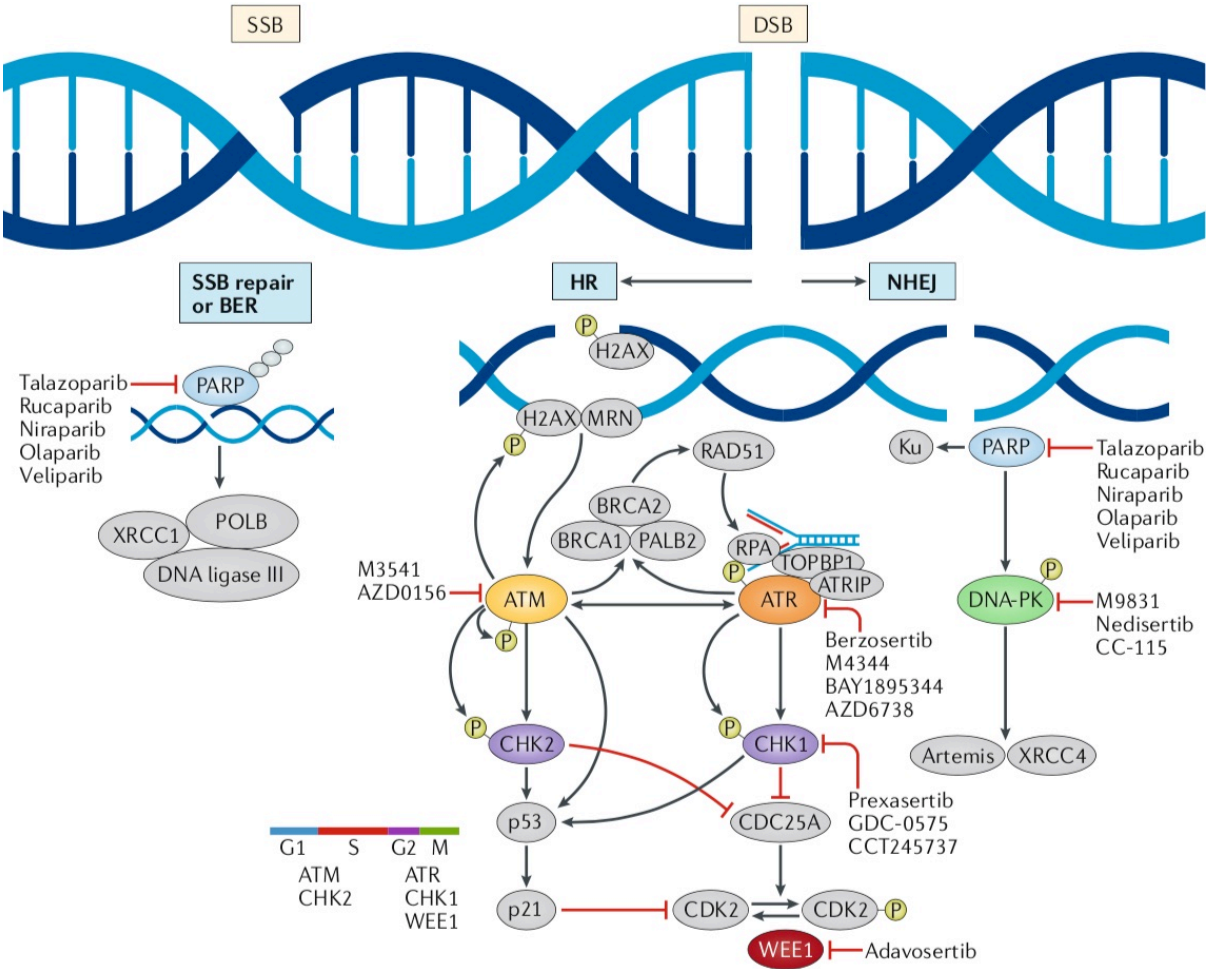

Figure 1.1.7. DDR pathways and clinical compounds. After IR induces single strand breaks (SSBs) or double strand breaks (DSBs), the damage is repaired by activating DDR pathways such as base excision repair (BER), homologous recombination (HR), or non-homologous end joining (NHEJ). Proteins within these pathways can be targeted by compounds to inhibit their function and signalling and ultimately, impair repair processes (Reproduced and modified from Pilie et al., 2019).

One recently initiated study called the CONCORDE trial (NCT04550104) has been developed to evaluate several DDR inhibitors in combination with radiotherapy in stage II and III NSCLC (**Fig. 1.1.8**) (Faivre-Finn et al., 2020; Walls et al., 2020). The platform is a multi-arm, multi-centre phase I trial using 5 DDR inhibitors (olaparib, AZD1390, AZD6738, AZD7648, and AZD1775) combined with radiotherapy, which will be compared to the standard radical dose radiotherapy regimen (Faivre-Finn et al., 2020; Walls et al., 2020). Patients will be assigned to a study arm and randomised in a 3:1 allocation of DDRi and radiotherapy against radiotherapy alone; dose limiting

toxicities will be measured as the primary endpoint for the first 12 months, but patients will continue to be monitored for up to 2 years for secondary outcomes (Faivre-Finn et al., 2020; Walls et al., 2020). By efficiently evaluating multiple DDR inhibitors in combination with radiotherapy in a single phase I study, the CONCORDE trial will provide robust insights into the clinical development of each combination and a potential framework for future studies investigating radiotherapy and drug combinations.

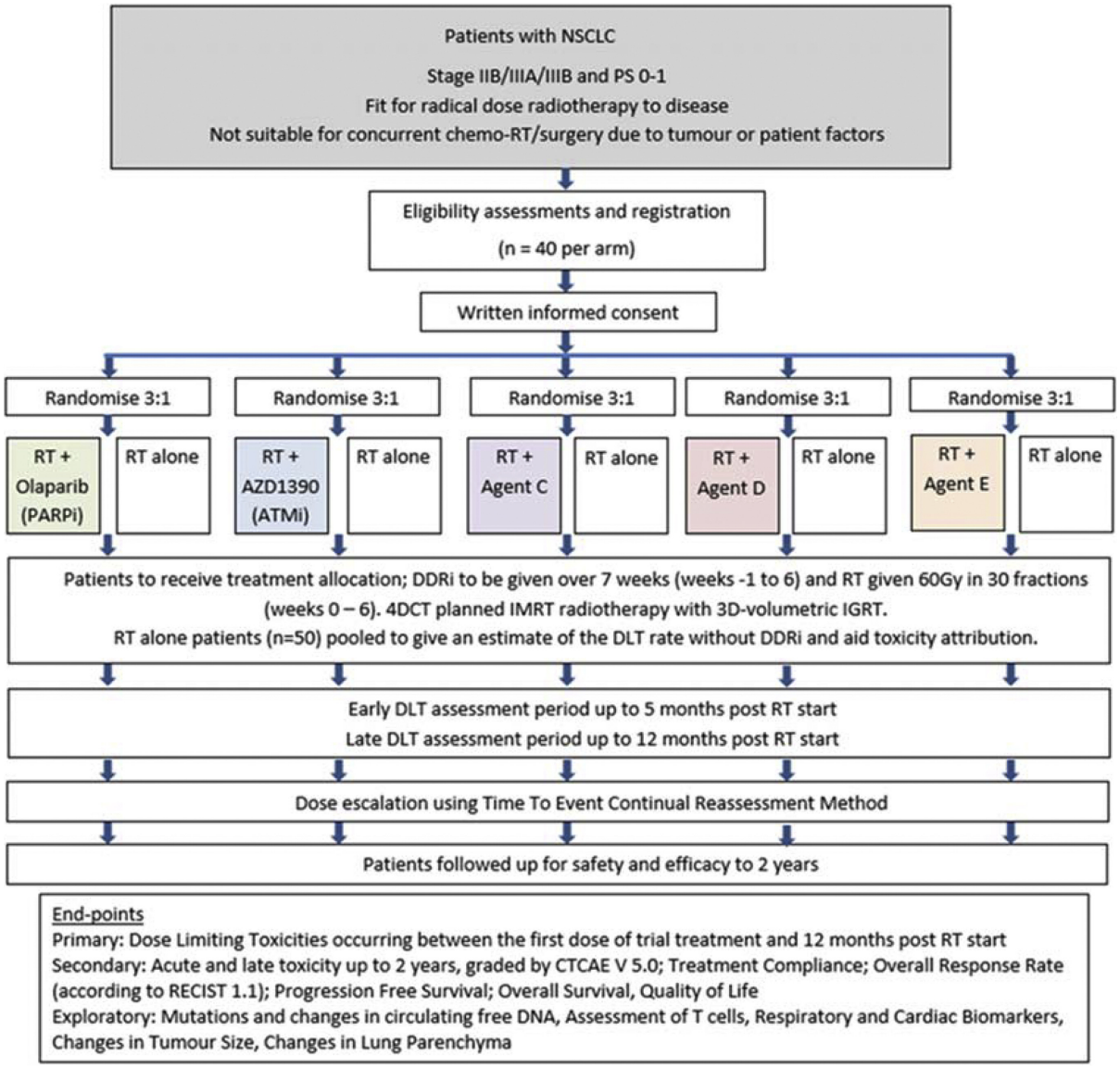

Figure 1.1.8. The CONCORDE platform summary. Five DDR inhibitors will be used across the arms of the study, each with a separate comparator group of radiotherapy alone and an allocation ratio of 3:1. Radiotherapy will be given as 60 Gy in 30 fractions over 6 weeks, and each DDRi will be given for one week up to the start of radiotherapy and concurrently for the following 6 weeks of radiotherapy (Reproduced from Faivre-Finn et al., 2020).

1.5. The therapeutic window of response to IR

Normal tissue IR response times broadly fit into two categories, early (acute) and late, based on their IR sensitivity and proliferation rates as well as the fractionation schedule of treatment and patient characteristics (Bar-Ad et al., 2012; Dehing-Oberije et al., 2009; Hall and Giaccia, 2012; Kasmann et al., 2020; McBride and Schaue, 2020; Vogelius and Bentzen, 2012). These effects can manifest over the days, weeks, months, and years following treatment (**Fig. 1.1.9**).

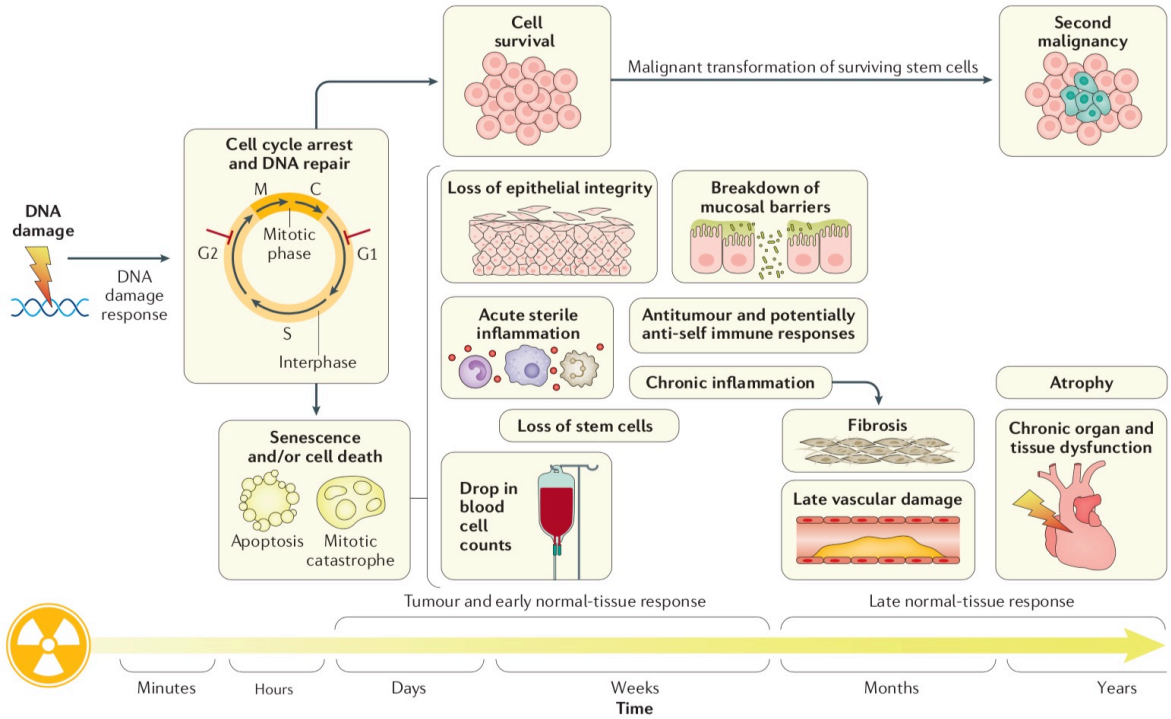

Figure 1.1.9. IR-induced tissue response timeline. After IR-induced DNA damage, cells initially respond according to the type of damage and cell cycle phase over minutes to days. If the damage is unrepaired, cells may undergo apoptosis, mitotic catastrophe, or become senescent. As cells die, the resulting inflammation within tissues can be acute or chronic and can eventually lead to permanent organ or tissue dysfunction months or years later. Surviving cells with mutations from the initial damage may also undergo malignant transformation (Reproduced from De Ruysscher et al., 2019).

Unfortunately, normal tissue effects from thoracic radiotherapy are measured in the clinic (**Table 1.1.3**). Three important side effects involving oesophageal and lung tissue responses to thoracic radiotherapy are oesophagitis, pneumonitis, and fibrosis.

Side effect	SPACE trial conventional radiotherapy (n=53)		
	Grade 1	Grade 2	Grade 3
Oesophagitis	15 (28%)	1 (2%)	0
Pneumonitis	13 (24%)	4 (8%)	1 (2%)
Dyspnoea	22 (42%)	16 (30%)	5 (9%)
Fibrosis	24 (45%)	2 (4%)	1 (2%)
Cough	31 (58%)	3 (6%)	0
Skin reactions	17 (32%)	5 (10%)	0
Rib fractures	5 (9%)	1 (2%)	0

Table 1.1.3. Side effects from conventional radiotherapy. Normal tissue side effects were measured in the SPACE trial resulting from conventional radiotherapy treatment of NSCLC (Reproduced from Nyman et al., 2016).

The oesophagus is an early responding tissue and OAR with a rapid proliferation rate sustained by stem cell populations needed for high cell turnover. In the clinic, IR-induced effects on the oesophagus, dysphagia and oesophagitis, can manifest within days to weeks from the start of treatment but onset timing varies depending on the treatment regimen (Adebahr et al., 2016; Berkey, 2010; Fleming et al., 2016; Murro and Jakate, 2015). Mild or moderate effects (Grade ≤ 2) are managed with a bland diet or dietary supplements while severe effects (Grade 3+) may require either a topical anaesthetic, tube feeding, or dose-interruption; grading of side effects is classified using the internationally recognised common terminology criteria for adverse events (CTCAE) guidelines of the National Cancer Institute (Berkey, 2010; Fleming et al., 2016; National Cancer Institute, 2017; Sasso et al., 2001; Shadad et al., 2013).

Oesophagitis can develop over the course of three interdependent stages: initial inflammation, degradation of the epithelial stem cell population, and ulceration or bacterial invasion (Duncan and Grant, 2003; Sonis, 1998). After direct and indirect IR damage to the oesophagus, inflammatory cells are recruited to the tissue and cytokines are released, which can amplify the damage (Duncan and Grant, 2003; Sonis, 1998). This is followed by apoptosis of epithelial progenitor cells and the loss of tissue renewal (Duncan and Grant, 2003; Murro and Jakate, 2015; Sonis, 1998). Finally, as the oesophageal tissue integrity is lost and ulceration occurs, opportunistic

pathogenic infections can exacerbate the tissue damage and inflammation (Duncan and Grant, 2003; Sonis, 1998). Importantly, repopulation of the epithelium can occur within days to repair the tissue, but the daily dosing schedule of fractionated thoracic IR treatments can worsen the condition; while interrupting cancer treatments due to high-grade toxicity can allow for healing, it is also associated with poorer overall survival and worse local recurrence-free survival (Duncan and Grant, 2003; Jeremic et al., 2003; Yazbeck et al., 2013).

Pneumonitis is a lung inflammation that manifests within 12 weeks of the end of treatment (Giuranno et al., 2019; Kasmann et al., 2020; Tsoutsou and Koukourakis, 2006). It can be identified either with clinical symptoms in 5-15% of patients treated with thoracic radiotherapy or by a follow-up chest radiography in between 50-90% of patients, and the incidence has been directly correlated with V_{20Gy} values (Abid et al., 2001; Jain and Berman, 2018; McDonald et al., 1995; Robinson et al., 2020; Tsoutsou and Koukourakis, 2006; Tsujino et al., 2003). In instances of Grade 2 pneumonitis, medical intervention with corticosteroids is suggested and with Grade 3 pneumonitis, supplemental oxygen may be required (Jain and Berman, 2018). Pneumonitis is an inflammatory response following IR due to both the apoptosis of lung cells as well as residual ROS (Azzam et al., 2012; Graves et al., 2010). As damaged alveolar cells undergo apoptosis, damage associated molecular pattern molecules (DAMPs) are released, recruiting immune cells such as leukocytes and macrophages to the lung interstitial space (Giuranno et al., 2019). Additionally, damaged lung epithelial cells may undergo senescence, a process that triggers the senescence-associated secretory phenotype (SASP) of pro-inflammatory cytokines and recruits further immune cells (Coppe et al., 2010; Kasmann et al., 2020).

While pneumonitis is considered treatable, initial IR lung damage and the evoked immune response can develop into the late chronic tissue response of pulmonary

fibrosis, which can be independent of a prior diagnosis of acute pneumonitis (Giuranno et al., 2019; Graves et al., 2010; Jain and Berman, 2018; Kasmann et al., 2020). Pulmonary fibrosis develops between 6 months and 2 years after radiotherapy and is characterised by activated fibroblasts restructuring lung architecture through the deposition of collagen (Graves et al., 2010; Gross and Hunninghake, 2001; Kasmann et al., 2020). However, the complex signalling and immune cell interplay by which IR-induced lung damage progresses to pulmonary fibrosis is not well understood, and current knowledge is outlined extensively in reviews of IR induced lung injury (**Fig. 1.1.10**) (Citrin and Mitchell, 2017; Giuranno et al., 2019; Graves et al., 2010; Kasmann et al., 2020; Tsoutsou and Koukourakis, 2006).

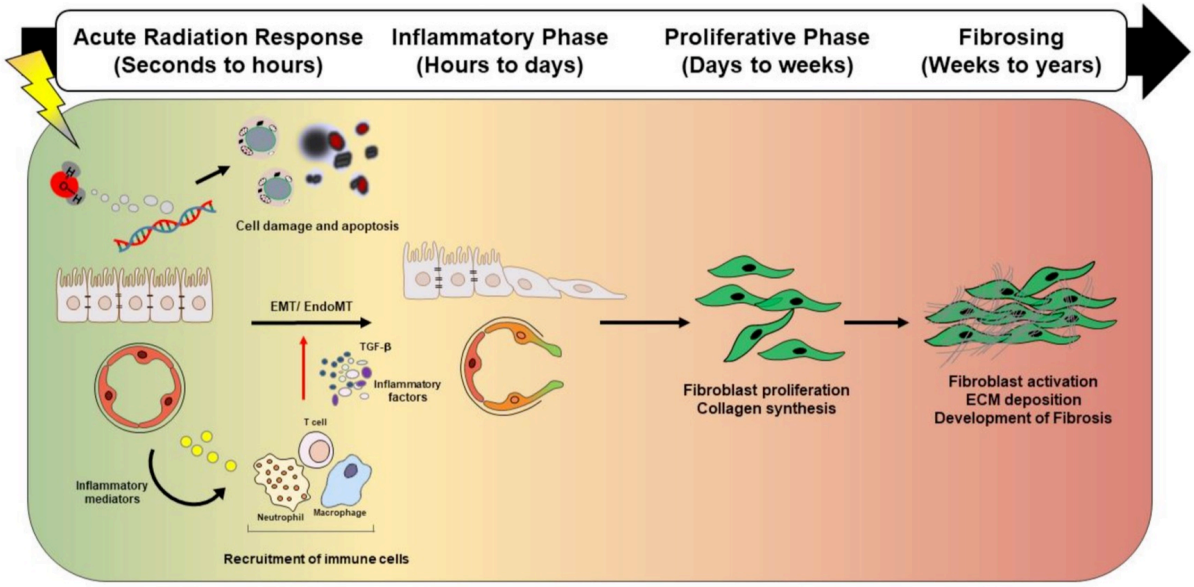

Figure 1.1.10. IR-induced lung damage progression. In response to initial damage to alveolar and vascular cells from IR, immune cells are quickly recruited as part of an inflammatory response. Over the following days, weeks, and months, fibroblasts proliferate and are eventually activated, beginning the deposition of collagen that is characteristic of fibrosis (Reproduced from Jin et al., 2020).

The heart and spinal cord also have a late response to thoracic radiation and are important OARs to consider when treatment planning (Kong et al., 2011). Radiation-induced heart disease and radiation myelopathy are without effective treatments, and avoidance by improved dose planning and delivery are essential to limiting toxicities (U.S. Department of Health and Human Services, 2017; Ming et al., 2016).

1.6. Preclinical mouse models

Before potential lung cancer treatments can enter human trials, they must be effectively and reliably supported by preclinical data. The primary mouse models for assessing new treatments reviewed by Kellar *et al.* (2015) include xenografts, syngeneic studies, transgenic lines, and carcinogen-inducible systems. In xenograft models, human lung cancer cell lines are implanted into immunocompromised mice, allowing for the direct measurement of human tumour response to treatment within weeks of tumour initiation (Kellar et al., 2015). Although these models are advantageous for their use of human cell lines, the tumours do not develop within the lung microenvironment, potentially limiting their translatability to human disease progression. Orthotopic xenograft models, in which tumour cells are directly implanted into the lung, address this limitation but also introduce the complexity of imaging and quantifying tumour growth (Kellar et al., 2015). Additionally, neither xenograft model reflects a tumour microenvironment with an immunocompetent background, and orthotopic tumours will contain a mixture of mouse stroma and human cancer cells (de Seranno and Meuwissen, 2010). Patient-derived xenografts (PDXs) can be used to more closely model the tumour microenvironment of human cancer and predict more clinically relevant treatment outcomes, although human derived stromal cells are quickly replaced by murine cells (Moro et al., 2012). Generation of PDXs requires surgically resected human tissue samples that can be challenging to successfully implant and maintain *in vivo* and may also require the establishment of a heterogenous PDX panel to model human cancer genetic subtypes (Kwon and Berns, 2013; Moro et al., 2012).

In syngeneic models, mouse lung cancer cell lines are subcutaneously or orthotopically injected into immunocompetent mice (Kellar et al., 2015). Although

immune responses to therapies can be assessed, subcutaneous syngeneic models are not in the correct thoracic microenvironment; for those injected orthotopically such as in the Lewis lung carcinoma syngeneic model, metastases to the lymph nodes occurred within 3 weeks, making this model impracticable for long term treatment studies (Doki et al., 1999).

There are also several transgenic mouse models that develop autochthonous tumours, arising in the tissue of origin, using lung-specific promoters of oncogenes, growth factor receptors, and tumour suppressor genes such as Kirsten rat sarcoma (*K-ras*), *Egfr*, and tumour protein 53 (*p53*, *TP53*) (de Seranno and Meuwissen, 2010; Kellar et al., 2015; Kwon and Berns, 2013). For example, activating mutated *K-ras* (a driver mutation commonly found in NSCLC) using the Cre-lox system induces multiple lung lesions which, when followed in a time course, model early-stage human lung cancer development; however, a large tumour burden develops within weeks and leads to respiratory distress, making them difficult to use for studies of long term treatment effects (Kellar et al., 2015; Meuwissen et al., 2001). The aggressive invasiveness of tumours is a common limitation of many transgenic models along with the artificially high expression levels of the driver mutations that do not represent human pathology (Kellar et al., 2015; Kwon and Berns, 2013; Singh et al., 2012).

Carcinogen-induced models can also be used to create autochthonous tumours in susceptible mouse strains such as A/J and SWR (Eferl et al., 2015; Jiang et al., 2021). A number of carcinogens have been identified for these studies and are reviewed by Kellar *et al.* (2015). After injection, independent tumours arise spontaneously within the lungs and undergo a multistep progression characteristic of human disease (Kellar et al., 2015). While some carcinogens display variability in growth patterns between mice, urethane has demonstrated high reproducibility and induces mutations in known lung cancer genes of *K-ras* and *p53* in the A/J strain

(Cazorla et al., 1998; de Seranno and Meuwissen, 2010; Gurley et al., 2015; Horio et al., 1996; Ohno et al., 2001). The use of urethane has also been tested in the more resistant strain of C57BL/6, but induction of tumours required multiple urethane doses to achieve smaller tumour numbers (Forkert, 2010; Janker et al., 2018; Miller et al., 2003; Xu et al., 2016).

In order to evaluate new treatment regimens and IR responses of preclinical cancer models, the appropriate IR dosing technologies must be developed and implemented to provide reliably translatable data. The advances seen in clinical targeting have also evolved in the preclinical field through the development of new radiation platforms and image-guided systems that can selectively target small volumes (Butterworth, 2019; Ghita et al., 2019; Ghita et al., 2017). One such platform, the small animal radiation research platform (SARRP), is capable of accurately delivering localised X-rays by using different sized beam collimators (Butterworth, 2019; Deng et al., 2007). While this platform can provide a controlled dose delivery direct to tumours, there is also a need to evaluate the dose delivered to normal tissues and investigate any toxicities that may arise from treatment.

As new radiotherapy combination treatments enter clinical trials, the ability to reliably model normal tissue responses in addition to anti-tumour effects is critical to creating translatable preclinical data. Currently, there are few preclinical models of the acute oesophagitis response. A study by Kim *et al.* compared the effects of whole thorax radiation of two mouse strains, BALB/c and C57BL/6, and successfully demonstrated radiation-induced oesophagitis in BALB/c mice (Kim et al., 2016; Kim et al., 2015). However, the BALB/c strain is known to have a low expression of DNA-PK, an essential protein in DDR, which makes this strain inherently radiosensitive and using it as a model of IR-induced oesophagitis less directly translatable to human health (Butterworth, 2019; Fabre et al., 2011; Okayasu et al., 2000; Yu et al., 2001).

Additionally, using the BALB/c strain would be inappropriate for studies of combination therapies that rely on functional DDR mechanisms to explore treatment efficacies or toxicities.

In investigations of pneumonitis and fibrosis, numerous models have been used and are extensively reviewed by Dabjan *et al.* (2016) (**Fig. 1.1.11**). In their review, the authors examined the emergence of C57BL/6 as the primary model of IR-induced lung effects through 4 main factors: strain availability, standard background for transgenic lines, most characterised, and fibrosis prone (Dabjan et al., 2016).

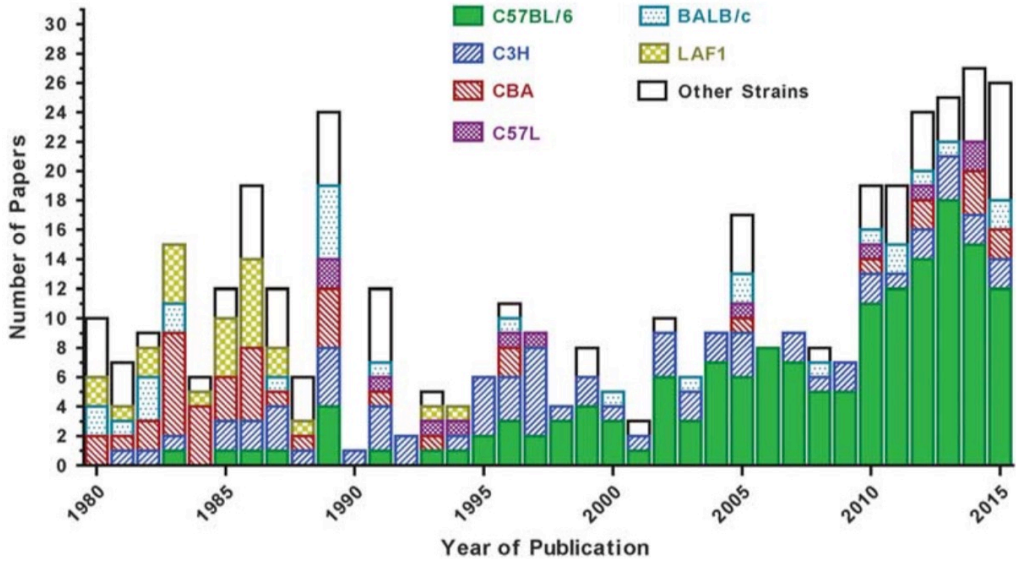

Figure 1.1.11. IR-induced lung damage mouse strains by paper numbers and year published. (Reproduced from Dabjan et al., 2016).

They expand on the complexities of using C57BL/6 as the standardised model because of the past common use of morbidity and mortality as endpoints ascribed to fibrosis rather than confirmed by histology, plethysmography, or imaging (Dabjan et al., 2016). Additionally, the majority of studies in C57BL/6 have used whole thorax irradiation (86%) and many with limited consideration of how pleural effusions affect these end points (Dabjan et al., 2016; Jackson et al., 2010). As explored earlier, IR-induced lung damage in patients may lead to pneumonitis, fibrosis, or both, and this mixture of disease pathologies is challenging to model because specific strains are considered susceptible to one or the other pathology (Dabjan et al., 2016).

Importantly, both *in vitro* and *in vivo* studies are used to provide evidence before the initiation of clinical trials, but a recent review has questioned the robustness of some preclinical data used in the justification of drug and radiation combination clinical trials (Stone et al., 2016). To allow for better study design and interpretation of results, the authors created a helpful reporting checklist, which includes (i) using an appropriate representative preclinical model, (ii) calibrating and determining the dosimetry of the radiation source, (iii) accurately detailing the experimental set up and procedures, and (iv) selecting clinically relevant dosing regimens and endpoints (Coleman et al., 2016; Stone et al., 2016). Using several models to examine new IR combination therapies for the treatment of NSCLC, one for IR-induced lung damage, one for IR-induced oesophagitis, and one for anti-tumour efficacy, combines the challenges of each with a limitation on direct translation to patient health outcomes.

Following the checklist from Stone *et al.* (2016) and establishing a single model of all three IR effects will allow for a thorough assessment of emerging IR combination therapies with potentially beneficial and translatable clinical implications. The therapeutic window of radiotherapy and drug combinations can be efficiently evaluated in a single model and effectively established before treating patients while the predictability and backwards translatability of the model could also be assessed using already approved treatment regimens (Coleman et al., 2016; Shakhnovich, 2018). A comprehensive therapeutic window mouse model of thoracic IR and drug combination therapies for NSCLC should include (i) an evaluation of acute and late normal thoracic tissue responses, (ii) a clinically relevant dosing regimen and endpoint, (iii) tumours that arise within the normal lung microenvironment and develop in a multistep progression, (iv) reproducible tumour and normal tissue responses, (v) a competent immune system, and (vi) an identification of potential biomarkers and responsive

tumour subpopulations (Coleman et al., 2016; Kellar et al., 2015; Sharma et al., 2016; Stone et al., 2016).

1.7. Aims

This work aims to (i) characterise the A/J model of both tumour response and normal tissue damage and (ii) use the model to evaluate the impact of DDR inhibitors on the normal tissue and anti-tumour effects of IR.

2. Materials and Methods

2.1. Reagents

A list of reagents used in the following methods can be found in **Appendix Table 6.3**. Equipment and machine manufacturers are indicated in each method.

2.2. In vivo experiments

All mouse studies were approved by a local animal welfare ethical review committee and performed according to national guidelines under a Home Office issued project licence (30/3395) held by Dr Anderson Ryan under the UK Animals (Scientific Procedures) Act of 1986. The A/J mice used in this project were purchased from Envigo (UK), and all were female and 6-10 weeks old at the start of each experimental protocol. All tumour xenograft experiments were performed on female CD-1 nude mice at 6-10 weeks old that were purchased from Charles River (UK).

2.3. Subcutaneous xenograft tumour induction

Calu6 cells (human lung carcinoma) were purchased from American Type Culture Collection (ATCC HTB-56). Cells were grown in advanced Dulbecco's Modified Eagle Medium/Ham's F-12 with an addition of 5% foetal bovine serum, 2 mM GlutaMAX, 50 U/ml penicillin / 50 µg/ml streptomycin in a 37°C incubator maintained at 5% CO_2. Cells were routinely tested for mycoplasma using a SYBR Green-based real-time polymerase chain reaction, and studies were performed with mycoplasma-free cells (Ishikawa et al., 2006). Before injection, cells were resuspended in a 1:1 mixture of Matrigel and medium and kept on ice. CD-1 nude mice were anaesthetised with 4% isoflurane in 1.4 L/min of air/O_2 for initial induction and 2-3% isoflurane for maintenance of anaesthesia. Anaesthetised mice were injected subcutaneously (s.c.) on either the back (1 cm above the tail) or on the left flank with 5 x 10^6 cells in 100 µl

of the Matrigel/cell mixture and then allowed to fully recovered. Tumours were measured with callipers, and the size was calculated using following formula:

$$\text{Volume } (\text{mm}^3) = \frac{1}{2} \text{ x } [\text{length } (\text{mm}) \text{ x width } (\text{mm}) \text{ x height } (\text{mm})]$$

When tumours reached a mean size of 100 mm^3, animals were allocated to experimental treatment groups. After treatment, tumours were measured until the group mean size reached 400 mm^3 or for up to 42 days. Tumour growth inhibition was calculated on the last measurement of all tumours in both control and treatment groups for each comparison by using the following formula:

$$\text{Tumour growth inhibition} = 1 - \frac{\text{mean treated tumour volume } (\text{mm}^3)}{\text{mean control tumour volume } (\text{mm}^3)} \text{ x } 100$$

2.4. Urethane induction of tumours

Urethane was weighed and dissolved in sterile 1 x phosphate buffered saline (PBS) as either a 10% weight/volume (w/v) or 5% w/v solution. Urethane solutions were injected intraperitoneally (i.p.) at doses of either 5 mg (5%) or 10 mg (10%) of urethane per 10 g body weight (0.1 ml per 10 g body weight), and mice were monitored for up to 6 h post injection to ensure a return to normal behaviour. Control animals were injected with PBS (0.1 ml per 10 g body weight, i.p.).

2.5. Animal welfare

Mice were observed daily for general welfare and clinical signs and weighed twice weekly. For body weight change graphs, group average data is presented relative to baseline (100%) before treatment start until the experimental endpoint or when animals were euthanised due to welfare concerns, whichever occurred first. For skin desquamation, a fusidic acid and betamethasone gel (Isaderm) was used as a topical steroid and antibiotic skin treatment. In the event of more than 10% body weight loss for 2 consecutive days, greater than 15% weight loss in one day, sporadic coughing,

or laboured breathing, mice were euthanised and tissues collected. After any procedure requiring anaesthesia, either irradiation or magnetic resonance imaging, mice were allowed to fully recover on a heated mat and provided with softened food for up to 24 h post treatment. In line with National Centre for the Replacement, Refinement & Reduction of Animals in Research (NC3R) principles, the following experiments contained the same control groups to reduce the number of animals used in each study: xenograft studies of AZD7648 and AZD1390 (**Fig. 3.3.2** and **Fig. 3.4.2)**, early intervention studies of AZD6738 and AZD7648 (**Fig. 3.2.7** and **Fig. 3.3.9),** late intervention studies of AZD7648 and AZD1390 (**Fig. 3.3.14** and **Fig. 3.4.12)**, and pharmacodynamics studies of AZD7648 and AZD1390 (**Fig. 3.3.20** and **Fig. 3.4.18)**.

2.6. Irradiation

2.6.1. Xenograft, whole thorax, or hemithorax IR

Mice were anaesthetised (4% isoflurane in 1.4 L/min of air/O_2 for initial induction; 2-3% isoflurane for maintenance) and placed on a rig within an irradiator, either an RS320 system (Gulmay Medical, UK) or Small Animal Radiation Research Platform (SARRP, Xstrahl Ltd., UK). Each animals' breathing rate was monitored with breathing balloons, maintained at 40-60 breaths per minute, and adjusted by minor alterations in the percentage of isoflurane that was vaporised into the air/O_2 supply. For whole thorax and hemithorax IR, the dosimetry of the rig set up was experimentally determined before use (**Appendix Fig. 6.1**). For xenograft IR, previously measured dosimetry was used for the xenograft rig.

For xenograft experiments, lead tubes were placed over animals exposing the tumours either on the lower back or left flank (**Fig. 2.6.1.1 A & B**). X-rays were delivered from above at a dose rate of 1.82 Gy/min using 300 kV and 10 mA for 2 min and 45 sec (5 Gy) or 5 min and 30 sec (10 Gy).

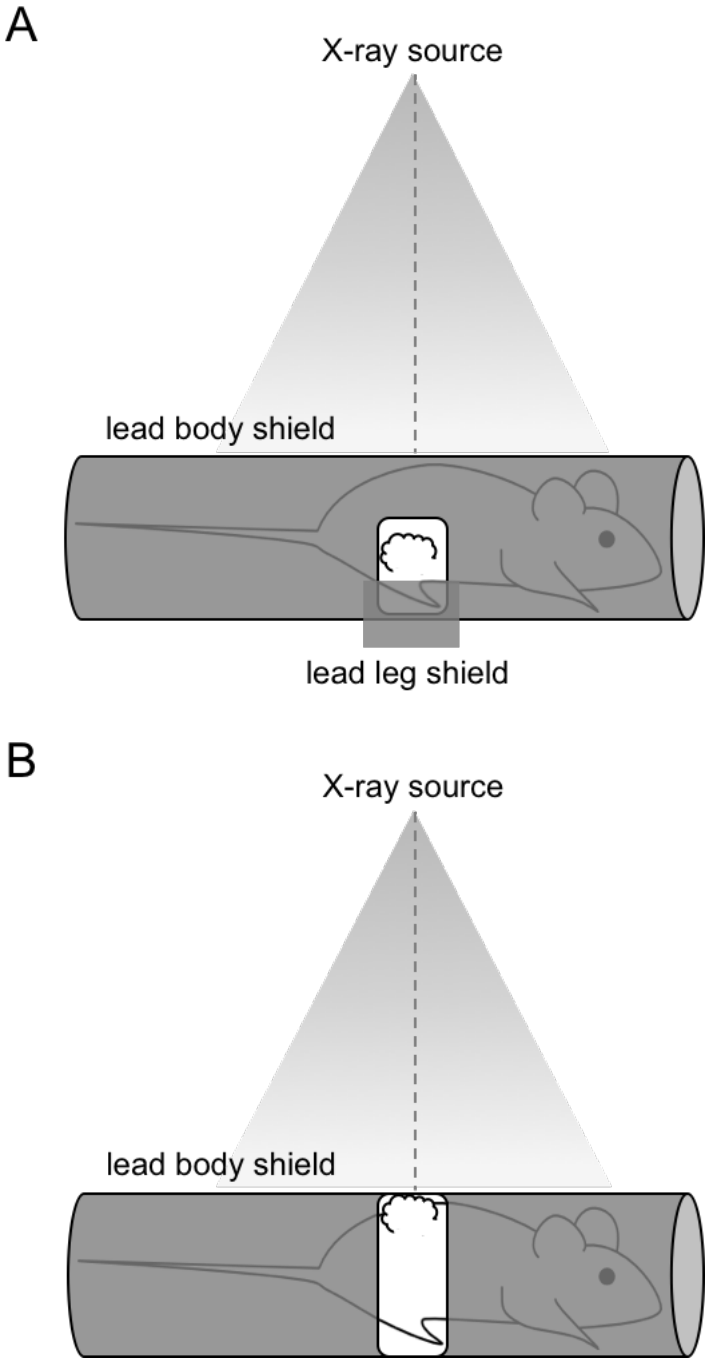

Figure 2.6.1.1. Xenograft irradiation rig. Anaesthetised CD-1 mice were placed in the supine position on a rig. Lead tube shielding was placed over each animal and aligned with the location of tumours, either on the flank (A) or lower back (B). A second lead shield was placed over the leg in the flank irradiation setup (A). X-rays were delivered from above each animal at a dose rate of 1.82 Gy/min using 300 kV and 10 mA for 2 min and 45 sec (5 Gy) or 5 min and 30 sec (10 Gy). All lead shields were 6 mm in thickness.

For whole thorax irradiation, lead shields were placed to cover the animals, with 1.7 to 1.9 cm of the whole thorax exposed (**Fig. 2.6.1.2 A & B**). X-rays were delivered from above using the Gulmay RS320 irradiator at a dose rate of 2.02 Gy/min using 300

kV and 10 mA for 2 min and 28 sec (5 Gy), 4 min and 57 sec (10 Gy), 6 min and 26 sec (13 Gy) or 7 min and 25 sec (15 Gy).

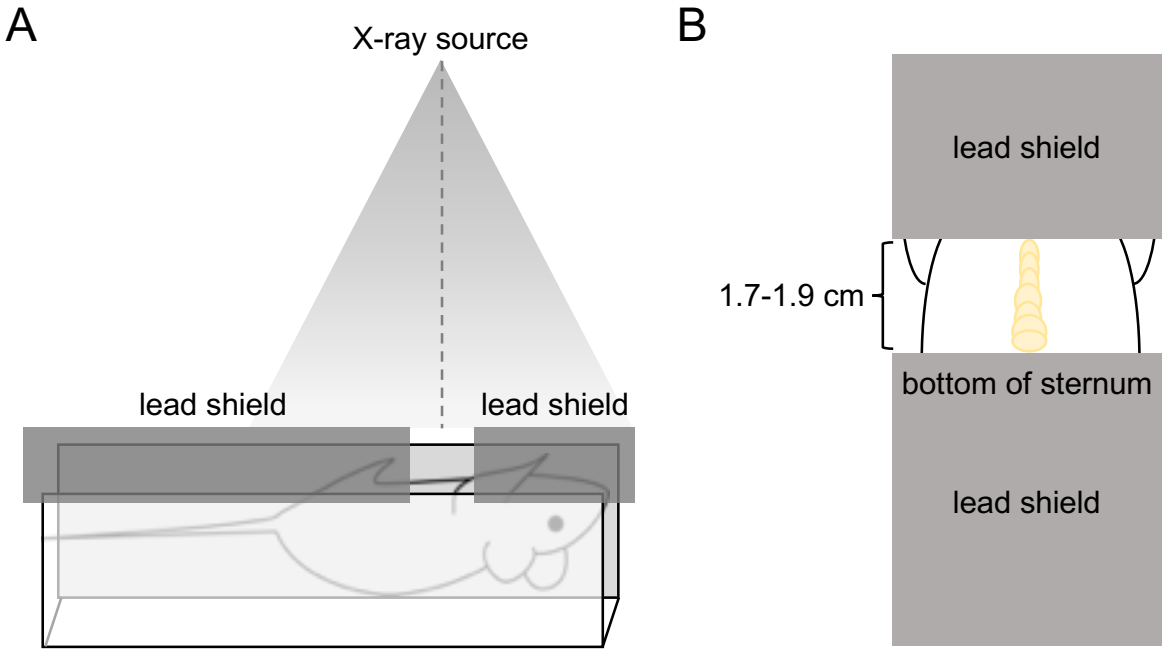

Figure 2.6.1.2. Whole thorax irradiation rig. Anaesthetised A/J mice were placed in the supine position on a rig. Lead shielding was placed over each animal and aligned with the bottom of the sternum. A second lead shield was placed over the head and a gap of 1.7 to 1.9 cm was exposed of the whole thorax. X-rays were delivered from above each animal at a rate of 2.02 Gy/min using 300 kV and 10 mA. Side view (A); X-ray source position view (B). All lead shields were 6 mm in thickness.

For hemithorax irradiation, the thorax of anaesthetised mice was shaved to allow for correct positioning. A lead window (25 x 10 mm) was used to create a left thorax IR field by aligning the window with the bottom and along the vertical axis of the sternum (**Fig. 2.6.1.3 A & B**). A second lead shield was placed to cover the animals, with a large opening (50 x 15 mm) above the thorax aligned to the lead window (**Fig. 2.6.1.3 B**). For **Chapters 3.2 & 3.3**, X-rays were delivered from above using the Gulmay irradiator at a dose rate of 2.02 Gy/min using 300 kV and 10 mA for 2 min and 28 sec (5 Gy), 4 min and 57 sec (10 Gy), 6 min and 26 sec (13 Gy) or 7 min and 25 sec (15 Gy). For **Chapter 3.4**, X-rays were delivered from above using the SARRP without a collimator at a dose rate of 0.606 Gy/min using 225 kV and 10 mA for 8 min and 15 sec (5 Gy).

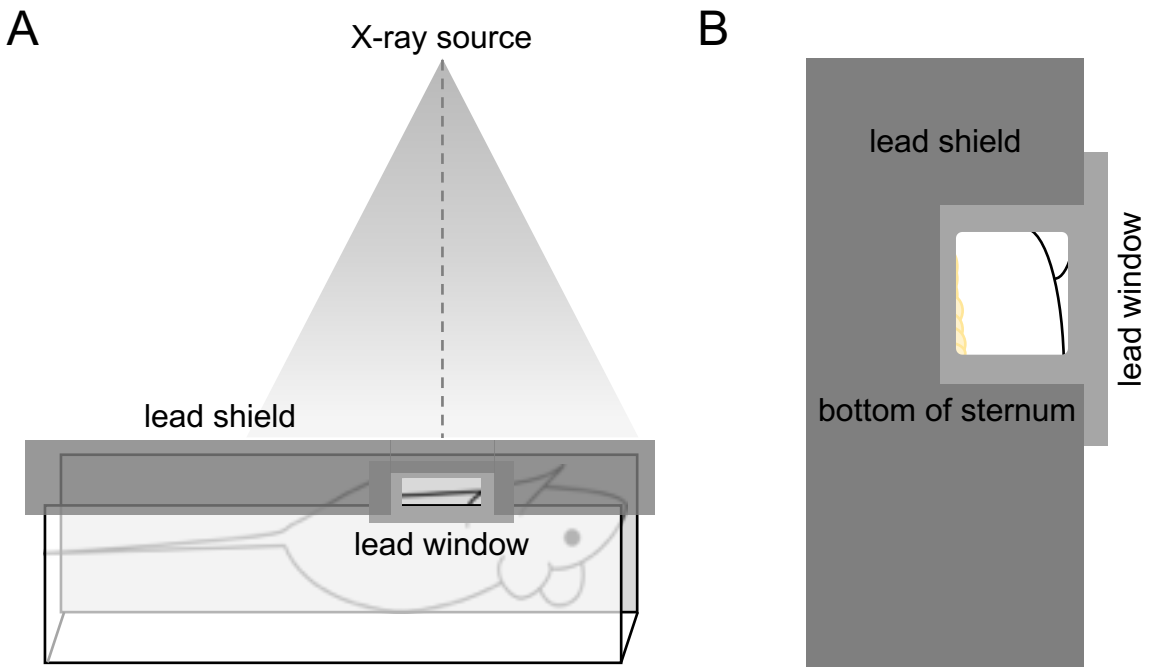

Figure 2.6.1.3. Hemithorax irradiation rig. Anaesthetised A/J mice were placed in the supine position on a rig. A lead shield with a refined window (lead window, 25 x 10 mm) was placed above each animal and aligned with the bottom of the sternum and approximately 1 mm to the right of the sternum along the vertical axis. A second larger lead shielding (lead shield, 50 x 15 mm) was placed over the animals and the opening was aligned with the lead window (**Appendix Fig. 6.2**). X-rays were delivered from above each animal at a rate of 2.02 Gy/min using 300 kV and 10 mA. Side view (A); X-ray source position view (B). All lead pieces were 6 mm in thickness.

2.6.2. Image-guided IR of the left lung

For IR guided by cone beam computed tomography (CT), anaesthetised mice were placed on a cradle fixed to the SARRP (**Fig. 2.6.2.4 A**). The breathing rate was monitored with a fibre optic sensor detecting thoracic movement, maintained at 40-60 breaths per minute, and adjusted by minor alterations in the percentage of isoflurane that was vaporised into the air/O_2 supply. A 3D reconstruction of 720 projections taken of mice rotated 360° at even intervals using 50 kVp X-rays was made using a modified Feldkamp-Davis-Kress reconstruction algorithm (0.16 mm isotropic voxels). Imaging was performed by the Biophysics Scientific Research Facility staff of the Department of Oncology (University of Oxford, UK). The resulting 3D reconstruction was used to segment and plan treatment to the left lung using Muriplan (Xstrahl Ltd.) (**Fig. 2.6.2.4**

B). X-rays were delivered to the dorsal and ventral sides (parallel-opposed) of each animal at a dose rate of 2.16 Gy/min using 225 kV, 10 mA, and a collimator (8 x 8 mm) targeted to the left lung by selecting an isocentre that maximised left lung IR volume and minimised oesophageal and liver IR volumes (**Fig. 2.6.2.4 B**). Treatment times were calculated based on the CT of each individual animal in order to deliver the appropriate dose to the lung isocentre and varied slightly from animal to animal, typically approximately 3 min on each side to deliver 13 Gy total.

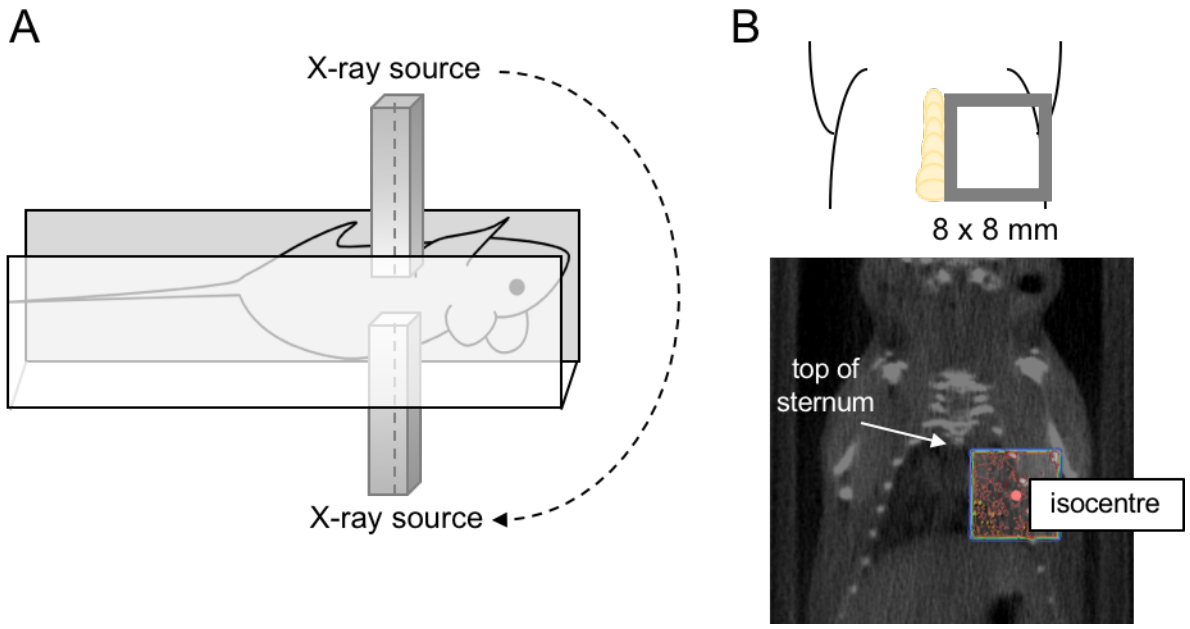

Figure 2.6.2.4. CT-guided left lung irradiation rig. Individual anaesthetised A/J mice were placed in the supine position on a cradle (A). CT images were taken to create a 3D reconstruction of the mouse and rig (B). Images were segmented into 5 categories (air, lung, fat, tissue, and bone) and used to calculate correct exposure times for each mouse based on the desired lung dose. The beamline was fitted with an 8 x 8 mm square collimator and aimed at the left lung using the sternum and the top of the liver as guides for two edges of the beam. X-rays were delivered in parallel and opposed. Dosimetry was calculated for each individual animal to deliver the appropriate dose to the isocentre using a dose rate of 2.16 Gy/min with 225 kV and 10 mA.

2.7. Cardio-respiratory gated magnetic resonance imaging

Cardio-respiratory gated magnetic resonance imaging (MRI) was used to image tumours *in vivo* while also accounting for the motion of both the heart and lungs that can interfere with the imaging process and quality. Mice were anaesthetised (4% isoflurane in 1.4 L/min of air/O_2 for initial induction; 2-3% isoflurane for maintenance)

and then placed inside a pre-heated 37°C cradle. To obtain gating information, needles were inserted (s.c.) under the skin of the abdomen for the heart rate, and a pressure-sensing balloon was placed between the cradle and animal to measure breathing rate. Magnetic resonance imaging (MRI) scanning methodology has been recently published (Gomes et al., 2019). All imaging sessions were performed with support from the Imaging Scientific Research Facility staff of the Department of Oncology (University of Oxford). Lung images were segmented and reconstructed using ITK-SNAPK software (Yushkevich et al., 2006). Automatic segmentation was used for the lungs and manual segmentation was done for individual tumours, which were used to calculate tumour counts and volumes.

2.8. Drug formulation and dosing

The inhibitors AZD6738 (ATR), AZD7648 (DNA-PK), and AZD1390 (ATM) used for in vivo experiments were kindly provided by AstraZeneca. AZD6738 was weighed and resuspended in dimethyl sulfoxide (DMSO) and then in 80% polyethylene glycol. This suspension was diluted by half in order to make the final AZD6738 solution in 2.5% DMSO and 40% polyethylene glycol. For the formulation of AZD7648 and AZD1390, hydroxypropyl methylcellulose was first diluted in filter-sterilised dH_2O overnight at 4°C. Once fully dissolved, 0.5% Tween 80 was added and the solution used to dilute either AZD7648 or AZD1390 overnight at 4°C. All inhibitors were made weekly, kept for one week, and stored in the dark at 4°C between usages. Mice were treated *per os* (p.o.) by gavage with 100 µl of suspension per 10 g of body weight using plastic feeding tubes (Instech, FTP-20-38) attached to 1 ml syringes (Terumo, GS572).

5-Bromo-2′-deoxyuridine (BrdU) was weighed out and dissolved in PBS to make a 10 mg/ml solution that was injected (100 mg/kg, i.p.) 30 min prior to euthanasia. Pimonidazole HCl was weighed out and dissolved in PBS to make a 6 mg/ml solution that was injected (60 mg/kg, i.p.) 1.5 to 2 h prior to euthanasia.

2.9. Euthanasia and sample processing

Mice were euthanised using an injection of pentobarbitone sodium (200 mg/kg, i.p.) and exsanguination by cardiac puncture. Tissues were collected and placed into greater than 10 volumes of 10% neutral buffered formalin for 24 h at 4°C. Oesophagi were collected using the 'Swiss roll' technique prior to fixation (Moolenbeek and Ruitenberg, 1981). After fixation, all samples were transferred to 70% ethanol. Within 2 weeks, tissues were placed into a Spin Tissue Processor (Thermo Fisher Scientific, STP-120) and processed overnight at room temperature through a series of baths: 6 baths of 100% ethanol, 3 baths of citroclear, and 3 baths of 50°C paraffin wax. Samples were embedded in paraffin blocks using a HistoStar™ Embedding Workstation (Thermo Fisher Scientific, A81000003).

2.10. Slide preparation

Formalin fixed tissues embedded in paraffin blocks were cut in 4 µm sections using a microtome (Leica, Germany, RM2125). Slices were put onto charged slides (ThermoFisher Scientific, J3800AMNZ) and dried at 37°C overnight in an incubator.

2.11. Dewaxing and hydration

Slides were incubated for 15 min at 50°C and then submerged in the following series of baths for 3 min each: citroclear, citroclear, 100% ethanol, 100% ethanol, 70% ethanol, and 50% ethanol. Slides were then placed in tap water for 1 min and rinsed in dH_2O.

2.12. Immunohistochemistry

After dewaxing and rehydrating, slides were immersed in citrate buffer (1 x dilution of citrate buffer and 0.05% TWEEN 20, pH 6) or Tris EDTA (1.21 g Tris Base,

0.37 g EDTA, 1 L dH_2O, pH 9), heated to either 110°C or 125°C in a Decloaker Chamber (Biocare Medical, USA) for 2 min and cooled to 80°C before the containers were placed in ice for 20 min and then washed 3 times in PBS. Samples were encircled by liquid blocker ink (Daido Sangyo, Japan).

For rabbit primary antibodies, the Dako Dual Endogenous Enzyme Blocking Reagent was added to cover each sample for an incubation of 1 h. Next, the primary antibody was diluted in antibody diluent and used to cover each sample for an incubation time according to **Table 2.12.1**. Samples were washed 3 times in PBS and then incubated with the anti-rabbit HRP conjugated secondary antibody (Dako EnVision+ System-HRP Labelled Polymer Anti-Rabbit) for 30 min at room temperature. Slides were again washed 3 times in PBS before detection (**Chapter 2.13**).

For mouse primary antibodies, the Mouse on Mouse Blocking Reagent was diluted (1:50) in PBS and used to cover samples for a 1 h incubation. The reagent was removed, and Dako Dual Endogenous Enzyme Blocking Reagent was added to cover each sample for an incubation of 1 h. Next, the primary antibody was diluted in antibody diluent according to **Table 2.12.1** and used to cover each sample for an overnight incubation at 4°C. Samples were washed 3 times in PBS and then incubated with the anti-mouse HRP conjugated secondary antibody (Dako EnVision+ System-HRP Labelled Polymer Anti-mouse) for 30 min at room temperature. Slides were again washed 3 times in PBS before detection (**Chapter 2.13**).

For the Ly6G/C antibody, the Elite ABC Rat IgG kit (Vectastain) was used according to the manufacturer's instructions. Samples were incubated with 3% hydrogen peroxide for 15 min at room temperature before a PBS wash and then incubated with 5% rabbit serum from the Elite ABC Rat IgG kit. Slides were washed again with PBS and then incubated with the Ly6G/C antibody diluted in antibody diluent

overnight at 4°C (**Table 2.12.1**). Next, slides were washed twice in PBS for 5 min. Slides were then incubated with 0.5% anti-rat secondary antibody provided in the Elite ABC Rat IgG kit diluted with 1.5% rabbit serum for 30 min at room temperature. After incubation, slides were washed twice in PBS for 3 min. Then, slides were incubated in a solution of PBS containing 2% of reagent A and 2% of reagent B (both Elite ABC Rat IgG kit reagents) for 30 min at room temperature. Finally, slides were washed twice in PBS for 5 min before detection (**Chapter 2.13**).

Antigen	Target function	Company (catalogue number)	Host	Dilution
H2AX (ser139)	DNA damage repair signal	Cell Signaling Technology (9718)	Rabbit	1:500
KAP1 (ser824)	DNA damage repair and chromatin remodelling	Bethyl Laboratories (A300-767A)	Rabbit	1:5000
BrdU	Incorporated into DNA during replication	BD (347580)	Mouse	1:2000
Pimonidazole	Reduced in low oxygen and binds to cellular macro-molecules	Hypoxyprobe Inc. (HP1-1000Kit)	Mouse	1:50
Ly6G/C	Lymphocytic antigen presented on granulocytes/neutrophils	Life Technologies (RM3000)	Rat	1:500

Table 2.12.1. Antibodies used for immunohistochemistry.

2.13. Chromogenic detection and counterstaining

Detection of antigens was performed using 3,3'-diaminobenzidine (DAB) diluted in DAB substrate buffer (Dako Liquid DAB+ Substrate Chromogen System) and incubating slides for between 1-5 min until positive staining could be observed on control slides using a light microscope. Slides were placed in tap water after DAB reaction, immersed in Gill's haematoxylin for 20 seconds, and then left in tap water for 5 min before being covered with a cover slip using the Aquatex mounting agent. Slides were left to dry overnight at room temperature.

2.14. Haematoxylin and eosin

After dewaxing and rehydration, slides were immersed in filtered Harris's haematoxylin for 5 min, washed in running tap water for 3 min, and rinsed in dH_2O. Next, slides were dipped 15 times in acid alcohol (1% hydrochloric acid in 70% ethanol in dH_2O), rinsed in dH_2O, immersed in Scott's tap water for 1 min (42 mM of sodium bicarbonate, 166 mM of magnesium sulfate in dH_2O), rinsed in dH_2O, immersed in 0.5% lithium carbonate in dH_2O for 1 min, and then rinsed in dH_2O. Slides were dipped 15 times in baths of 50%, 70% and 90% ethanol and placed in eosin for 15 seconds. Next, slides were dipped 15 times in 5 solutions of 100% ethanol and then placed in 2 consecutive xylene baths for 1 min each. Samples were covered by coverslips coated with a DPX mounting agent.

2.15. Masson's trichrome

After dewaxing and rehydration, slides were placed for 15 min in Coplin jars filled with Bouin's Solution pre-heated to 56°C using a water bath. Slides were next washed with running tap water. Samples were stained using a Trichrome Stains (Masson) kit (Sigma-Aldrich, HT15) following the modified kit instructions in **Table 2.15.1**.

Step	**Time**
Weigert's iron hematoxylin	5 min
Running tap water	5 min
dH_2O	Rinse
Biebrich scarlet-acid fucshin (kit)	5 min
dH_2O	Rinse
Phosphotungstic/phosphomolybdic acid solution (kit)	15 min
Aniline blue (kit)	5 min
1% acetic acid (diluted with dH_2O)	2 second dip
dH_2O	Rinse

Table 2.15.1. Masson's trichrome staining procedure modified for lung tissues.

After rinsing, slides were placed in 3 solutions of 100% ethanol and then in 3 consecutive xylene baths for 10 min each. Samples were covered by coverslips coated with a DPX mounting agent.

2.16. Slide scanning and image analysis

Slides were scanned using the Aperio ScanScope CS (Leica) at 40 x and images were analysed using Aperio ImageScope Software (v12.3.2.8013). For positive nuclei counts of tumours, the Aperio nuclear stain was adjusted for each antibody and set of staining. Equivalent regions of interest (ROI) of 281091 μm^2 were selected for oesophageal epitheliums stained with Ly6GC and quantified using the Aperio nuclear stain algorithm. Manual counting of 100 cells was used for oesophageal and bronchial epithelial cell positive counts, and γH2AX categories were defined in all tissue types (**Fig. 2.16.1**). The separated and overlapping foci categories were counted to differentiate between cells with a countable, distinct number of foci and cells with an abundance of foci. Counts using only a category of foci-positive cells would be 100% for all IR-treated cells and would have impaired the ability to measure nuances in repair kinetics and damage compared between IR levels of foci and IR + drug levels of foci. The two categories of pan-nuclear staining intensities were used to differentiate between low and high levels of replication stress.

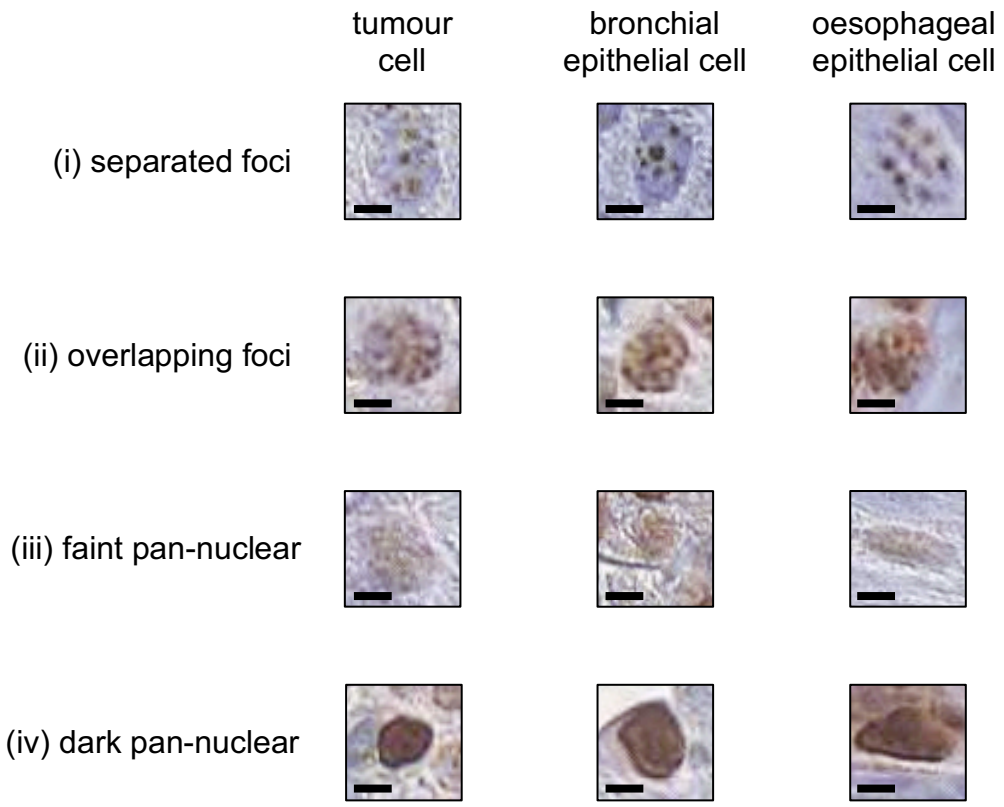

Figure 2.16.1. Immunohistochemistry of γH2AX categories. Categories are defined as (i) clear, separated foci, (ii) abundant distinct but overlapping foci, (iii) faint pan-nuclear staining, and (iv) dark pan-nuclear staining. Scale bars represent 4 μm.

Fibrosis was assessed using the modified Ashcroft score (Hubner et al., 2008). A single whole left lung slice stained by Masson's trichrome was scored per mouse by two observers. Observer 2 was blinded to the group allocations. Comparison of the scores on a single dataset (n=29) returned a linear trendline with a goodness of fit (R^2) value of 0.8051 (**Fig. 2.16.2**). Observer 1 fibrosis scores were used for all subsequent graphs and statistical analysis.

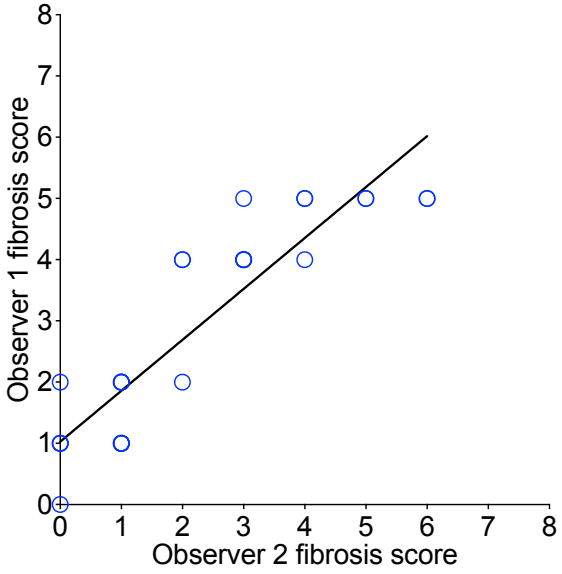

Figure 2.16.2. Fibrosis scoring comparison. Fibrosis scores using the modified Ashcroft scoring were determined by two observers on a single dataset (n=29). Observer 2 was blinded to the group allocations. Comparison of the two sets of scores revealed a linear trendline with a slope of 0.8319 and a goodness of fit (R^2 value) of 0.8051.

2.17. Statistical analysis

A two tailed Student's t test was performed on each experiment unless otherwise indicated in the figure legend. No formal statistical analysis was performed on data sets with groups presenting an n < 3. Exploratory comparisons, indicated with a grey bar on each figure, that suggested significance were followed up with a formal experiment and larger group sizes (**Appendix Figures 6.4-6.9**). The primary group comparisons are in black (e.g. IR + vehicle and IR + drug) and were only made between groups with appropriate sizes (n ≥ 3). No correction for multiple testing was used. A normal distribution was assumed, but no testing for normality was done. IR groups were combined with IR + vehicle groups after any potential vehicle biological effect was considered non-significant. All values are expressed as the group average ± the standard error of the mean (SEM) unless otherwise indicated. For all statistical indications on graphs, non-statistically significant (ns) is p ≥ 0.05 and statistical significance levels are *p < 0.05, **p < 0.01, ***p < 0.001, ****p < 0.0001.

3. Results

3.1. A/J mouse model of therapeutic intervention

3.1.1. Introduction

Mouse models can be used to assess the anti-tumour and late normal tissue effects of treatments involving IR. However, these models are typically limited in their ability to concurrently assess both efficacy and toxicity of therapeutic interventions. To address these shortcomings, we developed an A/J mouse model which has biological features associated with human disease and treatment side effects.

Carcinogen-induced lung cancer in A/J mice is initiated by an injection of urethane (ethyl carbamate), a known carcinogen commonly found in tobacco smoke (Forkert, 2010; U.S. Food & Drug Administration, 2012). Within 6 months of a urethane injection, A/J mice develop numerous independent autochthonous pulmonary tumours, with a year-long latency period for tumour development in other tissues (Chen et al., 1994; Mostofi and Larsen, 1951; White et al., 1970). Histological examination of urethane-induced tumours in A/J mice has identified them as adenomas and adenocarcinomas, classified into three histological subtypes of papillary, solid, and mixed (Forkert, 2010; Gunning et al., 1991; Mostofi and Larsen, 1951; To et al., 2008; Westcott et al., 2015). However, the tumourigenic process and the cell type of origin of these lesions is not fully understood. Although research evidence has proposed alveolar type 2 cells, Clara or club cells, or bronchoalveolar stem cells as potential cells of origin for these tumours, it is still unclear due to the challenges of cell type labelling and the genetic changes during tumourigenesis (Forkert, 2010; Kim et al., 2005a; Kim et al., 2005b; Meuwissen and Berns, 2005; To et al., 2008). A recent study using urethane-induced tumours in the more resistant C57BL/6 strain revealed strong

evidence for the bronchial epithelial club cells as the origin of tumours, in particular those driven by *K-ras* mutations in codon 61 (Spella et al., 2019).

Initial investigations into lung tumour induction by urethane in A/J mice revealed the pulmonary adenoma susceptibility locus 1 (*Pas1*) on chromosome 6, a region containing *K-ras* (Gariboldi et al., 1993; Lin et al., 1998). Tumours sequenced after 6, 8 and 10 weeks revealed a majority (66%) had *K-ras* mutations at codon 61 while after 40 weeks, 82% had *K-ras* mutations and 36% had additional *p53* mutations (Horio et al., 1996). Exome sequencing of A/J lung tumours after 32 weeks confirmed that 94% of urethane-induced tumours contain a *K-ras* mutation as well as a heterogeneous pattern of other mutations (Westcott et al., 2015).

Further studies in A/J mice uncovered a 37-base pair deletion in an intron of *K-ras* that correlated with a susceptibility to urethane tumour induction as well as to a high expression of messenger ribonucleic acid (mRNA) for the *K-ras* 4A isoform in lung tissue, suggesting the region may act as a quantitative trait locus (Chen et al., 1994; Dassano et al., 2014; To et al., 2006). In mouse strains such as C57BL/6 or C3H/He, the *K-ras* sequence contains the 37-base pair region, which is associated with higher resistance to tumour induction by urethane and lower levels of *K-ras* 4A mRNA (Chen et al., 1994; Dassano et al., 2014). This region, considered a possible transcription regulatory binding region, may be responsible for higher *K-ras* 4A mRNA levels in A/J mouse lungs (Chen et al., 1994; Dassano et al., 2014). Importantly, the *Pas1* locus and tumour susceptibility phenotype have also been associated with altered mRNA expression of numerous genes within the mitogen-activated protein kinase (MAPK) and phosphatidylinositol 3-kinase (PI3K) pathways in lung tumours, further supporting *K-ras* as the upstream effector of tumour susceptibility (Cotroneo et al., 2016).

Another factor involved in the susceptibility of murine lungs to tumour induction is the metabolism of urethane. Urethane is metabolised by the cytochrome P450 2E1

enzyme (CYP2E1) into vinyl carbamate and vinyl carbamate epoxide which can induce promutagenic DNA adducts (**Fig. 3.1.1**) (Dahl et al., 1978; Forkert, 2010; Hernandez and Forkert, 2007; Titis and Forkert, 2001).

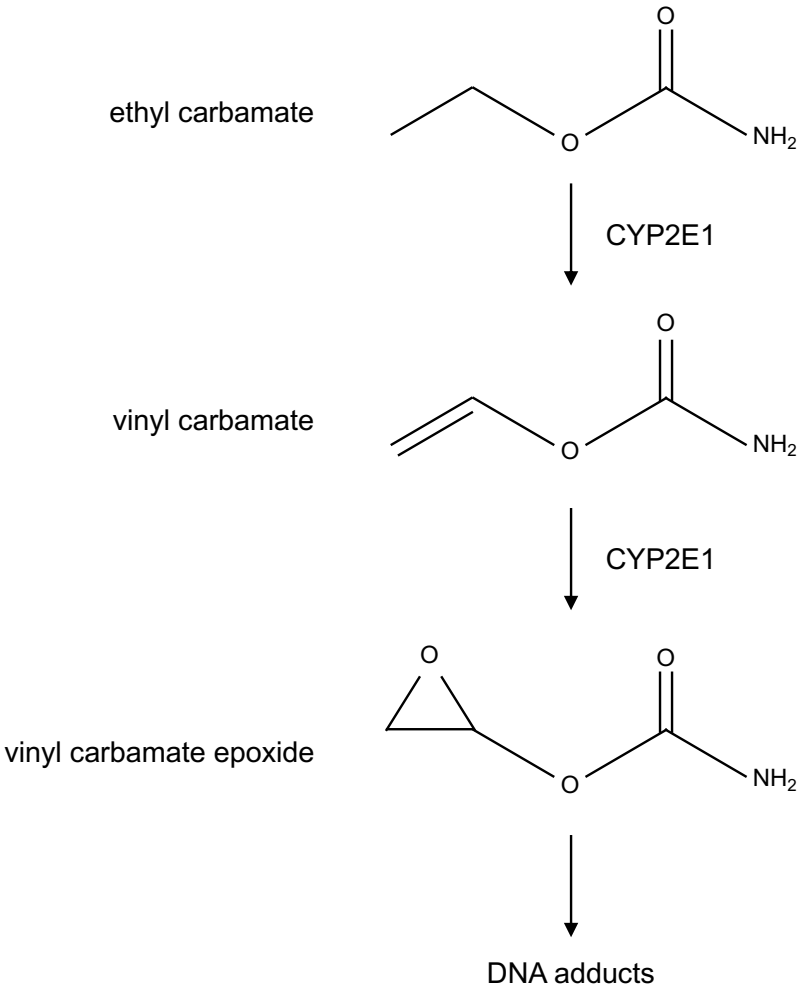

Figure 3.1.1. Ethyl carbamate (urethane) metabolism by CYP2E1. (Hernandez and Forkert, 2007).

A comparison of CYP2E1 expression in the lungs of A/J, CD-1 and C57BL/6 mice revealed that A/J mice have a higher level of CYP2E1 activity than the other two strains (Titis and Forkert, 2001). The conversion of urethane into vinyl carbamate epoxide leads to DNA adducts, the mutational frequency of which has been directly measured in A/J lung tissue (Hernandez and Forkert, 2007; Titis and Forkert, 2001). Analysis of tumours directly induced by vinyl carbamate epoxide revealed nearly half had base substitutions in codon 61 of *K-ras*, which is known to produce an activating mutation (Borrego et al., 2018; Forkert, 2010; Malkinson, 1992). Taken together, the high mRNA

levels of *K-ras* 4A, the high urethane metabolism into the DNA damaging carcinogen vinyl carbamate epoxide, and the consistent activating oncogenic mutation in *K-ras* identify the A/J mouse as suitable model for studying the effects of anti-tumour treatments in *K-ras* driven lung cancer, which is relevant to smoking related disease.

In addition to its use in urethane-induced lung cancer studies, the A/J strain can also be used to investigate IR-induced lung fibrosis. Previous studies have shown that A/J mice treated with a single dose of whole thorax IR (15 or 18 Gy) develop pneumonitis and pleural effusions, although the development of fibrosis was not reported (Jackson et al., 2011; Paun and Haston, 2012). However, experiments in our laboratory have revealed that fibrosis can be induced in the A/J strain using fractionated whole thorax IR at 24 weeks post-IR or 26 weeks from the start of IR treatment (**Fig. 3.1.2**) (Luiza Lourenço DPhil thesis, 2017).

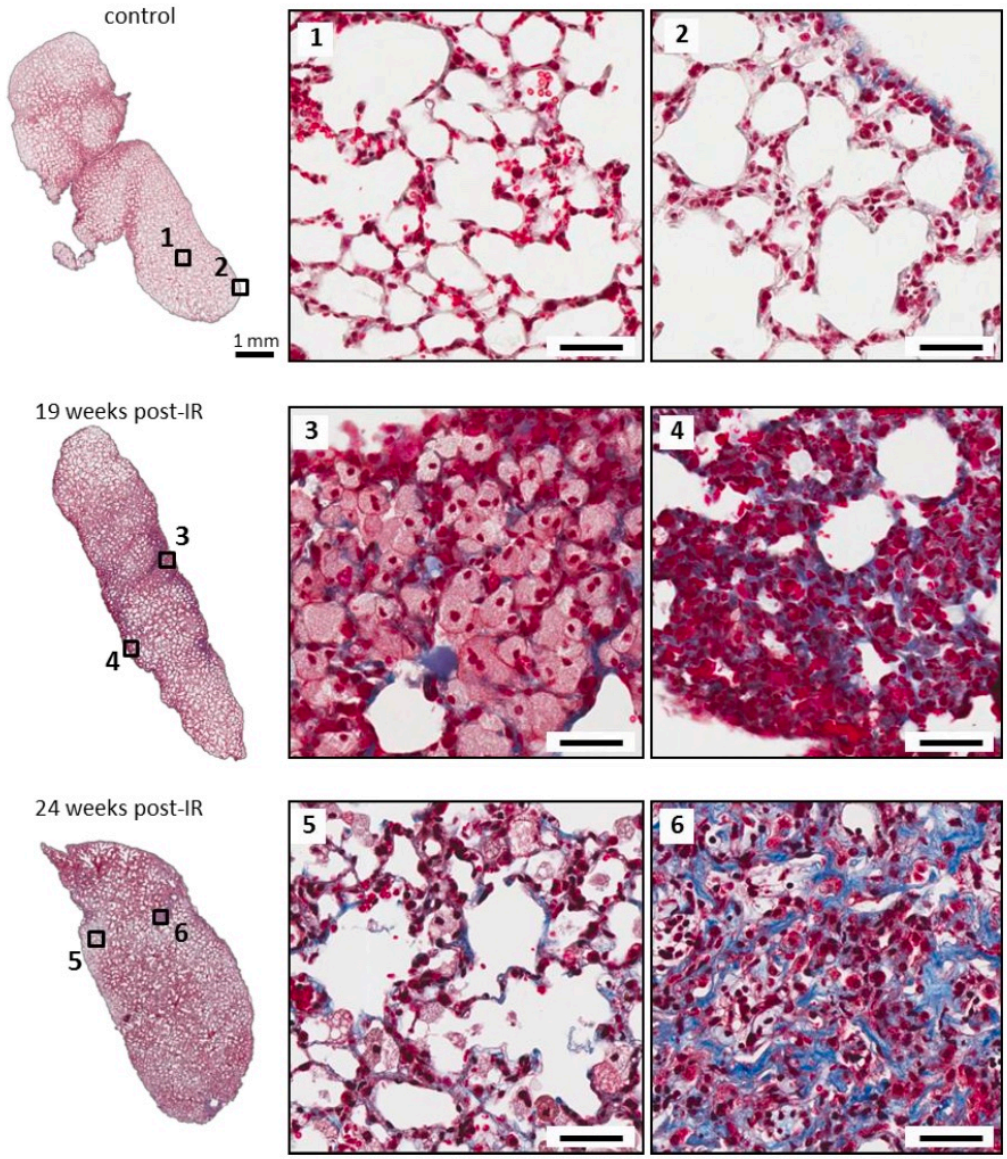

Figure 3.1.2. Fractionated whole thorax IR induces collagen deposition in A/J mice. Lungs from mice irradiated with 5 doses of 5 Gy and stained by Masson's trichrome show lipid-laden macrophages after 19 weeks (image 3) and an increase in collagen accumulation at 24 weeks (image 6) after IR as compare to control lungs. (Luiza Lourenço DPhil thesis, 2017).

The ability to generate collagen deposition at 24 weeks after fractionated IR and initiate urethane-induced autochthonous lung tumours in A/J mice suggests that this mouse strain would be useful for investigations of new IR combination therapies to evaluate both tumour and late normal tissue effects.

This chapter aims to characterise the potential of the A/J model for future therapeutic window studies by (i) evaluating tumour histological characteristics (e.g.

size, proliferation, low oxygen content), (ii) establishing a urethane dose regimen and tracking tumour growth using MRI, and (iii) assessing single dose IR-induced late term lung effects (**Fig. 3.1.3**).

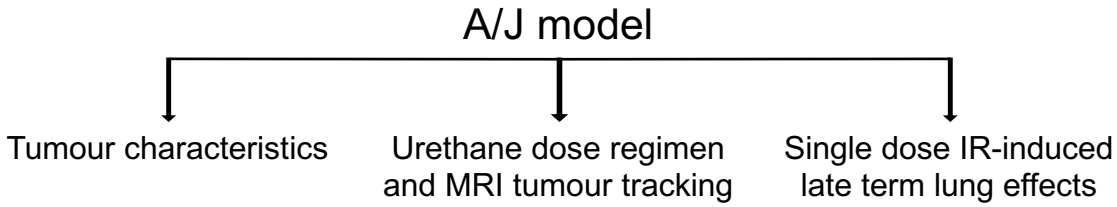

Figure 3.1.3. Main aims and experimental arms.

3.1.2. A/J urethane-induced tumour characterisation

To investigate A/J mice as a model of lung cancer, animals were injected with urethane (10 mg per 10 g body weight), and 39 weeks later the lungs were collected and processed for analysis (**Fig 3.1.4 A**). After 39 weeks, tumours were clearly visible on the surface of the lungs and could be directly quantified, particularly on the single lobe comprising the left lung (**Fig 3.1.4 B**). Fixing and embedding the lungs in paraffin allowed for histological analysis of a single, mid-section left lung slice stained by haematoxylin and eosin (H&E) staining (**Fig 3.1.4 C**). Superficial counts per lung (**Fig 3.1.4 D**), number of tumours per lung slice (**Fig 3.1.4 E**), and tumour area burden (**Fig 3.1.4 F**) are three measures that were used to assess tumour burden.

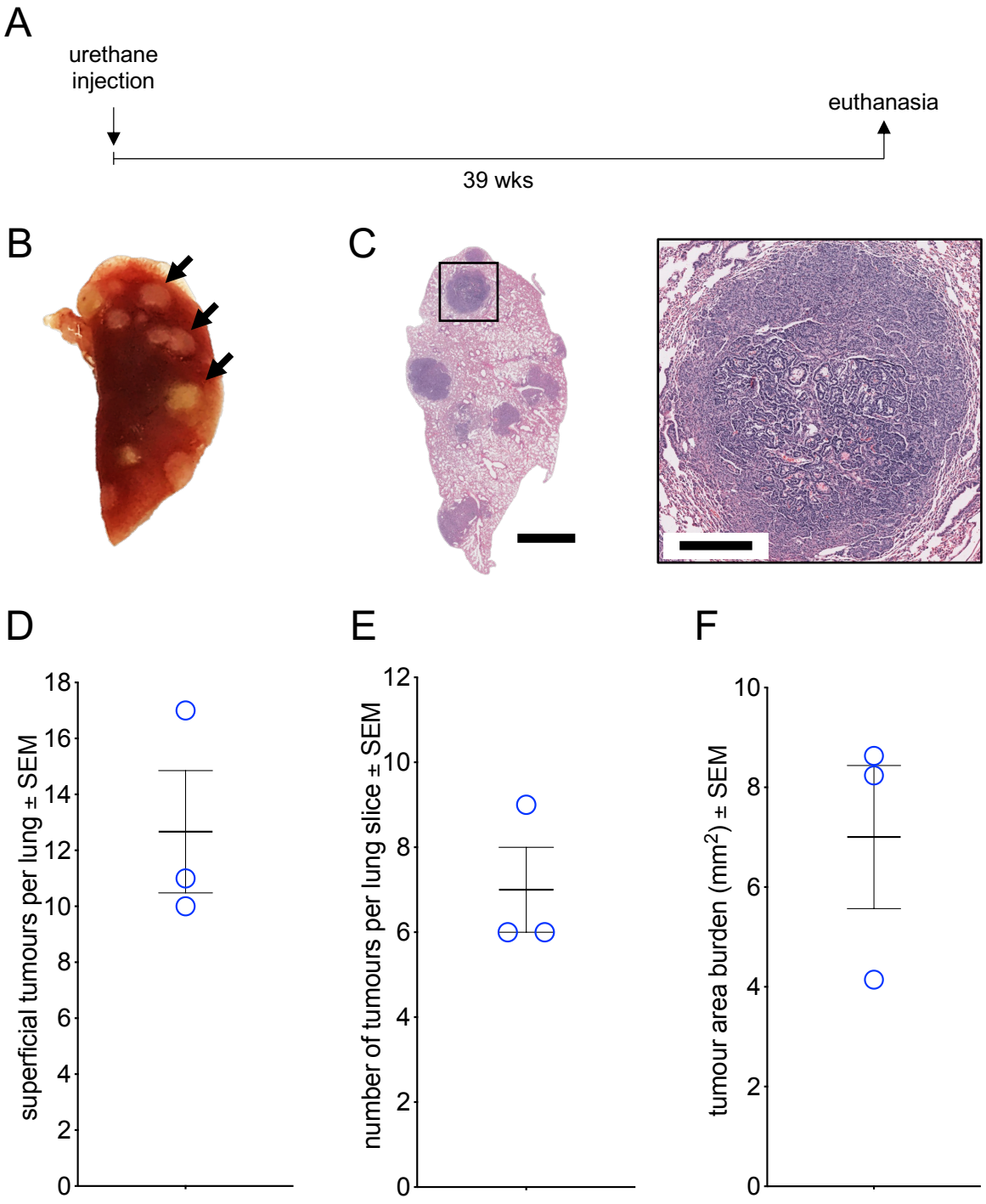

Figure 3.1.4. A/J urethane-induced tumours can be visually and histologically assessed. A/J mice (n=3) were injected with urethane (10 mg per 10 g of body weight, i.p.). After 39 weeks, mice were euthanised and lungs were collected and analysed (A). Tumours are visible on the surface of left lungs (B). Lungs can be formalin fixed and paraffin embedded for H&E staining (C). Three experimental endpoint measures are superficial tumours per lung (D), number of tumours per lung slice (E), and tumour area burden per lung slice in mm^2 (F). Scale bars represent 2 mm for the whole lung slice and 50 µm for the individual tumour.

Next, the proliferation rate and low oxygen (hypoxic) content of urethane-induced lung tumours were explored. A/J mice were injected with urethane (2 x 5 mg per 10 g

body weight). After 30 weeks, mice were injected with either bromodeoxyuridine (BrdU, 100 mg/kg, i.p.) 30 min before euthanasia or injected with pimonidazole (60 mg/kg, i.p.) 1.5 to 2 h before euthanasia (**Fig. 3.1.5 A**). BrdU is incorporated into DNA during replication and can be visualised by immunohistochemistry (IHC) to estimate the proportion of cells undergoing DNA replication at the time between injection and euthanasia. Pimonidazole is reductively activated in low oxygen (hypoxic) conditions (pO_2 of < 10 mm Hg at 37°C) to form a reactive intermediate that binds to cellular macromolecules (e.g. thiol-containing proteins) forming stable adducts that can be detected by IHC.

After 30 weeks, tumours contained approximately 1.5% BrdU-positive cells (**Fig. 3.1.5 B & C**). Pimonidazole staining of tumours revealed 3 out of 10 tumours with pimonidazole-positive regions at 30 weeks, with large variation ranging from 4 to 32% of total tumour area (**Fig. 3.1.5 D & E**). Regions of pimonidazole staining were positively correlated with tumour size, and each region was > 200 μm from an alveolar space or a blood supply, a distance which is known to give rise to hypoxia (Hall and Giaccia, 2012).

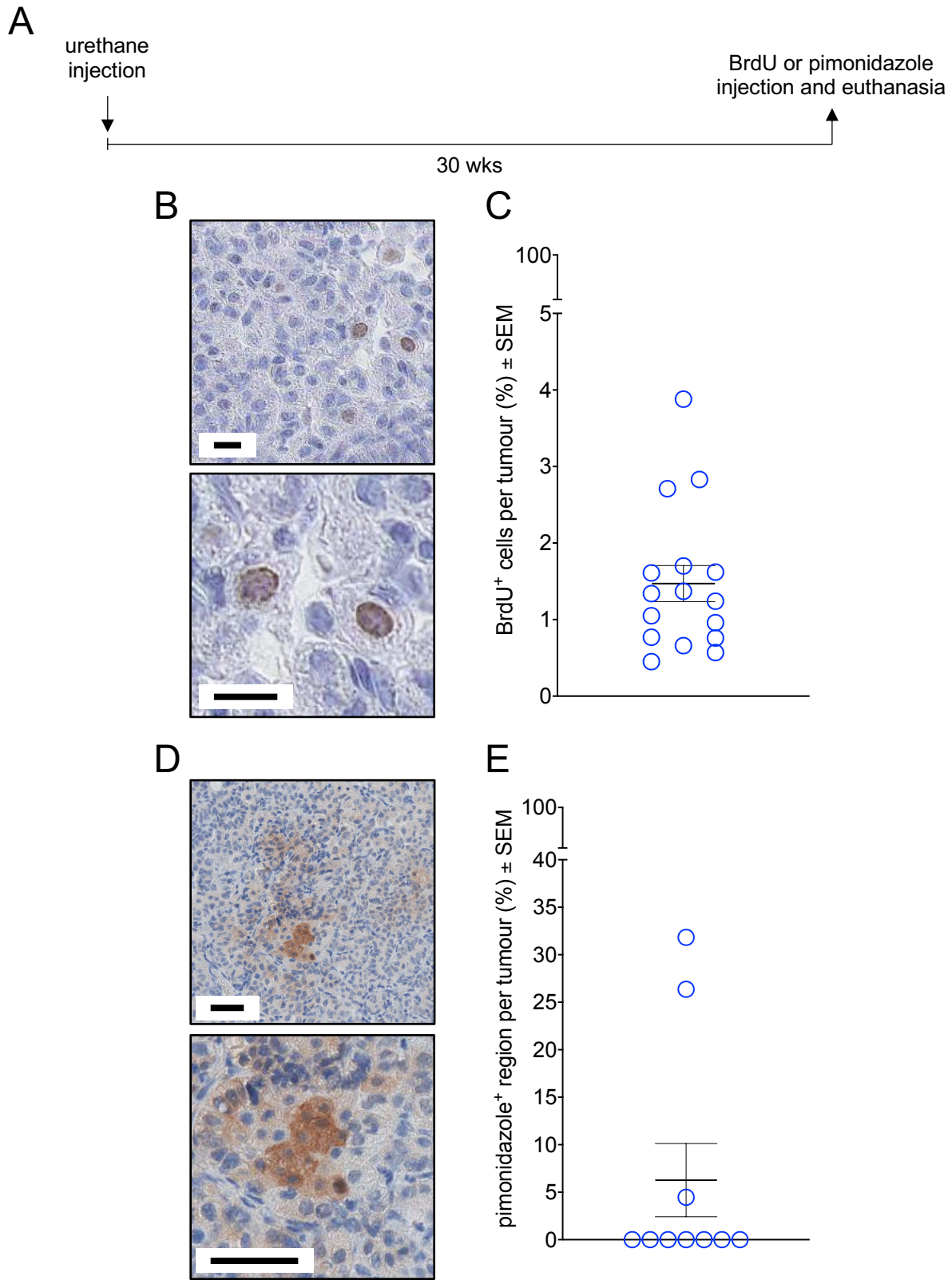

Figure 3.1.5. A/J urethane-induced tumours show few BrdU-positive cells and few pimonidazole-positive regions. A/J mice were injected with urethane (2 x 5 mg per 10 g of body weight, i.p.). After 30 weeks, mice were injected with either pimonidazole (60 mg/kg, i.p.) 2 h before euthanasia or BrdU (100 mg/kg, i.p.) 30 min before euthanasia, lung collection and processing (A). BrdU IHC in lung tumours from mice 30 weeks after urethane treatment (B). BrdU quantitation of individual tumours (C). Pimonidazole IHC in lung tumours (D). Out of 10 tumours analysed, only 3 were pimonidazole-positive (E). (o) represent individual tumours. Scale bars are 50 µm.

These data suggest that urethane-induced tumours in the A/J strain can be readily assessed using visual and histological measures to evaluate tumour burden. Additional features of urethane-induced tumours in A/J mice include a low percentage of BrdU incorporation suggesting a low fraction of proliferating cells and variable but limited regions of pimonidazole staining suggesting hypoxia is not a characteristic feature of these tumours.

3.1.3. Urethane induction of A/J lung tumours is dose dependent and can be assessed by magnetic resonance imaging

To determine the appropriate dose of urethane to initiate tumours and compare tumour growth patterns *in vivo*, two dosing regimens were explored. Previous experiments in A/J mice used a single dose of 10 mg, 5 mg, or two doses (6 d between) of 5 mg urethane per 10 g of mouse body weight (White et al., 1970). In the experiments of White *et al.* (1970), 10 mg or 2 x 5 mg of urethane yielded similar numbers of superficial lung tumours while a single dose of 5 mg resulted in approximately half the number of tumours. Previous studies in our laboratory determined that single injections of urethane at 10 mg per 10 g body weight by i.p. were occasionally not tolerated, albeit infrequently, possibly due to batch variations in A/J mice although the underlying cause was not identified. To avoid future tolerability issues, lower dosing regimens of urethane were explored.

Urethane (5 mg per 10 g body weight) was injected as a single dose or as two doses separated by 6 days. During the experiment, magnetic resonance imaging (MRI) was used to visualise tumours at week 14, 18, 24, and 28 post urethane treatment. Mice were euthanised at week 30 (**Fig. 3.1.6 A**). Importantly, both urethane dosing schedules (1 x and 2 x 5 mg per 10 g body weight) did not result in any tolerability issues upon injection and post-injection monitoring and were considered well tolerated.

The effect of the different urethane dosing regimens on tumour initiation was assessed by superficial tumour counts and histological counts of lung slices. Superficial tumour counts were significantly increased on the left lungs of individuals treated with 2 doses (n=3) group as compared with the single dose group (n=3) but not in the right lungs (**Fig. 3.1.6 B**). By histological assessment, tumour counts were not significantly different between the two doses (**Fig. 3.1.6 C**). However, tumour area burden in the left lungs was significantly higher in mice treated with 2 doses (**Fig. 3.1.6 D**).

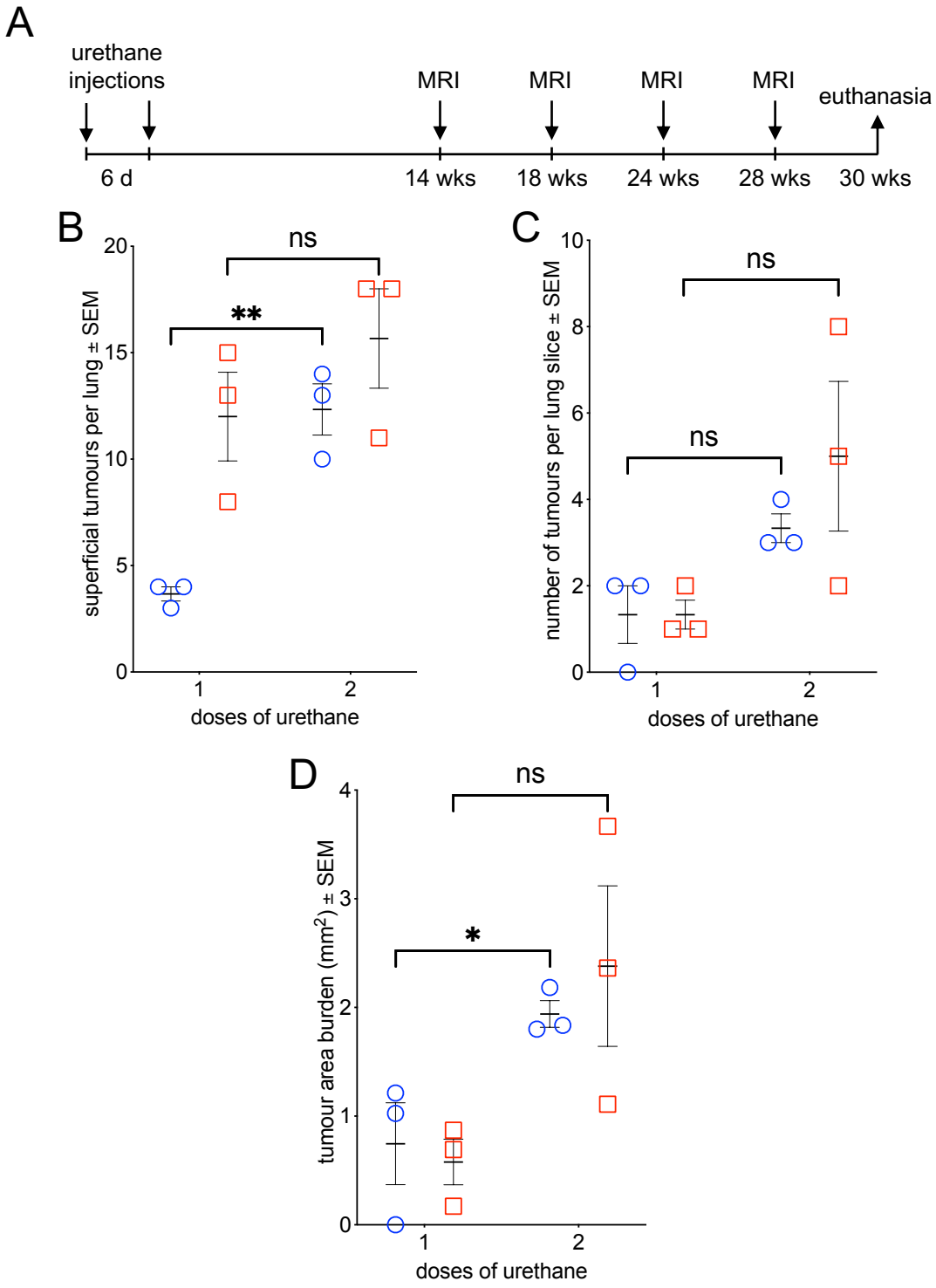

Figure 3.1.6. Superficial tumour numbers and total tumour area burden are urethane dose dependent. A/J mice were injected (i.p.) with either one or two doses of 5 mg urethane per 10 g mouse body weight. The two doses were separated by 6 days. At week 14, 18, 24, and 28 from the second urethane dose, mice were imaged using MRI (A). A/J mice treated with 2 doses of urethane (2 x 5 mg per 10 g body weight) had significantly more tumours in the left lungs as measured by superficial counts (B). The number of tumours per lung slice stained by H&E was higher in the group treated with 2 doses, but this did not reach statistical significance (C). Tumour area burden was significantly higher in the left lungs of mice treated with 2 urethane doses (D). (o) are individual left lungs and (□) are individual right lungs.

Tumour growth was also assessed by MRI. Individual tumours were identified in each MRI scan to determine the tumour counts, volumes, and volume change over time. From week 14 to 28, all tumour measures increased for both dose groups (**Fig. 3.1.7 A-C**). At week 28, the number of detectable tumours and total tumour volume was significantly higher in mice treated with 2 urethane doses as compared with mice treated with a single dose (**Fig. 3.1.7 A & B**).

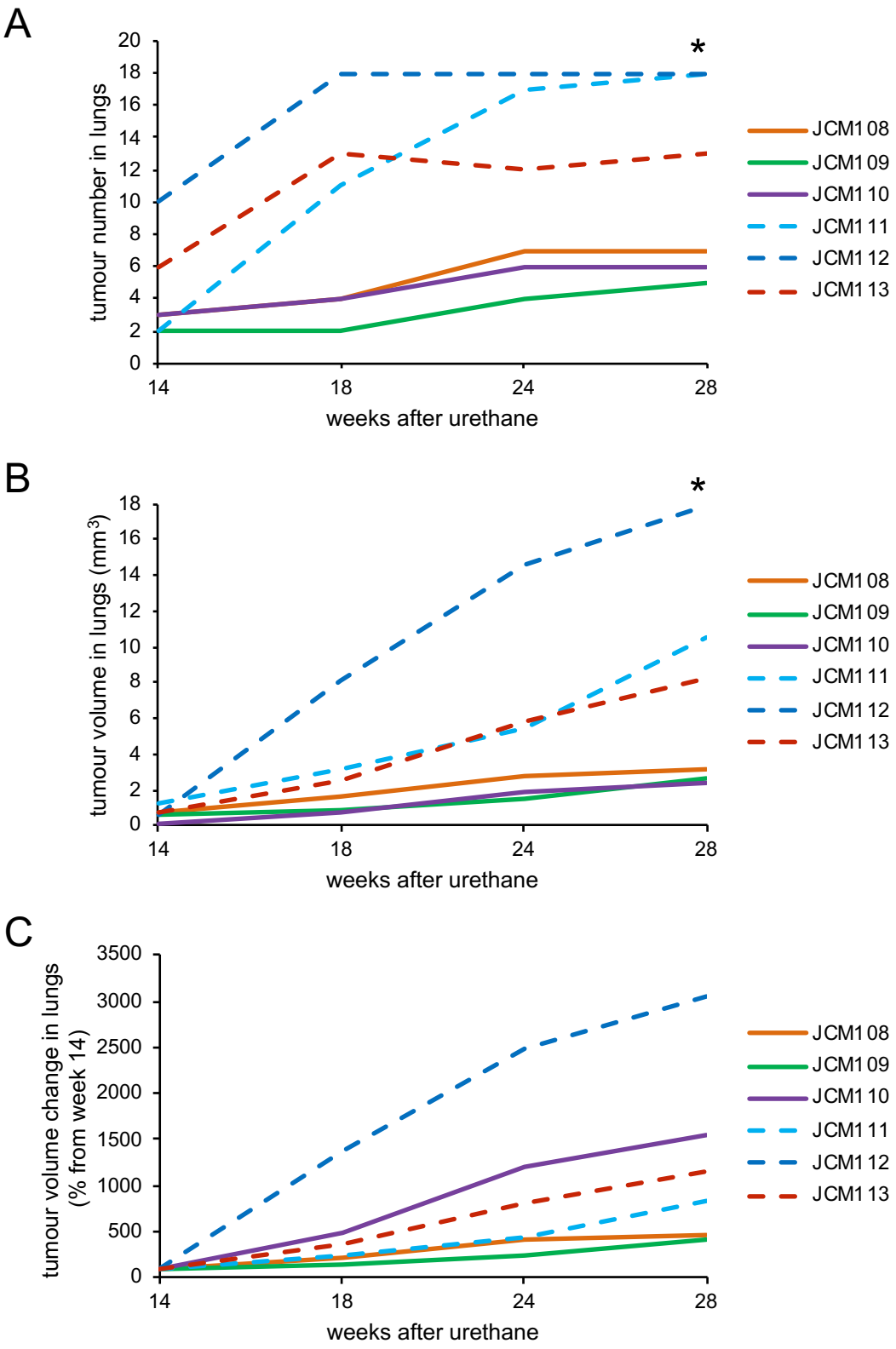

Figure 3.1.7. Tumour numbers, total volume, and total volume change are urethane dose dependent and can be measured by MRI. Individual A/J mouse lung tumour numbers (A), volumes (B), and volume changes (C) can be tracked over time *in vivo* using MRI. Treatment of A/J mice with 2 urethane doses resulted in significantly more tumours and a higher tumour volume compared with treatment with a single dose (A & B). Individuals treated with 1 urethane dose (JCM108, JCM109, JCM110) are solid lines and 2 urethane doses (JCM111, JCM112, JCM113) are dashed lines. All measurements include tumours from both left and right lungs.

Taken together, these data suggest that, compared with a single dose, 2 doses of urethane significantly increase the number of superficial tumours and tumour area burden in left lungs and tumour volume by MRI assessment of both lungs.

3.1.4. Single fraction whole thorax IR of A/J mice leads to collagen accumulation in lungs and increased fibrosis score

A consideration for establishing the A/J model was implementing a single dose IR regimen which could induce a similar effect as the fractionated IR schedule. A biologically effective dose (BED) calculation is commonly used to determine iso-effective IR treatments by considering total dose, dose per fraction and the α/β ratio (a measure of the fractionation sensitivity) of a tissue. The BED was calculated for both single and fractionated IR, and the appropriate experimental single doses of 13 and 15 Gy were investigated for a biologically similar endpoint (**Table 3.1.1**). A single dose of 13 Gy and a fractionated dose of 5 x 5 Gy had similar calculated biological effective doses for normal lung tissue (64.2 Gy and 62.9 Gy, respectively). In contrast, 1 x 15 Gy and 5 x 5 Gy had the same calculated biological effective dose for tumour tissue (37.5 Gy for both). The α/β ratio estimates for the BED calculations were 3.3 for lung tissue and 10 for tumour tissue based on previous work (Scheenstra et al., 2014; Williams et al., 1985).

Total dose (Gy)	Fractionation	BED (Gy)	α/β ratio
25	5 x 5 Gy	62.9	3.3 (lung tissue)
13	1 x 13 Gy	64.2	3.3 (lung tissue)
15	1 x 15 Gy	83.2	3.3 (lung tissue)
25	5 x 5 Gy	37.5	10 (tumour)
13	1 x 13 Gy	29.9	10 (tumour)
15	1 x 15 Gy	37.5	10 (tumour)

Table 3.1.1. α/β ratio and biological effective dose evaluation for fractionated and single dose thoracic IR.

To assess the BED *in vivo*, A/J mice were injected with urethane. After 8 weeks, mice were treated with IR (13 or 15 Gy) to the whole thorax (**Fig. 2.6.1.2**). Euthanasia was planned for 26 weeks after IR (**Fig. 3.1.8 A**). Three mice in the 15 Gy group lost greater than 15% body weight at weeks 13, 15, and 17 (animals 15_No4, 15_No3 and 15_No1, respectively) and were euthanised (**Fig. 3.1.8 B**). At week 22, 2 mice in the 13 Gy group (animals 13_No2 and 13_No4) lost greater than 15% weight, and the study was ended.

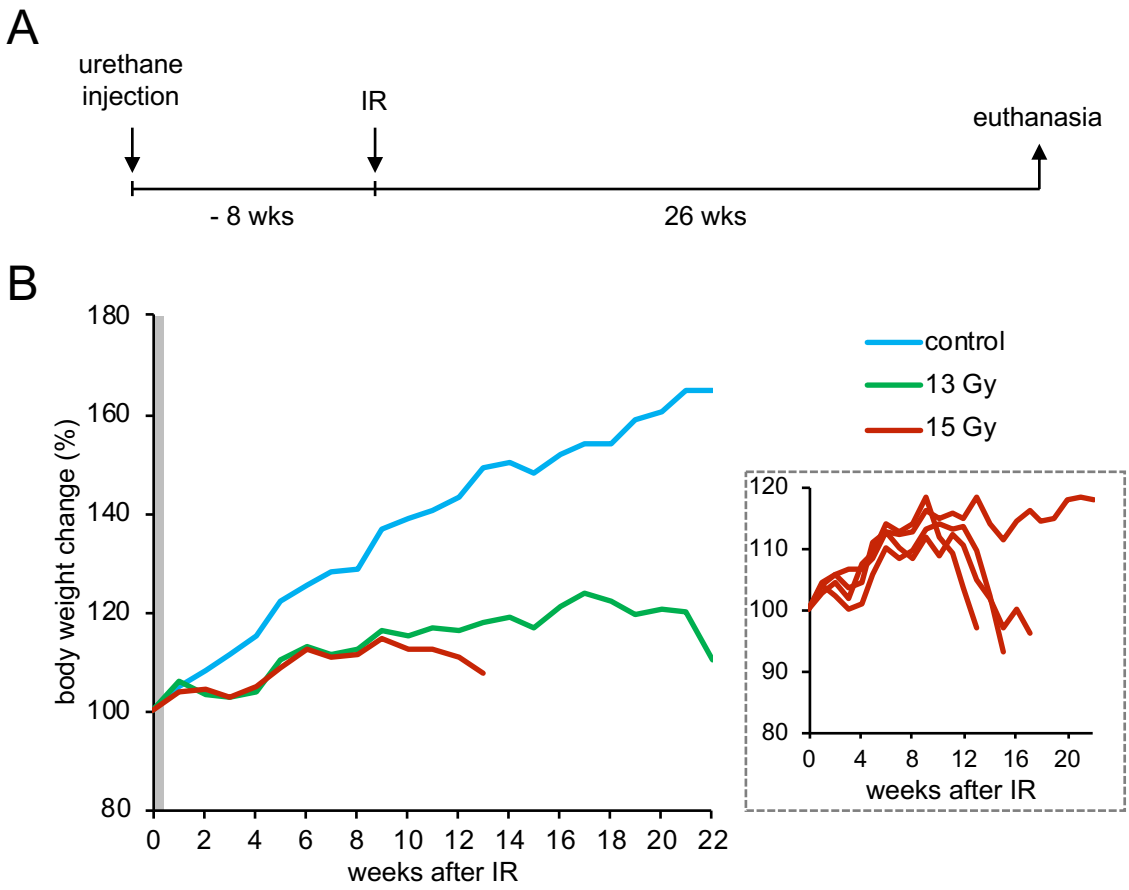

Figure 3.1.8. Whole thorax IR with 13 or 15 Gy induces body weight loss. A/J mice were injected with urethane (10 mg per 10 g body weight, i.p.). After 8 weeks, mice were allocated into 3 groups (n=3 for control and n=4 per IR group) and treated with whole thorax IR (13 or 15 Gy). Euthanasia was planned for 26 weeks after IR (A). Three mice in the 15 Gy group were euthanised early due to greater than 15% body weight loss at weeks 13, 15, and 17 (15_No4, 15_No3 and 15_No1, respectively, B). After 22 weeks, 2 mice in the 13 Gy group (13_No2 and 13_No4) had greater than 15% body weight loss, and the study was ended at week 22. For each group average, the remaining mice were weighed until the end of study, but the average weight measurement was ended when one mouse was euthanised. Individual weights of the 15 Gy group are shown in the graph inset. Grey bar represents treatment (unpublished data, Yanyan Jiang).

Regions of collagen deposition were identified by Masson's trichrome staining, and modified Ashcroft scoring was used to assess the fibrosis score (**Chapter 2.16**). Average left lung fibrosis scores of mice treated with 13 and 15 Gy (4.75 and 3.5, respectively) were increased compared with the control group score (0) (**Fig. 3.1.9 A & B**).

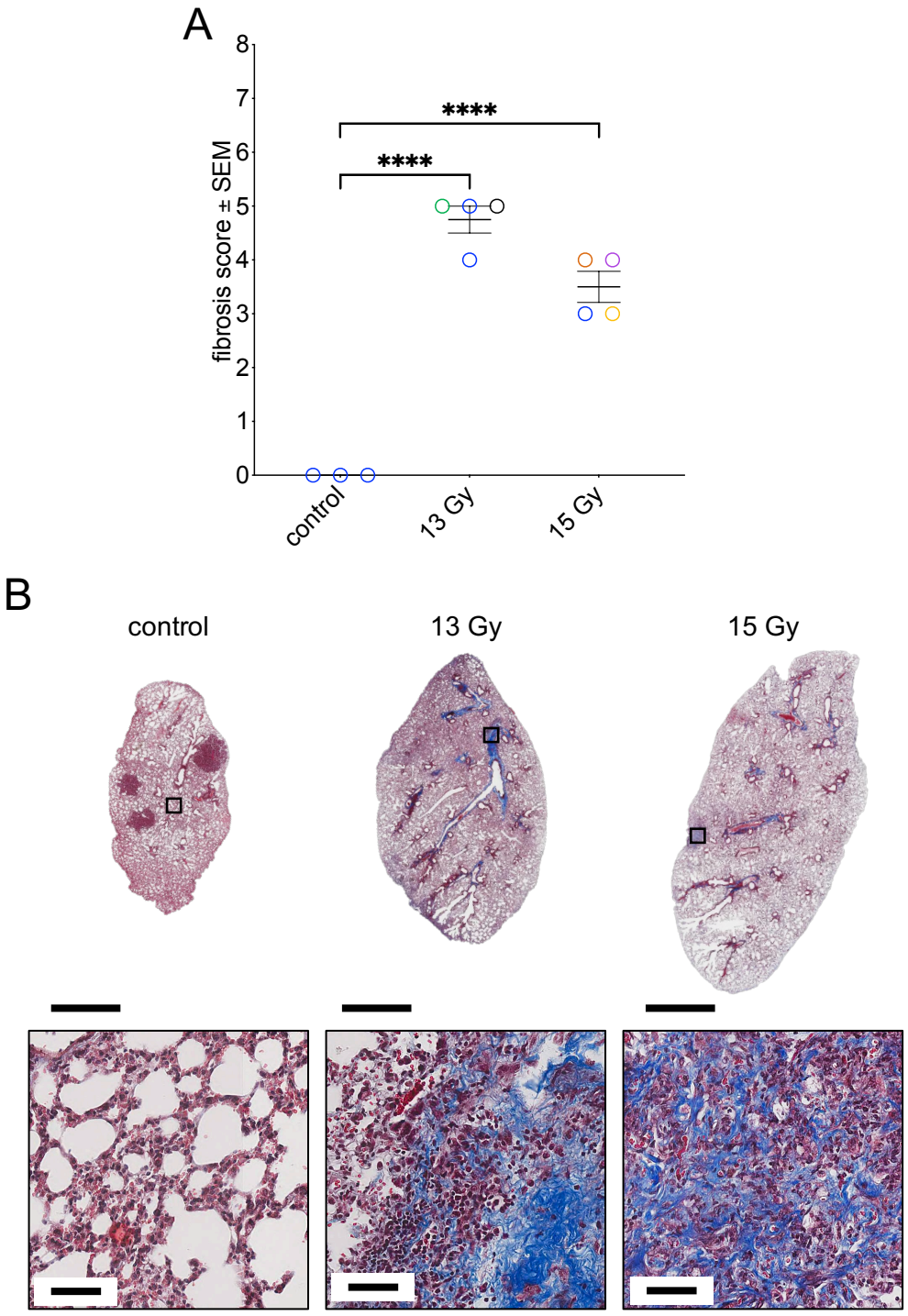

Figure 3.1.9. Fibrosis scoring of whole thorax IR. Fibrosis scoring of lungs stained by Masson's trichrome revealed a significant increase in fibrosis in the 13 Gy and 15 Gy groups as compared with the control group (A & B). (o) represent individual lung fibrosis scores and fibrosis scores of individuals that were euthanised due to weight loss are (o) for 13_No2, (o) for 13_No4, (o) for 15_No1, (o) for 15_No3, and (o) for 15_No4. Scale bars represent 2 mm for whole lung slices and 50 µm for representative image. Statistical analysis: 1-way ANOVA, post hoc Dunnett's multiple comparisons test (unpublished data, Yanyan Jiang).

These data reveal that single whole thorax IR doses of 13 and 15 Gy induced collagen deposition in the lungs of A/J mice following IR treatment.

3.1.5. CT-guided left lung IR of A/J mice leads to limited collagen accumulation and fibrosis score

Further investigations of the A/J model evaluated the late lung effects of a single hemithoracic IR dose to the left lung. A/J mice were injected with urethane and, after 8 weeks, treated with IR (13 or 15 Gy) to the left lung using the CT-guided SARRP (**Chapter 2.6.2**). SARRP treatment used an 8 x 8 mm collimator and a parallel-opposed beamline fit to cover the maximum left lung volume. Euthanasia was planned for 26 weeks after IR (**Fig. 3.1.10 A**).

At week 21 after IR, one mouse in the control group (JCM267) developed a spontaneous subcutaneous mass on the lower abdomen and was euthanised (**Fig. 3.1.10 B**). None of the groups showed significant weight loss. However, after 24 weeks 1 mouse in the 13 Gy group (JCM274) and 3 mice in the 15 Gy group (JCM275, JCM277, JCM278) developed mild sporadic coughing while breathing, and the study was ended.

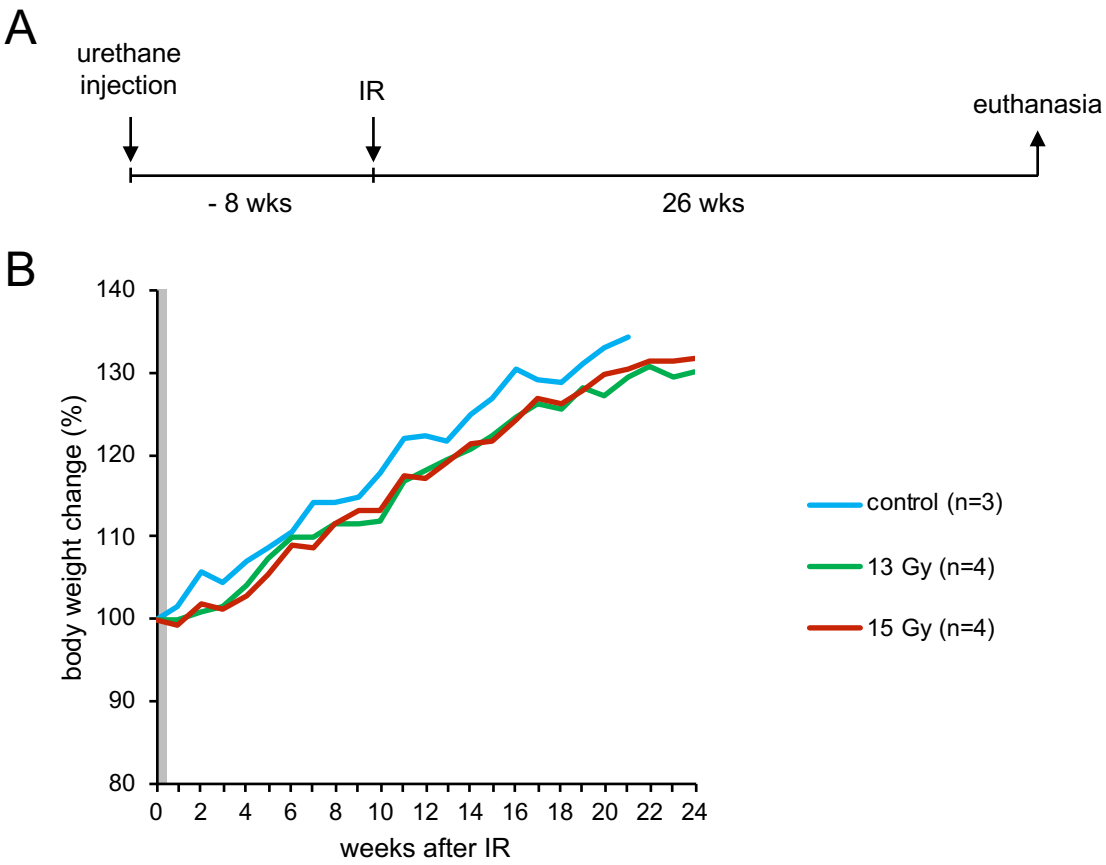

Figure 3.1.10. CT-guided left lung IR did not induce body weight loss. A/J mice were injected with urethane (2 x 5 mg per 10 g body weight, i.p.). After 8 weeks, mice were allocated into groups (n=3 for control and n=4 for both IR groups) and treated with IR (13 or 15 Gy) to the left lung. Euthanasia was planned for 26 weeks after IR (A). All groups gained weight during the study (B). At week 21, JCM267 (control) was euthanised due to a spontaneous subcutaneous mass on the lower abdomen[1]. The remaining control group mice gained weight until the end of study, but the average weight measurement was ended when JCM267 was euthanised. All other groups showed no significant weight loss during the study. During week 24, one mouse from the 13 Gy group (JCM274) and 3 mice from the 15 Gy group (JCM275, JCM277, and JCM278) presented with sporadic coughing while breathing, and the study was ended. Grey bar represents treatment.

Masson's trichrome was used to determine the fibrosis score of the lungs using modified Ashcroft scoring (**Chapter 2.16**). The average left lung fibrosis score of mice treated with 15 Gy (2.25) were significantly higher compared with the control group score (0) (**Fig. 3.1.11 A & B**).

[1] JCM267 post mortem revealed a subcutaneous vaginal mass and was included in all subsequent analysis.

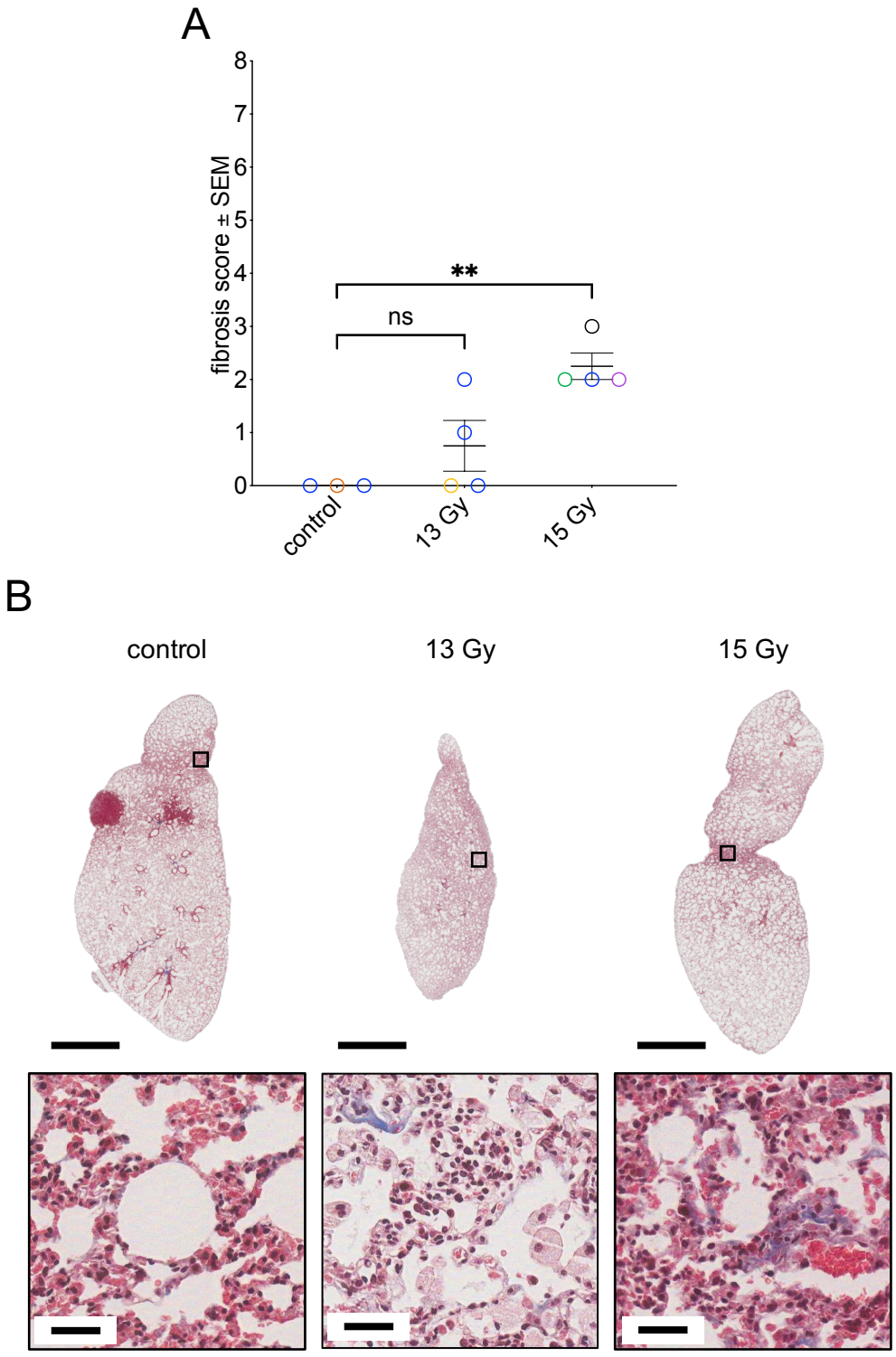

Figure 3.1.11. Fibrosis scoring of CT-guided hemithoracic left lung IR. Fibrosis scoring of lungs stained by Masson's trichrome revealed a mild increase in fibrosis in the 13 and 15 Gy groups as compared with the control group (A & B). Lungs in the 13 Gy group displayed an increased immune cell infiltrate consisting of eosinophils and lipid-laden macrophages indicative of pneumonitis. (o) represent individual lung fibrosis scores, (o) is JCM267 (control group, spontaneous mass), and fibrosis scores of individuals with sporadic coughing are (o) for JCM274, (o) for JCM275, (o) for JCM277, and (o) for JCM278. Scale bars represent 2 mm for whole lung slices and 50 µm for representative image. Statistical analysis: 1-way ANOVA, post hoc Dunnett's multiple comparisons test.

3.1.6. Discussion

The tumour growth capability and IR-induced fibrosis in A/J mice suggest that this model could have great potential for evaluating the therapeutic window of IR and IR combinations in preclinical studies. Several experimental designs can be developed using the A/J strain: early intervention studies (e.g. 8 weeks after tumour induction), late intervention studies (e.g. 19 weeks after tumour induction), and pharmacodynamic studies (e.g. 1 h – 7 d after treatment of established tumours at 18 weeks post induction).

Early intervention studies can be used to assess the effects of whole thorax or hemithorax IR and drug combinations on tumours early in their development (8 weeks) as well as the effects on late lung toxicity (fibrosis) that develops within 26 weeks after the start of fractionated IR (**Fig. 3.1.12**).

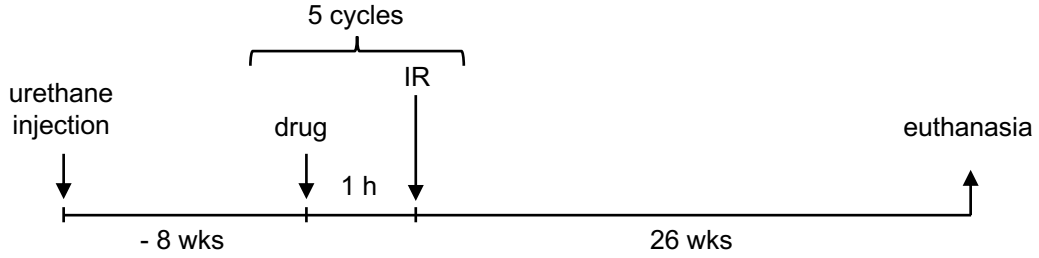

Figure 3.1.12. Experimental design for early intervention whole thorax or hemithorax IR therapeutic window studies. A/J mice are injected with urethane (2 x 5 mg per 10 g body weight, i.p.) and allocated into treatment groups. After 8 weeks, mice are treated with 5 cycles of IR combined with a drug, with 2 days between IR doses. Drug dose timing and duration can be adjusted depending on mechanism of action, clearance, and tolerability. Euthanasia is planned for 26 weeks after the first IR dose.

Late intervention studies can be used to evaluate the effect of left lung IR and drug combinations on established tumours (~250-500 μm^3) in A/J mice at 19 weeks after urethane. For this study design we use the CT-guidance capabilities of the Small Animal Radiation Research Platform (SARRP) to more closely model the delivery method in clinical practice. Optional MRI sessions before treatment and at 7 weeks post treatment allow for an analysis of the combination treatment effect on tumour

growth, which is also similar to patient treatment follow-up imaging sessions (**Fig. 3.1.13**).

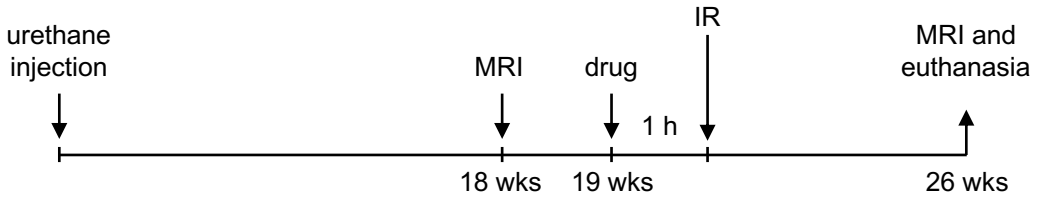

Figure 3.1.13. Experimental design for late intervention CT-guided IR therapeutic window study. A/J mice are injected with urethane (2 x 5 mg per 10 g body weight, i.p.). After 18 weeks, mice are allocated into groups and imaged using MRI. During week 19, mice are treated e.g. with a single dose of drug 1 h before left lung IR. Mice are imaged using MRI before euthanasia during week 26. Drug dose timing and duration can be adjusted depending on mechanism of action, clearance, and tolerability.

With established tumours at 18 weeks, a pharmacodynamics (PD) study can be used to evaluate both tumour and normal thoracic tissue responses to combination treatments (**Fig. 3.1.14**). Time points post IR chosen for the following chapters are 2 h and 24 h. Future experiments can use this study design to investigate a time course of responses ranging from hours to days after IR.

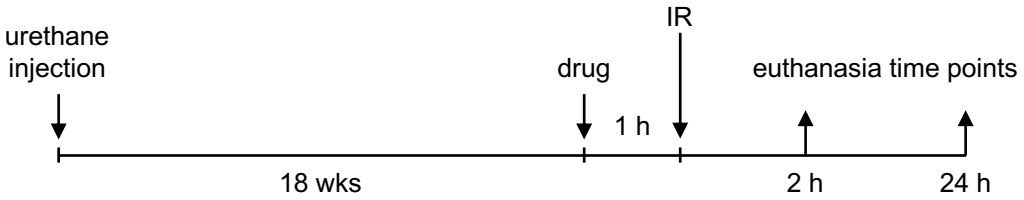

Figure 3.1.14. Experimental design for pharmacodynamic studies. A/J mice are injected with urethane (10 mg per 10 g body weight, i.p.). After 18 weeks, mice are allocated into groups and treated with a single dose of drug 1 h before whole thorax IR. Mice are euthanised at time points following IR (e.g. 2 and 24 h).

In developing the A/J model study designs, the BED of different tissues and the late lung responses between whole thorax and left lung IR must be carefully considered. There was a similar late lung biological response in both fractionated (5 x 5 Gy) and single dose (13 Gy) whole thorax IR, which is consistent with the BED calculations and the α/β ratio estimate for lung tissue of 3.3 (**Table 3.1.1**). Additionally, the higher single dose of 15 Gy to the whole thorax was not tolerated and resulted in

significant weight loss. However, a clear biological difference in the left lung responses between treatment with whole thorax and left lung IR was observed. Both 13 and 15 Gy to the whole thorax resulted in an increase in collagen deposition in the left lungs with fibrosis scores of 4.75 and 3.5, respectively, and 15 Gy was not tolerated. The 15 Gy fibrosis score was lower than the 13 Gy score most likely due to the early euthanasia of 3 mice, which curtailed further collagen accumulation. CT-guided left lung IR using the same doses (13 and 15 Gy) resulted in the markedly low fibrosis scores of 0.75 and 2.25, respectively, but several mice had begun to develop breathing clinical signs (n=1 in 13 Gy group and n=3 in 15 Gy group).

The difference in the biological response of the lung in whole thorax and CT-guided left lung IR can be attributed to dose volumes, dose delivery, and the interplay between thoracic organs. Unlike human lungs that have 2 left lobes and 3 right lobes, mouse lungs consist of 1 left lung lobe and 4 right lung lobes (superior, middle, inferior, post-caval). With selective IR of the left lung lobe, the 4 right lung lobes can still functionally compensate to maintain breathing; although not fully understood, this has been seen in both humans and other mammals after a lobe or lung is removed (Butler et al., 2012; Dabjan et al., 2016; Mentzer, 2018). In the whole thorax study, this compensation was not possible and therefore led to the early clinical signs and lack of tolerability of the 15 Gy group.

However, a further explanation is needed to understand the difference in fibrosis scores between the whole thorax and hemithorax (left lung) IR studies. Whole thorax treatment was achieved by using the whole thorax irradiation rig, in which X-rays are delivered from a single direction to the ventral side of the animal using a Gulmay RS320 irradiator (**Fig. 2.6.1.2**). Dosimetry of a phantom mouse revealed that upon irradiation, the actual delivered dose decreases with increasing depth into the phantom (**Appendix Table 6.4**). The dose rate is estimated for 7.5 mm into the animal (at the

approximate centre of the lung); however, the dose is not uniform (due to scatter and dose deposition) and at the surface of the animal, the dose can be up to 12% higher. The CT-guided treatment of the left lung by the SARRP used a collimator of 8 x 8 mm to target the left lung (**Fig. 2.6.2.4**). X-rays were delivered in 2 successive treatments to the left dorsal and ventral sides of the animals (parallel-opposed) to account for the dose rate decrease with increasing depth, which has been measured for the SARRP (Ghita et al., 2017). A more uniform dose distribution across the left lung using the SARRP may have contributed to a lower overall biological response measured by fibrosis score.

A third important consideration for the difference between whole thorax vs. left lung IR is the other thoracic organs in the field of irradiation. A study in rats demonstrated that irradiation of both the heart and lungs increased the IR-induced toxicity of each respective organ, including fibrosis, when compared with selective IR of each organ (Ghobadi et al., 2012). The pulmonary and cardiac interplay have been shown to affect overall lung function and may contribute to the biological consequences of whole thorax IR (van Luijk et al., 2007; van Luijk et al., 2005). Avoidance of the heart using hemithorax or left lung IR may be important in reducing normal tissue effects from treatments.

Overall, we have further characterised a urethane-induced model of lung cancer and developed it for use in studies of IR-induced lung fibrosis and cancer treatments. We have identified several possible experimental study designs and outcome measurements for the assessment of lung cancer treatments involving combination therapies with IR. The three main studies (early intervention, late intervention and pharmacodynamics) will be used in the following chapters to investigate the therapeutic window of IR in combination with current clinical compound candidates,

providing insight into their anti-tumour and normal tissue effects in the A/J model of urethane-induced lung cancer.

3.2. Therapeutic window of AZD6738 and IR in A/J mouse model

3.2.1. Introduction

The effectiveness of IR on tumour control can be modulated by the addition of drugs that selectively target cancer cells due to their intrinsic radiosensitivity (**Chapter 1.3**). An emerging area of targeted therapeutics involves using inhibitors of the DDR pathway in combination with radiotherapy. One of the proteins involved in this pathway, ataxia telangiectasia and Rad3-related (ATR), is currently under investigation as a promising candidate for inhibitory combination therapies (Karnitz and Zou, 2015; O'Connor, 2015).

ATR is a member of the phosphatidylinositol 3-kinase-related kinase (PIKK) family of protein kinases that also includes ataxia-telangiectasia mutated (ATM), DNA-dependent protein kinase catalytic subunit (DNA-PKcs), and mechanistic target of rapamycin (mTOR) (Weber and Ryan, 2015). ATR is involved in regulating the cell cycle and cellular responses to replication stress. It is considered an essential gene for cellular functioning and is embryonically lethal if knocked out in mice (Brown and Baltimore, 2000). When single-stranded DNA (ssDNA) forms at stalled replication forks during S phase of the cell cycle, replication protein A (RPA) binds and recruits ATR-interacting protein (ATRIP) in a complex with ATR (**Figure 3.2.1**) (Ball et al., 2005; Cortez et al., 2001; Wold and Kelly, 1988; Zou and Elledge, 2003). The RAD17/RFC2-5 clamp loader forms at the junction between ssDNA and double stranded DNA (dsDNA) and loads the RAD9-HUS1-RAD1 (9-1-1) clamp complex (Lee et al., 2007; Zhou and Elledge, 2000). In turn, the 9-1-1 complex, along with the RAD9-HUS1-RAD1-interacting nuclear orphan (RHINO), recruits topoisomerase II binding protein 1 (TOPBP1), which can bind to ATR to activate it (Delacroix et al., 2007; Kumagai et al., 2006; Lee et al., 2007). Ewing's tumour-associated antigen 1 (ETAA1) is also recruited by RPA and can serve as a secondary activator of ATR signalling (Haahr et al., 2016; Lee et al., 2016).

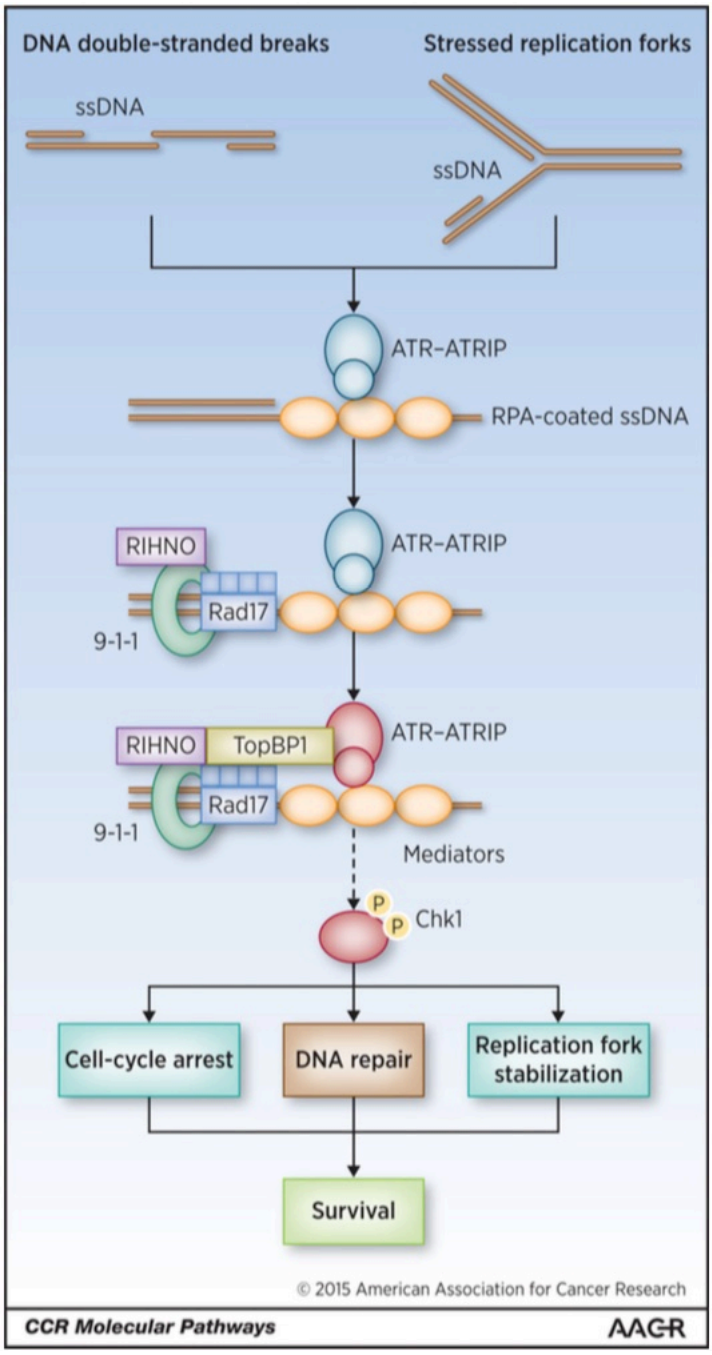

Figure 3.2.1. ATR signalling pathway after activation by DNA damage or replication stress. (Reproduced from Karnitz and Zou, 2015).

Once these proteins are present at the stalled replication fork, ATR is activated and phosphorylates checkpoint kinase 1 (CHK1) (Liu et al., 2000). Through its activation of CHK1, ATR regulates cell cycle progression to prevent further DNA damage (Liu et al., 2000; Saldivar et al., 2017). CHK1 activation leads to the phosphorylation and subsequent ubiquitin-dependent degradation of cell division cycle 25 (CDC25) phosphatases which results in the inhibition of cyclin dependent kinases (CDK1/2) and subsequent inhibition of cyclin E/A and cyclin B1-dependent cell cycle

progression (Donzelli and Draetta, 2003; Saldivar et al., 2017; Takizawa and Morgan, 2000; Uto et al., 2004). CHK1 and ATR are also involved in negatively regulating origin firing and stabilising replication forks (Katsuno et al., 2009; Lopes et al., 2001; Shechter et al., 2004). ATR also promotes fork repair and restart by phosphorylating proteins at stalled forks and preventing DSBs forming when replication forks collapse (Cimprich and Cortez, 2008; Trenz et al., 2006). Although a major mechanism of action is through the phosphorylation of CHK1, ATR also phosphorylates other targets involved in the DNA damage response such as breast cancer gene 1 (BRCA1) and p53 (Cimprich and Cortez, 2008; Tibbetts et al., 1999; Tibbetts et al., 2000; Weber and Ryan, 2015).

The essential functions of ATR in controlling cell cycle progression and responding to replication stress provide a key rationale for using inhibitors of ATR in cancer treatments since it is known that cancer cells have a high level of endogenous DNA replication stress compared with normal tissues (Gaillard et al., 2015). Tumour cells have oncogenic driver mutations that overcome normal cellular checkpoint controls and allow for uncontrolled growth (**Figure 1.1.1**) (O'Connor, 2015). When tumour cells replicate their DNA, they rely on ATR signalling to withstand the replication stress caused by the oncogenic mutations and to prevent replication fork collapse. By inhibiting ATR, tumour cells are less able to regulate DNA replication and cell cycle progression or use compensatory DDR pathways which are commonly mutated in cancer, and the increased genome instability can lead to cell death.

Inhibition of ATR signalling has been demonstrated to be synthetically lethal in tumours with *K-ras* mutations (Gilad et al., 2010; Schoppy et al., 2012). Synthetic lethality of ATR inhibition has also been shown in cell lines deficient in p53 or ATM *in vitro* and in xenografts (Kwok et al., 2016; Min et al., 2017). Other studies have demonstrated increased efficacy of ATR inhibitors in combination with IR in cancer cell lines, tumour xenografts with *K-ras* mutations, and, importantly, with evidence of

limited normal cell damage (Fokas et al., 2014; Middleton et al., 2018; Pires et al., 2012).

Several ATR inhibitors are currently in development, either as combination therapies or as single agents (**Table 3.2.1**). Clinical trial updates from berzosertib (VX-970, VE-822 or M6620), BAY1895344, M4344 (VX-803) and AZD6738 (ceralasertib) have recently been reviewed (Mei et al., 2019; Rundle et al., 2017; Topatana et al., 2020).

ATR inhibitor	Treatment	Cancer type	Phase	Identifier
berzosertib (M6620, VX-970, or VE-822)	berzosertib + radiotherapy	Lung cancer	I	NCT02589522
	berzosertib + radiotherapy	Breast cancer	I	NCT04052555
	berzosertib + topotecan	Lung cancer	I/II	NCT02487095
	berzosertib + topotecan Hydrochloride	Lung cancer	II	NCT03896503
	berzosertib + carboplatin + docetaxel	Prostate cancer	II	NCT03517969
	berzosertib + radiotherapy + cisplatin + capecitabine	Oesophageal cancer	I	NCT03641547
AZD6738 (ceralasertib)	AZD6738 + radiotherapy	Advanced solid tumours	I	NCT02223923
	AZD6738 + olaparib	Gynaecologic cancer	II	NCT04065269
	AZD6738 + olaparib + durvalumab	Breast cancer	II	NCT03740893
	AZD6738 + acalabrutinib	Chronic lymphocytic leukaemia	I/II	NCT03328273
	AZD6738 + durvalumab	Biliary tract cancer	II	NCT04298008
BAY1895344	BAY1895344	Advanced solid tumours	I	NCT03188965
	BAY1895344 + pembrolizumab	Advanced solid tumours	I	NCT04095273
	BAY1895344 + niraparib	Ovarian cancer	I	NCT04267939
M4344 (VX-803)	M4344 + niraparib	Ovarian cancer	I	NCT04149145
	M4344 + carboplatin	Advanced solid tumours	I	NCT02278250
RP-3500	RP-3500 RP-3500 + talazoparib	Advanced solid tumours	I	NCT04497116

Table 3.2.1. ATR inhibitors currently in clinical trials. (Modified from Topatana et al., 2020).

This chapter focuses on AZD6738, an ATR inhibitor developed by AstraZeneca. AZD6738 is orally active and highly selective with a 50% inhibitory concentration (IC_{50}) of 0.001 μM against ATR kinase activity while other closely related PIKKs require > 30 μM (Vendetti et al., 2015). In combination with IR, it has been shown to be a radiosensitiser in two RAS mutated human lung cancer cell lines *in vitro* and *in vivo* xenografts but not to affect a human bronchial epithelial cell line *in vitro* (Dunne et al., 2017). Additionally, the combination treatment of AZD6738 (25 mg/kg, 1 h before IR) with a 5 x 5 mm right lung IR field using the Small Animal Radiation Research Platform

(SARRP) has been tested in C57BL/6 mice, and no difference was found between IR alone and combination treatment groups in lung fibrosis as measured by the modified Ashcroft scores (Dunne et al., 2017).

AZD6738 is also currently being evaluated in a number of clinical trials as a monotherapy or in combination. The PATRIOT trial (NCT02223923) is a phase I dose escalation study and includes two cohorts of patients that will receive palliative radiotherapy in combination with the maximum tolerated dose of AZD6738 (Dillon et al., 2018). Additionally, AZD6738 will be used in one arm of the CONCORDE platform, which aims to combine DDR inhibitors with radical radiotherapy in patients with locally advanced NSCLC (Faivre-Finn et al., 2020; Walls et al., 2020).

While there is sufficient evidence to support the clinical trials of AZD6738 for the treatment of cancer, the therapeutic window of AZD6738 as a combination therapy with thoracic radiotherapy has not yet been evaluated in a single model encompassing the effects of IR on lung cancer growth and normal tissue damage. The following study aims to address this knowledge gap in the context of both tumour treatment efficacy and normal tissue damage in the A/J mouse model of urethane-induced lung cancer (**Fig. 3.2.2**).

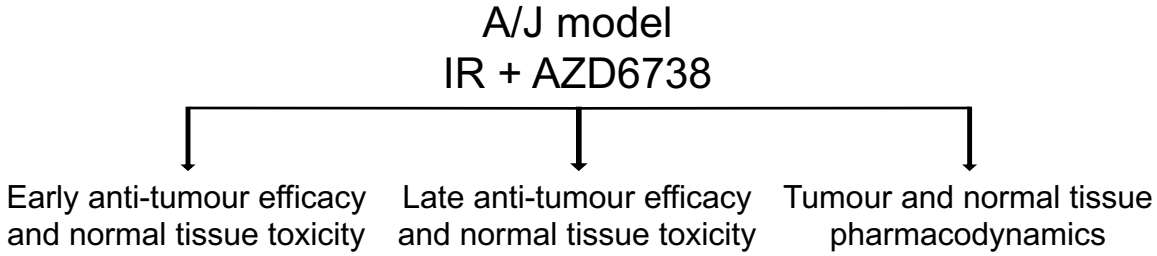

Figure 3.2.2. Main aims and experimental arms.

3.2.2. AZD6738 radiosensitises Calu6 xenograft tumours in CD-1 nude mice

To evaluate the 50 mg/kg dose of the ATR inhibitor AZD6738 *in vivo*, a subcutaneous xenograft tumour growth model was used. Human lung carcinoma cells (Calu6) were injected into the back of CD-1 nude mice. Once tumours reached a mean

size of 100 mm^3, mice were treated with 4 cycles of AZD6738 (50 mg/kg) 1 h before and 24 h after local IR (5 Gy). Tumour growth was measured for up to 42 d after treatment or until tumours reached 400 mm^3 (**Fig. 3.2.3 A**). A fractionated schedule of 4 treatments of 5 Gy (IR + vehicle, n=4) resulted in tumour growth inhibition compared with control treatment (**Fig. 3.2.3 B**). When tumours were treated with IR + AZD6738 (n=5), growth was significantly inhibited compared with the IR + vehicle treated tumours. No AZD6738 monotherapy group was included in this study.

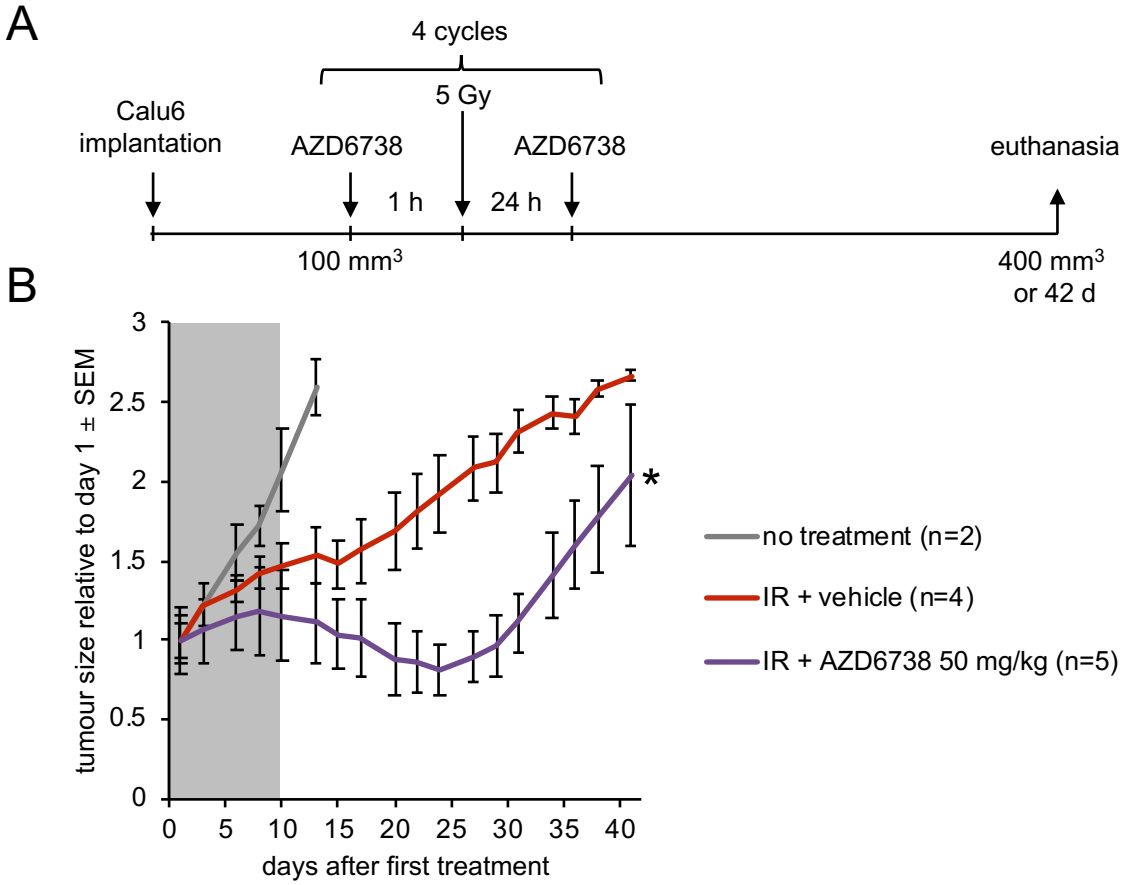

Figure 3.2.3. AZD6738 in combination with IR increased tumour growth inhibition in Calu6 xenografts. Calu6 cells (5 x 10^6) were implanted (s.c.) into the back of CD-1 nude mice. When tumours reached a mean size of 100 mm^3, mice were allocated into groups (n=2 for control, n=4 for IR + vehicle, and n=5 for IR + AZD6738). Mice treated with 4 cycles of AZD6738 (50 mg/kg, p.o.) 1 h before and 24 h after IR (5 Gy), with 2 days between IR doses. Tumours were measured 3 times per week. When tumours reached 400 mm^3 or at 42 days after the first treatment, mice were euthanised, and tumours were collected (A).Tumour growth inhibition (57%) was measured in the IR group as compared with the untreated group on day 13 (B). Tumour growth inhibition (58%) was observed in the IR + AZD6738 group as compared with the IR + vehicle group on day 24. There was a significant difference in mean tumour size between IR + vehicle and IR + AZD6738 on day 24. Grey region indicates treatment cycles (Luiza Lourenço DPhil thesis, 2017).

3.2.3. AZD6738 and fractionated whole thorax IR leads to oesophageal inflammation in the A/J early intervention therapeutic window study

To examine the effect of AZD6738 in combination with fractionated whole thorax IR, the A/J early intervention therapeutic window model was used (**Fig. 3.1.12**). A/J mice were injected with urethane to initiate tumour growth. Eight weeks later, mice were treated with 5 cycles of AZD6738 (50 mg/kg) 1 h before and 24 h after whole thorax IR (5 Gy), with 2 days between IR doses. The study was planned to end 26 weeks after the first IR dose (**Fig. 3.2.4 A**). During treatment, all groups lost between 5 to 10% of their starting weights from the beginning of treatment. However, after the final cycle, all mice in the IR + AZD6738 group (n=6) had lost greater than 15% body weight despite intervention with softened food, and therefore the study was ended early on day 16 (**Fig. 3.2.4 B**).

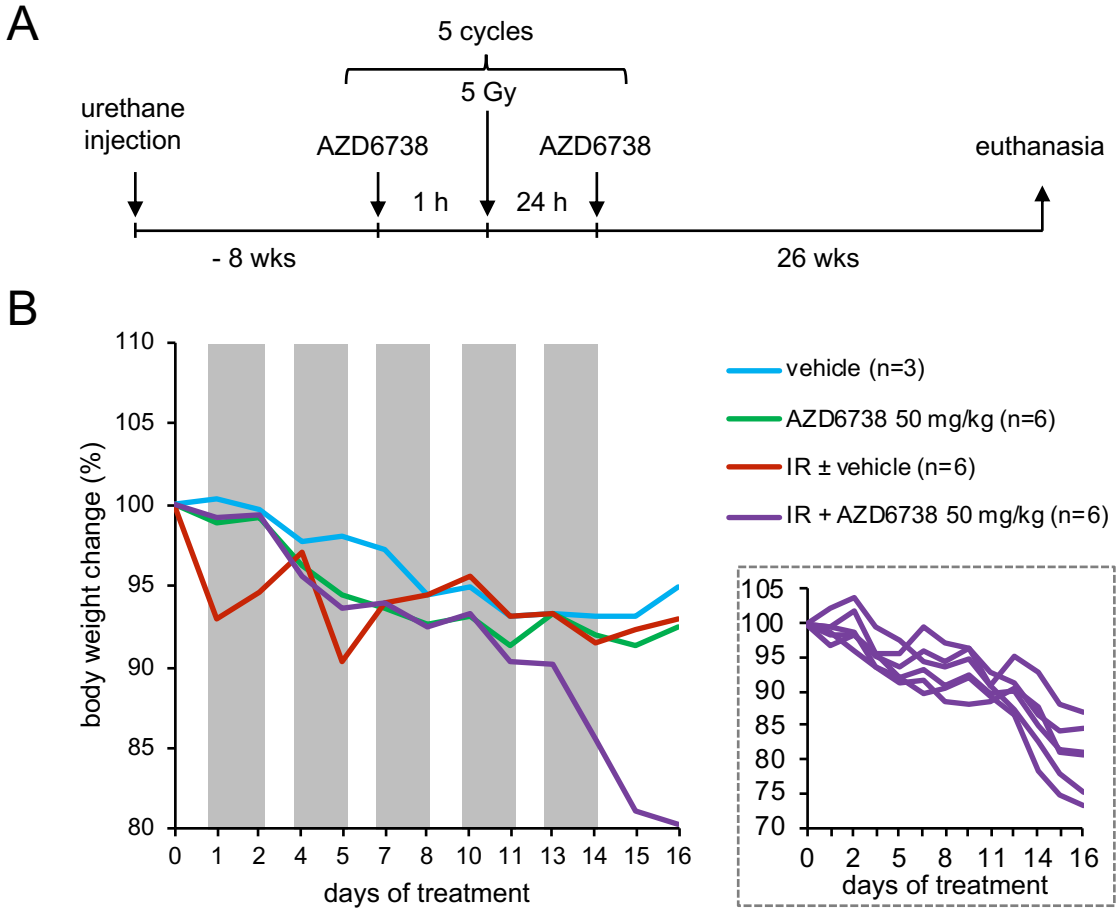

Figure 3.2.4. Early intervention with whole thorax IR combined with AZD6738 induced sustained body weight loss in A/J mice. A/J mice were injected with urethane (10 mg per 10 g body weight, i.p., A). After 8 weeks, mice were allocated into groups (n=3 for vehicle treated, and n=6 for AZD6738, IR ± vehicle, and IR + AZD6738). Mice were treated with 5 cycles of AZD6738 (50 mg/kg, p.o.) 1 h before and 24 h after whole thorax IR (5 Gy), with 2 days between IR doses. Euthanasia was planned for 26 weeks after the first IR dose. All mice in the IR + AZD6738 group (n=6) lost greater than 15% weight after the final treatment cycle and were euthanised on day 16 (B). Individual weights of the IR + AZD6738 group are shown in the graph inset. Grey bars represent 24 h treatment cycles.

Upon post mortem examination, enlarged oesophagi were visible, and H&E staining revealed disruption of oesophageal layers and infiltration of immune cells in the IR + AZD6738 group as compared with IR controls (**Fig. 3.2.5 A**). Further staining by IHC identified these infiltrating cells as Ly6G/C-positive, a marker of granulocytes/neutrophils (**Fig. 3.2.5 B**). Oesophagi from mice treated with IR + AZD6738 showed a significant increase in Lyc6G/C-positive cells as compared with oesophagi from mice treated with IR ± vehicle (**Fig. 3.2.5 C**). All other treatment groups had no evidence of disrupted oesophagi or infiltration of granulocytes/neutrophils (**Fig.**

3.2.5 C). These results suggest that 2 doses of AZD6738 (50 mg/kg) with 5 fractions of 5 Gy to the whole thorax is not tolerated in A/J mice because it was associated with unacceptable weight loss due to acute oesophagitis.

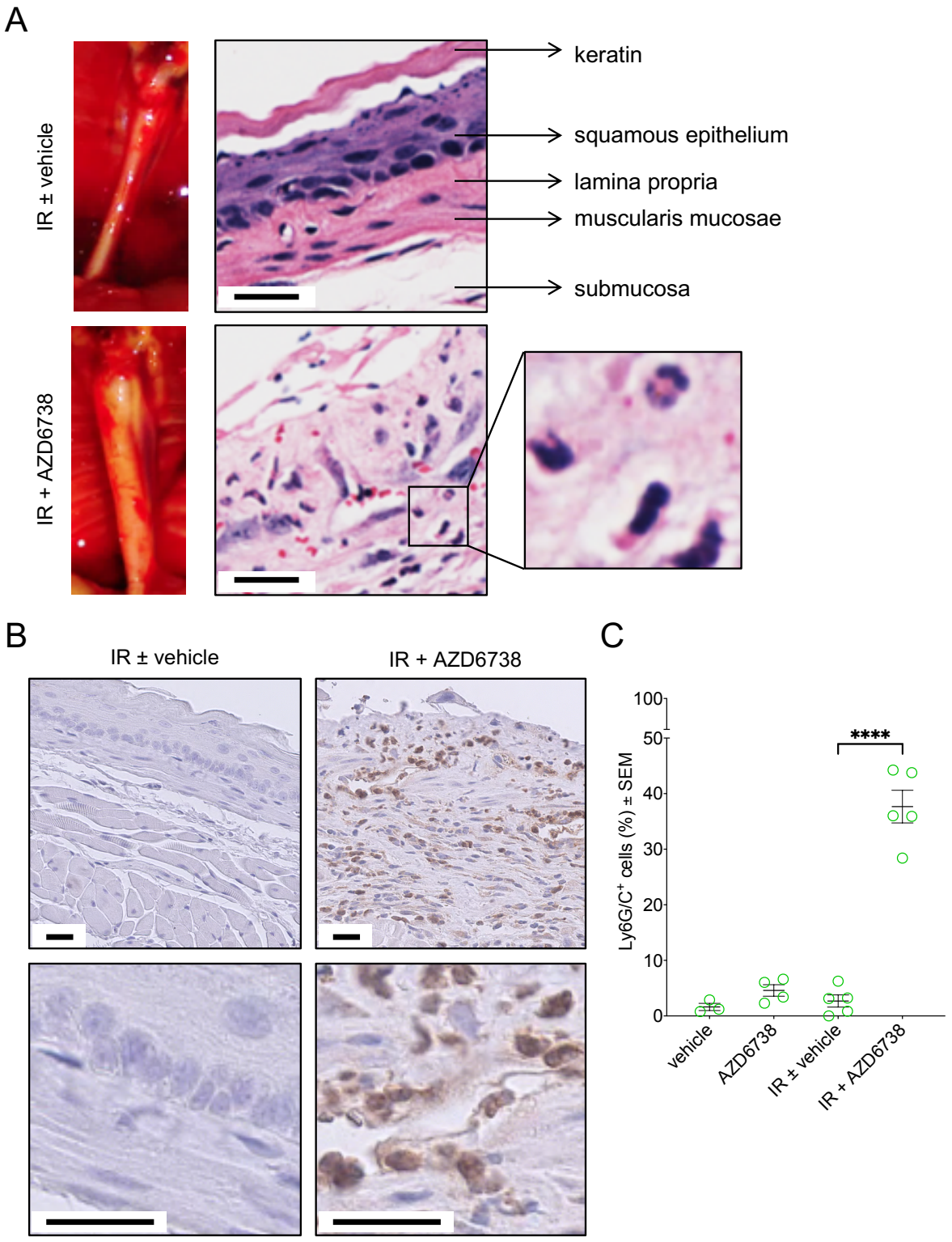

Figure 3.2.5. AZD6738 combined with whole thorax IR results in oesophageal inflammation. Mice in the combination treatment group (IR + AZD6738) showed enlarged oesophagi upon euthanasia at day 16 with disruption of oesophageal layers and immune infiltrate evident by H&E (A). Oesophagi of the IR + AZD6738 treated group presented with an infiltrate of Ly6G/C-positive cells when compared with IR ± vehicle as shown by IHC (B) and quantified per representative region[1] (C). All scale bars represent 25 μm and (o) are individual oesophagi.

[1] Mice in the ATRi group (2), IR + vehicle group (1), and IR + ATRi group (1) were excluded from quantitative analysis due to insufficient evaluable tissue.

3.2.4. AZD6738 combined with hemithorax fractionated IR is well tolerated but shows limited efficacy in A/J early intervention therapeutic window study

To explore the efficacy and tolerability of AZD6738 with IR treatment in the tumours and late responding normal tissues of the A/J model while mitigating the potential for substantial toxicity from the combination, the treatment schedule and set up was altered (**Fig. 2.6.1.3** and **Appendix Fig. 6.2**). A hemithorax IR rig was designed with adjustable lead shielding to align with the sternum of each individual mouse, avoiding the oesophagus and only exposing the left thorax (**Fig. 2.6.1.3**). Additionally, to further mitigate potential combination therapy toxicity, only a single dose of AZD6738 was used per IR fraction. A/J mice were injected with urethane to initiate tumour growth for 8 weeks before 5 cycles of AZD6738 (50 mg/kg) 1 h before hemithorax IR (5 Gy), with 2 days between IR doses (**Fig. 3.2.6 A**).

During treatment, all groups lost up to 10% of their pre-treatment body weights but began recovering after treatment finished (**Fig. 3.2.6 B**). Four mice were euthanised during the study due to large or spontaneous tumours (JCM78, JCM92, JCM99, JCM103) (**Fig. 3.2.6** legend). None of the other groups showed any further weight loss, skin effects, or other clinical signs during the experiment, and all groups were euthanised 26 weeks after the start of treatment.

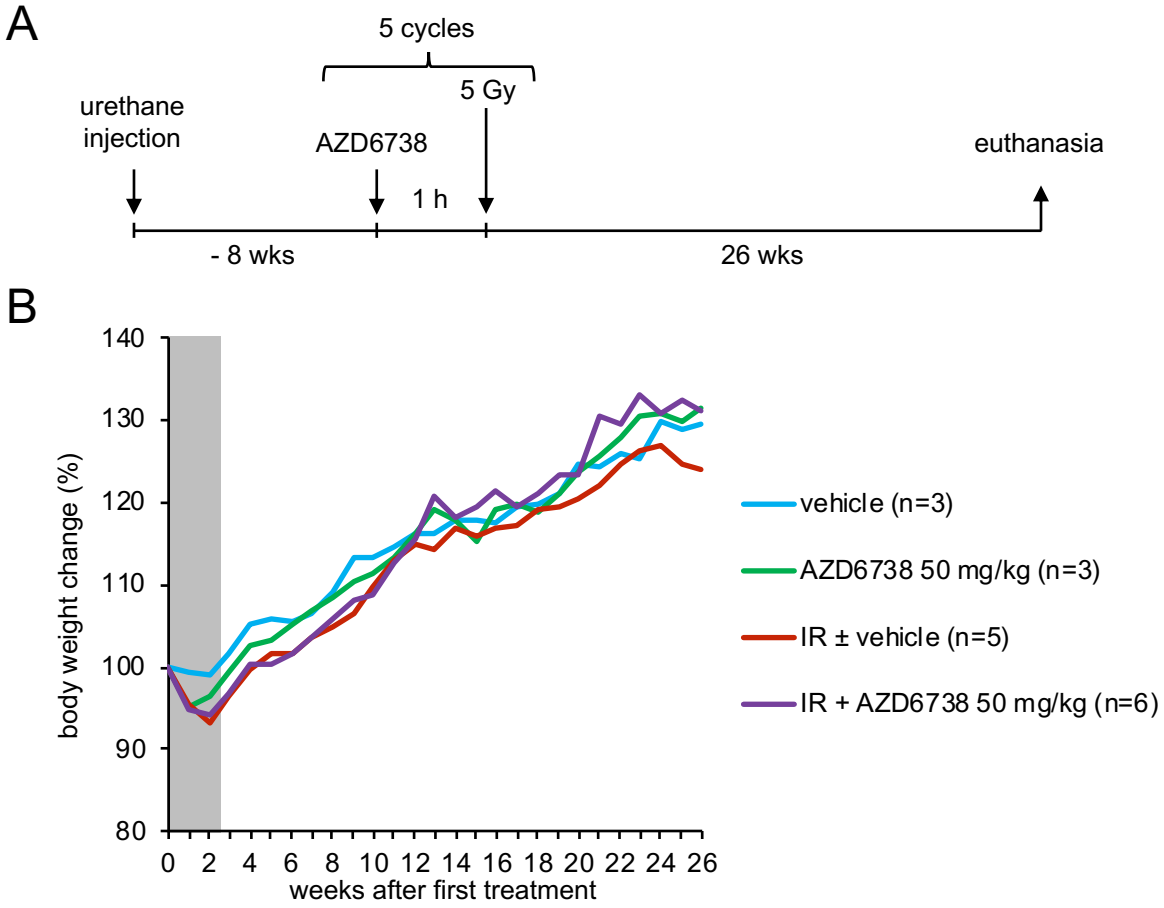

Figure 3.2.6. AZD6738 in combination with hemithorax IR did not induce body weight loss. A/J mice were injected with urethane (10 mg per 10 g body weight, i.p., A). After 8 weeks, mice were allocated into groups (n=3 for vehicle and AZD6738, n=6 for IR ± vehicle, and n=6 for IR + AZD6738). Mice were treated with 5 cycles of AZD6738 (50 mg/kg, p.o.) 1 h before left thorax IR (5 Gy), with 2 days between IR doses. Euthanasia was planned for 26 weeks after the first IR dose. During treatment, all groups showed mild (5-10%) weight loss but recovered within 2-3 weeks (B). At week 19, one mouse in the IR + AZD6738 group, JCM103, was euthanised due to a spontaneous subcutaneous mass on the lower left flank[1]. During week 20, JCM99 (IR + AZD6738) was euthanised due to vaginal bleeding and 7% weight loss[2]. At week 21, JCM92 (IR ± vehicle) was euthanised due to laboured breathing and greater than 15% weight loss[3]. JCM78 (IR ± vehicle) was euthanised at week 23 due to laboured breathing and 9% weight loss[4]. Subsequently, each group weight average was adjusted for the remaining mice. All other mice showed no significant weight loss during the study and were euthanised 26 weeks after treatment. Grey bar represents treatment cycles.

[1] JCM103 was included in all subsequent analyses.
[2] JCM99 post mortem revealed a vaginal mass as the source of bleeding and was included in all subsequent analysis. A/J mice are prone to myoepitheliomas arising from exocrine glands (Sundberg et al., 1991).
[3] JCM92 post mortem H&E analysis revealed a large tumour mass on apex of the left lung and large immune infiltrate throughout alveolar space. JCM92 was not included in any analyses.
[4] JCM78 post mortem revealed a large mass above the left lung attached to the thymus and was not included in fibrosis scoring or lung weights analysis.

The effect of AZD6738 and IR on tumour burden was evaluated using superficial tumour counts and histological counts of lung slices. Superficial tumour counts were reduced on the left lungs of individuals in IR ± vehicle (n=5) group as compared with the vehicle control (n=3); however, the IR + AZD6738 group (n=6) did not show a further reduction in tumour numbers as compare to the IR ± vehicle group (**Fig. 3.2.7 A**). Surprisingly, the AZD6738 group (n=3) also showed a reduction in superficial tumour counts as compared with the vehicle controls. When this result was examined with a larger group size (n=6) and two sets of 5 daily dosing regimens, the effect was not reproduced (**Appendix Figures 6.4-6.6**).

Because the hemithorax lead shielding is aligned with each mouse's sternum to avoid the oesophagus, it also shields the right lung from IR; therefore, the ratio of left to right lung tumour counts was also used to compare superficial tumour numbers using the right lung as an internal control in each animal. This further demonstrated that IR ± vehicle reduced the ratio of left to right lung tumour numbers as compared with vehicle alone and also confirmed that the combination treatment did not reduce this ratio as compared with the IR ± vehicle group (**Fig. 3.2.7 B**).

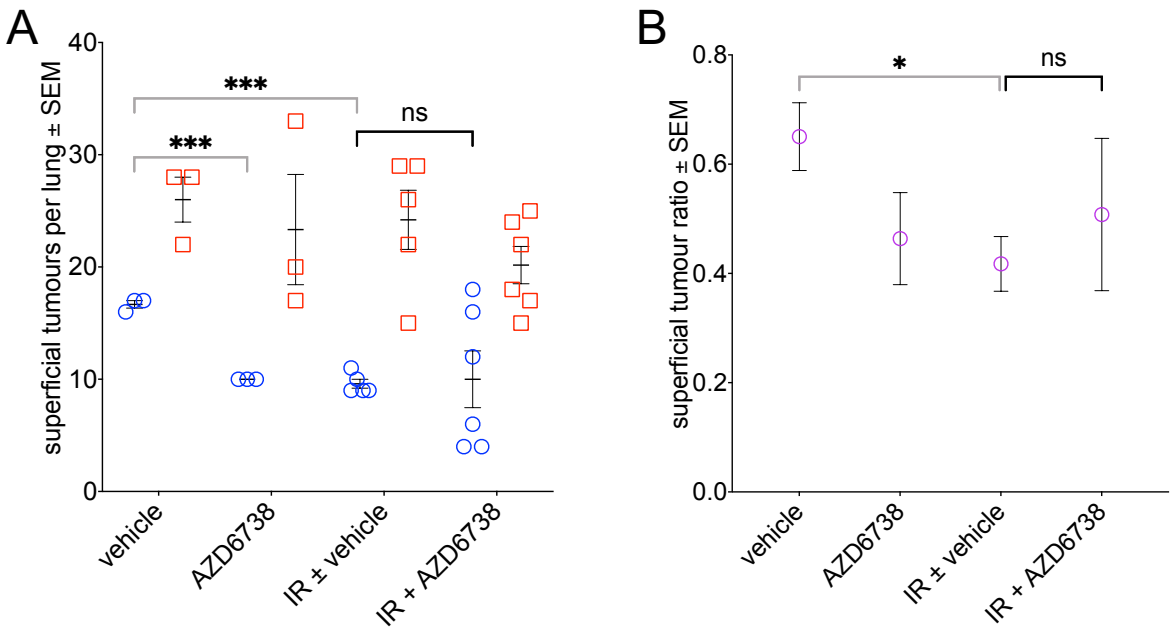

Figure 3.2.7. AZD6738 in combination with hemithorax IR did not reduce superficial tumour counts or ratio compared with hemithorax IR alone. Irradiated left lungs (IR ± vehicle) had a significant reduction in both superficial tumour numbers and ratio between lung tumour counts. Mice treated with AZD6738 alone also had a reduced tumour count. Mice in the IR + AZD6738 group did not show a reduction in either tumour counts or count ratio. (o) are individual left lungs, (□) are individual right lungs, (o) are a ratio of left lung counts divided by right lung counts.

Histological analysis of a single midsection left lung slice allowed the number and total tumour area (tumour area burden) per slice to be measured to further assess treatment efficacy. None of the treatment groups reduced either tumour number or tumour area burden compared with controls (**Fig. 3.2.8 A & B**).

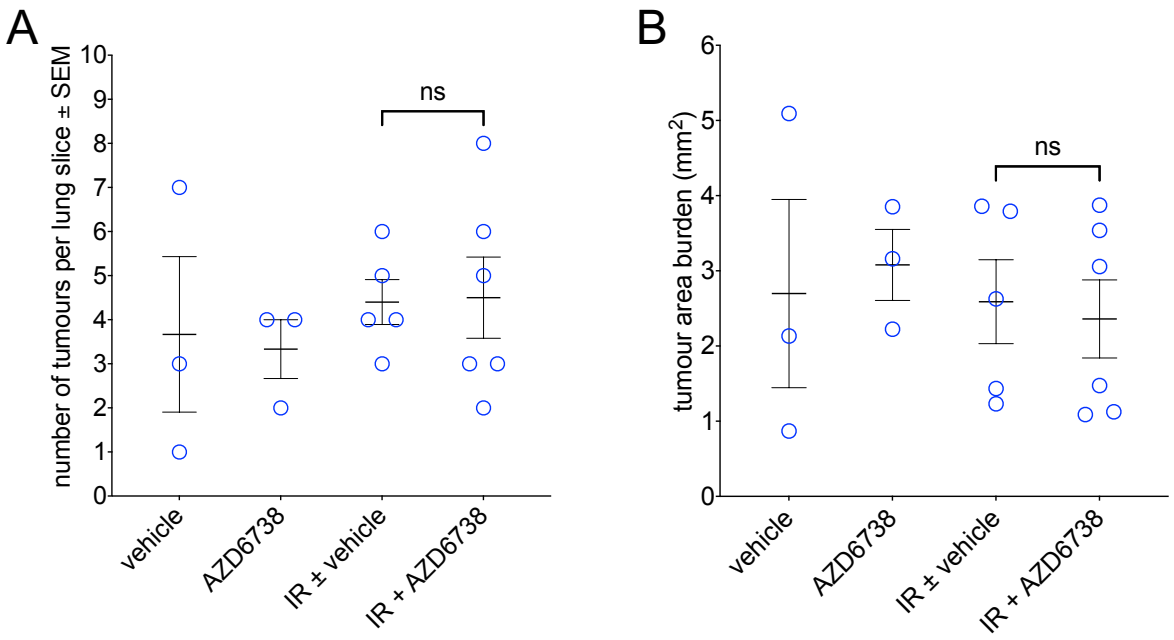

Figure 3.2.8. AZD6738 in combination with hemithorax IR did not reduce tumour number or area per lung slice compared with hemithorax IR alone. Mice in the IR + AZD6738 group did not show a reduction in either tumour counts per left lung slice (A) or total tumour area burden (B) as compared with IR ± vehicle. IR ± vehicle did not show a reduction in either measure compared with vehicle alone. (o) are individual left lungs.

To determine the treatment effects on the normal tissue of the lungs, both lungs were weighed upon collection and showed no difference between treatment groups (**Fig. 3.2.9 A**). Lungs were additionally assessed using the modified Ashcroft scoring of left lungs stained by Masson's trichrome (**Chapter 2.16**). Fibrosis assessment revealed that treatment with IR ± vehicle increased individual fibrosis scores compared with vehicle alone; however, there was no significant difference between the IR ± vehicle and IR + AZD6738 groups (**Fig. 3.2.9 B & C**).

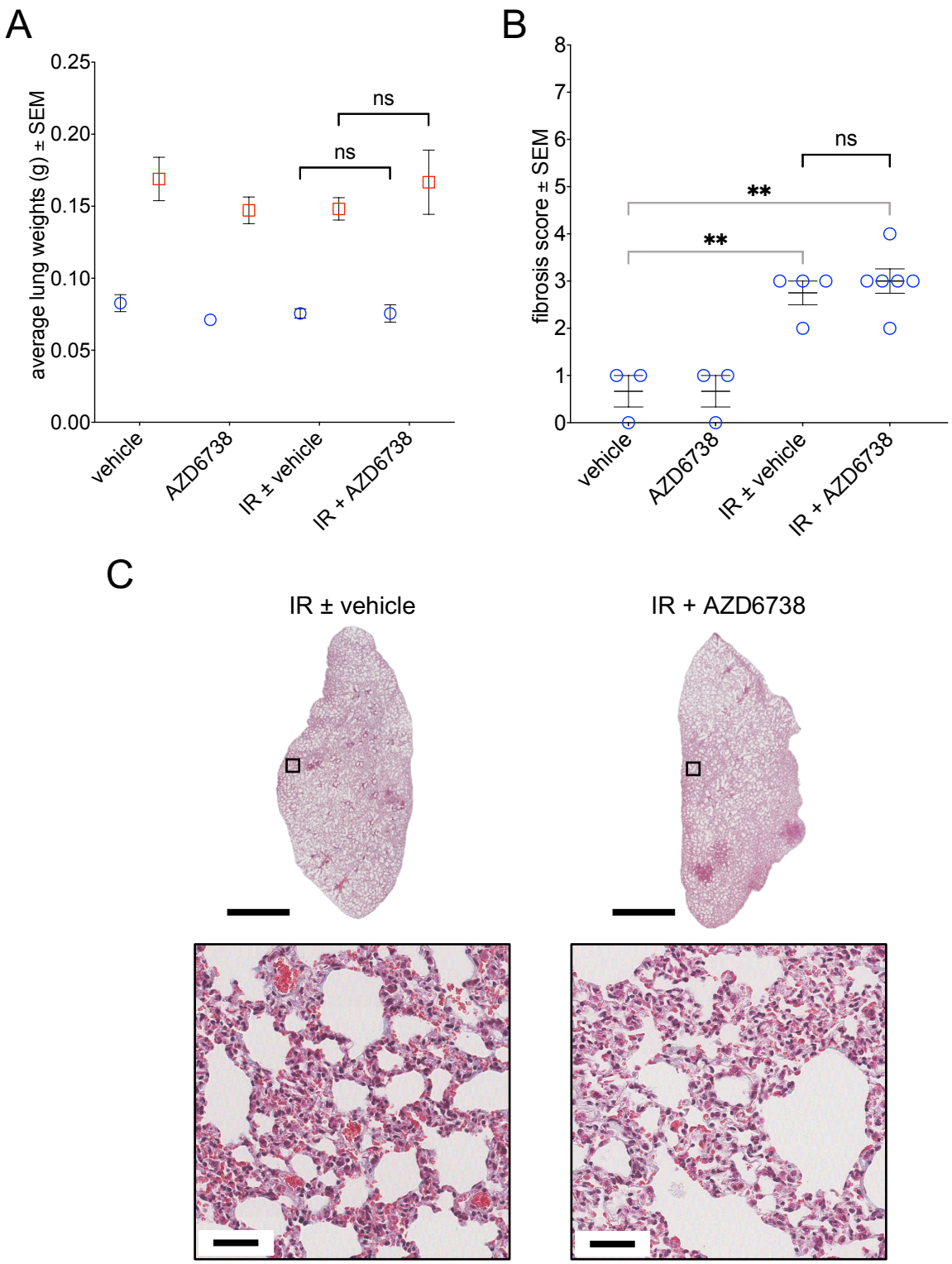

Figure 3.2.9. AZD6738 in combination with hemithorax IR did not affect lung weights or fibrosis scores compared with hemithorax IR alone. None of the treatment groups showed significant normal tissue effects as measured by lung weight (A). Fibrosis scoring of lungs stained by Masson's trichrome revealed an increase in fibrosis in the IR ± vehicle and IR + AZD6738 groups, but there was no significant difference between these two groups (B and C). (o) are average left lungs, (□) are average right lungs in A. (o) represent individual total lung fibrosis score in B. Scale bars represent 2 mm for whole lung slices and 50 μm for representative image.

Taken together, these results suggest that AZD6738 at 50 mg/kg given once prior to each fraction of hemithorax IR shows limited efficacy in the treatment of the early tumours of the A/J model but, importantly, does not increase IR induced fibrosis and lung damage.

3.2.5. AZD6738 and CT-guided left lung IR is well tolerated but shows limited efficacy in A/J late intervention therapeutic window study

The efficacy and tolerability of AZD6738 at 50 mg/kg in combination with IR in the A/J model was assessed using the late intervention therapeutic window study. A/J mice were injected with urethane to initiate tumour growth. After 19 weeks, mice were treated with AZD6738 (50 mg/kg) 1 h before IR (10 Gy) to the left lung using the CT-guided SARRP (**Chapter 2.6.2**). IR was delivered using parallel-opposed 5 Gy doses that limited the IR beam using a square collimator (8 x 8 mm); the edge of the beam was aligned to the edge of the sternum, avoiding the oesophagus while including a majority of the left lung (**Fig. 2.6.2.4**). Mice were also imaged by MRI pre-treatment and before euthanasia at 7 weeks after treatment (**Fig. 3.2.10 A**). During the 7 weeks after treatment, all groups showed no significant weight loss or other clinical signs, and the study was ended as planned (**Fig. 3.2.10 B**).

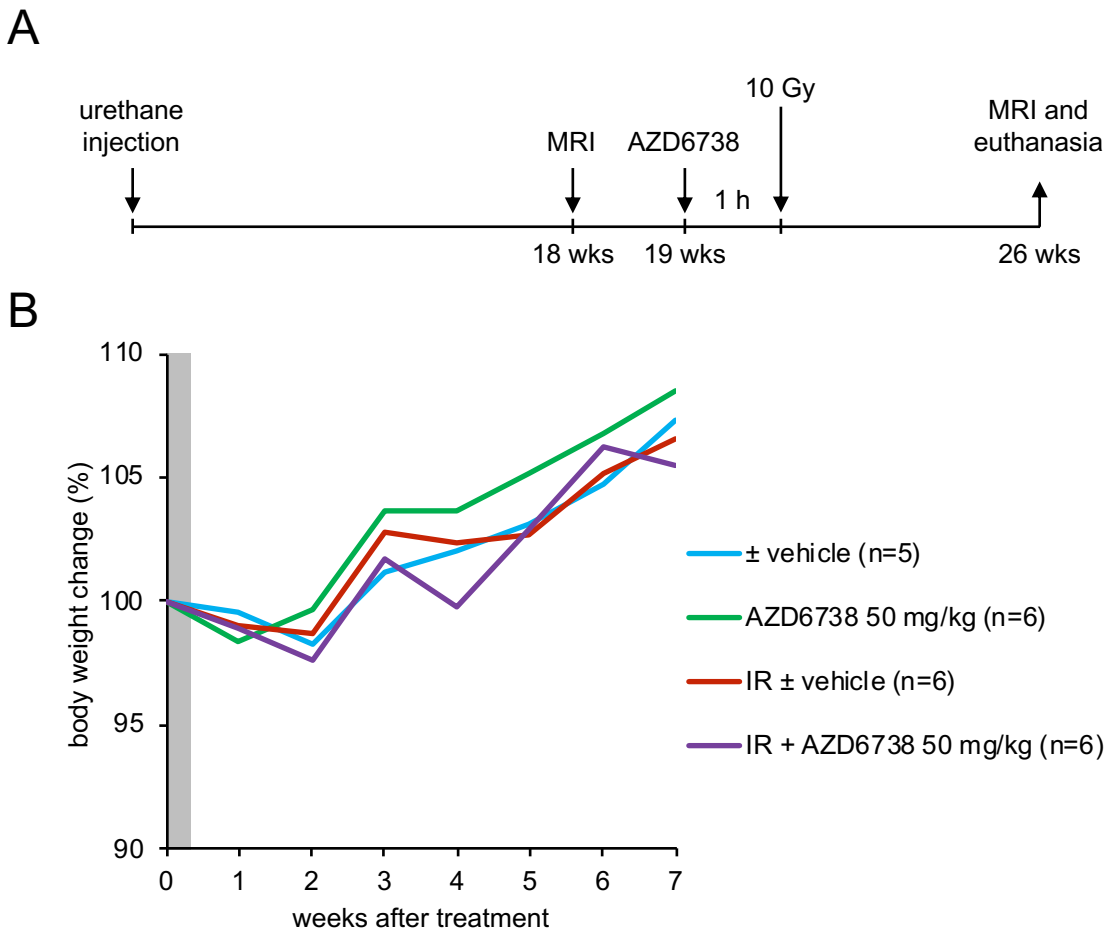

Figure 3.2.10. AZD6738 in combination with CT-guided left lung IR did not induce body weight loss. A/J mice were injected with urethane (10 mg per 10 g body weight, i.p., A). After 18 weeks, mice were allocated into groups (n=5 for ± vehicle group, n=6 for AZD6738, IR ± vehicle, and IR + AZD6738) and were imaged using MRI. During week 19, mice were treated with a single dose of AZD6738 (50 mg/kg, p.o.) 1 h before left lung IR (10 Gy). Mice were imaged using MRI before euthanasia during week 26. All groups showed no significant weight loss during the study and were euthanised 7 weeks after treatment (B). Grey bar represents treatment.

Superficial counts of left lung tumours and tumour count ratios of left to right lungs showed no significant difference between the IR + vehicle (n=6) and IR + AZD6738 (n=6) groups (**Fig. 3.2.11 A & B**). Mice treated with AZD6738 alone (n=6) showed an increase in tumour count ratio as compared with the vehicle control (± vehicle, n=5), but it was not statistically significant (**Fig. 3.2.11 B**).

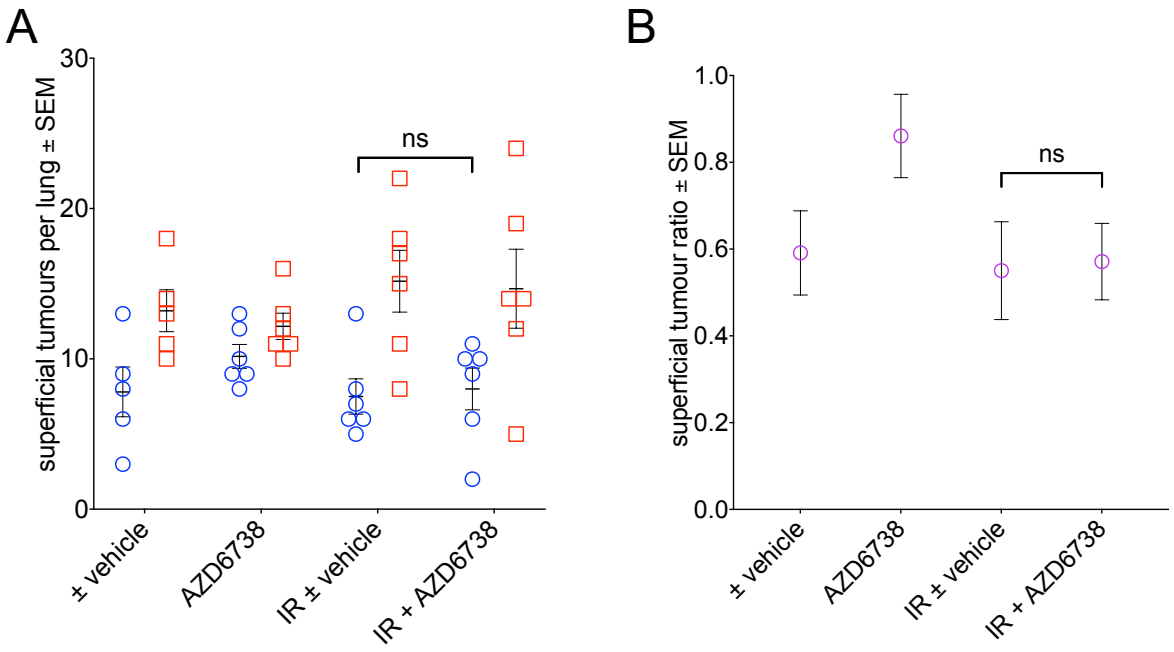

Figure 3.2.11. AZD6738 in combination with CT-guided left lung IR did not reduce superficial tumour counts or ratio. Mice in the IR + AZD6738 group did not show a reduction in either tumour counts (A) or count ratio (B) as compared with IR ± vehicle. (o) are individual left lungs, (□) are individual right lungs, (o) are a ratio of left lung counts divided by right lung counts.

Additionally, no difference was observed between the groups as measured by either tumour count per left lung slice or tumour area burden (**Fig. 3.2.12 A & B**).

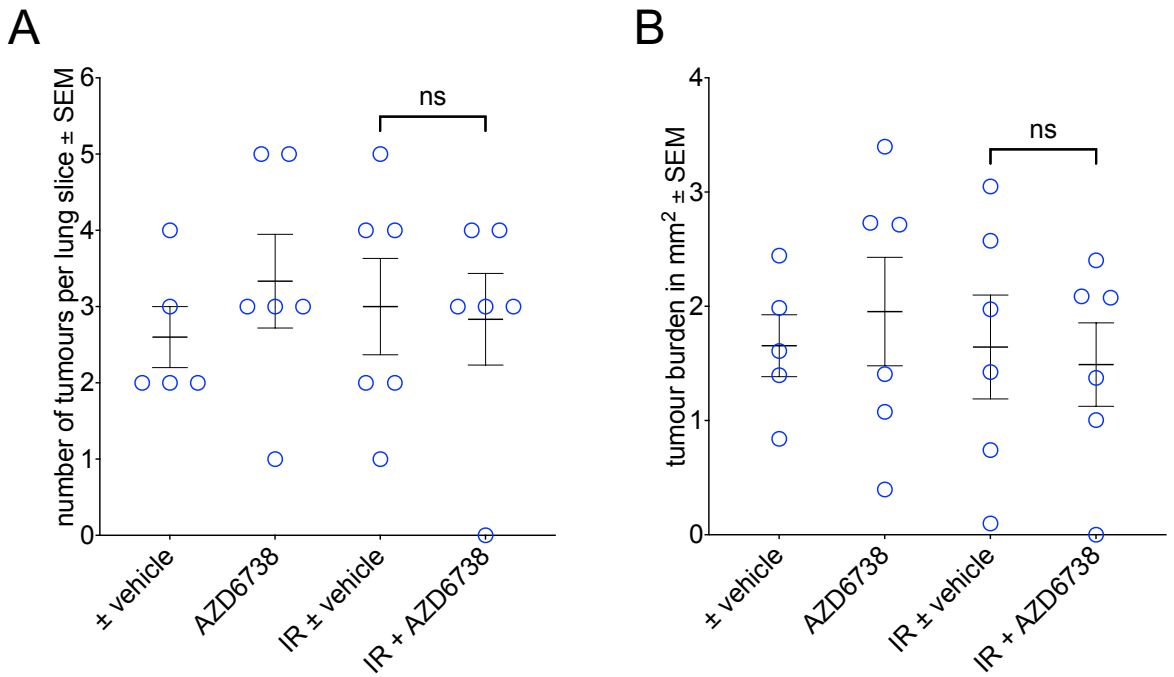

Figure 3.2.12. AZD6738 in combination with CT-guided left lung IR did not reduce tumour numbers or area per lung slice. Mice in the IR ± vehicle group did not show a reduction in either tumour number per left lung slice (A) or tumour area burden (B) as compared with the control group (± vehicle). Mice in the IR + AZD6738 group also showed no reduction in either measure when compared with IR ± vehicle. (o) are individual left lungs.

Total left lung tumour volume changes from pre-treatment to week 7 were assessed using MRI (**Fig. 3.2.13 A & B**). The total left lung tumour volume changes for mice treated with IR + AZD6738 were similar to individuals treated with IR ± vehicle.

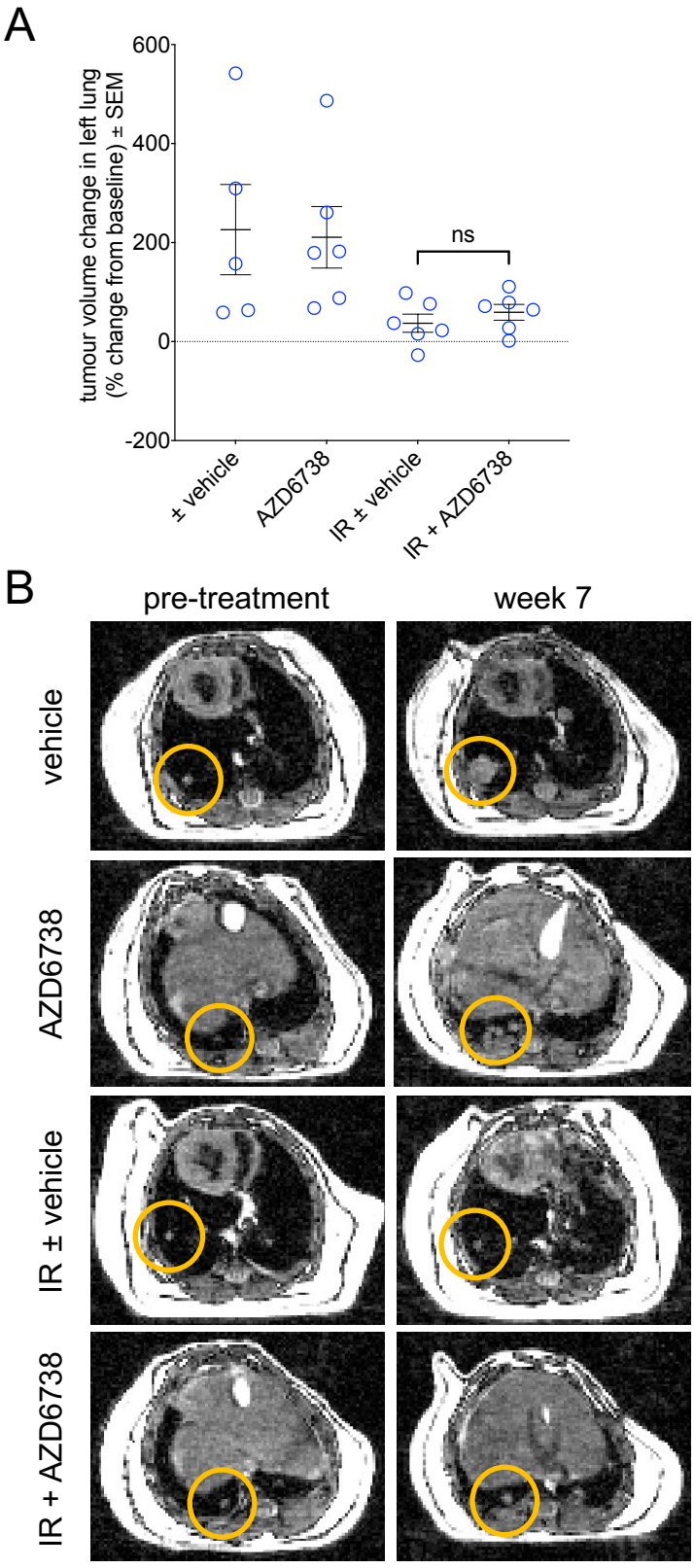

Figure 3.2.13. AZD6738 in combination with CT-guided left lung IR did not affect MRI tumour volume change compared with IR alone. Total left lung tumour volume changes of mice treated with IR + AZD6738 were similar to mice treated with IR ± vehicle (A). Representative axial MR images of the mouse chest with tumours circled in yellow (B). (o) are individual left lung tumour volume changes from baseline (pre-treatment) to week 7.

Lung weights and H&E staining revealed no increase in normal lung tissue effects by gross pathology or histology (**Fig. 3.2.14 A & B**).

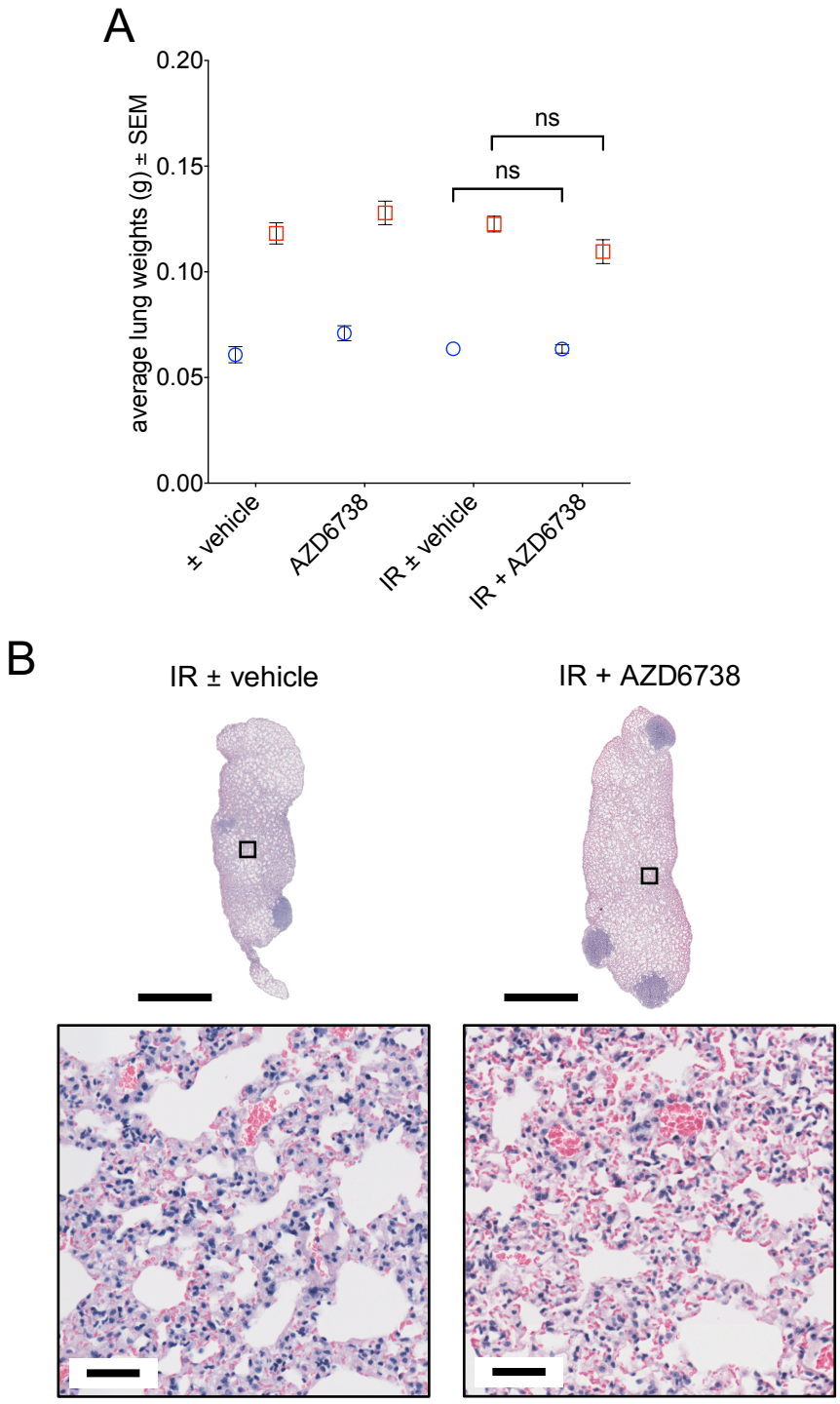

Figure 3.2.14. AZD6738 in combination with CT-guided left lung IR did not affect lung weight or histology. None of the treatment groups showed significant normal lung tissue effects as measured by lung weight (A) or by H&E staining (B). (o) are average left lungs, (□) are average right lungs. Scale bars represent 2 mm for whole lung slices and 50 μm for representative image.

Taken together, these results suggest that AZD6738 at 50 mg/kg is not able to modulate the effect of IR on established tumours of the A/J model in 7 weeks.

3.2.6. Pharmacodynamics of AZD6738 at 50 mg/kg combined with IR does not significantly affect pan-nuclear γH2AX levels in lung tumours or the bronchial or oesophageal epithelium

A PD study of AZD6738 and IR in the A/J model was undertaken to analyse drug-IR-tissue interactions over 24 h post treatment. A/J mice were injected with urethane to initiate tumour growth. After 18 weeks, mice were treated with AZD6738 (50 mg/kg) 1 h before IR (10 Gy) to the whole thorax (**Fig. 2.6.1.2)**. Mice were euthanised at 2 and 24 h after IR (**Fig. 3.2.15 A**).

Pan-nuclear phosphorylation of histone H2AX on serine 139 (γH2AX) has been shown previously to be a marker of replication stress induced by ATR inhibition, and therefore is a potential indirect indicator of AZD6738 activity (Patel et al., 2020; Toledo et al., 2011b). After 2 h, tumours in both IR + vehicle (n=3) and IR + AZD6738 (n=7) showed an increase in the percentage of pan-nuclear γH2AX-positive cells compared with the vehicle control tumours as measured by IHC; however, there was no difference between the IR groups (**Fig. 3.2.15 B & D**). After 24 h, the percentage of pan-nuclear γH2AX-positive cells was lower in both the IR + vehicle (n=4) and IR + AZD6738 (n=9) groups, with no difference between the groups (**Fig. 3.2.15 C & D**).

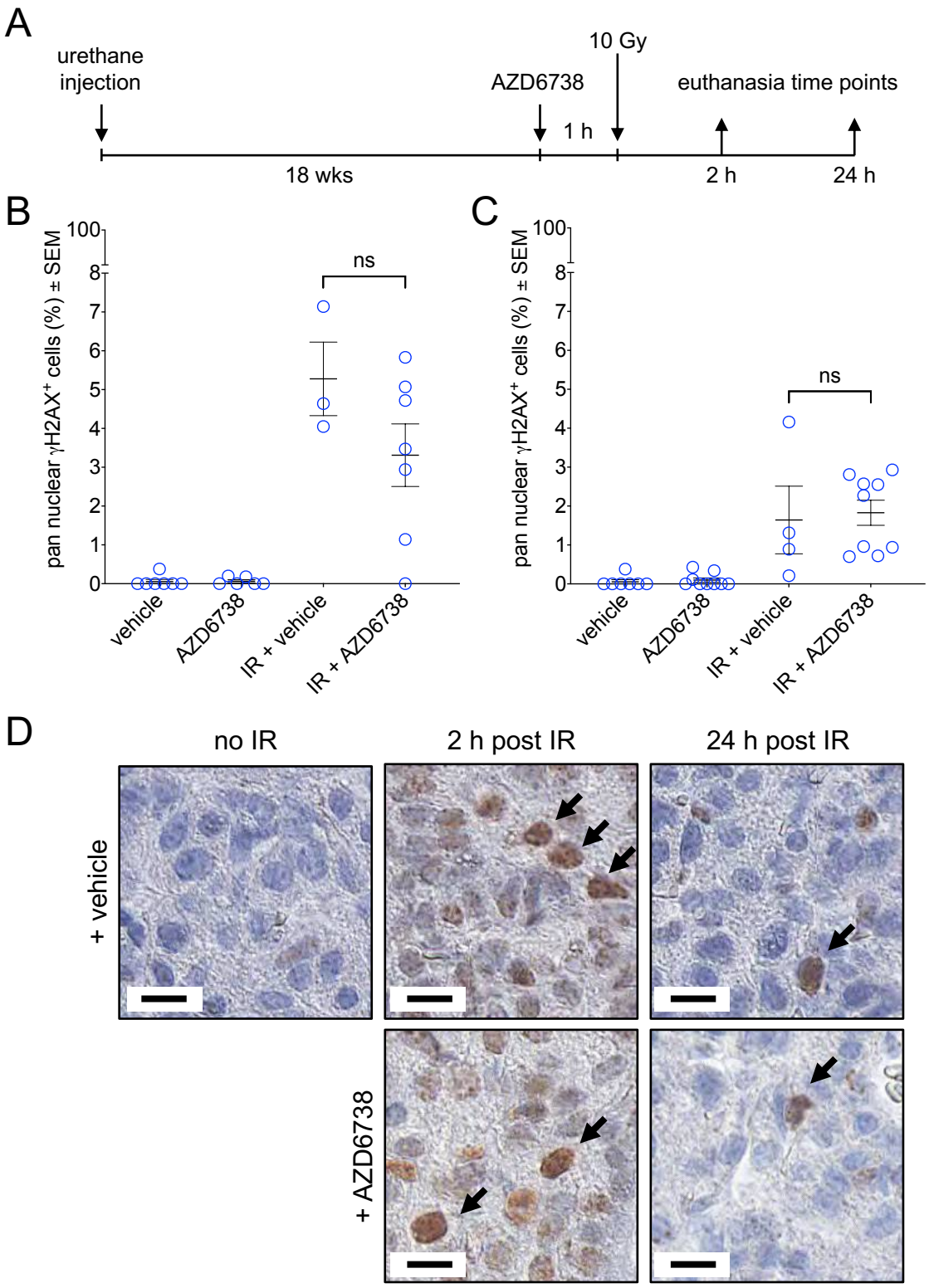

Figure 3.2.15. AZD6738 in combination with IR did not affect pan-nuclear γH2AX levels in tumours. A/J mice were injected with urethane (10 mg per 10 g body weight, i.p., A). After 18 weeks, mice were allocated into groups (n=2 for vehicle, n=4 for IR + vehicle and AZD6738, and n=6 for IR + AZD6738). During week 18, mice were treated with a single dose of AZD6738 (50 mg/kg, p.o.) 1 h before whole thorax IR (10 Gy). Mice were euthanised at 2 and 24 h after IR. Pan-nuclear γH2AX levels in tumours treated with IR + AZD6738 were not significantly different as compared with the IR + vehicle control after 2 h (B) or 24 h (C). IHC of representative pan-nuclear γH2AX in lung tumours (D). (o) are individual tumours. Arrows mark pan-nuclear γH2AX positive cells. Scale bars represent 10 μm.

To determine the effect on normal tissue, the percentage of γH2AX-positive cells was measured in the bronchial epithelium of the lung as well as the epithelium of oesophagi. Four categories were used for counting γH2AX positive cells: (i) clear, separated foci, (ii) abundant distinct but overlapping foci, (iii) faint pan-nuclear staining, and (iv) dark pan-nuclear staining (**Fig. 2.16.1**). When treated with IR + vehicle or IR + AZD6738, a majority of bronchial epithelial cells (> 70%) displayed overlapping γH2AX foci after 2 h (**Fig. 3.2.16 A & C**). After 24 h, a majority of cells (> 60%) treated with IR + vehicle or IR + AZD6738 had clear, separated γH2AX foci, but there was no difference between the groups (**Fig. 3.2.16 B & C**). Neither pan-nuclear γH2AX measure was significantly increased at either time point for any treatment.

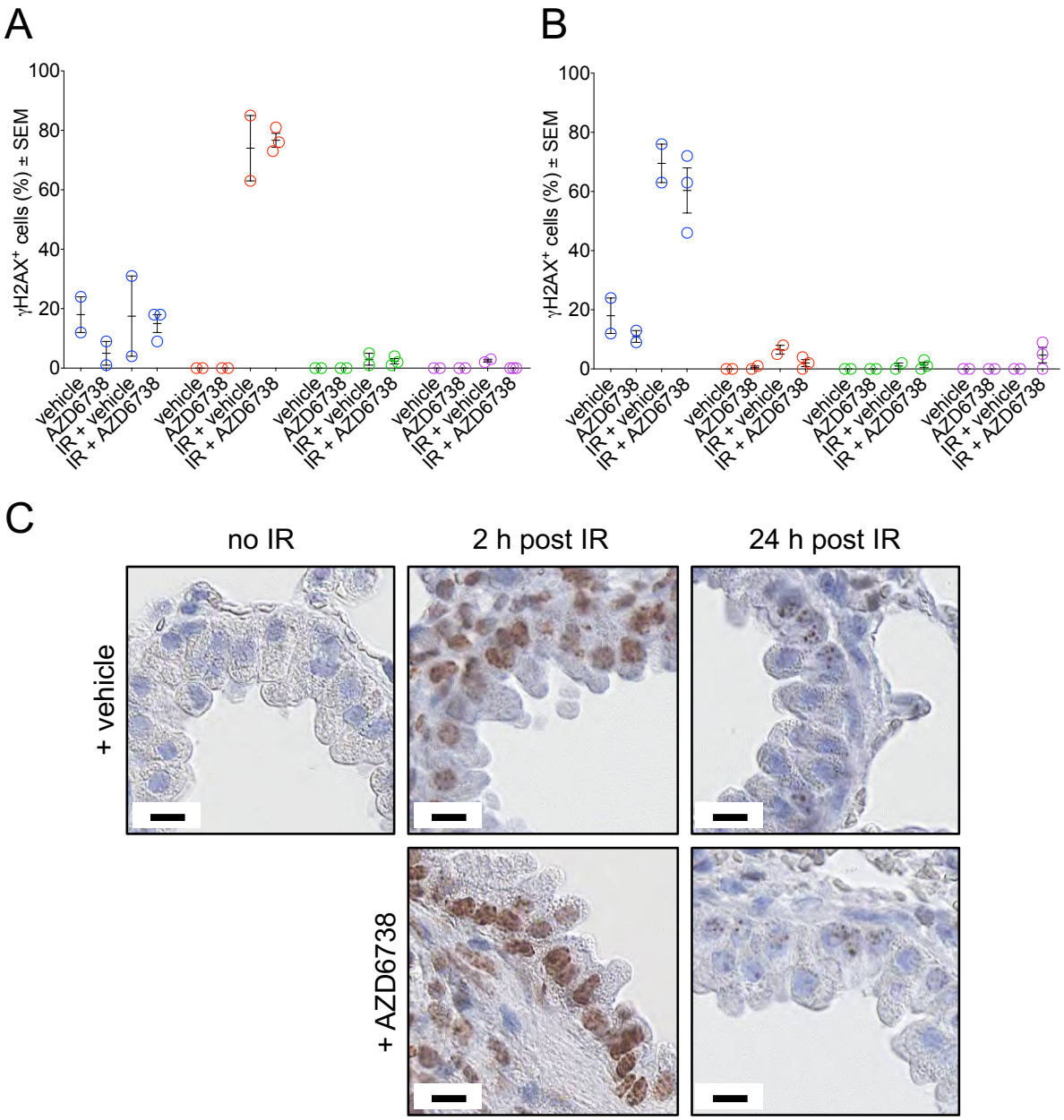

Figure 3.2.16. AZD6738 in combination with IR did not affect pan-nuclear γH2AX levels in bronchial epithelial cells. Pan-nuclear γH2AX levels in bronchial epithelial cells treated with IR + AZD6738 were similar to the IR + vehicle control after 2 h (A) or 24 h (B). IHC of representative γH2AX staining in bronchial epithelial cells (C). Circles are individual mice and (o) is clear, separated foci, (o) is abundant distinct but overlapping foci, (o) is faint pan-nuclear staining, (o) is dark pan-nuclear staining. Scale bars represent 10 μm.

In the oesophageal epithelium treated with IR + vehicle or IR + AZD6738, a majority (> 50%) had an overlapping γH2AX foci after 2 h, but there was no difference between the groups (**Fig. 3.2.17 A & C**). At 24 h after IR, both the IR + vehicle or IR + AZD6738 groups had more than 35% of cells with clear, separated γH2AX foci (**Fig.**

3.2.17 B & C). There was a slight increase in dark pan-nuclear γH2AX after 2 h for both IR groups, which was no longer evident after 24 h.

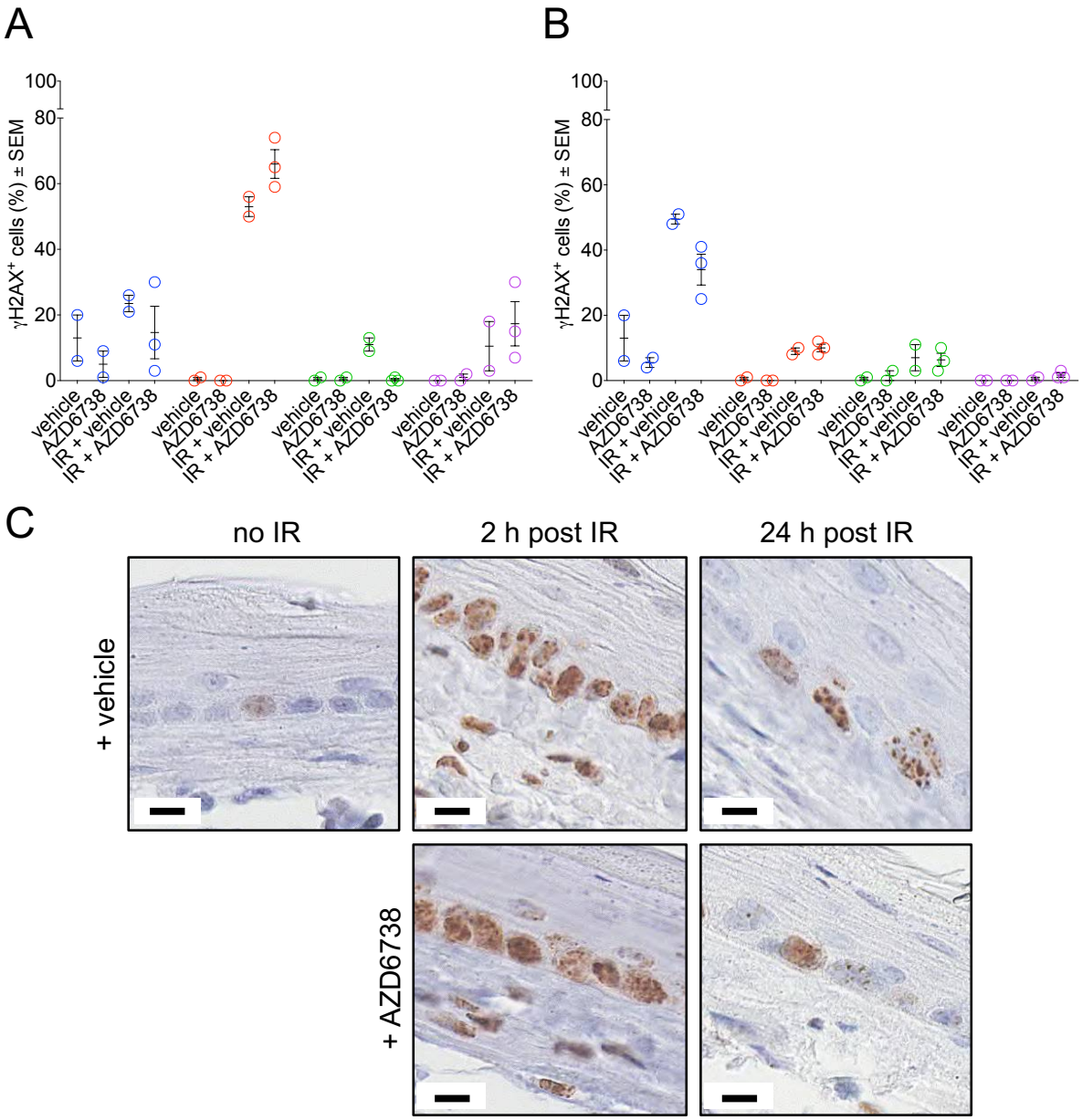

Figure 3.2.17. AZD6738 in combination with IR did not affect pan-nuclear γH2AX in oesophageal epithelial cells. γH2AX levels in oesophageal epithelial cells treated with IR + AZD6738 were similar to the IR + vehicle control after 2 h (A) or 24 h (B). IHC of representative γH2AX staining in oesophageal epithelial cells (C). Circles are individual mice and (o) is clear, separated foci, (o) is abundant distinct but overlapping foci, (o) is faint pan-nuclear staining, (o) is dark pan-nuclear staining. Scale bars represent 10 μm.

Together, these data suggest that the AZD6738 dose of 50 mg/kg combined with 10 Gy does not increase pan-nuclear γH2AX in either the tumour or normal tissue of this model as compared with IR controls at 2 or 24 h.

3.2.7. Pharmacodynamics of AZD6738 at 50 mg/kg combined with IR decreases pKAP1 in tumours but not in bronchial or oesophageal epithelial cells

KRAB-associated protein 1 (KAP1) phosphorylation on serine 824 (pKAP1), a site known to be phosphorylated in response to IR, was used as an additional marker of tumour response to IR and AZD6738 as measured by IHC (White et al., 2006). At 2 h after IR, tumours treated with IR + AZD6738 (n=10) showed a decrease in the percentage of pKAP1-positive cells as compared with IR + vehicle (n=3) (**Fig. 3.2.18 A & C**). This difference between pKAP1 levels in tumours treated IR + AZD6738 (n=5) and IR + vehicle (n=7) was not apparent after 24 h (**Fig. 3.2.18 B & C**).

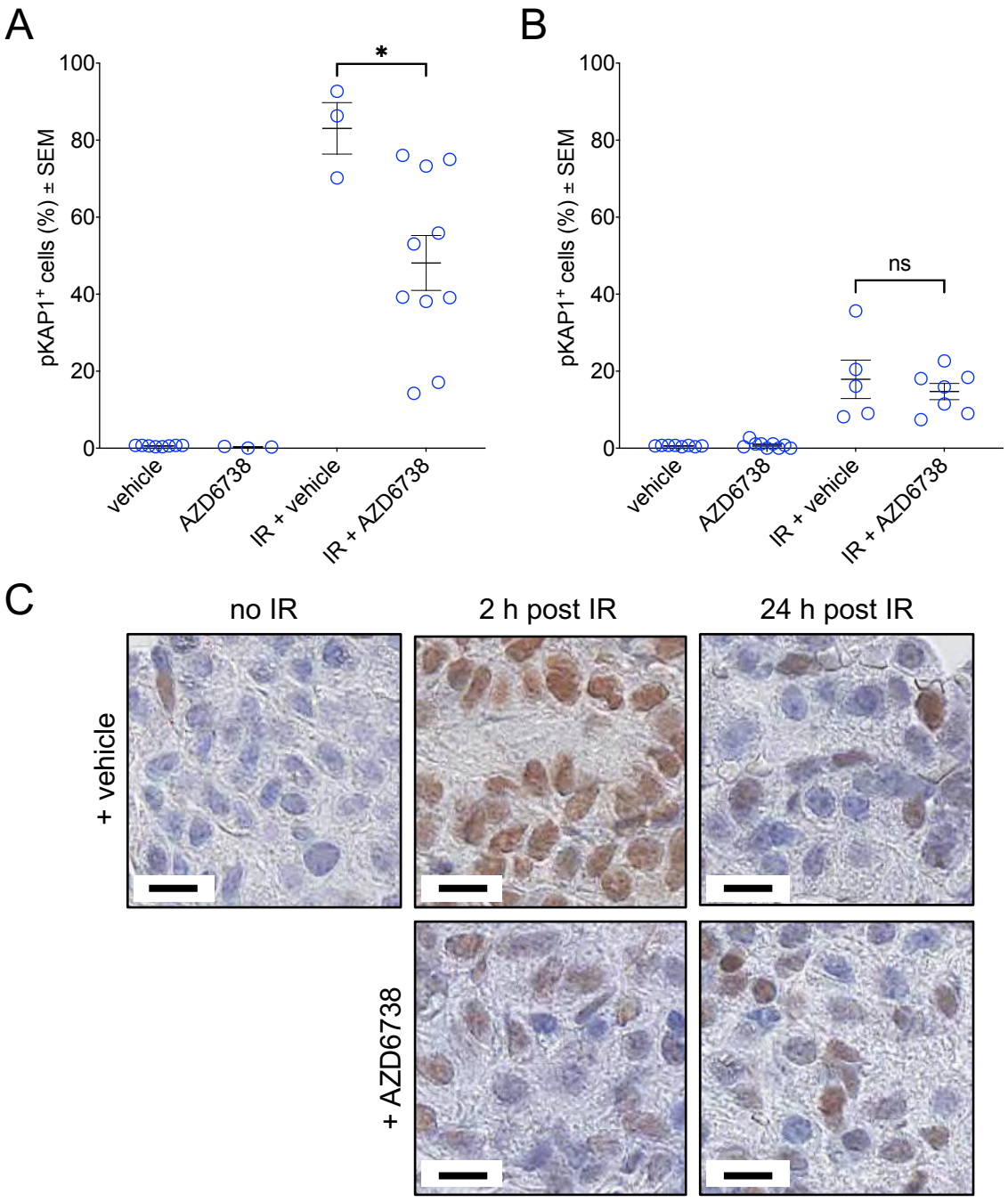

Figure 3.2.18. AZD6738 in combination with IR decreased pKAP1 levels in tumours. Levels of KAP1 phosphorylation on serine 824 in tumours treated with IR + AZD6738 were significantly decreased compared with IR + vehicle after 2 h (A). After 24 h, both IR groups showed a similar level of pKAP1 (B). IHC of representative pKAP1 (ser824) staining in lung tumours (C). (o) are individual tumours. Scale bars represent 10 μm.

Phosphorylation of KAP1 was also used to evaluate the effect of AZD6738 and IR on the bronchial epithelial cells of the lung. No difference was found between IR + vehicle and IR + AZD6738 at either 2 or 24 h after IR (**Fig. 3.2.19 A-C**).

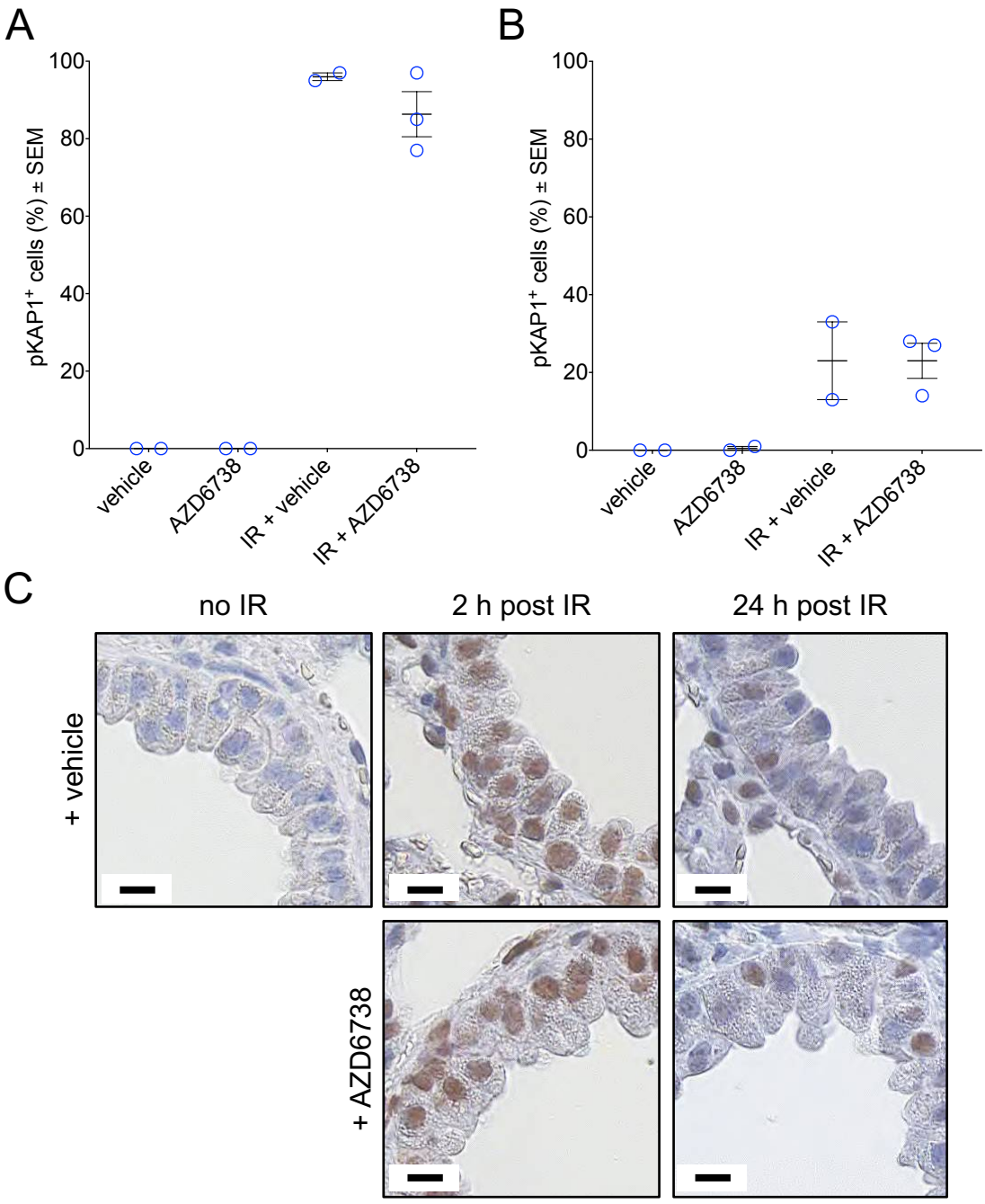

Figure 3.2.19. AZD6738 in combination with IR did not affect pKAP1 levels in bronchial epithelial cells. Levels of pKAP1 in bronchial epithelial cells treated with IR + AZD6738 were similar compared with IR + vehicle after 2 h (A) or 24 h (B). IHC of representative KAP1 (ser824) staining in bronchial epithelial cells (C). (o) indicate individual mice. Scale bars represent 10 μm.

Phosphorylation of KAP1 was also examined in oesophageal epithelial cells to evaluate the effect of AZD6738 and IR. No difference was found between IR + vehicle and IR + AZD6738 at either 2 or 24 h after IR in the oesophageal epithelium (**Fig. 3.2.20 A-C**).

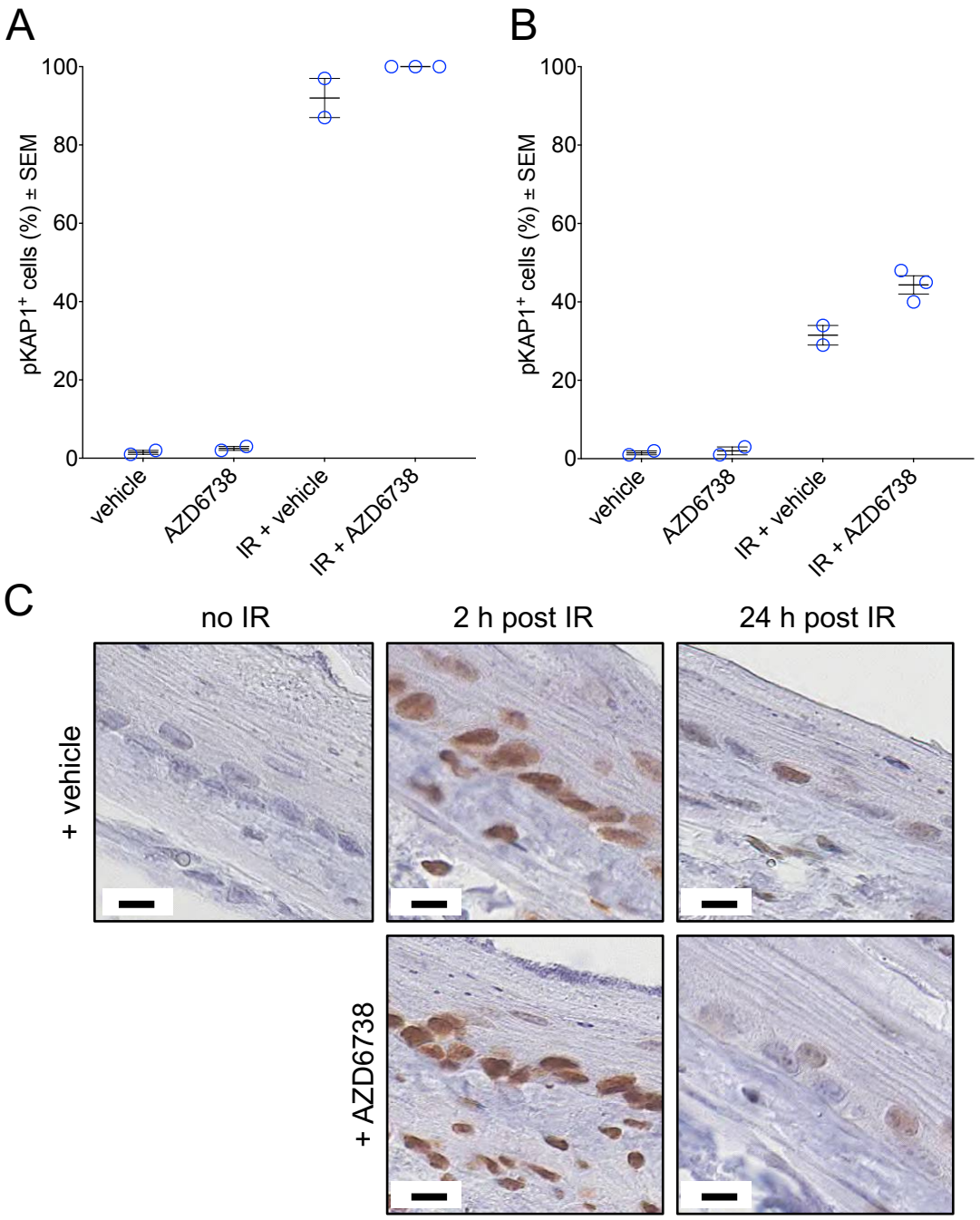

Figure 3.2.20. AZD6738 in combination with IR did not affect pKAP1 levels in oesophageal epithelial cells. Levels of pKAP1 in oesophageal epithelial cells treated with IR + AZD6738 were similar to the IR + vehicle control after 2 h (A) or 24 h (B). IHC of representative KAP1 (ser824) staining in oesophageal epithelial cells (C). (o) indicate individual mice. Scale bars represent 10 μm.

These data suggest that when AZD6738 at 50 mg/kg is combined with 10 Gy, the percentage of pKAP1-positive cells is reduced in tumours at 2 h as compared with IR controls but, after 24 h, the percentage is are similar. In contrast, both normal epithelial

tissues of this model demonstrated similar pKAP1 levels between the combination and the IR groups at both time points.

3.2.8. Discussion

While the combination treatment of IR and AZD6738 at 50 mg/kg was able to significantly inhibit tumour growth in xenografts, it was not found to be as efficacious in the early or late therapeutic window studies in A/J mice. In the early intervention therapeutic window study, fractionated whole thorax IR combined with 2 doses of AZD6738 at 50 mg/kg resulted in weight loss caused by damage to the oesophageal epithelial integrity, revealing an early normal tissue side effect from treatment. Using a hemithorax rig to irradiate only the left thorax as well as single dose of AZD6738 at 50 mg/kg was able to avoid the oesophageal damage and assess the long-term treatment effect on both urethane-induced tumours and lung tissue. While the hemithorax early intervention using AZD6738 was not found to decrease overall tumour burden in any measurement of efficacy after 26 weeks, it also revealed no increase in the late term toxicity of lung fibrosis as compared with IR treatment alone. However, both the efficacy and toxicity endpoints may have been partially affected by the removal of the second AZD6738 dose after IR in each treatment cycle.

Late intervention using AZD6738 with left lung IR was unable to affect all tumour burden measurements compared with IR treatment alone. A single dose of 10 Gy to the left lung was also unable to reduce tumour burden measures, suggesting that the larger, more established tumours of the A/J model at 19 weeks may be inherently less radiosensitive, or a single 10 Gy dose (tumour tissue BED of 20 Gy) is too low to elicit a reduction in tumour burden as compared with the 5 fractions of 5 Gy (tumour tissue BED of 37.5 Gy). Future late intervention studies should use a dose (e.g. 13 Gy) that more closely matches the BED used in the early intervention fractionated IR schedule.

A possible explanation for the limited efficacy of AZD6738 at 50 mg/kg in this model may involve the mechanisms upon which ATR inhibition as a therapy relies. In **Chapter 3.1**, the A/J model tumours were shown to be slowly replicating, with approximately 1.5% of tumour cells positive for BrdU incorporation (**Fig. 3.1.5 A**). Tumours commonly have mutations in cell cycle regulation that contribute to a high proliferation rate but also induce replication stress (Karnitz and Zou, 2015; Toledo et al., 2011a). ATR inhibition has been shown to be effective in these tumours by further increasing replication stress (Toledo et al., 2011a). The slow replication rate of tumours in the A/J model may make them less sensitive to the AZD6738 combination with IR. The effect of AZD6738 on cells with a high replication rate can be demonstrated by the oesophagitis side effect (**Fig. 3.2.4 & 3.2.5**). More than 10% of A/J oesophageal epithelial cells are positive for BrdU incorporation, and this fraction of proliferating cells may have been more susceptible to the effects of IR + AZD6738, resulting in tissue damage and subsequent weight loss (**Appendix Fig. 6.3**). In order to understand the oesophageal inflammation due to AZD6738 and fractionated IR, a longer time course of tissue responses is needed to capture the early events.

Another important aspect of tumour sensitisation with ATR inhibition is the presence of hypoxic regions. As the ATR pathway is used to manage replication stress, which is caused by hypoxia, it is well-established that hypoxia confers additional sensitisation to ATR inhibition (Hammond et al., 2004; Ng et al., 2018; Pires et al., 2012). At 30 weeks after tumour induction, only 30% of A/J tumours have detectable hypoxic regions, suggesting this model may not be optimal for examining treatments in hypoxic lung tumours. Both the importance of a high replication rate and regions of hypoxia as well as the limited normal tissue damage seen in the combination of AZD6738 with IR suggest that this treatment may be more effective against specific tumour phenotypes and should be examined further.

The PD study of AZD6738 and IR in the A/J model is another important set of considerations for the therapeutic window of treatment. In A/J tumours, AZD6738 at 50 mg/kg in combination with 10 Gy was unable to detectably modulate pan-nuclear γH2AX levels, a marker of ATR inhibition, in comparison to IR alone. This contributes to the finding that this treatment in the left lung was unable to reduce tumour burden in the late intervention. Additionally, the similar γH2AX levels of bronchial epithelial cells in response to IR + vehicle and IR + AZD6738 also may be a promising result in demonstrating the limited normal lung tissue effect of AZD6738 when combined with IR. Although there was no difference γH2AX or pKAP1 levels in the oesophageal epithelial cells between IR + vehicle and IR + AZD6738, repeated dosing of AZD6738 and 5 fractions of 5 Gy may have been the main factors contributing to the oesophageal inflammation seen in the whole thorax early intervention study, which could be investigated in an oesophageal toxicity study with more early time points to understand the tissue specific pharmacodynamic responses. The characterisation of tissue responses to AZD6738 could benefit from further investigation using other biomarkers of ATR inhibition such as phosphorylation of CHK1 on serine 345 and phosphorylation of RPA32 on serine 33 in addition to the pan-nuclear γH2AX biomarker.

Interestingly, IR + AZD6738 treated tumours had significantly decreased levels of pKAP1 at 2 h. Although the phosphorylation of KAP1 is mainly attributed to ATM, a previous study found that ATR is also able to phosphorylate KAP1 upon IR treatment, which may explain the decrease with AZD6738 (White et al., 2006). Additionally, it may be suggestive of possible off-target inhibition of ATM by AZD6738 in the tumours. However, in pharmacokinetic studies, the IC_{50} of ATM activity inhibition by AZD6738 was found to be > 30 μM (Foote et al., 2018). Additionally, the normal tissue responses of the oesophageal and bronchial epithelium did not show a decrease in pKAP1 levels

with IR + AZD6738, suggesting that tumour KAP1 phosphorylation might be a tissue-specific response, potentially due to the inherent genome instability of tumours.

An important consideration for future studies will be the use of continuous or cyclic continuous dosing of AZD6738 in ATM mutant or inactivated tumours. Five daily doses of AZD6738 at 50 mg/kg inhibited xenograft tumour growth in one study, with ATM inactivation as an important factor in treatment efficacy (Min et al., 2017). In a another study, cyclic continuous dosing (3 d on/4 d off, 5 d on/9 d off, or 7 d on/7 d off) of AZD6738 at 25 mg/kg did not significantly inhibit tumour growth in an ATM-deficient xenograft model, but daily dosing for 130 days of an ATM mutant PDX model resulted in significant tumour growth inhibition (Lloyd et al., 2020). However, continuous dosing can also increase the incidence of normal tissue effects such as mucositis, which was increased when 5 daily doses of AZD6738 (15 mg/kg) were added to olaparib and IR treatment in an orthotopic lung cancer model (Tran Chau et al., 2020). Additionally, in a phase I dose escalation study with AZD6738, continuous dosing was limited by thrombocytopenia and a 21 d period without AZD6738 was required for platelet levels to recover (Berges et al., 2018). The normal tissue effects of AZD6738 will need to be carefully considered in future monotherapy and combination therapy studies, and the results from ongoing clinical trials of AZD6738 will provide key insights into the translatability of the preclinical findings relating to this compound.

3.3. Therapeutic window of DNA-PK and IR in A/J mouse model

3.3.1 Introduction

In the previous chapter, A/J therapeutic window intervention studies were used to examine an inhibitor of ATR and to investigate the potential of modulating the DDR pathway to increase the therapeutic window of radiotherapy treatment. Another protein involved in the DDR pathway, DNA-dependent protein kinase (DNA-PK), is also being evaluated as a promising candidate for inhibitory combination therapies for the treatment of cancer (Medova et al., 2020; Mohiuddin and Kang, 2019).

DNA-PK comprises three components: a catalytic subunit (DNA-PKcs) and a heterodimer of Ku70 and Ku80. DNA-PKcs, like ATR, is a member of the PIKK family and is involved in numerous processes including DSB repair, cell cycle progression, transcriptional regulation, the immune system, and telomere maintenance (Mohiuddin and Kang, 2019).

In response to DSBs, cells have two main repair pathways, NHEJ and HR. Throughout the cell cycle, cells are able to repair DSBs using NHEJ while HR is limited to when a sister chromatid is present as in S or G2 phase. The use of these pathways depends not only upon the phase of the cell cycle but also the interplay among key proteins (**Fig. 3.3.1**). When NHEJ is used to repair DSBs, the DNA ends are first bound by the Ku heterodimer, which recruits DNA-PKcs to the site of damage (Gottlieb and Jackson, 1993). The Artemis endonuclease then joins DNA-PKcs at the DSB site to process the ends (Drouet et al., 2006). XRCC4-like factor (XLF) interacts with the complex XRCC4/DNA Ligase IV at the break site, are stabilised by paralog of XRCC4 and XLF (PAXX), and the DNA is re-ligated (Ahnesorg et al., 2006; Buck et al., 2006; Grawunder et al., 1998; Ochi et al., 2015).

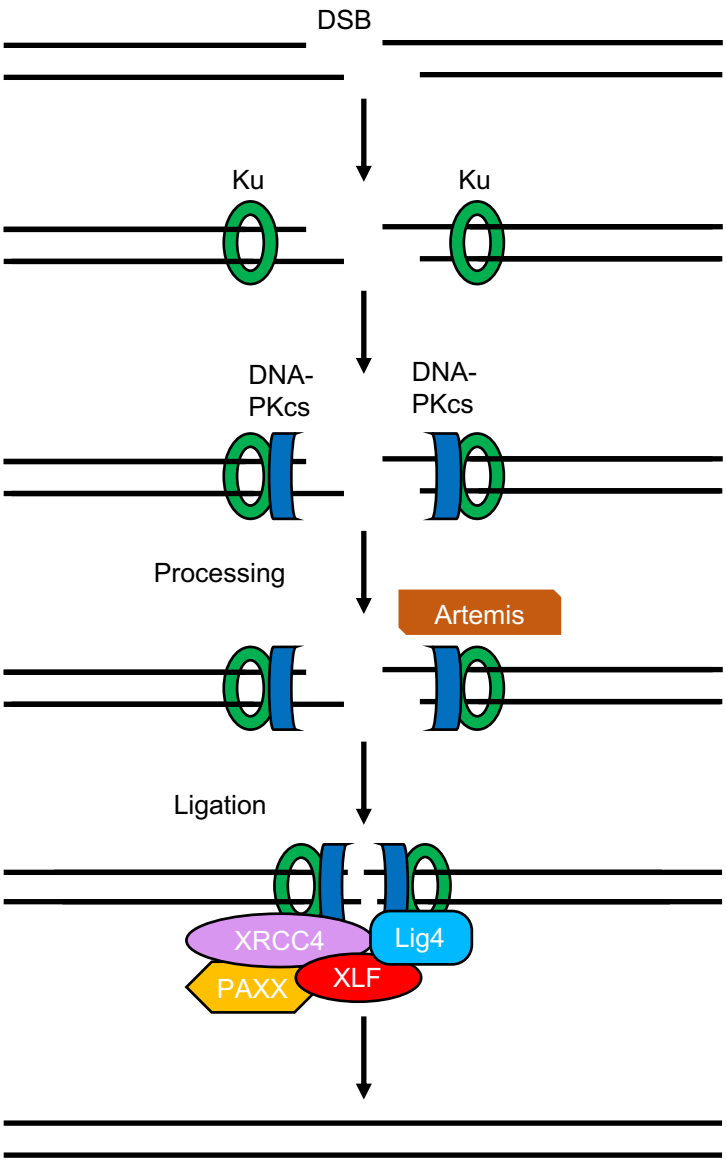

Figure 3.3.1. Non-homologous end joining. At a DSB site, the DNA ends are bound by the Ku heterodimer, which recruits DNA-PKcs. Artemis processes the DNA ends, PAXX stabilises the components, XLF and XRCC4/DNA Ligase IV interact to re-ligate the DNA strands (Blackford and Jackson, 2017).

The essential involvement of DNA-PK in DSB repair through NHEJ is the main rationale for using inhibitors against the protein in combination therapies, especially in tumours with mutations leading to HR-deficiency such as BRCA1/2.

Early investigations using mice with deficiencies in NHEJ components have demonstrated a hypersensitivity to irradiation, chromosomal instability, and severe effects on immune cell development (Ferguson et al., 2000; Gu et al., 1997; Nussenzweig et al., 1997). A mutation in DNA-PKcs has been well-established as the cause of the severe combined immunodeficiency (SCID) mouse, which exhibits both

radiosensitivity and a defective immune cell population (Bosma et al., 1983; Peterson et al., 1995). Therefore, the diverse roles of DNA-PK and the potential for short- and long-term toxicities involving normal tissue require that the broader impact of inhibiting this target be assessed alongside its development as an anti-cancer therapy.

There are currently several DNA-PK inhibitors in clinical trials as combination therapies or as single agents (**Table 3.3.1**). CC-122, CC-115, AZD7648, M9831 (VX-984), and nedisertib (peposertib or M3814) have been recently reviewed (Medova et al., 2020; Mohiuddin and Kang, 2019; Topatana et al., 2020).

DNA-PK inhibitor	Treatment	Cancer type	Phase	Identifier
CC-122	CC-122	Advanced solid tumours, non-Hodgkin's lymphoma, or multiple myeloma	I	NCT01421524
CC-115	CC-115	Advanced solid tumours	I	NCT01353625
	CC-115 + enzalutamide	Prostate cancer	I	NCT02833883
AZD7648	AZD7648 + olaparib + pegylated liposomal doxorubicin	Advanced solid tumours	I/II	NCT03907969
M9831 (VX-984)	M9831	Advanced solid tumours	I	NCT02644278
nedisertib (peposertib, M3814)	nedisertib + pegylated liposomal doxorubicin hydrochloride	Ovarian cancer	I	NCT04092270
	nedisertib + avelumab + radiotherapy	Hepatobiliary cancer	I/II	NCT04068194
	nedisertib + avelumab + radiotherapy	Advanced solid tumours	I	NCT03724890
	nedisertib + capecitabine + radiotherapy	Locally advanced rectal cancer	I/II	NCT03770689
	nedisertib + radiotherapy	Advanced solid tumours	I	NCT02516813
	nedisertib + radiotherapy	Advanced Head and Neck Cancer	I	NCT04533750
	nedisertib + temozolomide + radiotherapy + surgery	Glioblastoma or Gliosarcoma	I	NCT04555577

Table 3.3.1. DNA-PK inhibitors currently in clinical trials. (Modified from Topatana et al., 2020).

This chapter focuses on AZD7648, a DNA-PK inhibitor developed by AstraZeneca. AZD7648 is a selective DNA-PK inhibitor with an IC_{50} of 0.6 nM for DNA-PK with other PI3Ks requiring > 1 μM (Fok et al., 2019). In combination with IR, AZD7648 has been shown to radiosensitise human lung cancer cell lines with *K-ras* or *p53* mutations *in vitro* (Fok et al., 2019). In NSCLC xenograft experiments, AZD7648 (50 or 100 mg/kg, daily, 21 days) and IR (2 Gy for 5 days) was shown to be highly efficacious, leading to tumour regression of 55-85% (Fok et al., 2019).

Importantly, AZD7648 is currently in clinical trials, one of which involves combinations of AZD7648 with the other anti-cancer therapies of olaparib and doxorubicin (NCT03907969). Additionally, AZD7648 combined with radical radiotherapy is proposed as one arm of the CONCORDE platform (Faivre-Finn et al., 2020; Walls et al., 2020). Although there is good evidence to support clinical trials of AZD7648 as an anti-cancer treatment, the potential therapeutic window of AZD7648 combined with thoracic radiotherapy has not been assessed in a model of lung cancer and IR-induced normal tissue effects. The following study aims to address this knowledge gap in the context of both tumour treatment efficacy and normal tissue damage using the A/J mouse model of urethane-induced lung cancer (**Fig. 3.3.2**).

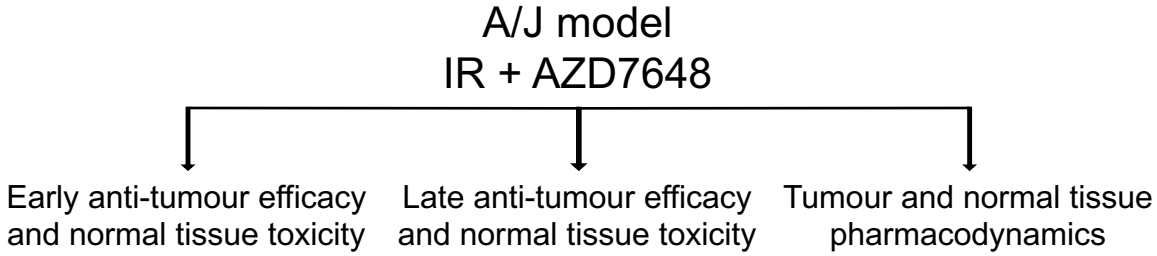

Figure 3.3.2. Main aims and experimental arms.

3.3.2. AZD7648 radiosensitises Calu6 xenograft tumours in CD-1 nude mice

In order to determine an effective dose of the DNA-PK inhibitor AZD7648 to use *in vivo*, a subcutaneous xenograft tumour growth model was used. Human lung carcinoma cells (Calu6) were injected into the flank of CD-1 nude mice. Once tumours

reached a mean size of 100 mm^3, they were treated with AZD7648 (either 12.5, 25, or 50 mg/kg) 1 h before local IR (10 Gy). Tumours were measured for up to 42 days after treatment or until tumours reached 400 mm^3 (**Fig. 3.3.3 A**). Tumour growth was inhibited with IR treatment alone (n=4), but tumours treated with IR + AZD7648 at either 25 or 50 mg/kg (n=4 per group) had significant tumour growth inhibition compared with the IR group (**Fig. 3.3.3 B**).

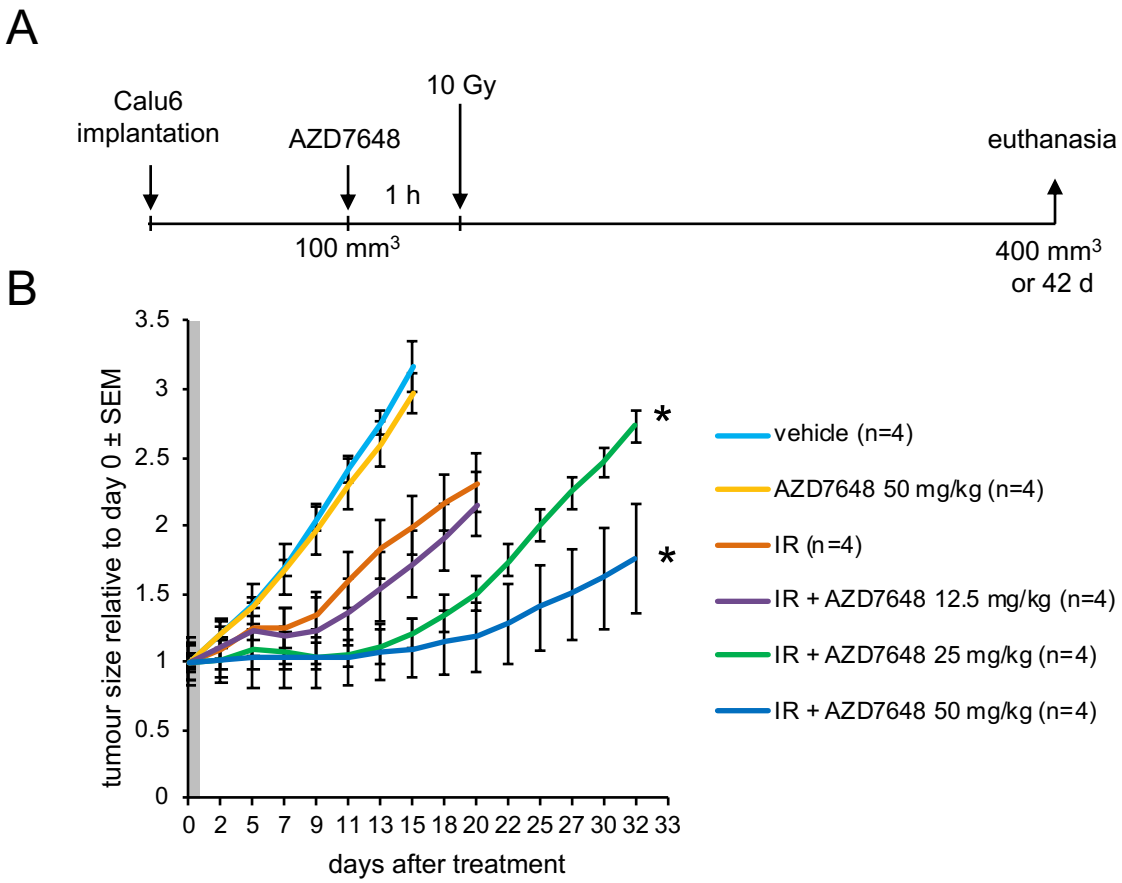

Figure 3.3.3. AZD7648 in combination with IR results in increased tumour growth inhibition in Calu6 xenografts. Calu6 cells (5 x 10^6) were implanted (s.c.) into the flank of CD-1 nude mice. When tumours reached a mean size of 100 mm^3, mice were allocated into groups (n=4 per group) and treated with AZD7648 (12.5, 25, or 50 mg/kg, p.o.) 1 h before IR (10 Gy). Tumours were measured 3 times per week. When tumours reached 400 mm^3 or at 42 days after treatment, mice were euthanised, and tumours were collected (A). Tumour growth inhibition of 30% was observed in the IR group compared with the vehicle group on day 15 (B). Tumour growth inhibition was measured for the IR + AZD7648 25 mg/kg (35%) and IR + AZD7648 50 mg/kg (48%) as compared with the IR group on day 20. There was a significant difference in mean tumour size between IR + vehicle and IR + AZD7648 at both 25 and 50 mg/kg on day 20. Grey region indicates treatment (unpublished data, Yanyan Jiang).

3.3.3. AZD7648 and fractionated whole thorax IR leads to oesophageal inflammation in A/J early intervention therapeutic window study

To investigate the effect of AZD7648 in combination with fractionated whole thorax IR, the A/J early intervention therapeutic window study was used (**Fig. 3.1.12**). A/J mice were injected with urethane to initiate tumour growth. Eight weeks later, mice were treated with 5 cycles of AZD7648 (50 mg/kg) 1 h before and 24 h after whole thorax IR (5 Gy), with 2 days between IR doses. The study was planned to end 26 weeks after the first IR dose (**Fig. 3.3.4 A**). During treatment, all groups lost up to 5% of their starting weights from the beginning of treatment. However, after the third cycle, all mice in the IR + AZD7648 group (n=9) had lost greater than 15% body weight despite intervention with softened food, and therefore study was ended on early day 10 (**Fig. 3.3.4 B**).

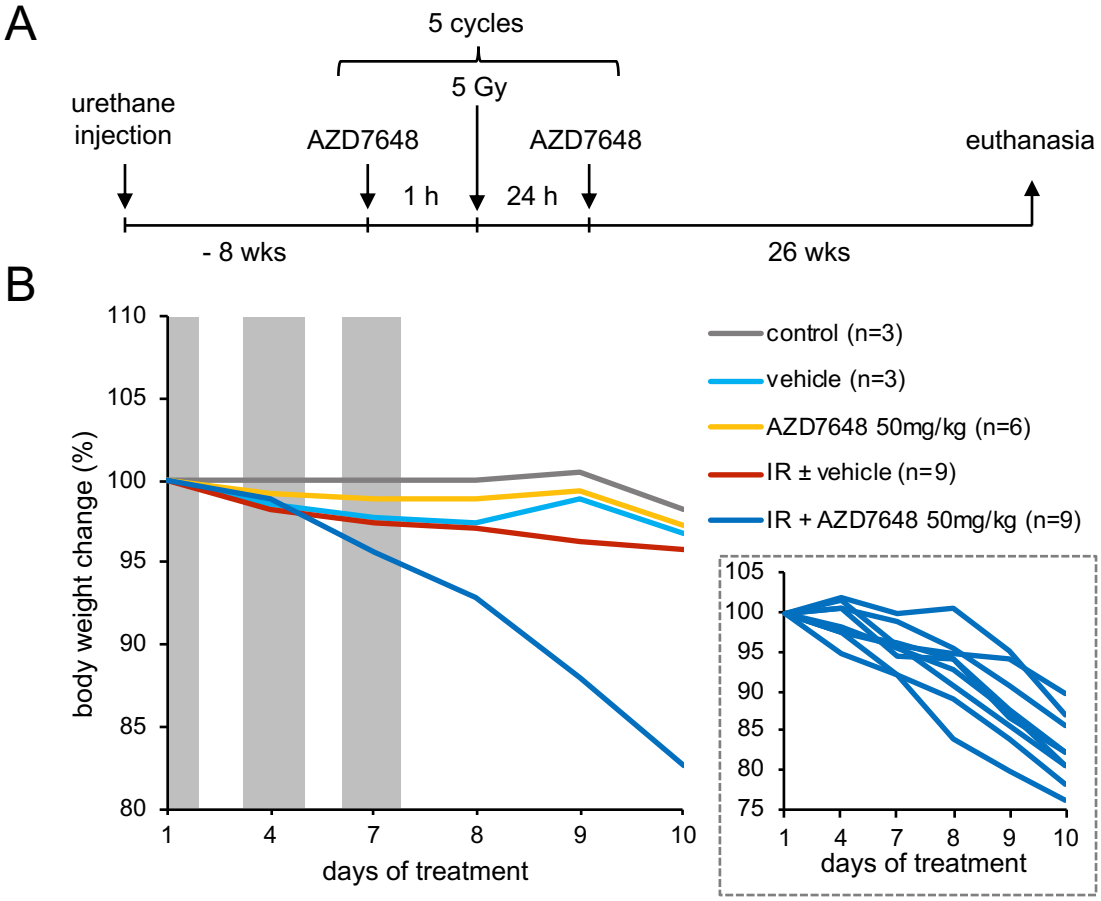

Figure 3.3.4. Whole thorax early intervention treatment with AZD7648 combined with IR induced sustained body weight loss in A/J mice. A/J mice were injected with urethane (10 mg per 10 g body weight, i.p., A). After 8 weeks, mice were allocated into groups (n=3 for control and vehicle treated, n=6 for AZD7648, and n=9 for IR ± vehicle and IR + AZD7648). Mice were treated with 5 cycles of AZD7648 (50 mg/kg, p.o.) 1 h before and 24 h after whole thorax IR (5 Gy), with 2 days between IR doses. Euthanasia was planned for 26 weeks after the final IR dose. All mice in the IR + AZD7648 group (n=9) lost greater than 15% weight during the treatment cycles and were euthanised after the third cycle on day 10 (B). Individual weights of the IR + AZD7648 group are shown in the graph inset. Grey bars represent 24 h treatment cycles.

Upon post mortem, enlarged oesophagi were visible, and H&E revealed the disruption of oesophageal layers and infiltration of immune cells in the IR + AZD7648 group as compared with IR controls (**Fig. 3.3.5 A**). IHC identified these infiltrating cells as Ly6G/C positive (**Fig. 3.3.5 B)**. Oesophagi from mice treated with IR + AZD7648 showed a significant increase in Ly6G/C-positive cells as compared with oesophagi from mice treated with IR ± vehicle (**Fig. 3.3.5 C**). All other treatment groups had no evidence of disrupted oesophagi or infiltration of granulocytes/neutrophils (**Fig. 3.3.5**

C). These results suggest that 3 fractions of 5 Gy to the whole thorax with 6 total doses of AZD7648 (50 mg/kg) is not tolerated in A/J mice because it was associated with unacceptable weight loss and acute oesophagitis.

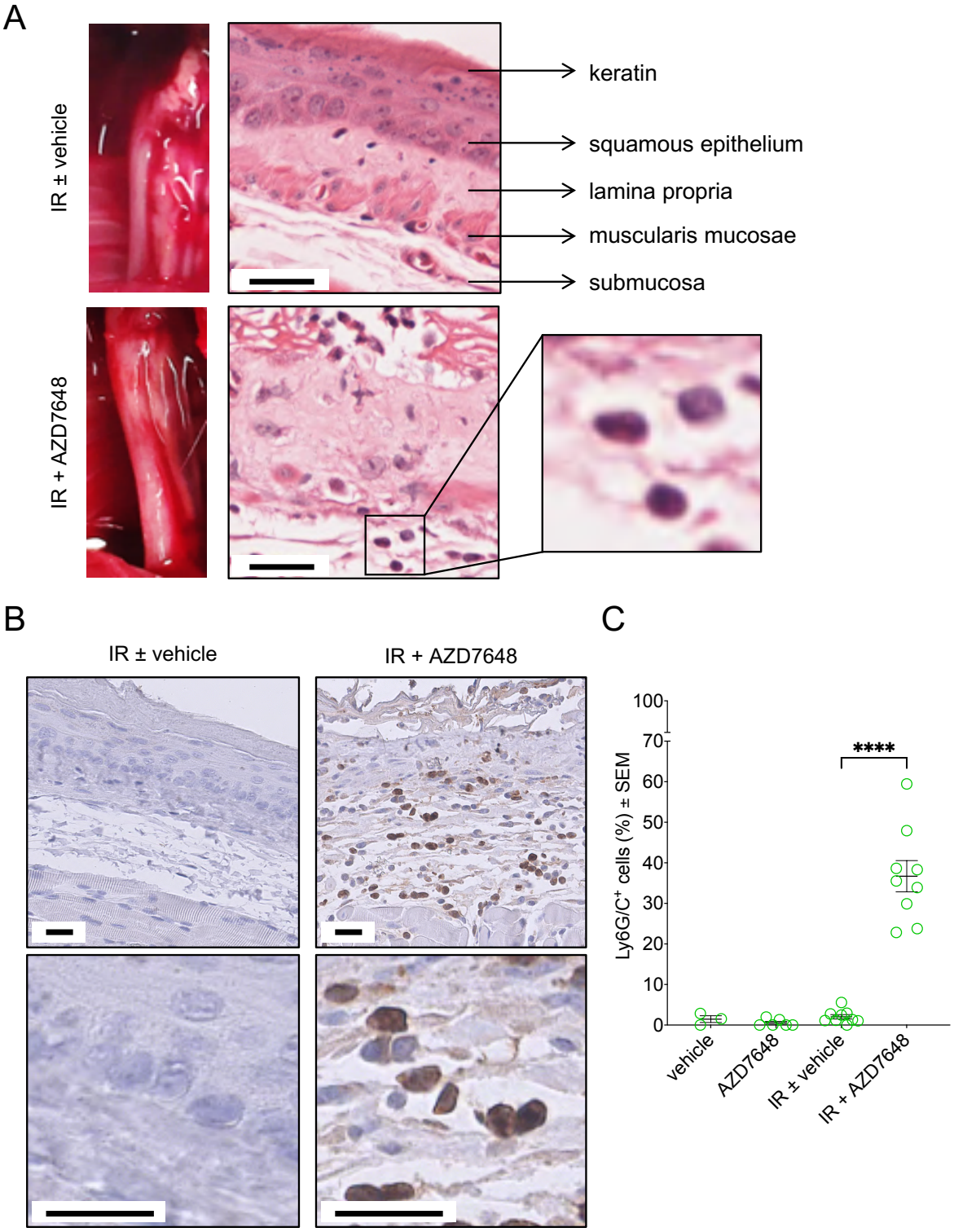

Figure 3.3.5. AZD7648 combined with whole thorax IR results in oesophageal inflammation. Mice in the combination group (IR + AZD7648) showed enlarged oesophagi upon euthanasia at day 10 and disruption of oesophageal layers with an immune infiltrate by H&E (A). Oesophagi of the IR + AZD7648 group were infiltrated with Ly6G/C-positive cells when compared with IR ± vehicle as shown by IHC (B) and quantified per representative region (C). All scale bars represent 25 μm and (o) are individual oesophagi.

3.3.4. Oesophageal tolerability of AZD7648 combined with IR disrupts tissue layers and leads to increased nuclear condensation

To further examine the early effects of AZD7648 in combination with IR on the oesophagus, A/J mice were treated with 3 cycles of AZD7648 (25 or 50 mg/kg, p.o.) 1 h before whole thorax IR (5 Gy) on day 1, 4, and 7. The study was ended 2 hours after the third dose of IR (**Fig. 3.3.6 A**). During the 7 days of treatment, no significant body weight loss was observed in any of the groups (**Fig. 3.3.6 B**).

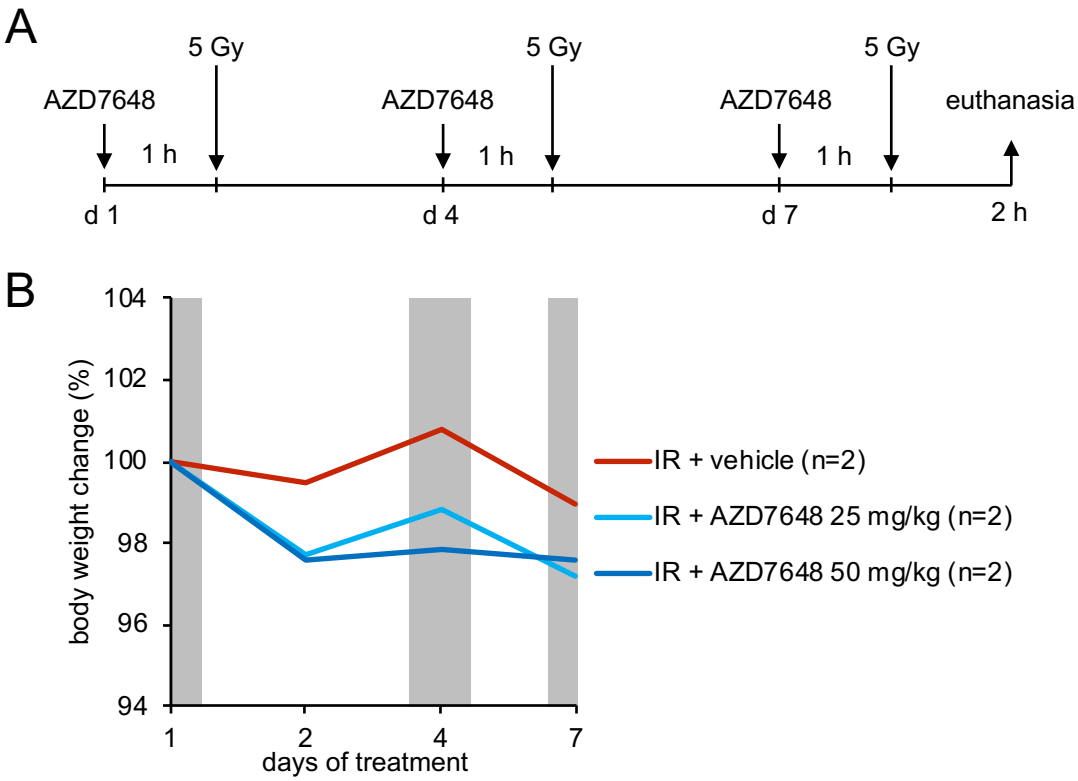

Figure 3.3.6. AZD7648 in combination with whole thorax IR did not induce body weight loss. A/J mice were allocated into groups (n=2) and treated with 3 cycles of AZD7648 (25 or 50 mg/kg, p.o.) 1 h before whole thorax IR (5 Gy), with 2 days between IR doses (A). Euthanasia was planned for 2 h after the final dose of IR. Mice in all treatment groups showed no significant weight loss during treatment cycles (B).

Histological investigations by H&E revealed a mild disruption of the oesophageal layers and nuclear condensation of epithelial cells in both IR + AZD7648 groups (**Fig. 3.3.7 A**). Further IHC of γH2AX levels in the oesophageal epithelium demonstrated darker, more intense staining within cells of the IR + AZD7648 25 mg/kg group and

fewer identifiable epithelial cell nuclei in the IR + AZD7648 50 mg/kg group (**Fig. 3.3.7 B**).

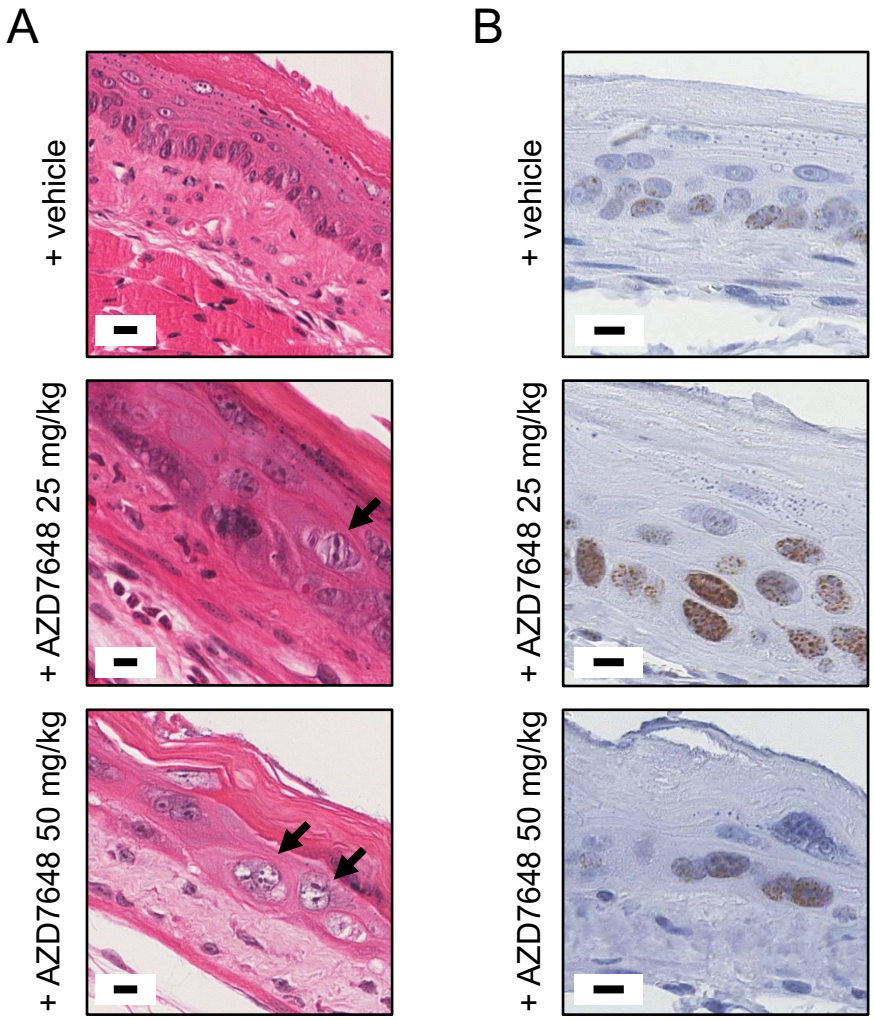

Figure 3.3.7. AZD7648 in combination with whole thorax IR shows subclinical histological evidence of oesophageal epithelium damage. H&E revealed a disruption of oesophageal layers with nuclear condensation (black arrows) in both IR + AZD7648 groups (A). Oesophagi of IR + AZD7648 groups demonstrated an increase γH2AX compared with IR + vehicle as shown by IHC (B). All scale bars represent 10 μm. Grey bars represent treatment cycles.

These data of AZD7648 combined with fractionated IR reveal the early subclinical and histological changes in the oesophagus of the A/J model.

3.3.5. AZD7648 and fractionated hemithorax IR is efficacious but damages normal tissue in A/J early intervention therapeutic window study

To examine the efficacy and tolerability of AZD7648 in combination with IR in the tumours and late responding normal tissues of the A/J model while mitigating against

the possibility of substantial toxicity of the combination, the hemithorax IR rig was used to avoid the oesophagus and a single dose of AZD7648 was given 1 h before IR (**Fig. 2.6.1.3**). A/J mice were injected with urethane to initiate tumour growth for 8 weeks before 5 cycles of AZD7648 (50 mg/kg) 1 h before hemithorax IR (5 Gy), with 2 days between IR doses (**Fig. 3.3.8 A**).

During treatment, all groups lost up to 10% of their pre-treatment body weights but began recovering after treatment finished (**Fig. 3.3.8 B**). At week 5, all mice in the IR + AZD7648 group began losing weight and developed fur loss and mild skin desquamation. Isaderm (an antibiotic/corticosteroid gel) was used as a topical skin treatment, and food was softened. Two mice lost 15% weight and were euthanised (JCM97 and JCM98)[1] while the remaining 4 recovered until the end of study. Upon euthanasia of JCM97 and JCM98, skin was collected and analysed by H&E (**Fig. 3.3.8 C**). A comparison of the right (exposed to systemic AZD7648) and left thorax (IR + AZD7648) skin revealed a clear thickening of the epithelial layer. Two mice were euthanised during the study due to large or spontaneous tumours (JCM78 and JCM92) (**Fig. 3.3.8** legend). For all other groups, there were no signs of significant weight loss, skin effects, or other clinical signs during the experiment, and all groups were euthanised 26 weeks after the start of treatment.

[1] JCM97 and JCM98 were only included in H&E analysis in Fig. 3.3.7 but no other analyses.

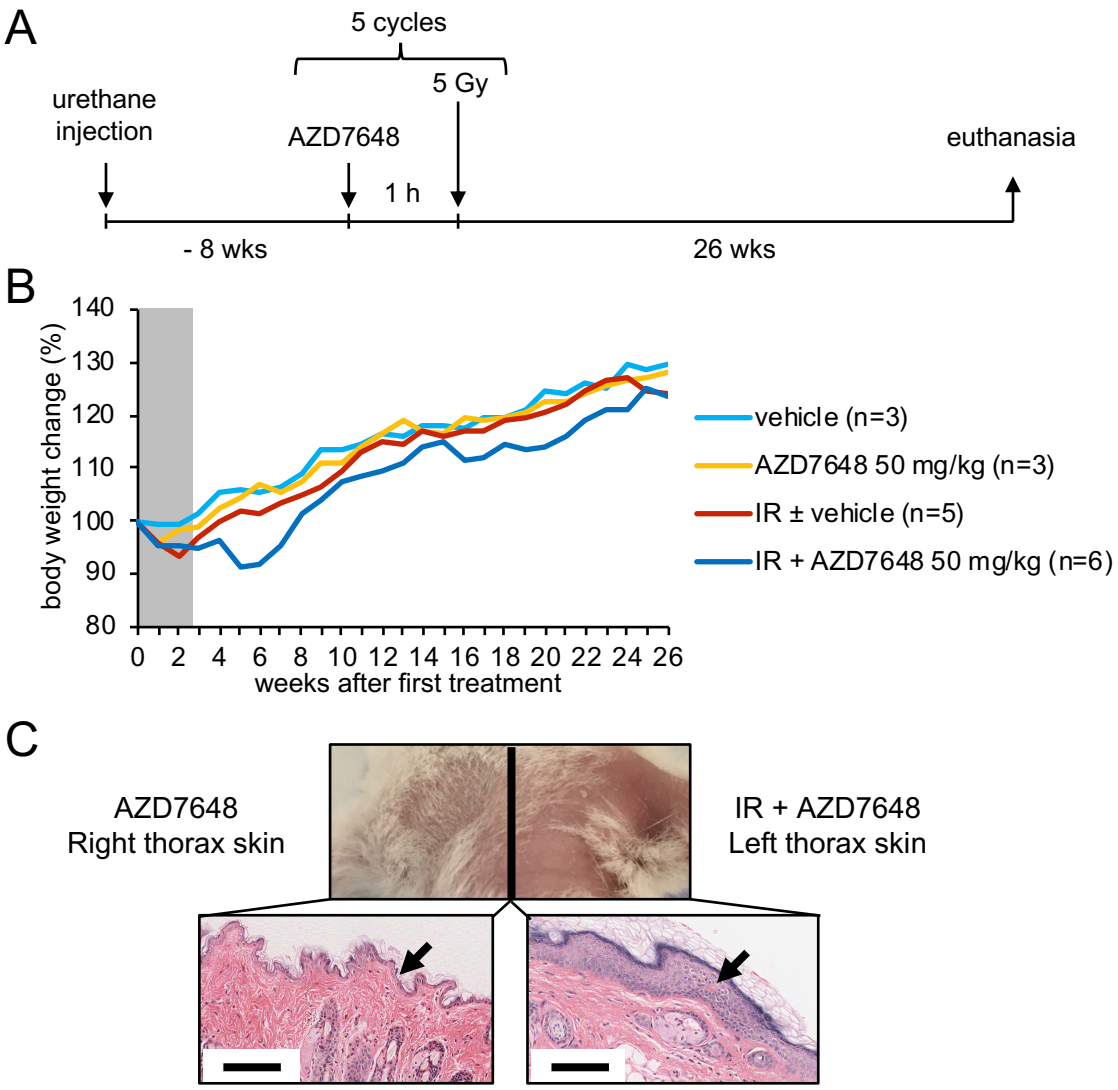

Figure 3.3.8. AZD7648 in combination with hemithorax IR induces mild body weight loss and skin effects. A/J mice were injected with urethane (10 mg per 10 g body weight, i.p., A). After 8 weeks, mice were allocated into groups (n=3 for vehicle and AZD7648, n=6 for IR ± vehicle, and n=6 for IR + AZD7648). Mice were treated with 5 cycles of AZD7648 (50 mg/kg, p.o.) 1 h before left thorax IR (5 Gy), with 2 days between IR doses. Euthanasia was planned for 26 weeks after the first IR dose. During treatment, all groups showed mild (up to 10%) weight loss but recovered after treatment finished (B). All mice in the IR + AZD7648 group began losing weight and fur on the left thorax during week 5. Two mice in the IR + AZD7648 group (JCM97 and JCM98) were euthanised due to greater than 15% weight loss and skin desquamation. The other 4 mice recovered after a week. At week 21, JCM92 (IR ± vehicle) was euthanised due to laboured breathing and greater than 15% weight loss[1]. JCM78 (IR ± vehicle) was euthanised at week 23 due to laboured breathing and 9% weight loss[2]. Subsequently, each group weight average was adjusted for the remaining mice. All other mice showed no significant weight loss or clinical signs during the study and were euthanised after 26 weeks. H&E staining of JCM97 and JCM98 revealed epithelial thickening (C, arrows) of the left thorax skin compared with the right thorax in the same mouse. Scale bar represents 100 µm. Grey bar represents treatment cycles.

[1] JCM92 post mortem H&E analysis revealed a large tumour mass on apex of the left lung and large immune infiltrate throughout alveolar space. JCM92 was not included in any analyses.
[2] JCM78 post mortem revealed a large mass above the left lung attached to the thymus and was not included in fibrosis scoring or lung weights analysis.

The potential therapeutic window of early intervention with AZD7648 and IR was investigated first by superficial tumour counts and histological counts of tumours in lung slices. Superficial tumour counts were reduced on the left lungs of individuals in the IR ± vehicle group (n=5) as compared with the vehicle control (n=3); the IR + AZD7648 group (n=6) showed a significant reduction in tumour numbers as compare to the IR ± vehicle group (**Fig. 3.3.9 A**). Surprisingly, the AZD7648 group (n=3) also showed a reduction in superficial tumour counts as compared with the vehicle controls. This result was investigated in an additional study with a larger group size (n=6) and two sets of 5 daily dosing regimens, but the effect was not reproduced (**Appendix Figures 6.7-6.9**).

The ratio of left to right lung tumour counts was also used to compare superficial tumour numbers using the right lung as an internal control in each animal. This further demonstrated that IR ± vehicle reduced the ratio of left to right lung tumour numbers as compared with vehicle alone and also that treatment with AZD7648 alone did not (**Fig. 3.3.9 B**). It also confirmed that the combination treatment was able to reduce this ratio as compared with the IR ± vehicle group.

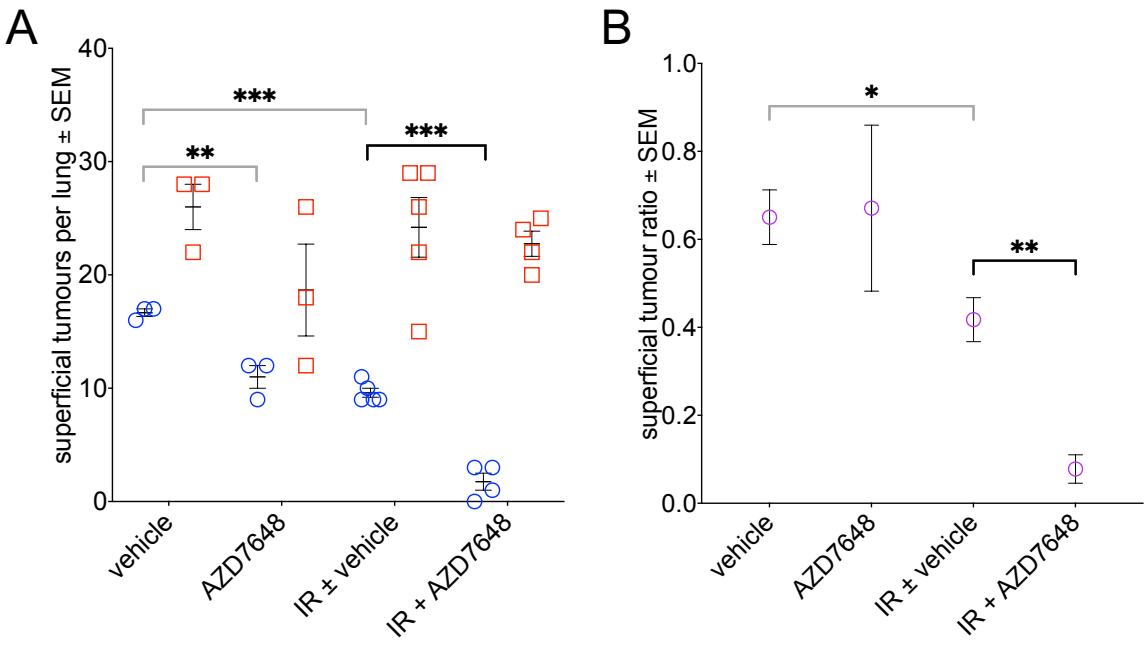

Figure 3.3.9. AZD7648 in combination with hemithorax IR reduced superficial tumour counts and ratio compared with hemithorax IR alone. Left lungs treated with IR ± vehicle had a significant reduction in both superficial tumour numbers and ratio between lung tumour counts (A and B). Mice treated with AZD7648 alone also had a reduced tumour count but not tumour ratio. Mice in the IR + AZD7648 group showed a significant reduction in both tumour counts and count ratio compared with the IR ± vehicle group. (o) are individual left lungs, (□) are individual right lungs, (o) are a ratio of left lung counts divided by right lung counts.

Histological counting of tumours from a single midsection left lung slice and the total area of tumour burden (tumour area burden) per slice were additional measures used to assess treatment efficacy. Both tumour counts and area burden were significantly decreased in the left lungs of the IR + AZD7648 group as compared with IR ± vehicle (**Fig. 3.3.10 A & B**).

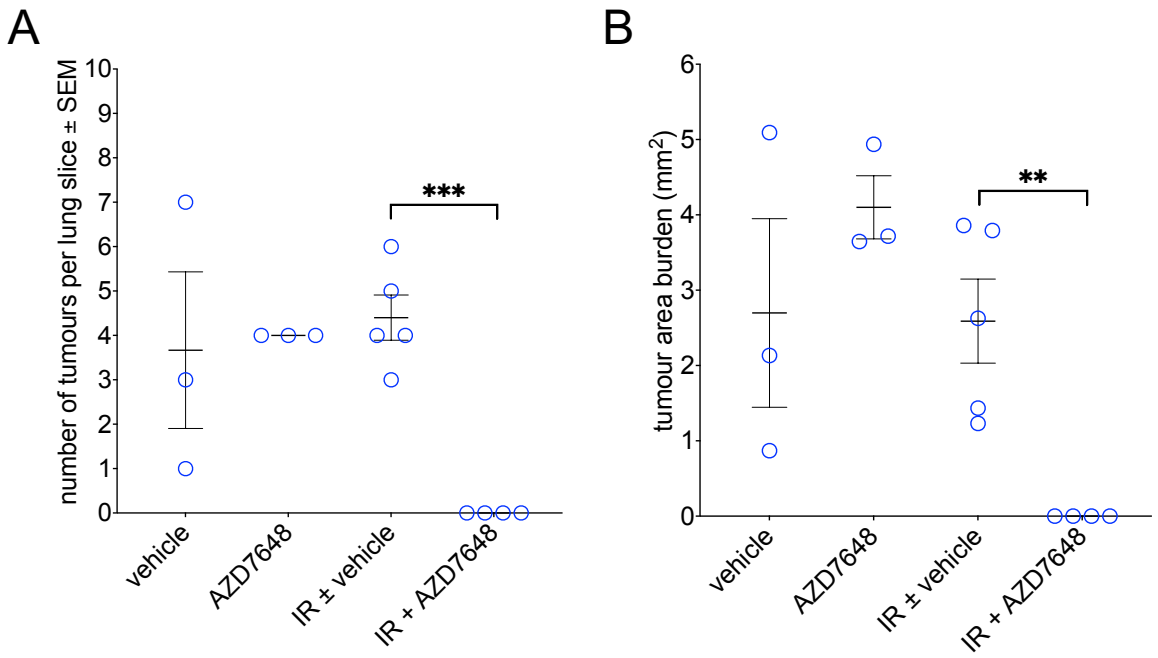

Figure 3.3.10. AZD7648 in combination with hemithorax IR reduced tumour numbers and area per lung slice compared with hemithorax IR alone. Mice in the IR + AZD7648 group showed a reduction in both tumour counts per left lung slice (A) and total tumour area (B) as compared with IR ± vehicle. IR ± vehicle did not show a reduction in either measure compared with vehicle alone. (o) are individual left lungs.

To examine the effect of each treatment on normal tissue, both lungs were weighed upon collection. Lungs weights in the combination treatment group were significantly altered. Left lungs had decreased in overall weight while, in contrast, right lungs had increased in weight (**Fig. 3.3.11 A**). Lungs were additionally assessed using the modified Ashcroft scoring of left lungs stained by Masson's trichrome (**Chapter 2.16**). Fibrosis scoring revealed that while IR ± vehicle increased scores as compared with the vehicle group, IR + AZD7648 treatment resulted in a significant increase in fibrosis score as compared with IR ± vehicle treatment (**Fig. 3.3.11 B & C**).

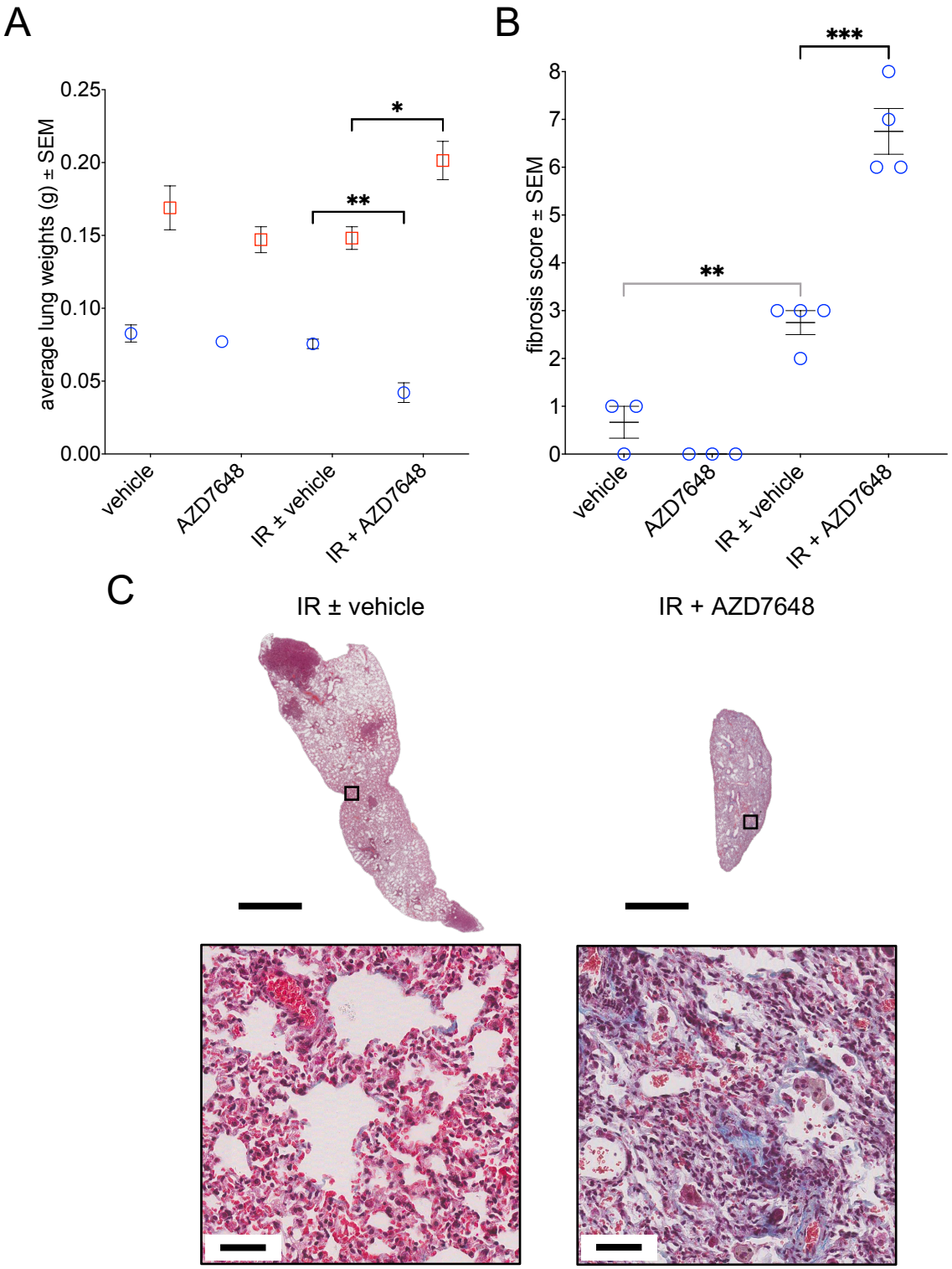

Figure 3.3.11. AZD7648 in combination with hemithorax IR significantly altered lung weights and fibrosis scores compared with hemithorax IR alone. The left and right lungs of mice treated with AZD7648 and IR were significantly altered as measured by lung weight: left lungs decreased while right lungs increased in weight (A). Analysis of left lungs stained by Masson's trichrome revealed that IR ± vehicle increased fibrosis scores compared with the vehicle treated group (B). Fibrosis scores of lungs treated with IR + AZD7648 were significantly higher compared with IR ± vehicle (B) and displayed a marked increase in collagen deposition (C, blue). (o) are average left lungs, (□) are average right lungs in A. (o) represent individual total lung fibrosis score in B. Scale bars represent 2 mm for whole lung slices and 50 μm for representative image.

These results from the early intervention study suggest that AZD7648 at 50 mg/kg combined with fractionated hemithorax IR is highly efficacious in the early tumours of A/J mice, reducing both overall tumour number and size. However, the normal tissues in the field of IR, left thorax skin and left lungs, were also shown to be significantly affected as a result of treatment.

3.3.6. AZD7648 and CT-guided left lung IR is tolerated but shows limited efficacy in A/J late intervention therapeutic window study

The A/J model late intervention study was used to assess the efficacy and tolerability of AZD7648 at 50 mg/kg in combination with IR at a late stage of tumour development. A/J mice were injected with urethane to initiate tumour growth. After 19 weeks, mice were treated with AZD7648 (50 mg/kg) 1 h before IR (13 Gy) to the left lung using the CT-guided SARRP (**Chapter 2.6.2**). Mice were also imaged by MRI pre-treatment and before euthanasia at 7 weeks after treatment (**Fig. 3.3.12 A**).

One animal in the IR + AZD7648 group (JCM264) lost 12% weight during week 4 but recovered after 24 h on softened food. No other mice developed significant body weight loss in the 7 weeks after treatment. During week 4, one mouse in the IR + AZD7648 group (JCM265) lost a small patch of fur and developed a skin erosion on the dorsal left shoulder. The skin erosion was treated with Isaderm for 2 days and was no longer evident after a week. At week 5, all animals treated with IR + AZD7648 lost a small patch of fur (approximately 8 x 8 mm) on the dorsal and ventral side of the left thorax, but there was no evidence of skin erosions. The study ended as planned after 7 weeks (**Fig. 3.3.12 B**).

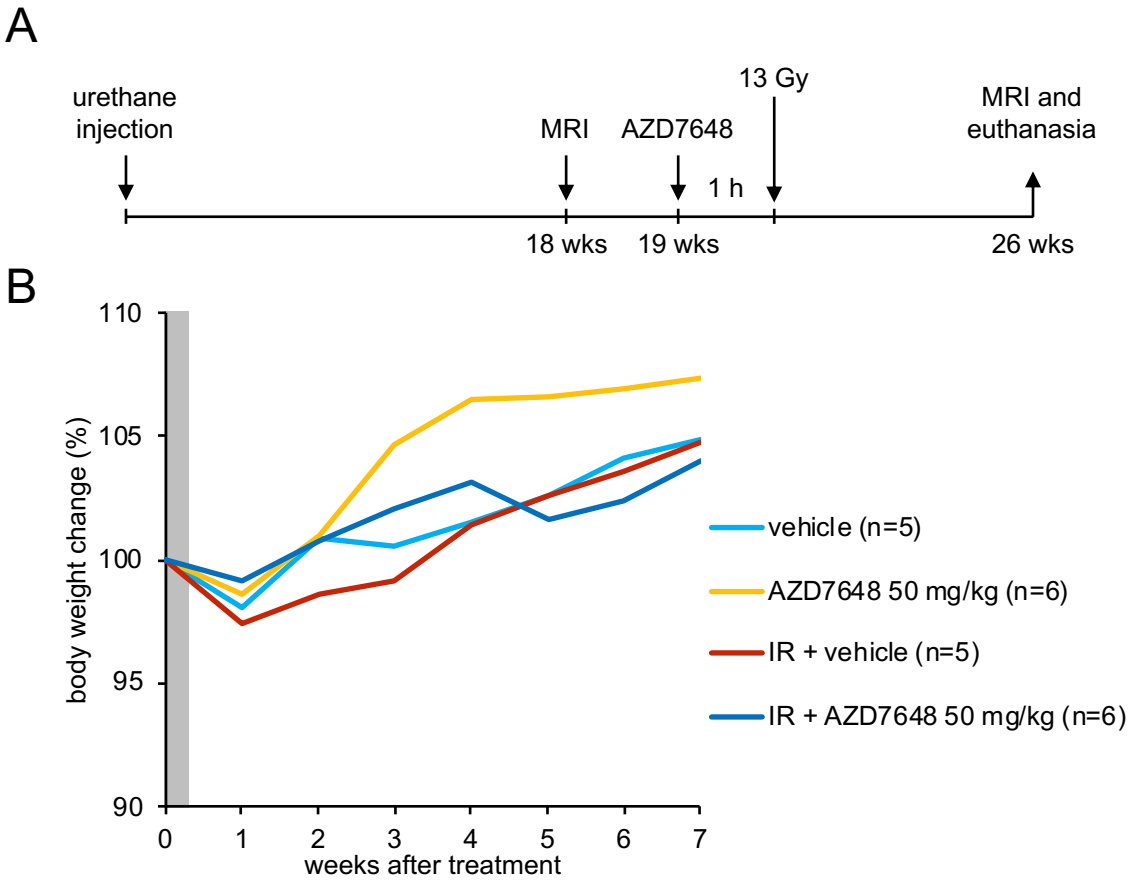

Figure 3.3.12. AZD7648 in combination with CT-guided left lung IR did not induce body weight loss. A/J mice were injected with urethane (10 mg per 10 g body weight, i.p., A). After 18 weeks, mice were allocated into groups (n=5 for vehicle and IR + vehicle groups, n=6 for AZD7648 and IR + AZD7648 groups) and were imaged using MRI. During week 19, mice were treated with a single dose of AZD7648 (50 mg/kg, p.o.) 1 h before left lung IR (13 Gy). Mice were imaged using MRI during weeks 22 and 26 and euthanised during week 26. During week 4, one mouse in the IR + AZD7648 group (JCM264) lost 12% weight but recovered after 24 h (B). All other mice groups showed no significant weight loss during the study and were euthanised 7 weeks after treatment. Grey bar represents treatment.

Superficial counts of left lung tumours and tumour count ratios between left to right lungs showed no significant difference between the IR + vehicle (n=5) and IR + AZD7648 (n=6) groups (**Fig. 3.3.13 A & B**).

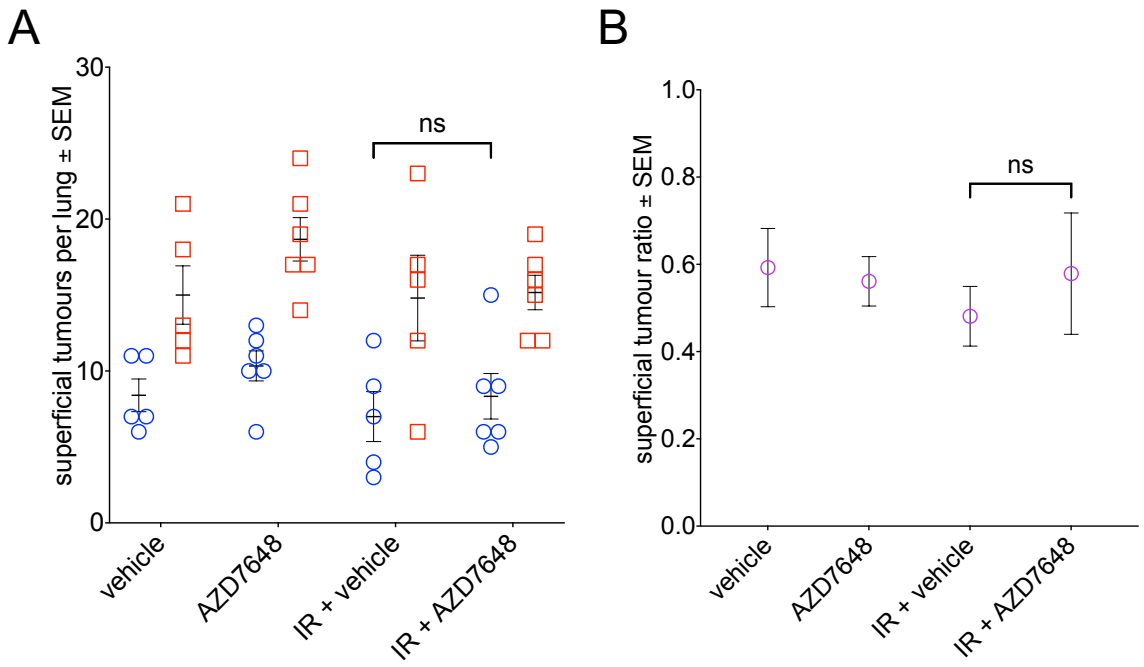

Figure 3.3.13. AZD7648 in combination with CT-guided left lung IR did not reduce superficial tumour counts or ratio. Mice in the IR + AZD7648 group did not show a reduction in either tumour counts (A) or count ratio (B) as compared with IR + vehicle. (o) are individual left lungs, (□) are individual right lungs, (○) are a ratio of left lung counts divided by right lung counts.

Additionally, a trend of decreasing tumour number per left lung slice and tumour area burden was observed in the IR + AZD7648 group as compared with the IR + vehicle group, but it did not reach statistical significance for either measure (**Fig. 3.3.14 A & B**).

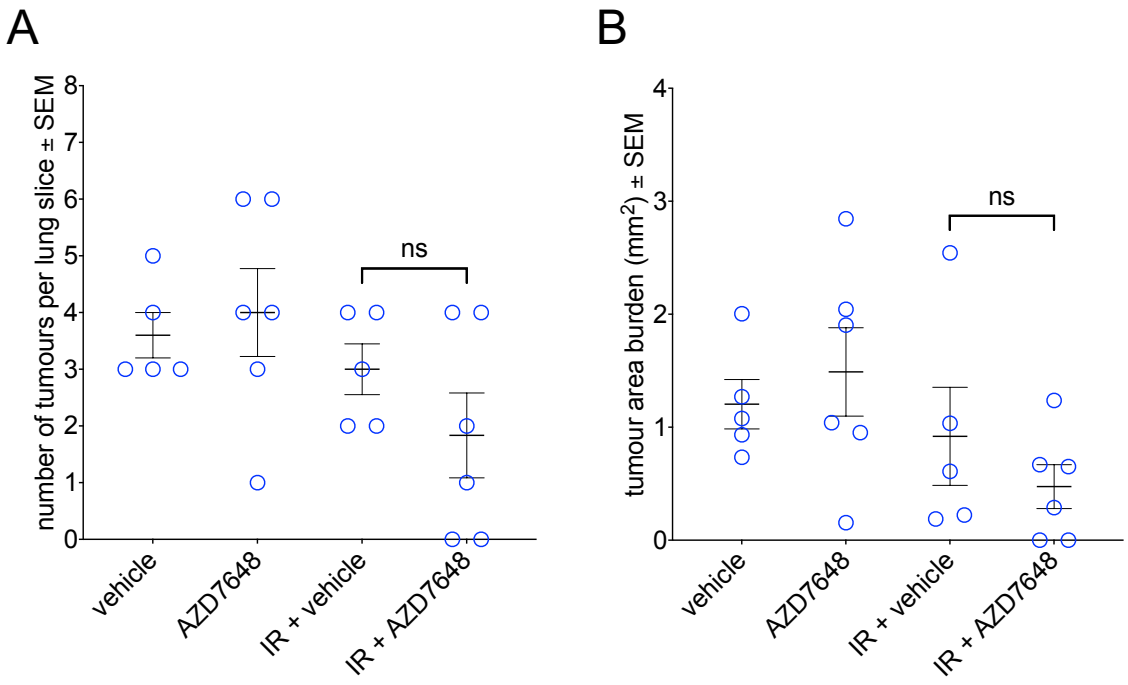

Figure 3.3.14. AZD7648 in combination with CT-guided left lung IR did not reduce tumour numbers or area per lung slice. Mice in the IR + vehicle group did not show a reduction in either tumour number per left lung slice (A) or tumour area burden (B) compared with the vehicle alone group. Treatment with IR + AZD7648 did not reduce either measure compared with the IR + vehicle group. (o) are individual left lungs.

Total left lung tumour volume changes from pre-treatment to week 7 were assessed using MRI (**Fig. 3.3.15 A & B**). The total left lung tumour volume changes of mice treated with IR + AZD7648 were significantly lower compared with individuals treated with IR + vehicle.

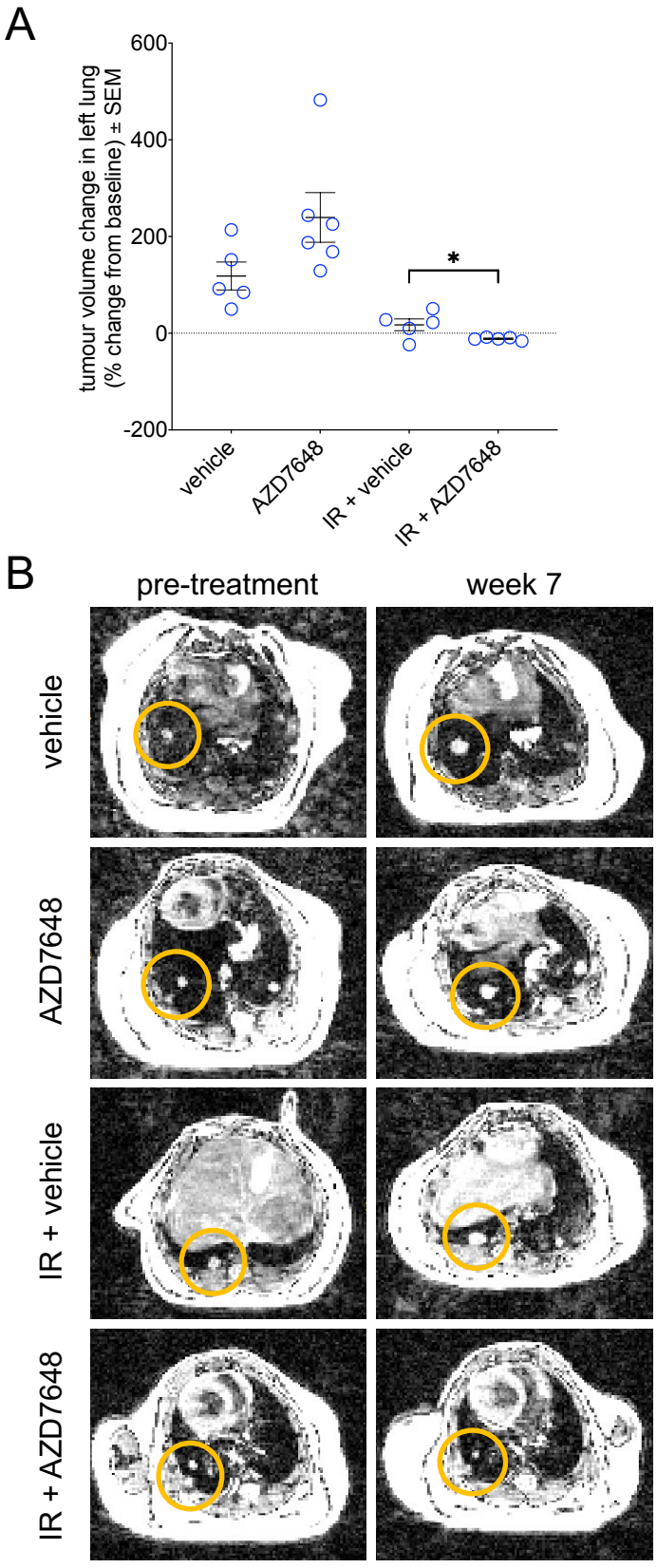

Figure 3.3.15. AZD7648 in combination with CT-guided left lung IR significantly reduced tumour volume change compared with IR alone. Total left lung tumour volume changes of mice treated with IR + AZD7648 were significantly lower compared with mice treated with IR + vehicle (A). Representative axial MR images of the mouse chest with tumours circled in yellow (B). (o) are individual left lung tumour volume changes from baseline (pre-treatment) to week 7.

Lung weights and H&E staining revealed no increase in normal lung tissue effects by gross pathology or histology (**Fig. 3.3.16 A & B**).

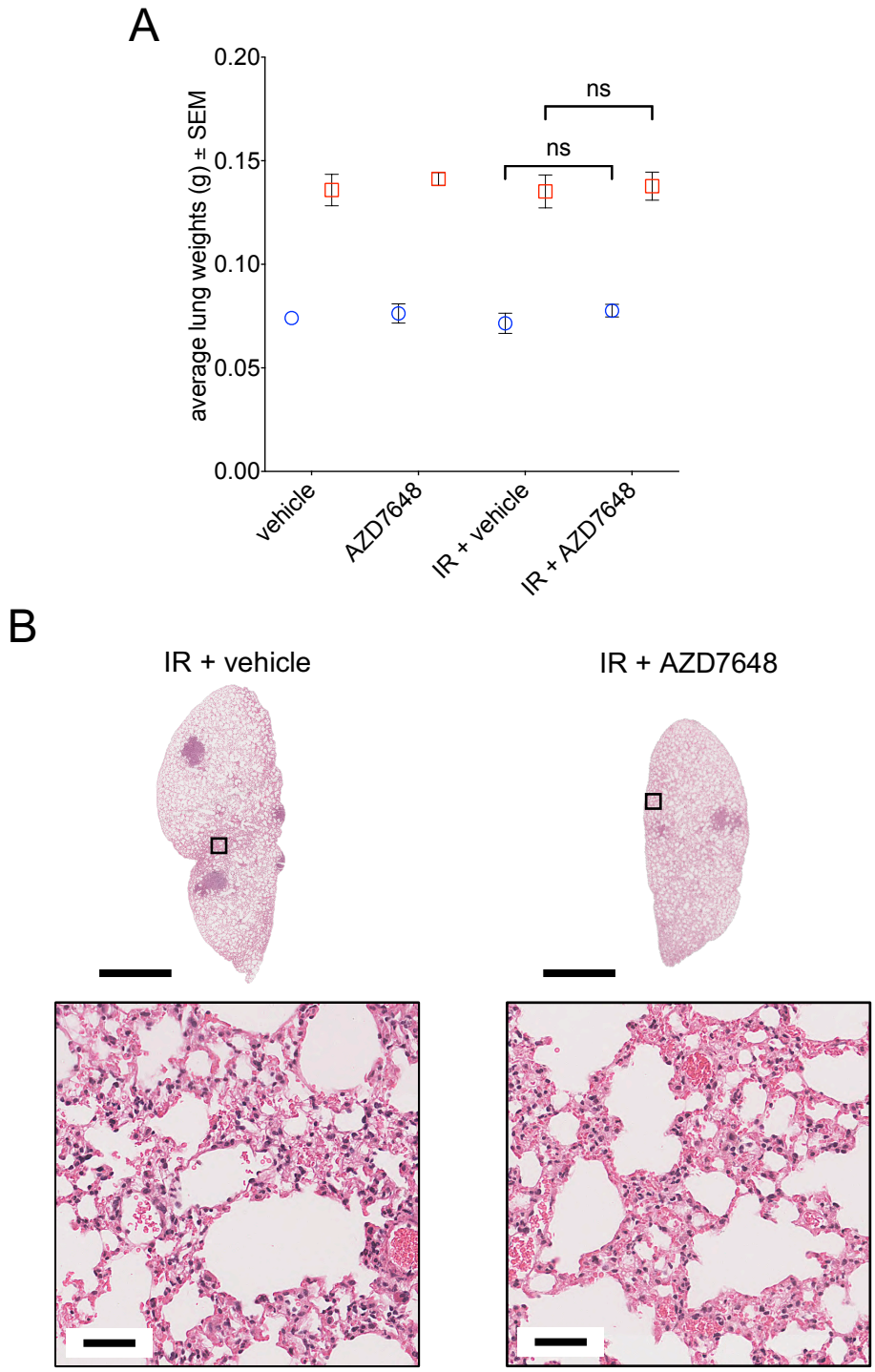

Figure 3.3.16. AZD7648 in combination with CT-guided left lung IR did not alter lung weight or histology. None of the treatment groups showed significant normal lung tissue effects as measured by lung weight (A) or by H&E staining (B). (o) are average left lungs, (□) are average right lungs. Scale bars represent 2 mm for whole lung slices and 50 μm for representative image.

These results suggest that AZD7648 at 50 mg/kg is not able to modulate the effect of IR on established tumours of the A/J model in 7 weeks.

3.3.7. Pharmacodynamics of AZD7648 at 50 mg/kg combined with IR does not significantly affect γH2AX levels in lung tumours or the bronchial or oesophageal epithelium

A PD study in the A/J model was also undertaken to analyse tissue responses to IR combined with AZD7648 over 24 h post IR treatment. A/J mice were injected with urethane to initiate tumour growth. After 18 weeks, mice were treated with AZD7648 (50 mg/kg) 1 h before IR (13 Gy) to the whole thorax (**Fig. 2.6.1.2**). Mice were euthanised at 2 and 24 h after IR (**Fig. 3.3.17 A**).

IHC of γH2AX levels in cells was used to assess tumour response to IR and AZD7648 as it is a well-established surrogate marker of DSBs that are caused by IR and has been used as a biomarker of AZD7648 activity (Fok et al., 2019). Upon irradiation, H2AX is rapidly phosphorylated on serine 139 at sites of DSBs (Valdiglesias et al., 2013). After 2 h, tumours in both IR + vehicle (n=5) and IR + AZD7648 (n=3) showed an increase in the percentage of γH2AX-positive cells as measured by IHC as compared with the vehicle control tumours. Tumours treated with IR + AZD7648 displayed a higher percentage of γH2AX positive cells than those treated with IR + vehicle, but the difference was not statistically significant (**Fig. 3.3.17 B & D**). After 24 h, the percentage of γH2AX-positive cells had decreased in both the IR + vehicle (n=7) and IR + AZD7648 (n=4) groups, and there was no difference between the groups (**Fig. 3.3.17 C & D**).

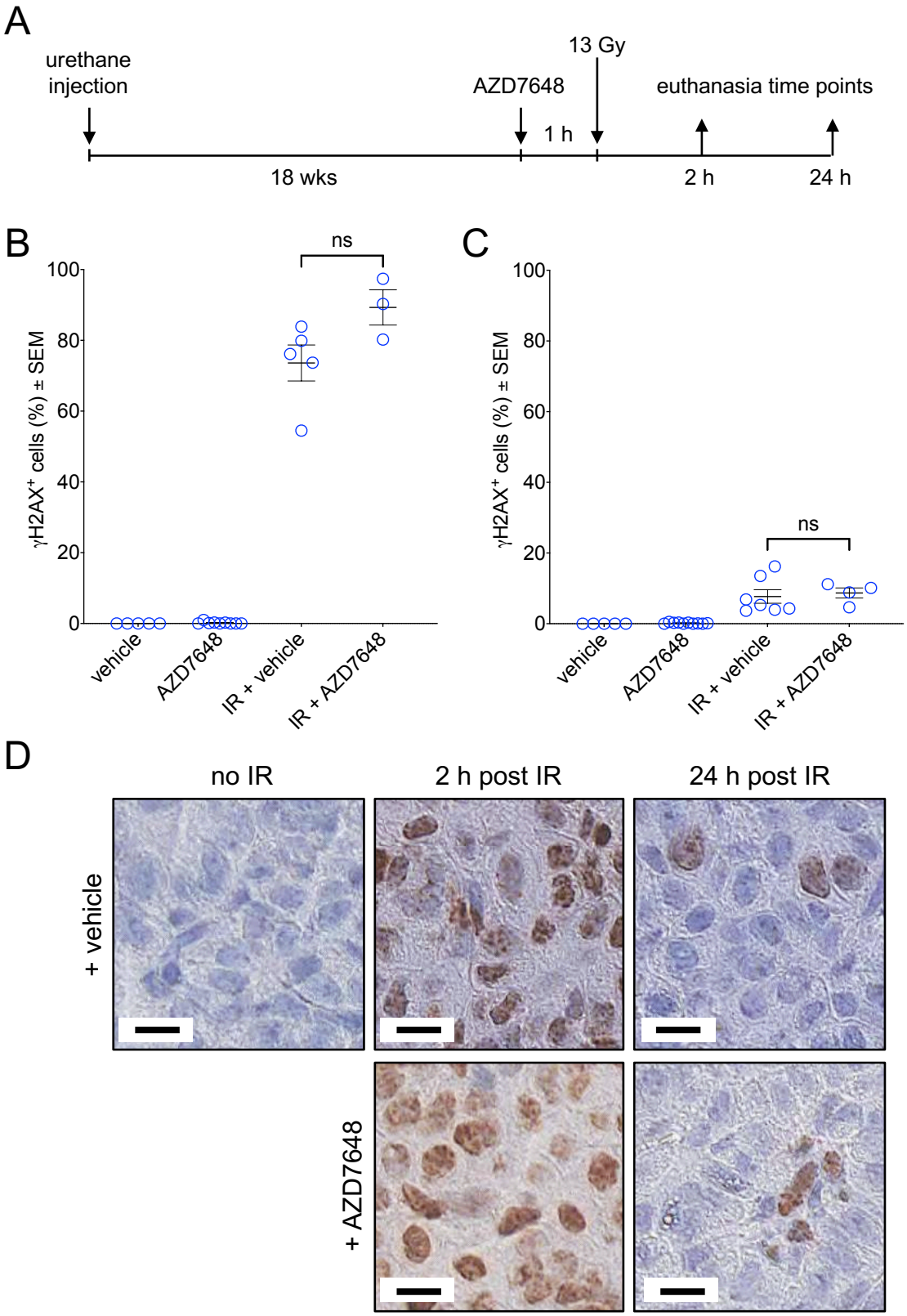

Figure 3.3.17. AZD7648 in combination with IR did not affect γH2AX levels in tumours. A/J mice were injected with urethane (10 mg per 10 g body weight, i.p., A). After 18 weeks, mice were allocated into groups (n=3 for vehicle, n=6 for IR + vehicle and AZD7648, and IR + AZD7648). At week 18, mice were treated with a single dose of AZD7648 (50 mg/kg, p.o.) 1 h before whole thorax IR (13 Gy). Mice were euthanised at 2 and 24 h after IR. γH2AX in tumours treated with IR + AZD7648 was not significantly different compared with IR + vehicle control after 2 h (B) or 24 h (C). IHC of representative γH2AX levels in lung tumours (D). (o) are individual tumours. Scale bars represent 10 μm.

To assess the effect on normal tissues, the percentage of γH2AX-positive cells was also measured in bronchial and oesophageal epithelial tissue. Four categories were used for counting γH2AX positive cells: (i) clear, separated foci, (ii) abundant distinct but overlapping foci, (iii) faint pan-nuclear staining, and (iv) dark pan-nuclear staining (**Fig. 2.16.1**). At 2 h after treatment with IR + vehicle and IR + AZD7648, a majority of bronchial epithelial cells (> 90%) displayed distinct but overlapping γH2AX foci, but there was no difference between the groups (**Fig. 3.3.18 A & C**). After 24 h, both the IR + vehicle and IR + AZD7648 groups had more than 40% of cells with clear, separated γH2AX foci (**Fig. 3.3.18 B & C**). Neither pan-nuclear γH2AX measure was significantly increased at either time point for any treatment.

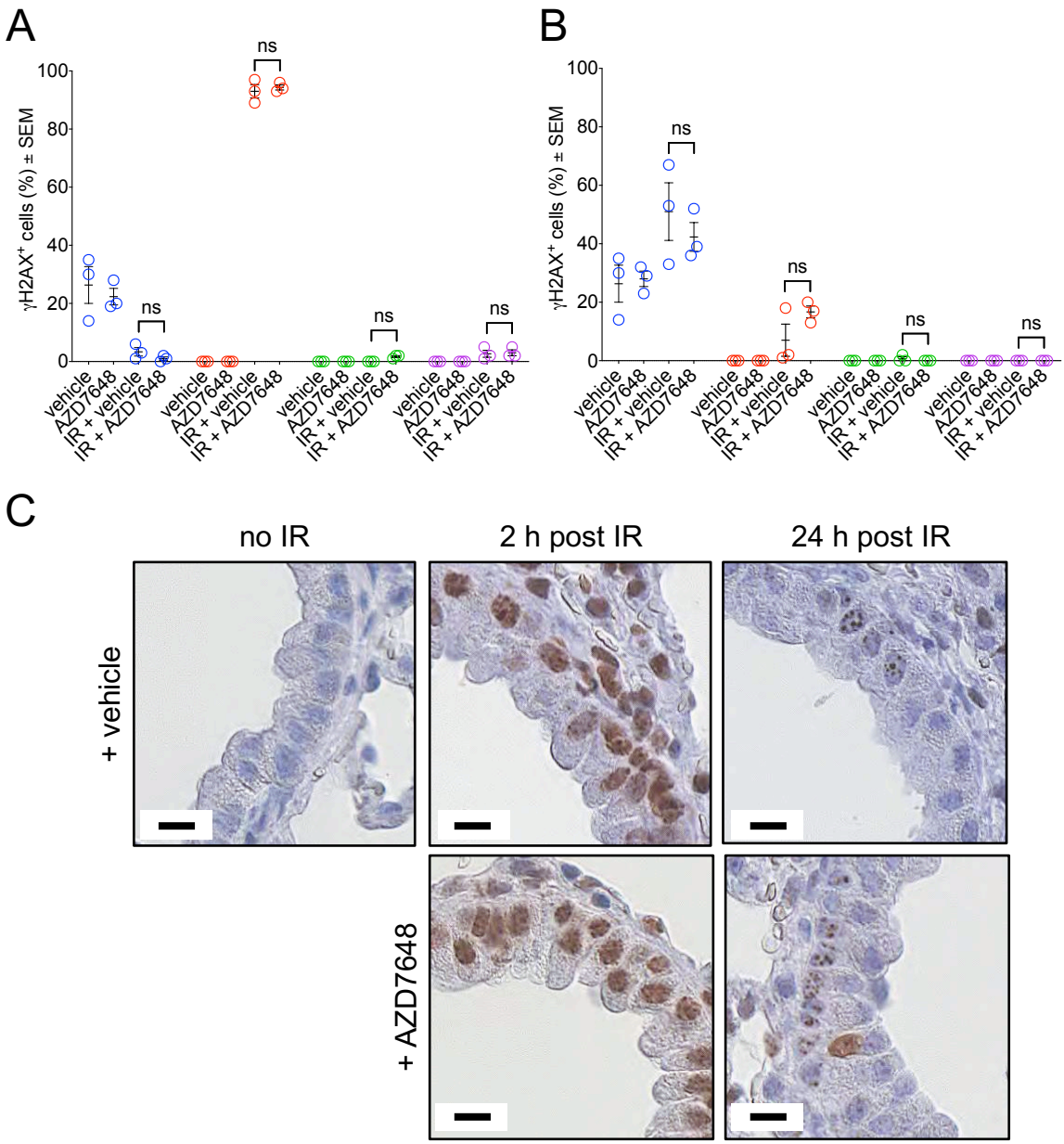

Figure 3.3.18. AZD7648 in combination with IR did not affect γH2AX levels in bronchial epithelial cells. γH2AX levels in bronchial epithelial cells treated with IR + AZD7648 were not significantly different when compared with IR + vehicle control after 2 h (A) or 24 h (B). IHC of representative γH2AX staining in bronchial epithelial cells (C). Circles are individual mice and (o) is clear, separated foci, (o) is abundant distinct but overlapping foci, (o) is faint pan-nuclear staining, (o) is dark pan-nuclear staining. Scale bars represent 10 μm.

In the oesophageal epithelium at 2 h after treatment with IR + vehicle or IR + AZD7648, a majority of cells (> 80%) contained overlapping γH2AX foci, but there was no difference between the groups (**Fig. 3.3.19 A & C**). At 24 h after IR, both the IR + vehicle and IR + AZD7648 groups had more than 35% of cells with clear, separated γH2AX foci (**Fig. 3.3.19 B & C**). There was a higher percentage of cells with clear,

separated γH2AX foci in the IR + AZD7648 group, but the difference was not significant. Neither pan-nuclear γH2AX measure was significantly increased at either time point for any treatment.

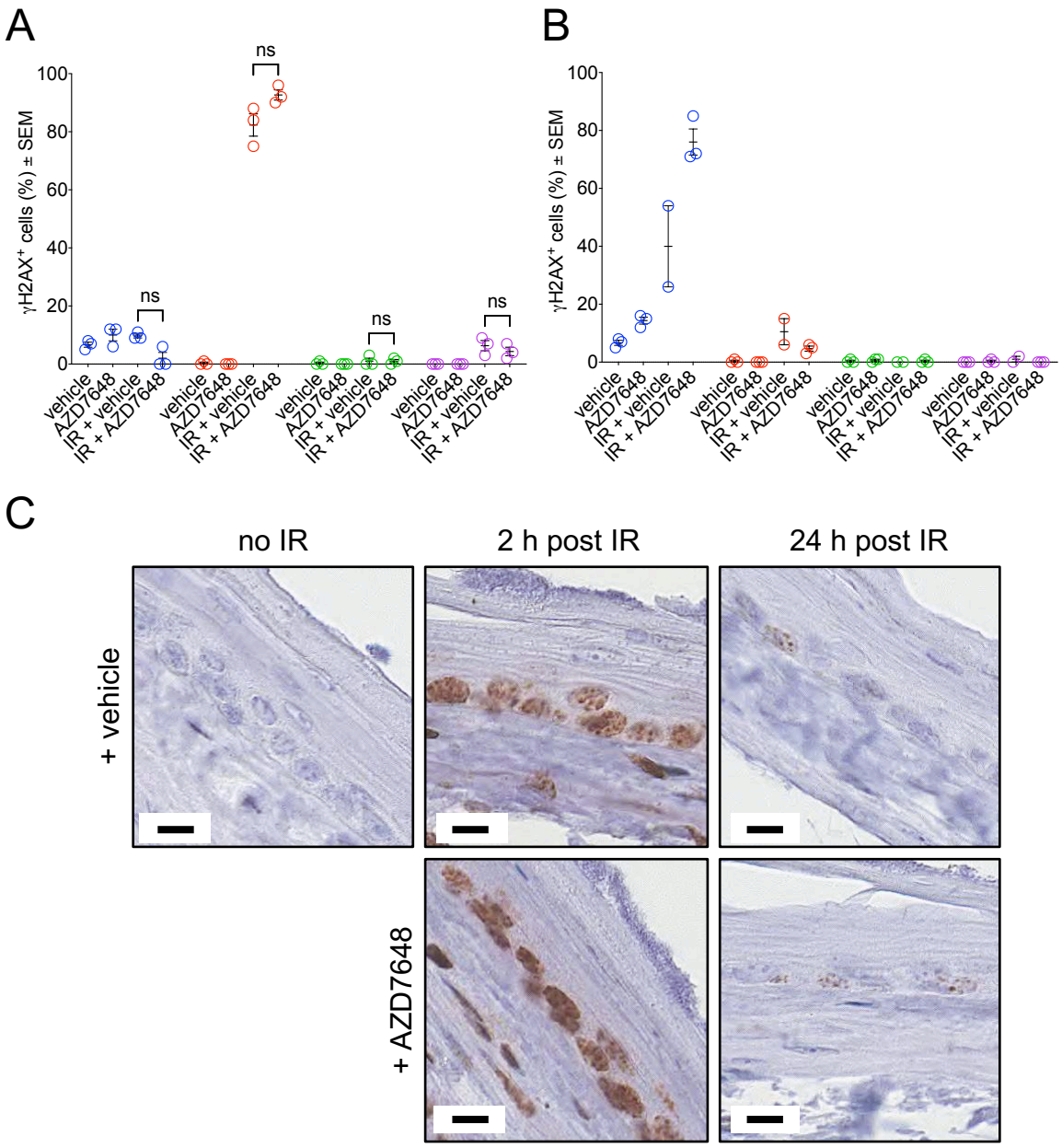

Figure 3.3.19. AZD7648 in combination with IR did not affect γH2AX in oesophageal epithelial cells. γH2AX levels in oesophageal epithelial cells treated with IR + AZD7648 were not significantly different when compared with IR + vehicle control after 2 h (A) or 24 h (B). IHC of representative γH2AX staining in oesophageal epithelial cells (C). Circles are individual mice and (o) is clear, separated foci, (o) is abundant distinct but overlapping foci, (o) is faint pan-nuclear staining, (o) is dark pan-nuclear staining. Scale bars represent 10 μm.

Together, these data suggest that AZD7648 at 50 mg/kg combined with 13 Gy increased the number of γH2AX-positive cells in tumours at 2 h, but this effect did not

reach statistical significance compared with IR alone. This trend was not observed in normal epithelial cells of either the bronchi or oesophagi at either time point.

3.3.8. Pharmacodynamics of AZD7648 at 50 mg/kg combined with IR decreases pKAP1 in tumours but not in bronchial or oesophageal epithelial cells

Phosphorylation of KAP1 on serine 824 was used as a second marker of tissue responses to IR and AZD7648 as measured by IHC. At 2 h after IR, tumours treated with IR + AZD7648 (n=3) showed a decrease in the percentage of pKAP1-positive cells as compared with IR + vehicle (n=5) (**Fig. 3.3.20 A & C**). This difference between pKAP1 levels in tumours treated IR + AZD7648 (n=3) and IR + vehicle (n=8) was not apparent after 24 h (**Fig. 3.3.20 B & C**).

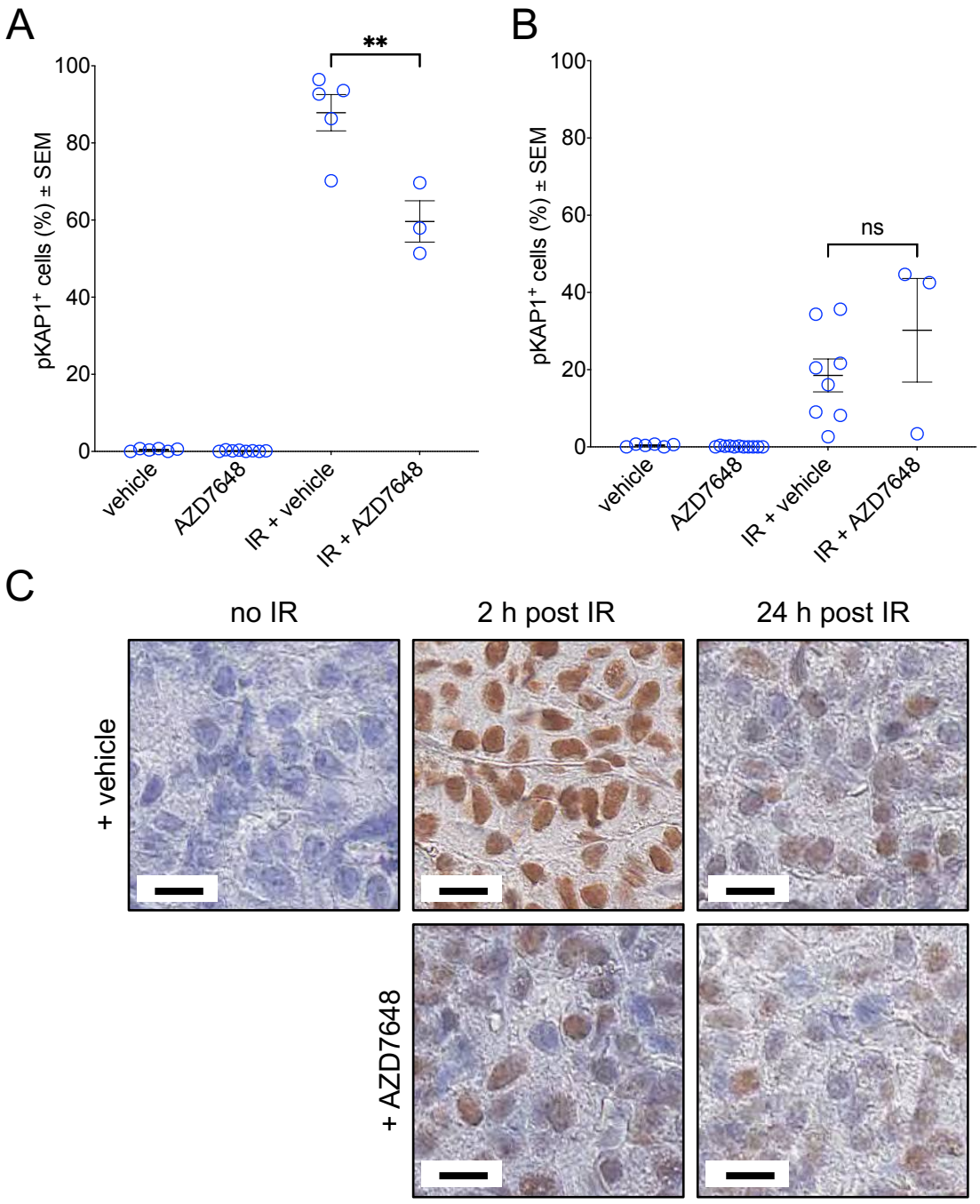

Figure 3.3.20. AZD7648 in combination with IR decreased pKAP1 levels in tumours. Levels of KAP1 phosphorylation on serine 824 in tumours treated with IR + AZD7648 were significantly decreased compared with IR + vehicle after 2 h (A). After 24 h, both IR groups showed a similar level of pKAP1 (B). IHC of representative pKAP1 (ser824) staining in lung tumours (C). (o) are individual tumours. Scale bars represent 10 μm.

KAP1 phosphorylation was also used to evaluate the effect of AZD7648 and IR on the cells of the bronchial epithelium. At both 2 and 24 h after IR, no difference was observed between the IR + vehicle and IR + AZD7648 groups (**Fig. 3.3.21 A-C**).

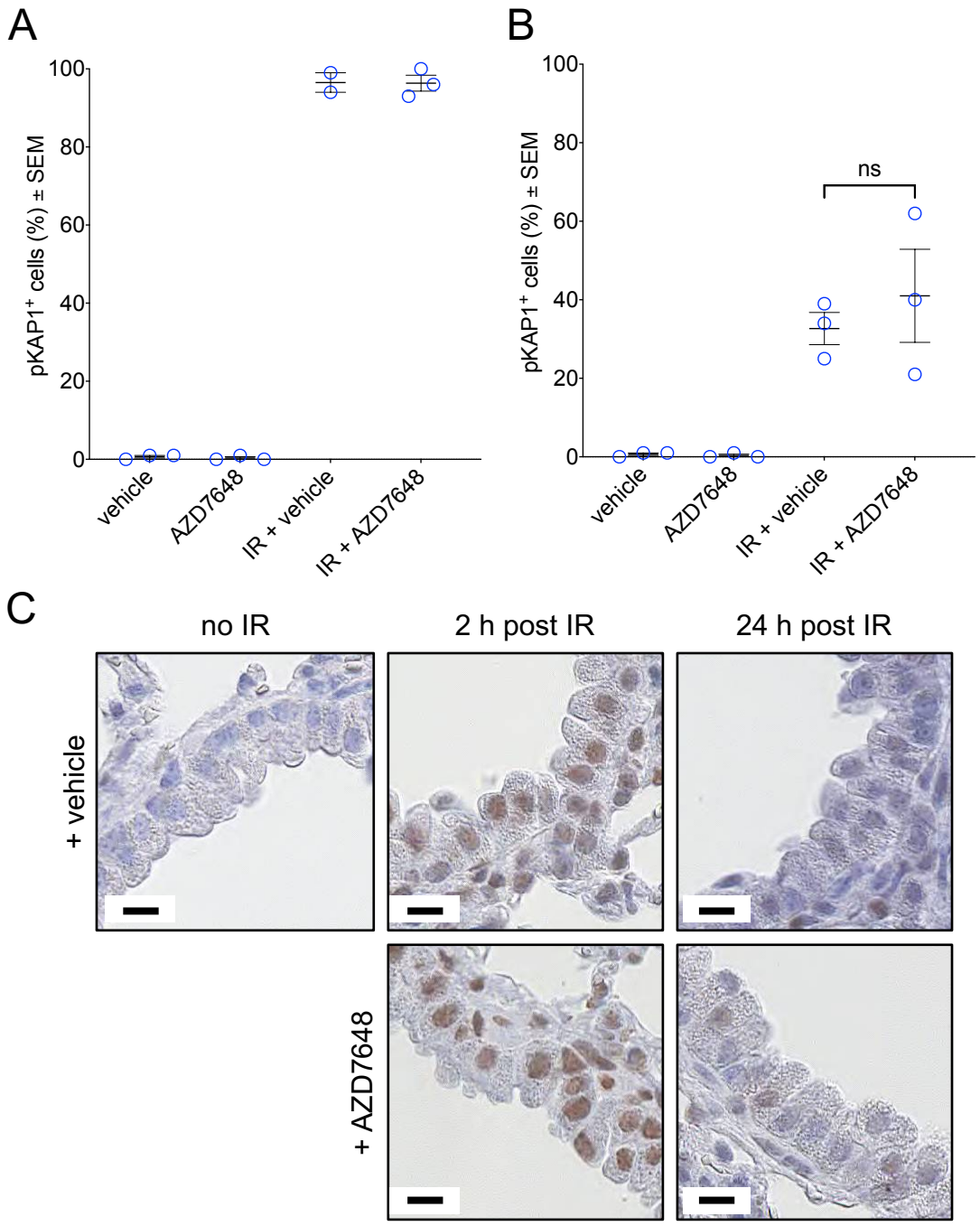

Figure 3.3.21. AZD7648 in combination with IR did not affect pKAP1 levels in bronchial epithelial cells. Levels of pKAP1 in bronchial epithelial cells treated with IR + AZD7648 were similar compared with IR + vehicle after 2 h (A) or 24 h (B). IHC of representative KAP1 (ser824) staining in bronchial epithelial cells (C). (o) indicate individual mice. Scale bars represent 10 µm.

IHC of KAP1 phosphorylation in the oesophageal epithelium also revealed no significant difference in the percentage of positive cells at 2 h between treatment with IR + vehicle or IR + AZD7648 (**Fig. 3.3.22 A-C**). A trend of an increasing percentage

of pKAP1-positive cells was observed in the oesophageal cells after 24 h, but it did not reach statistical significance.

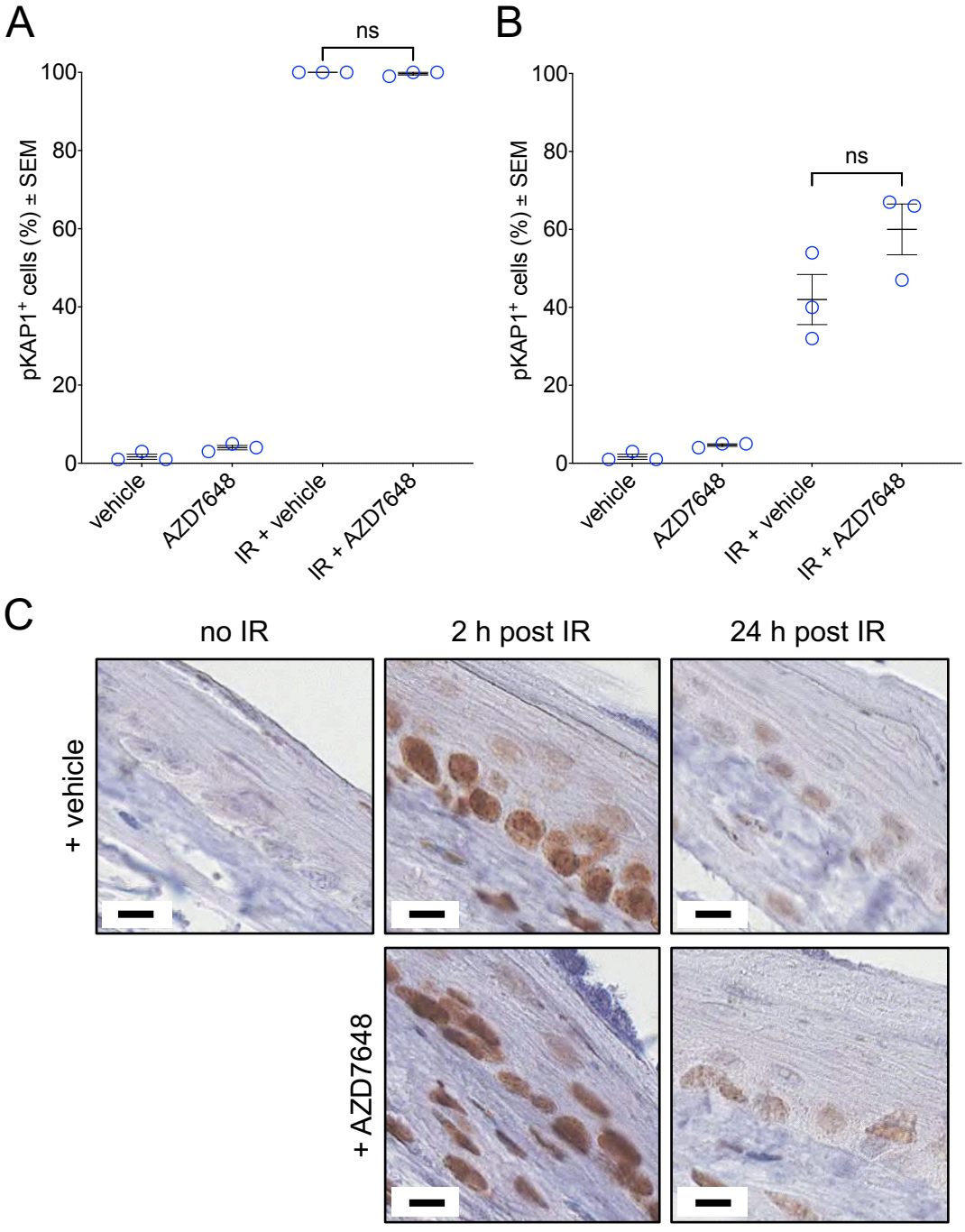

Figure 3.3.22. AZD7648 in combination with IR did not affect pKAP1 levels in oesophageal epithelial cells. Levels of pKAP1 in oesophageal epithelial cells treated with IR + AZD7648 were not significantly different compared with IR + vehicle control after 2 h (A) or 24 h (B). IHC of representative KAP1 (ser824) staining in oesophageal epithelial cells (C). (o) indicate individual mice. Scale bars represent 10 μm.

Together, these findings suggest that while AZD7648 at 50 mg/kg with IR does result a marked decrease in tumour KAP1 phosphorylation at 2 h, this difference in not

seen in the normal tissues of the bronchial or oesophageal epithelium at either time point.

3.3.9. Discussion

Treatment of tumours with AZD7648 at 50 mg/kg combined with IR has been demonstrated as highly efficacious in both tumour xenografts and the A/J therapeutic window early intervention study. While this is a promising outcome, the normal tissue damage implications from treatment are important considerations for this compound as it enters clinical trials. Oesophagitis, skin desquamation, and lung fibrosis in mice treated with AZD7648 and fractionated IR reveal the potential for radiosensitisation of thoracic tissues using this DNA-PK inhibitor. Interestingly, while there were severe histological changes in the irradiated left lungs, the lack of observed physiological effects on breathing and the right lung enlargement indicate an ability for the right lung to compensate for the damage caused by IR treatment of the left lung, which has been observed in both humans and other mammals (Butler et al., 2012; Mentzer, 2018). In contrast to AZD7648, inhibition of DNA-PK using another compound (NU5455, 30 mg/kg, p.o.) in combination with fractionated IR (4 x 5 Gy) in C57BL/6 mice resulted in similar levels of fibrosis in the lungs after 24 weeks as compared with fractionated IR alone (Willoughby et al., 2020). This may suggest that the pharmacological properties of DNA-PK inhibitors (including potency, selectivity, and pharmacokinetics) may be important factors in determining normal tissue toxicities.

The late intervention study outcomes contrasted with the early intervention in both the ability of AZD7648 to elicit an anti-tumour effect as well as damage the skin and lung tissue. While there was a limited efficacy measured by superficial tumour counts and histological measurements after 7 weeks, MRI data demonstrated the significant impact of IR + AZD7648 on tumour volume. Additionally, the more refined approach to treatment with a smaller field size and better targeting of radiation resulted

in better tolerability, suggesting a potentially viable approach combining with DNA-PK inhibitors. In patients, the toxicities from treatment are limited through advances in tumour targeting. With these treatment modalities, although the potential for the toxicity using IR and AZD7648 should be considered, it may be significantly reduced.

Another important set of considerations is the PD of AZD7648 in the A/J model. In urethane-induced tumours, the addition of AZD7648 at 50 mg/kg to IR was able to reduce the phosphorylation of KAP1 while a trend of increasing γH2AX levels was observed at 2 h. As pKAP1 on serine 824 is considered an ATM-specific phosphorylation site, this may be suggestive of potential off-target ATM inhibition by AZD7648 (Ziv et al., 2006). In the pharmacological study of AZD7648, the IC_{50} of ATM activity inhibition by AZD7648 was found to be 17.93 μM. However, with an initial oral dose of 100 mg/kg, after 30 minutes the AZD7648 free plasma levels in mice reduced to less than 20 μM, suggesting that this effect may only be a partial explanation of reduced KAP1 phosphorylation (Fok et al., 2019). The increased γH2AX levels in tumours upon IR + AZD7648 treatment at 2 h may be an indication of the plasma concentration of AZD7648 decreasing and delayed repair beginning, as seen by others (Fok et al., 2019). By 24 h, γH2AX levels in tumours had decreased in both IR groups, suggesting that cells had undergone repair processes.

The normal tissue responses to IR and AZD7648 have broader implications for the tolerability of this combination in the bronchial and oesophageal epithelial cells. While pKAP1 and γH2AX levels were similar in both tissues at 2 and 24 h for both IR groups, the oesophagi of mice treated with IR + AZD7648 had a slight trend of more clear, separated γH2AX foci and higher pKAP1 levels after 24 h, which may be due to delayed repair from AZD7648 activity and be a partial explanation of the oesophageal damage from fractionated IR and AZD7648. Although extensive fibrosis was observed in left lungs treated with fractionated IR and AZD7648 after 26 weeks, the PD of

bronchial epithelial cells at 2 and 24 h did not reveal an early indication of this damage by pKAP1 and γH2AX levels. More early time points should be used to examine the tissue responses to this compound to potentially help explain both the early and late term lung effects.

Unfortunately, there is still a need to establish robust biomarkers of DNA-PK inhibition for preclinical studies. Currently the primary biomarkers that have been used to demonstrate pharmacokinetics of DNA-PK inhibition are γH2AX, 53BP1, and phosphorylation of DNA-PKcs on serine 2056 (Fok et al., 2019; Willoughby et al., 2020). Both 53BP1 and γH2AX foci are considered markers of DSBs but are not specific to the inhibition of DNA-PK. Phosphorylation of DNA-PKcs on serine 2056 is specific to human DNA-PKcs and cannot be used in murine tumour models (Willoughby et al., 2020). However, the recent development of an antibody to the murine DNA-PKcs at serine 2053 may be a method of validating the inhibition of DNA-PK activity in mouse models in future studies to fully understand the impact of IR + AZD7648 treatment on tumour and normal tissue repair kinetics (Jiang et al., 2019).

In the oesophageal tolerability study, AZD7648 in combination with fractionated IR was able to elicit histological changes and increased γH2AX levels in the oesophageal epithelium (**Fig. 3.3.7 B & C**). Importantly, these data suggest that the A/J strain may be further developed in future to address the unmet need for clinically relevant IR-induced oesophagitis models. With appropriate modelling of IR combination therapies in the A/J strain, the potential for oesophageal toxicities could be predicted and mitigated against when compounds are used in clinical trials.

3.4. Therapeutic window of ATM and IR in A/J mouse model

3.4.1. Introduction

In the previous chapters, two DDR inhibitors were investigated as potential modulators of the therapeutic window of IR treatment in the A/J model. Another protein involved in the DDR pathway, ataxia-telangiectasia mutated (ATM), is also being studied as a potential anti-cancer treatment as part of a combination therapy (O'Connor, 2015; Weber and Ryan, 2015).

ATM is involved in numerous cellular processes, most notably in cell cycle regulation and DDR signalling (Weber and Ryan, 2015). Defects in the ATM gene were initially discovered as the cause of ataxia-telangiectasia (A-T), an autosomal recessive disorder in humans that leads to several conditions including increased radiosensitivity (Savitsky et al., 1995). Mutations in *ATM* are also commonly found in cases of sporadic cancer including lung adenocarcinoma and chronic lymphocytic leukaemia, and heterozygosity of pathogenic *ATM* variants leads to an increased risk of breast cancer (Choi et al., 2016; Ding et al., 2008; Jerzak et al., 2018; Jin and Oh, 2019; Landau et al., 2013). The radiosensitivity of A-T patients and tumours with ATM deficiencies have led to many further studies of how to target ATM as part of increasing the effectiveness of radiotherapy as a treatment of cancer (Ma et al., 2017).

In cells, ATM exists as inactive homodimers until activated by autophosphorylation on serine 1981 in response to DSBs (Bakkenist and Kastan, 2003). Activated ATM is then recruited to the site of DSBs by the MRE11-RAD50-NBS1 (MRN) complex, which allows for ATM to phosphorylate a number of its downstream targets such as checkpoint kinase 2 (CHK2), p53, KAP1, and H2AX (Choi et al., 2016; Matsuoka et al., 2007; Matsuoka et al., 1998; Shiloh, 2006; Shiloh and Ziv, 2013; Ziv et al., 2006). Phosphorylation of these proteins dictate a cascade of events including checkpoint and cell cycle arrest, chromatin relaxation, and eventual DNA repair (**Fig. 3.4.1**).

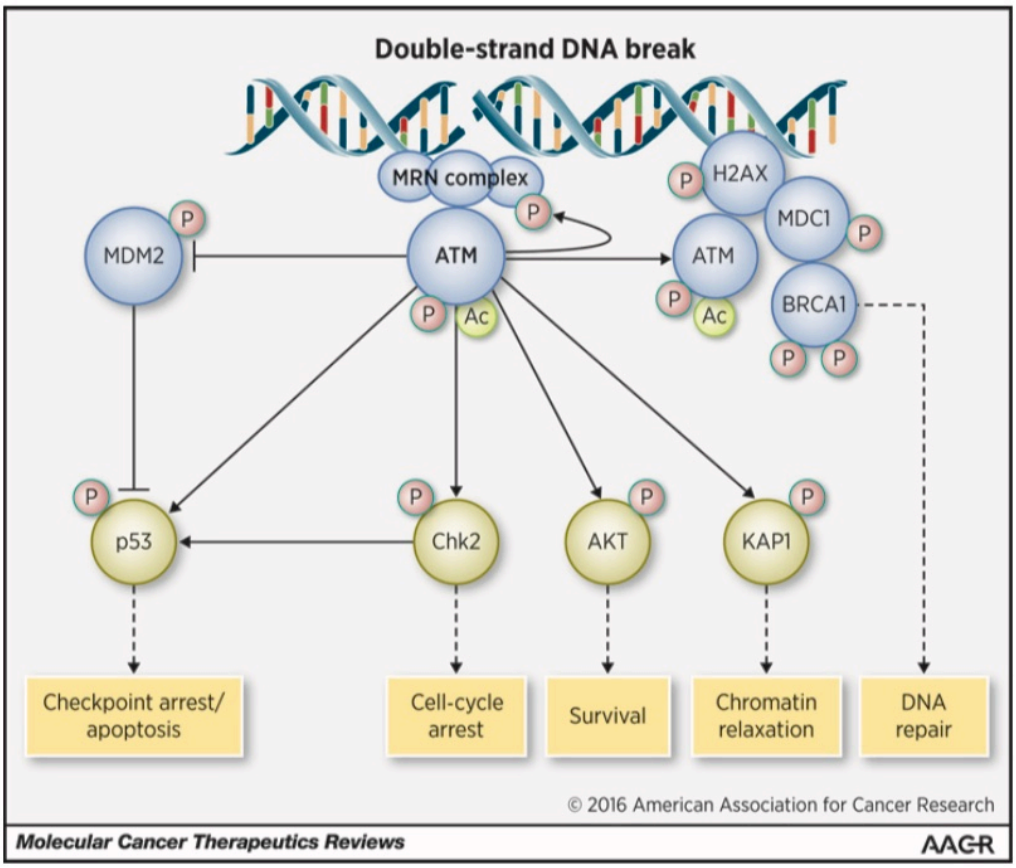

Figure 3.4.1. ATM phosphorylation and induction of DSB response. ATM targets a number of downstream effectors that mediate a highly coordinated response to DNA damage (Reproduced from Choi et al., 2016).

As part of its role in the cell cycle and checkpoint arrest, ATM phosphorylates CHK2 and p53, which is also phosphorylated and stabilised by CHK2 activity (Chehab et al., 2000; Hirao et al., 2000). ATM is also responsible for directly phosphorylating KAP1 at DSB sites, and pKAP1 migrates along the chromatin as part of chromatin relaxation and reorganisation response to damage (White et al., 2006; Ziv et al., 2006). H2AX is phosphorylated on serine 139 primarily by ATM in response to DSBs, allowing activation of the DDR pathways (Burma et al., 2001; Rogakou et al., 1998; Savic et al., 2009). Upon activation of the DDR pathway, other downstream targets of ATM, 53BP1 and BRCA1, also help initiate DNA DSB repair (Cortez et al., 1999; Matsuoka et al., 2007).

Due to the essential nature of ATM in numerous cellular functions and its potent radiosensitisation effect, it is crucial that the impact of ATM inhibition is fully investigated to ensure both the safety and efficacy of combination treatments with IR.

Currently, there are 3 ATM inhibitors in clinical trials being evaluated as either monotherapies or combination therapies (**Table 3.4.1**). AZD0156 and AZD1390, both developed by AstraZeneca, are in phase I dose escalation trials in patients while KU-60019 is being assessed in post-surgical resection renal cancer samples (Jin and Oh, 2019).

ATM inhibitor	Treatment	Cancer type	Phase	Identifier
AZD0156	AZD0156 monotherapy AZD0156 + olaparib AZD0156 + FOLFIRI[1]	Advanced solid tumours	I	NCT02588105
KU-60019	KU-60019 + CX4945 (CHK2 inhibitor)	Renal cancer (organotypic cultures)	N/A	NCT03571438
AZD1390	AZD1390 + radiotherapy	Brain cancer/metastases	I	NCT03423628
	AZD1390 + radiotherapy	NSCLC	I	NCT04550104

Table 3.4.1. ATM inhibitors currently in clinical trials. (Modified from Jin and Oh, 2019).
[1]FOLFIRI is a chemotherapy regimen combination of folinic acid, fluorouracil, and irinotecan.

This chapter focuses on AZD1390, a recently discovered compound (Durant et al., 2018). AZD1390 has an IC_{50} of 0.00078 μM against ATM kinase activity while other closely related PIKKs have IC_{50} values of > 12 μM. Importantly, PET scanning of cynomolgus macaques injected with [^{11}C]-AZD1390 demonstrated promising blood brain barrier penetration of the compound, and a clinical trial in healthy patients (NCT03215381) was able to validate this in humans (Durant et al., 2018; Jucaite et al., 2020). Several *in vitro* and *in vivo* studies by Durant et al. (2018) also confirmed the significant radiosensitisation effect of AZD1390 at different doses ranging between 5 and 20 mg/kg and the potential contribution of p53 mutation to the efficacy of ATM inhibition, observed previously with another ATM inhibitor, KU-60019 (Biddlestone-Thorpe et al., 2013).

In the two ongoing clinical trials (NCT03423628 & NCT04550104), AZD1390 is being combined with radiotherapy to investigate if the radiosensitisation seen in preclinical studies can be translated to patients (Faivre-Finn et al., 2020; Walls et al.,

2020). While there is sufficient supporting evidence for these clinical trials, AZD1390 combined with thoracic radiotherapy has not yet been evaluated in a therapeutic window model that includes both lung cancer and normal tissue effects. The aim of the following chapter is to address the need for understanding the anti-tumour efficacy and normal tissue damage of a combination treatment of IR and AZD1390 in the A/J model (**Fig. 3.4.2**).

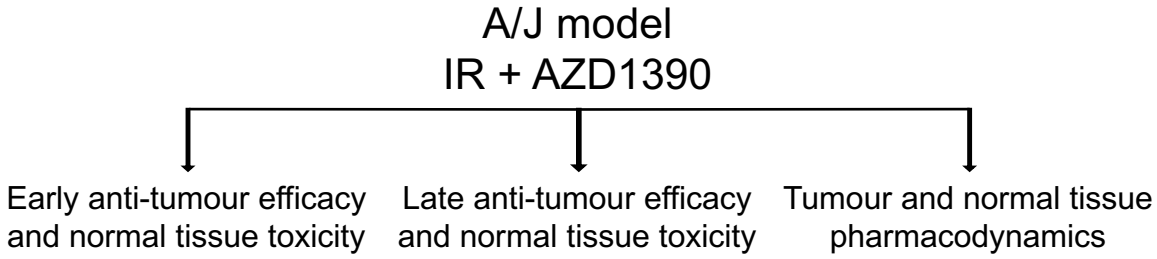

Figure 3.4.2. Main aims and experimental arms.

3.4.2. AZD1390 radiosensitises Calu6 xenograft tumours in CD-1 nude mice

In order to define an effective dose of the ATM inhibitor AZD1390 to use *in vivo*, a subcutaneous xenograft tumour growth model was used. Human lung carcinoma cells (Calu6) were injected into the flank of CD-1 nude mice. Once tumours reached a mean size of 100 mm^3, mice were treated with AZD1390 (either 5 or 20 mg/kg) 1 h before local IR (10 Gy). Tumour growth was measured for up to 42 days after treatment or until tumours reached 400 mm^3 (**Fig. 3.4.3 A**). While tumour growth was slowed with IR treatment alone (n=4), tumours treated with IR + AZD1390 at 20 mg/kg (n=4) showed significant growth inhibition compared with the IR group (**Fig. 3.4.3 B**).

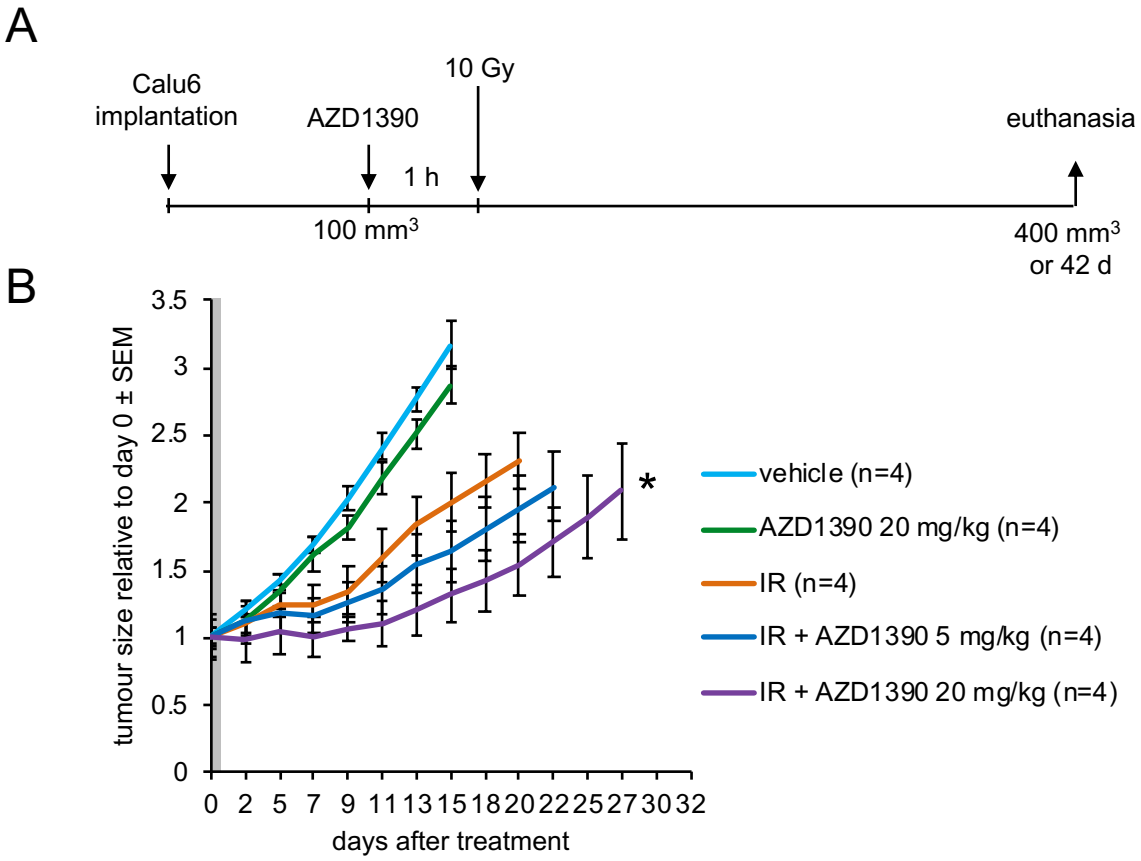

Figure 3.4.3. AZD1390 in combination with IR results in increased tumour growth inhibition in Calu6 xenografts. Calu6 cells (5 x 10^6) were implanted (s.c.) into the flank of CD-1 nude mice. When tumours reached a mean size of 100 mm^3, mice were allocated into groups (n=4 per group) and treated with AZD1390 (5 or 20 mg/kg, p.o.) 1 h before local IR (10 Gy). Tumours were measured 3 times per week. When tumours reached 400 mm^3 or at 42 days after treatment, mice were euthanised, and tumours were collected (A). Tumour growth inhibition (30%) was observed in the IR group compared with the vehicle group on day 15 (B). Tumour growth inhibition (35%) was measured in the IR + AZD1390 20 mg/kg group as compared with the IR group, and there was a significant difference in mean tumour size on day 20. Grey region indicates treatment (unpublished data, Yanyan Jiang).

3.4.3. AZD1390 and fractionated whole thorax IR leads to oesophageal inflammation in A/J mice

To assess the tolerability of AZD1390 at 20 mg/kg in combination with whole thorax IR, a modified early intervention A/J therapeutic window study was used (**Fig. 3.1.12**). A/J mice were allocated into 2 groups. The first group was treated with 5 cycles of AZD1390 (20 mg/kg) 1 h before whole thorax IR (5 Gy), with 2 days between IR doses. A second group was treated with AZD1390 (20 mg/kg) 1 h before whole thorax

IR (13 Gy). The study was planned to end 26 weeks after the first IR dose (**Fig. 3.4.4 A & B**).

Mice treated with fractionated IR + AZD1390 (50 mg/kg) lost approximately 10% body weight after the third treatment cycle and were euthanised early on day 9 because of rapidly declining body weight (**Fig. 3.4.4 C**). Mice treated with single dose IR + AZD1390 (50 mg/kg) had lost greater than 15% body weight on day 9 and therefore were also euthanised at that time point (**Fig. 3.4.4 D**).

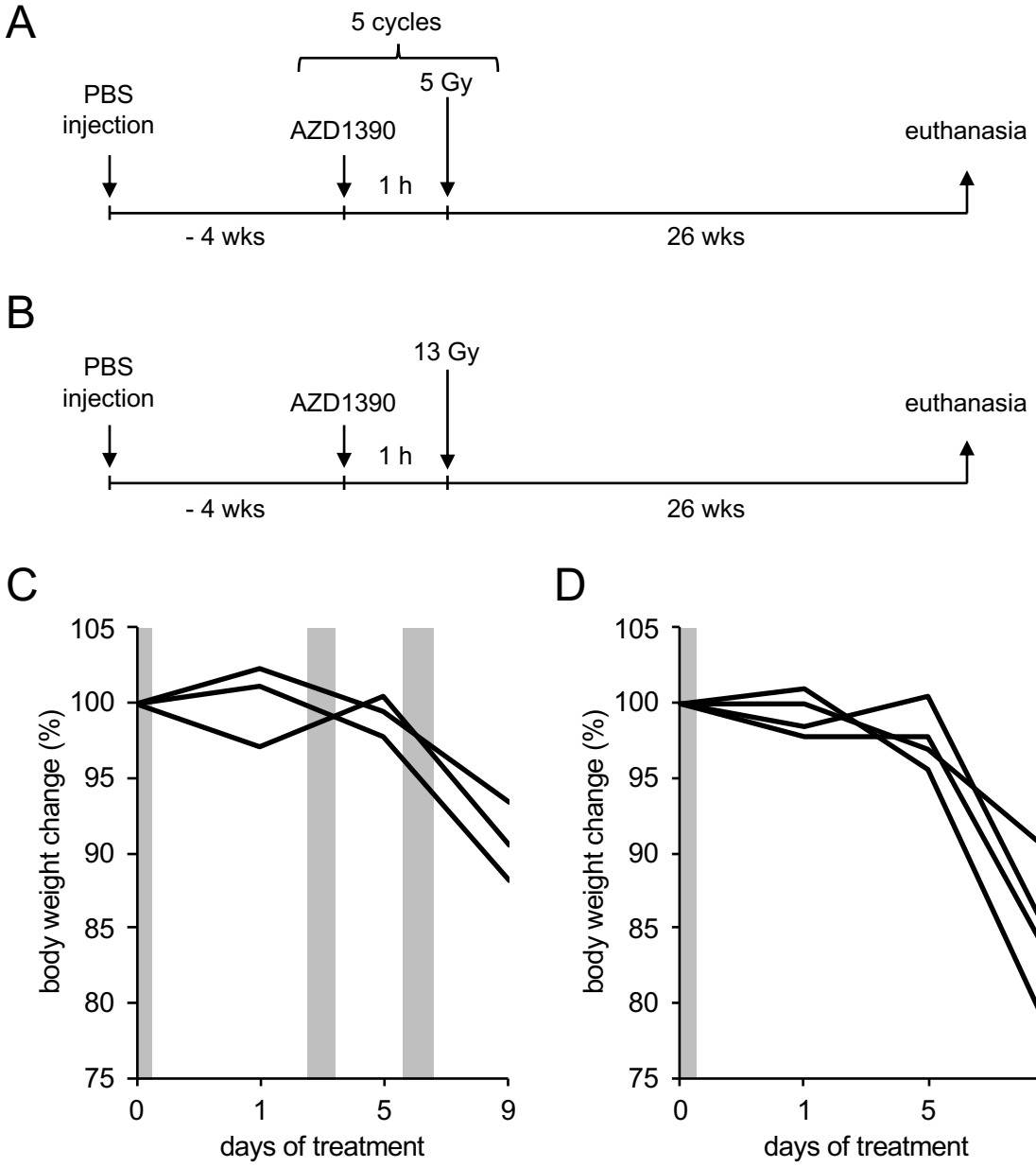

Figure 3.4.4. Whole thorax IR and AZD1390 induced significant body weight loss in A/J mice. A/J mice were injected with PBS (i.p.). After 4 weeks, mice were allocated into two groups. One group (n=3) was treated with 5 cycles of AZD1390 (20 mg/kg, p.o.) 1 h before whole thorax IR (5 Gy), with 2 days between IR doses (A). The second group (n=4) was treated with AZD1390 (20 mg/kg, p.o.) 1 h before whole thorax IR (13 Gy) (B). Euthanasia was planned for 26 weeks after the first IR dose for both groups. All mice in the fractionated IR + AZD1390 group (n=3) lost greater than 10% weight during the treatment cycles and were euthanised after the third cycle of treatment on day 9 (C). All mice in the single dose IR + AZD1390 group (n=4) lost greater than 15% weight and were euthanised on day 9 after treatment (D). Grey bars represent treatment days.

Post mortem results of both groups revealed enlarged oesophagi that showed an increased immune infiltrate and disrupted oesophageal layers when stained by H&E (**Fig. 3.4.5 A**). Further staining by IHC of the marker Ly6G/C identified the infiltrate as

granulocytes/neutrophils (**Fig. 3.4.5 B & C**). These results revealed that AZD1390 (20 mg/kg) combined with whole thorax IR, either 3 fractions of 5 Gy or a single dose of 13 Gy, is not tolerated in A/J mice because it was associated with unacceptable weight loss.

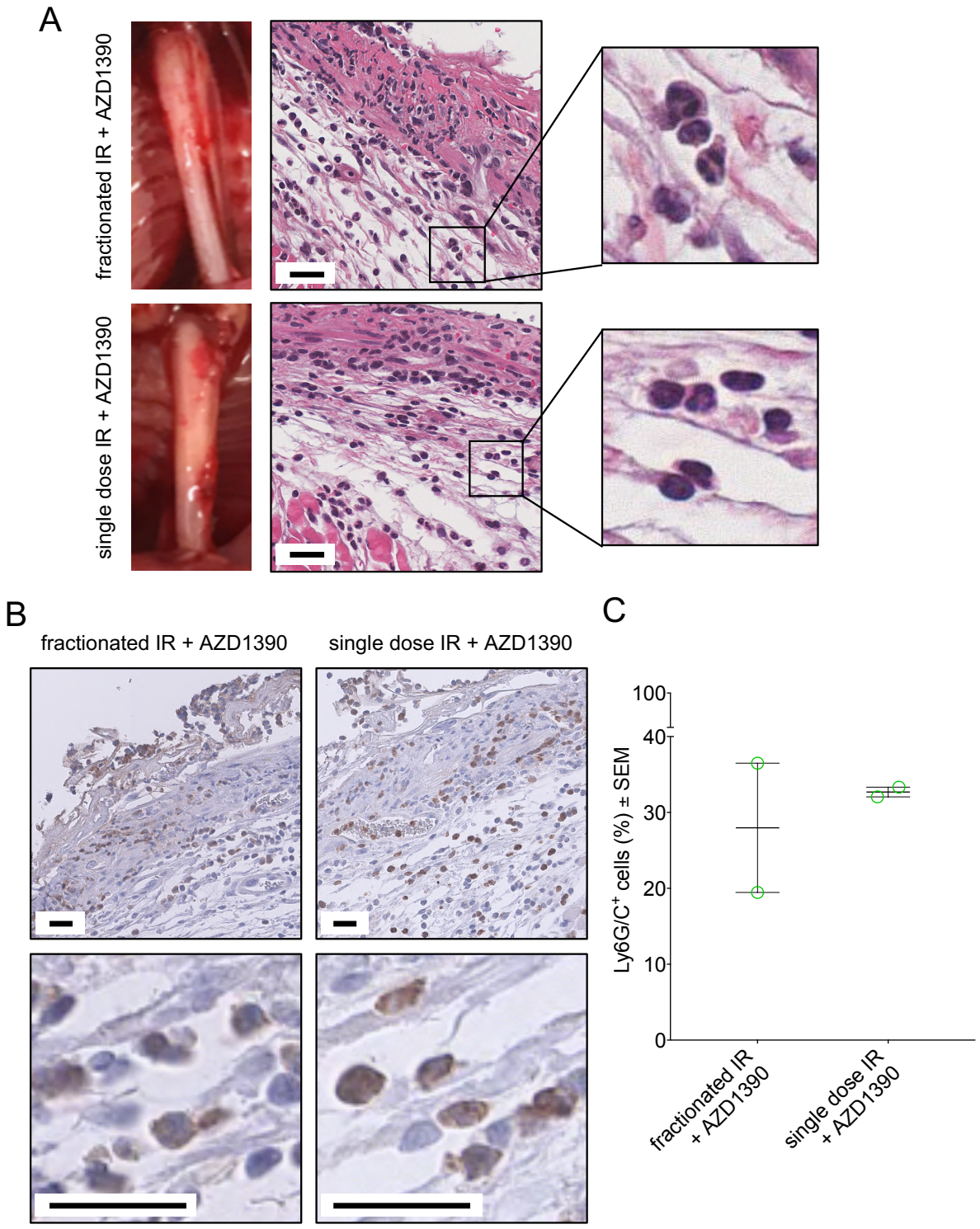

Figure 3.4.5. AZD1390 combined with whole thorax IR results in oesophageal inflammation. Mice treated with either single dose IR + AZD1390 or fractionated IR + AZD1390 had enlarged oesophagi upon euthanasia and displayed a disruption of epithelial cell layers with an immune infiltrate by H&E (A). Infiltrating cells were identified as Ly6G/C-positive (B) and quantified per representative region (C)[1]. We had shown previously that in IR treated and control oesophagi, Ly6G/C-positive staining is low (**Fig. 3.2.5 B & C** and **Fig. 3.3.5 B & C**). All scale bars represent 25 μm and (o) are individual oesophagi.

[1] Mice in the single dose IR + AZD1390 group (2), and fractionated IR + AZD1390 (1) were excluded from quantitative analysis due to insufficient evaluable tissue.

3.4.4. AZD1390 and fractionated hemithorax IR shows limited efficacy and damages normal tissue in A/J early intervention therapeutic window study

The efficacy and tolerability of AZD1390 as a combination treatment with IR was further tested in the tumours and late responding tissues of the A/J model. To decrease the possibility of toxicities of the combination, the hemithorax IR rig was used, avoiding the oesophagus (**Fig. 2.6.1.3**). Additionally, the dose of AZD1390 was reduced to 10 mg/kg, and the study was expanded to include a second AZD1390 combination group using 5 mg/kg to help better define a possible therapeutic window. A/J mice were injected with urethane to initiate tumour growth for 8 weeks before 5 cycles of AZD1390 (5 or 10 mg/kg) 1 h before hemithorax IR (5 Gy), with 2 days between IR doses (**Fig. 3.4.6 A**).

During treatment, all groups lost up to 10% of their pre-treatment body weight but began recovering after treatment (**Fig. 3.4.6 B**). However, at week 4 from the start of treatment, all mice in both IR + AZD1390 groups started losing weight and developed fur loss and mild skin desquamation. Despite intervention with Isaderm and softened food, two individuals from the IR + AZD1390 10 mg/kg group lost 15% weight and were euthanised (JCM193 and JCM194)[1]. Histological analysis of skin was performed by H&E (**Fig. 3.4.6 C**). Comparing the right (exposed to systemic AZD1390 only) and left thorax (IR + AZD1390) skin revealed a clear thickening of the epithelial layer. One mouse (JCM195, IR + AZD1390 10 mg/kg) was euthanised in week 25 due to a spontaneous tumour (see **Fig. 3.4.6** legend). No other mice developed signs of significant weight loss or skin effects during the experiment. During week 26 after the start of treatment, shallow breathing and sporadic coughing was observed in 13 mice, 2 treated with IR ± vehicle, 6 treated with IR + AZD1390 5 mg/kg, and 5 treated with IR + AZD1390 10 mg/kg, and all groups were euthanised.

[1] JCM193 and JCM194 were only included in H&E analysis in Fig. 3.4.7 but no other analyses.

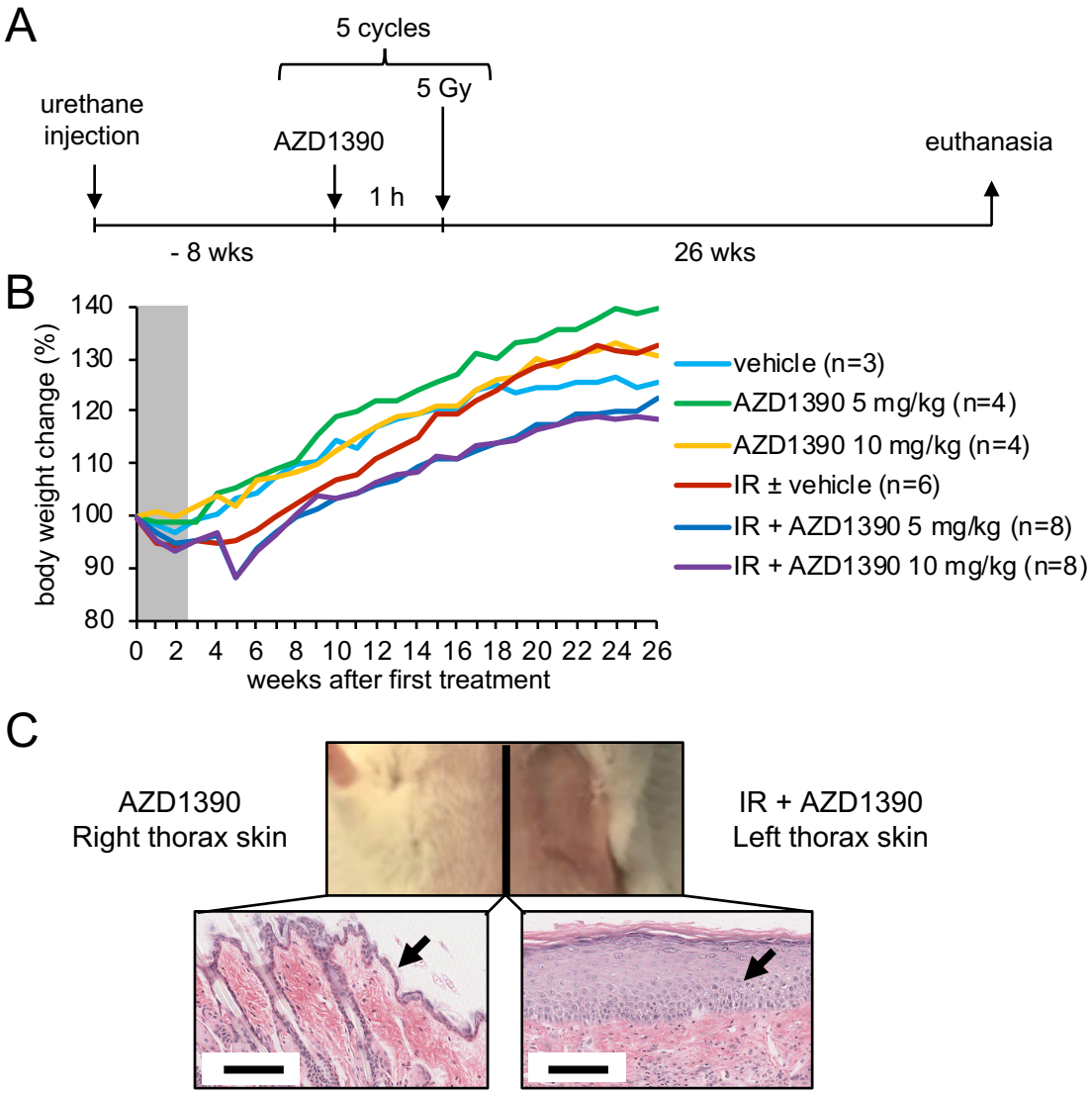

Figure 3.4.6. AZD1390 in combination with hemithorax IR induces body weight loss and skin effects. A/J mice were injected with urethane (10 mg per 10 g body weight, i.p., A). After 8 weeks, mice were allocated into groups (n=3 for vehicle treated, n=4 for both AZD1390 alone groups, n=6 for IR ± vehicle, and n=8 for both IR + AZD1390 groups). Mice were treated with 5 cycles of AZD1390 (5 or 10 mg/kg, p.o.) 1 h before left thorax IR (5 Gy), with 2 days between IR doses. Euthanasia was planned for 26 weeks after the first IR dose. During treatment, all groups showed mild (up to 10%) weight loss but recovered after treatment finished (B). All mice in both IR + AZD1390 groups began losing weight and left thorax fur and showed mild skin desquamation during week 4. Two mice in the IR + AZD1390 10 mg/kg group, JCM193 and JCM194, were euthanised due to 15% weight loss. All other IR + AZD1390 treated mice recovered after a week. At week 25, JCM195 (IR + AZD1390 10 mg/kg) was euthanised due to a rapid breathing rate and 12% body weight loss[1]. Subsequently, each group weight average was adjusted for the remaining mice. Shallow breathing and sporadic coughing were observed in a subset of mice treated with IR ± vehicle (n=2), IR + AZD1390 5 mg/kg (n=6), and IR + AZD1390 10 mg/kg (n=5). All other mice showed no significant weight loss or clinical signs during the study and were euthanised after 26 weeks. H&E staining of JCM193 and JCM194 revealed epithelial thickening (C, arrows) of the left thorax skin as compared with the right thorax in the same mouse. Scale bar represents 100 µm. Grey bar represents treatment cycles.

[1] JCM195 post mortem reveal an enlarged thymus above the lungs and was not included in fibrosis scoring or lung weight analysis.

Superficial tumour counts and histological assessment of lung slices were used to determine the early intervention therapeutic window of AZD1390 combined with IR. Tumour counts revealed no significant difference in treatments when IR ± vehicle (n=6) was compared with either IR + AZD1390 5 mg/kg (n=8) or IR + AZD1390 10 mg/kg (n=5) (**Fig. 3.4.7 A**). Interestingly, no difference was seen between the vehicle control group and IR ± vehicle. A trend of decreased tumour count ratios of the IR + AZD1390 groups was seen when compare to the IR ± vehicle group, but it did not reach significance (**Fig. 3.4.7 B**).

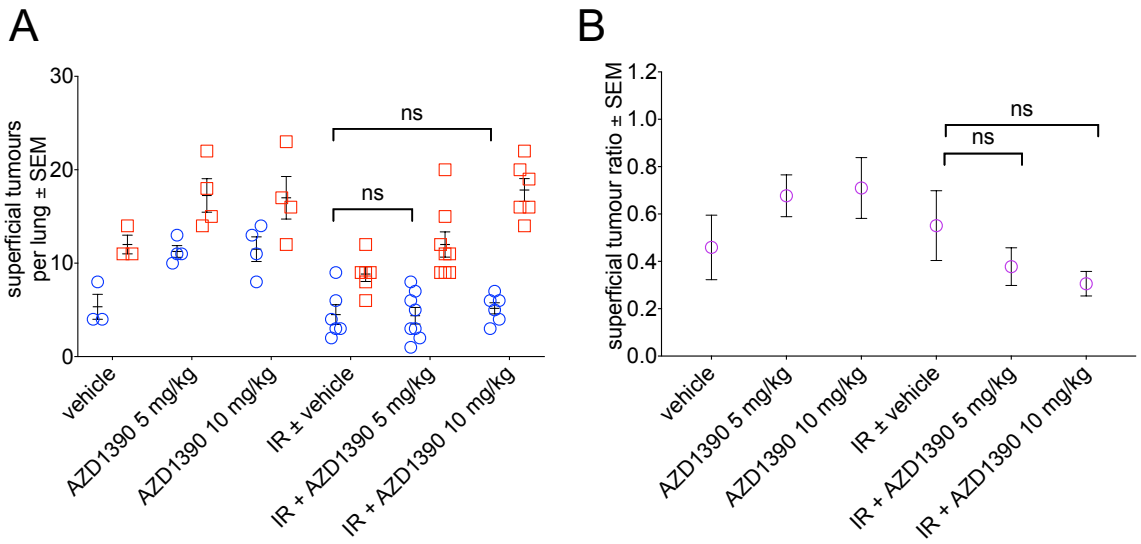

Figure 3.4.7. AZD1390 in combination with hemithorax IR did not reduce superficial tumour counts or ratio compared with hemithorax IR alone. Left lungs treated with IR ± vehicle did not show a difference in superficial tumour counts or tumour count ratio as compared with vehicle alone. Mice in both IR + AZD1390 groups also showed no difference in either tumour counts and count ratio as compared with those treated with IR ± vehicle. (o) are individual left lungs, (□) are individual right lungs, (o) are a ratio of left lung counts divided by right lung counts.

Histological assessment of tumours by H&E did not show a difference in number of tumours or tumour burden in either IR + AZD1390 treatment group as compared with IR ± vehicle (**Fig. 3.4.8 A & B**).

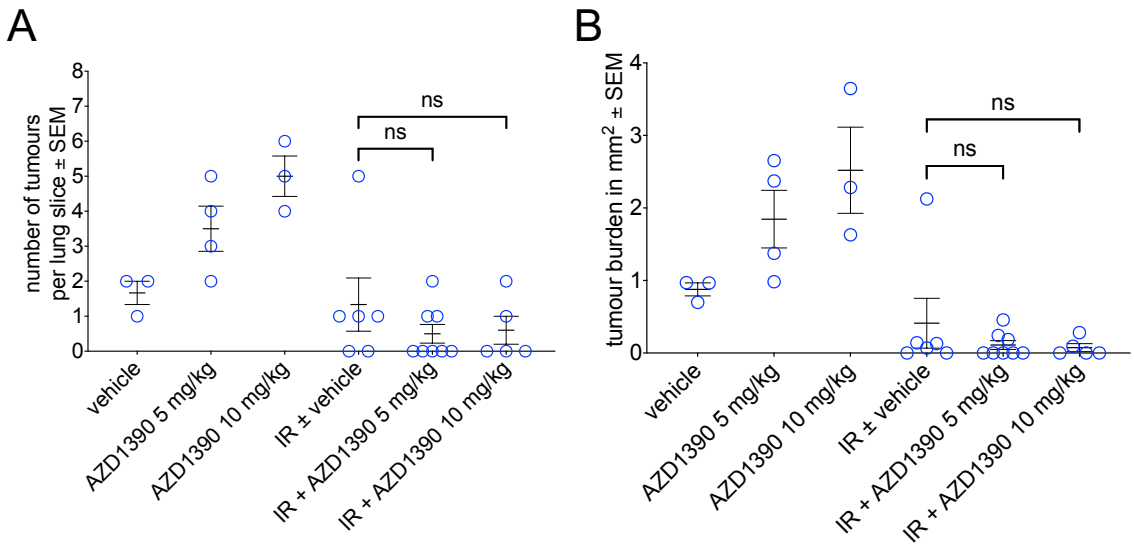

Figure 3.4.8. AZ1390 in combination with hemithorax IR did not reduce tumour numbers or burden compared with hemithorax IR alone. Mice in the IR + AZD1390 groups did not show a reduction in either tumour counts per left lung slice (A) or tumour burden (B) as compared with IR ± vehicle. IR ± vehicle did not show a reduction in either measure compared with vehicle alone. JCM186 (AZD1390 10 mg/kg) was not included in H&E due to a large left lung tumour. (o) are individual left lungs.

Normal tissue effects in the lung were measured by organ weight and Masson's trichrome staining was assessed using the modified Ashcroft scoring (**Chapter 2.16**). No significant difference in lung weight was found between IR groups although a trend of increasing right lung weights and decreasing left lung weights was observed in irradiated left lungs (**Fig. 3.4.9 A**). Fibrosis scoring revealed that while IR ± vehicle increased scores as compared with the vehicle group, treatment with IR + AZD1390 10 mg/kg resulted in a significantly higher fibrosis score compared with IR ± vehicle treatment (**Fig. 3.4.9 B & C**). The fibrosis score of the IR + AZD1390 5 mg/kg group was higher than the IR ± vehicle group, but it did not reach statistical significance.

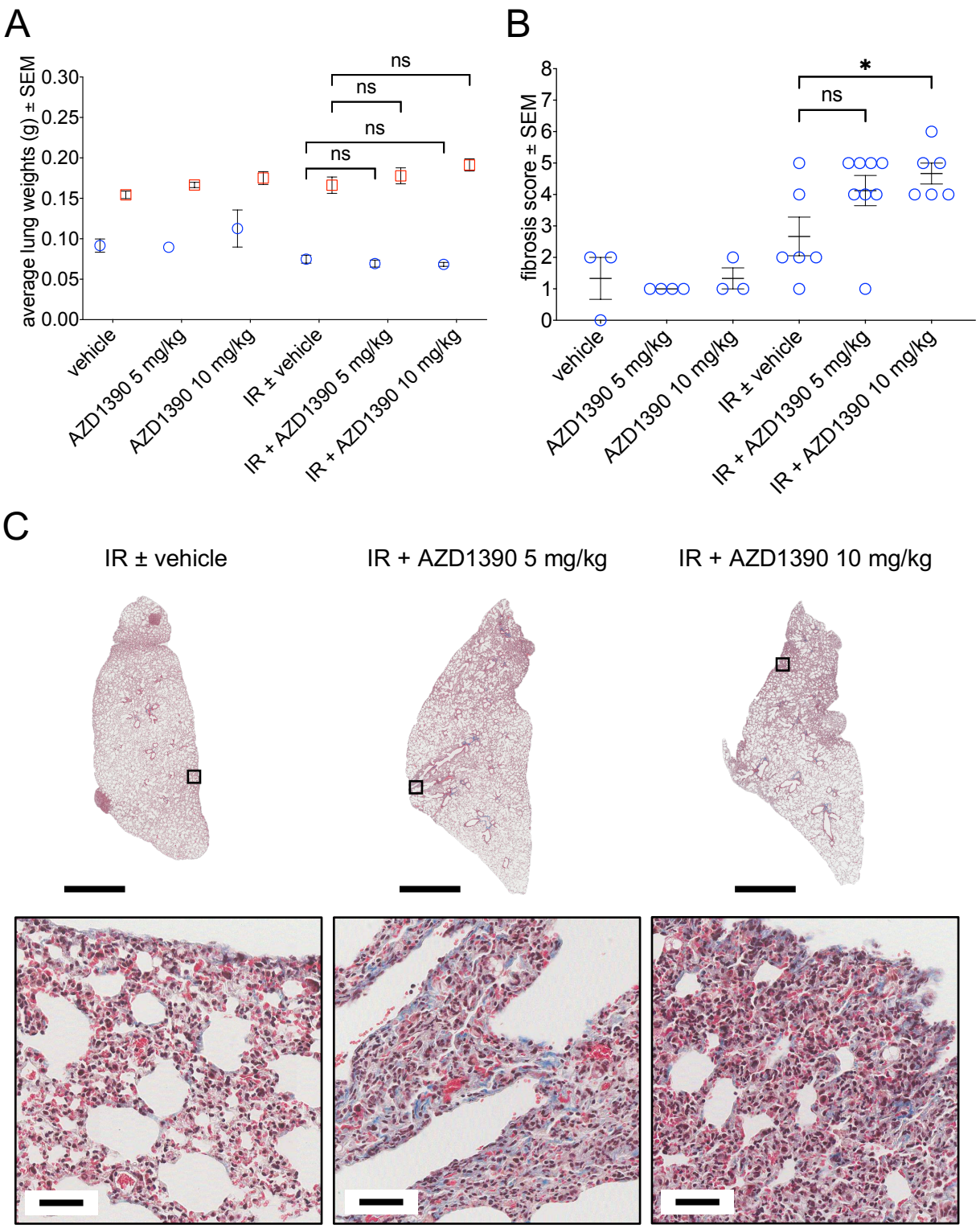

Figure 3.4.9. AZD1390 in combination with hemithorax IR did not alter lung weights but significantly increased fibrosis scores compared with hemithorax IR alone. None of the treatment groups showed significant normal lung tissue effects as measured by lung weight (A). The fibrosis score of the IR + AZD1390 10 mg/kg group was significantly higher compared with IR ± vehicle (B). IR + AZD1390 5 mg/kg did lead to a higher fibrosis score than IR ± vehicle, but it was not statistically significant. (o) are average left lungs, (□) are average right lungs in A. (o) represent individual total lung fibrosis score in B. Scale bars represent 2 mm for whole lung slices and 50 µm for representative image.

These results from the early intervention model suggest that AZD1390 at 10 mg/kg combined with fractionated hemithorax IR shows limited efficacy in the treatment of the early tumours of the A/J model. Additionally, the normal tissues in the field of IR, left thorax skin and left lungs, were also shown to be significantly affected as a result of treatment.

3.4.5. AZD1390 and CT-guided left lung IR is tolerated but shows limited efficacy in A/J late intervention therapeutic window study

To examine the AZD1390 at 10 mg/kg and IR combination treatment further, the late intervention therapeutic window model was used. A/J mice were injected with urethane to initiate tumour growth. After 19 weeks, mice were treated with AZD1390 (10 mg/kg) 1 h before IR (13 Gy) to the left lung using the CT-guided SARRP (**Chapter 2.6.2**). Mice were also imaged by MRI pre-treatment and before euthanasia at 7 weeks after treatment (**Fig. 3.4.10 A**).

No body weight loss was observed in the 7 weeks after treatment. During week 4, two mice in the IR + AZD1390 group (JCM176 and JCM180) were treated with Isaderm for a small skin erosion, which was no longer evident after a week. At week 5, all animals treated with IR + AZD1390 lost a small patch of fur (approximately 8 x 8 mm) on the dorsal and ventral side of the left thorax, but there was no evidence of further skin erosions. The study ended as planned after 7 weeks (**Fig. 3.4.10 B**).

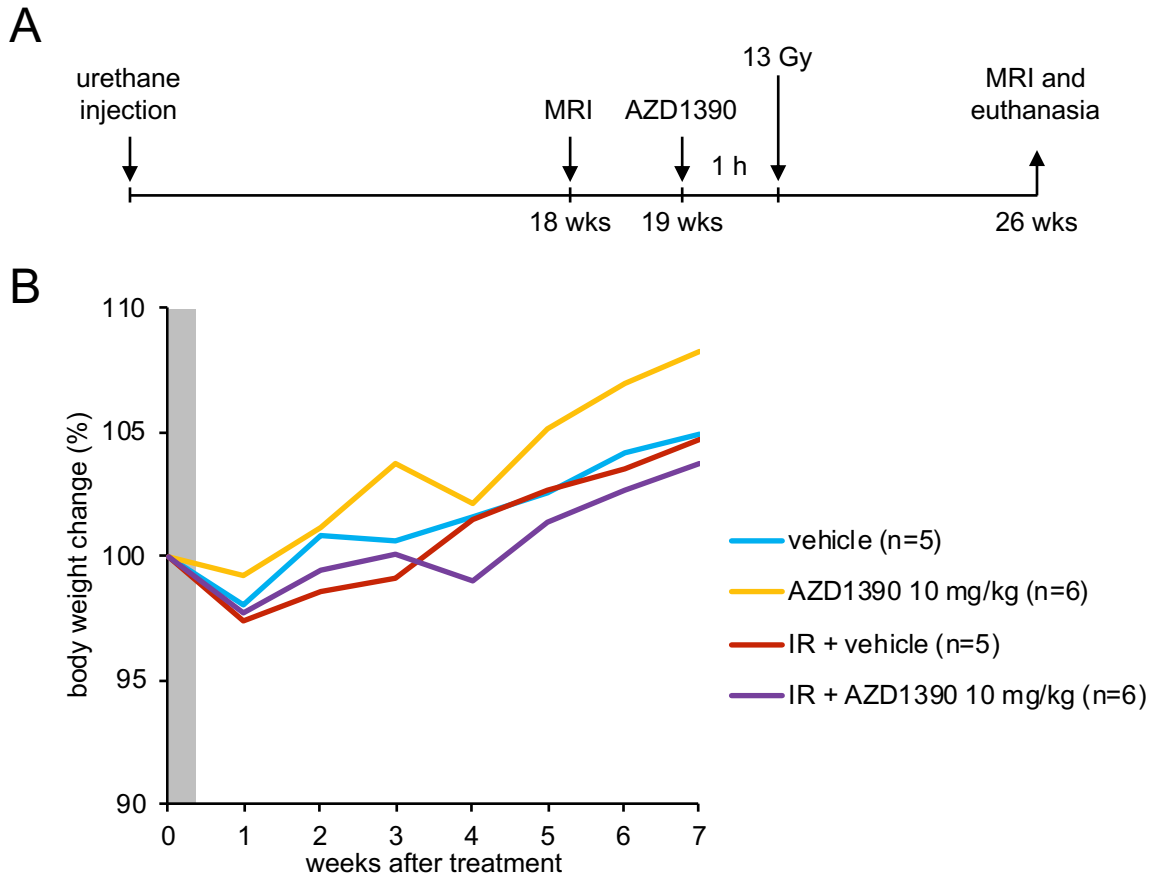

Figure 3.4.10. AZD1390 in combination with CT-guided left lung IR did not induce body weight loss. A/J mice were injected with urethane (10 mg per 10 g body weight, i.p., A). After 18 weeks, mice were allocated into groups (n=5 for vehicle and IR + vehicle groups, n=6 for AZD1390 and IR + AZD1390 groups) and were imaged using MRI. During week 19, mice were treated with a single dose of AZD1390 (10 mg/kg, p.o.) 1 h before left lung IR (13 Gy). Mice were imaged using MRI before euthanasia during week 26. All groups showed no significant weight loss during the study and were euthanised 7 weeks after treatment (B). Grey bar represents treatment.

Superficial counts of left lungs showed no significant difference in the number of tumours between the IR + vehicle (n=5) and the IR + AZD1390 (n=6) groups (**Fig. 3.4.11 A**). The tumour count ratio between left to right lungs of the IR + AZD1390 group increased compared with the IR + vehicle group (**Fig. 3.4.11 B**).

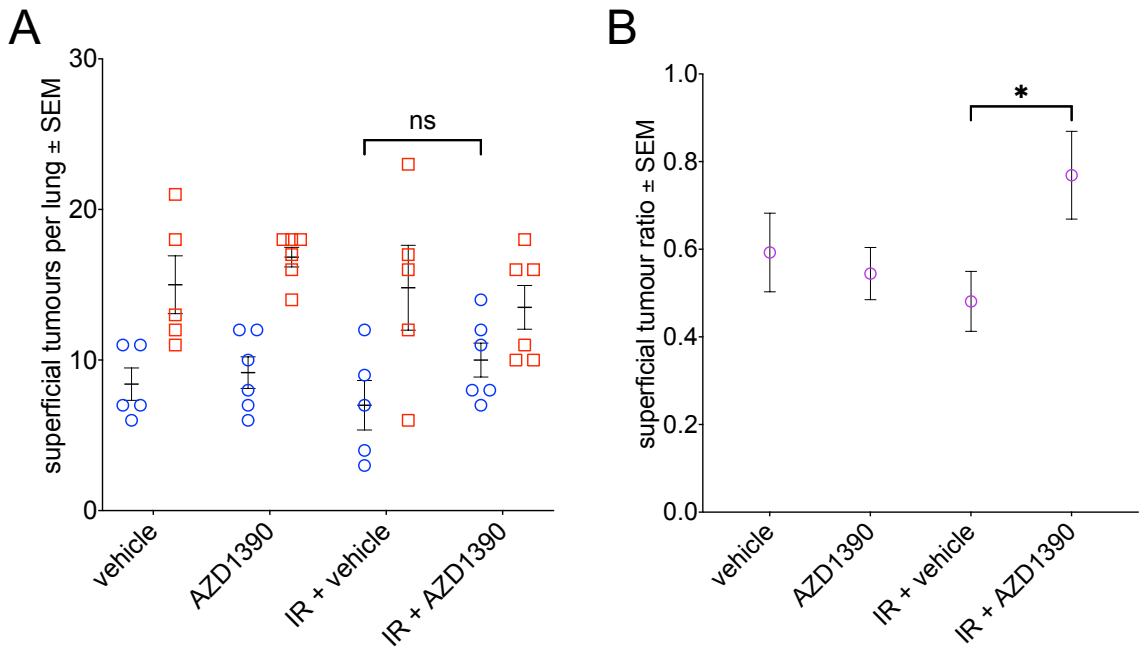

Figure 3.4.11. AZD1390 in combination with CT-guided left lung IR did not reduce superficial tumour counts and increased tumour ratio. Left lungs of mice treated with IR + AZD1390 did not show a significant change in tumour counts as compared with IR + vehicle (A). The tumour count ratio of individuals treated with IR + AZD1390 increased (B). (o) are individual left lungs, (□) are individual right lungs, (o) are a ratio of left lung counts divided by right lung counts.

A trend of decreasing tumour numbers per lung slice and tumour burden was observed in the IR + vehicle compared with the vehicle group, but it did not reach statistical significance for either measure (**Fig. 3.4.12 A & B**). Interestingly, a slight increase was seen for the IR + AZD1390 as compared with the IR + vehicle group in both measures, but this also did not reach statistical significance (**Fig. 3.4.12 A & B**).

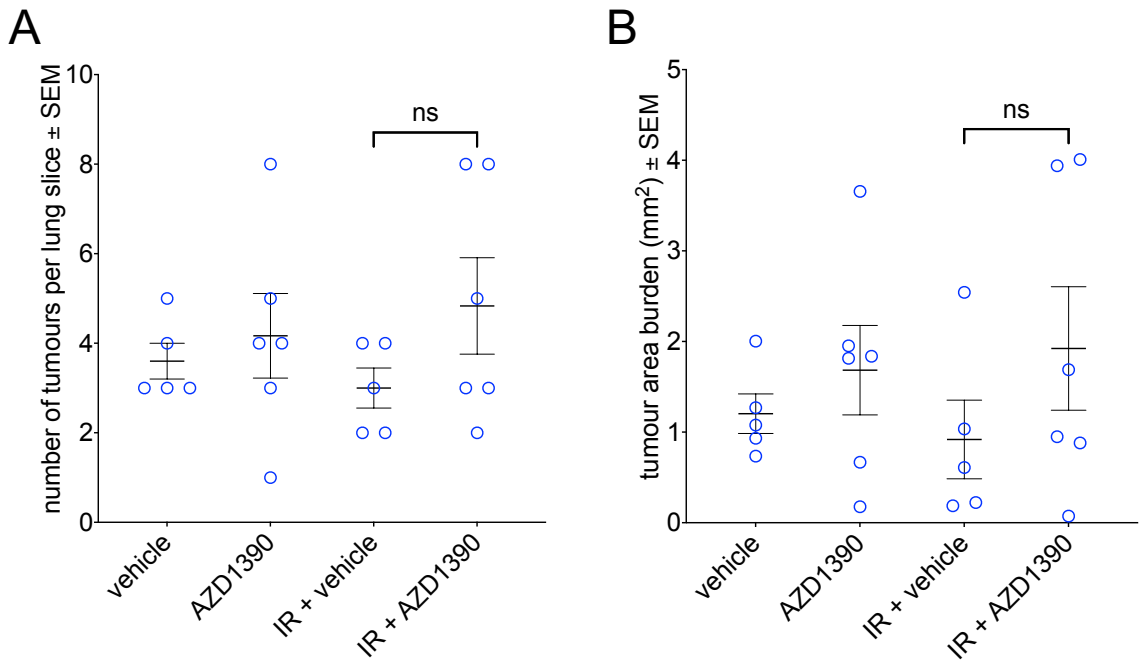

Figure 3.4.12. AZD1390 in combination with CT-guided left lung IR did not reduce tumour numbers or area per lung slice. IR + AZD1390 treatment of left lungs did not show a reduction in either tumour number per left lung slice (A) or tumour area burden (B) as compared with IR + vehicle. (o) are individual left lungs.

Total left lung tumour volume changes from pre-treatment to week 7 were assessed using MRI (**Fig. 3.4.13 A & B**). The total left lung tumour volume changes were similar for mice treated with either IR + vehicle or IR + AZD1390.

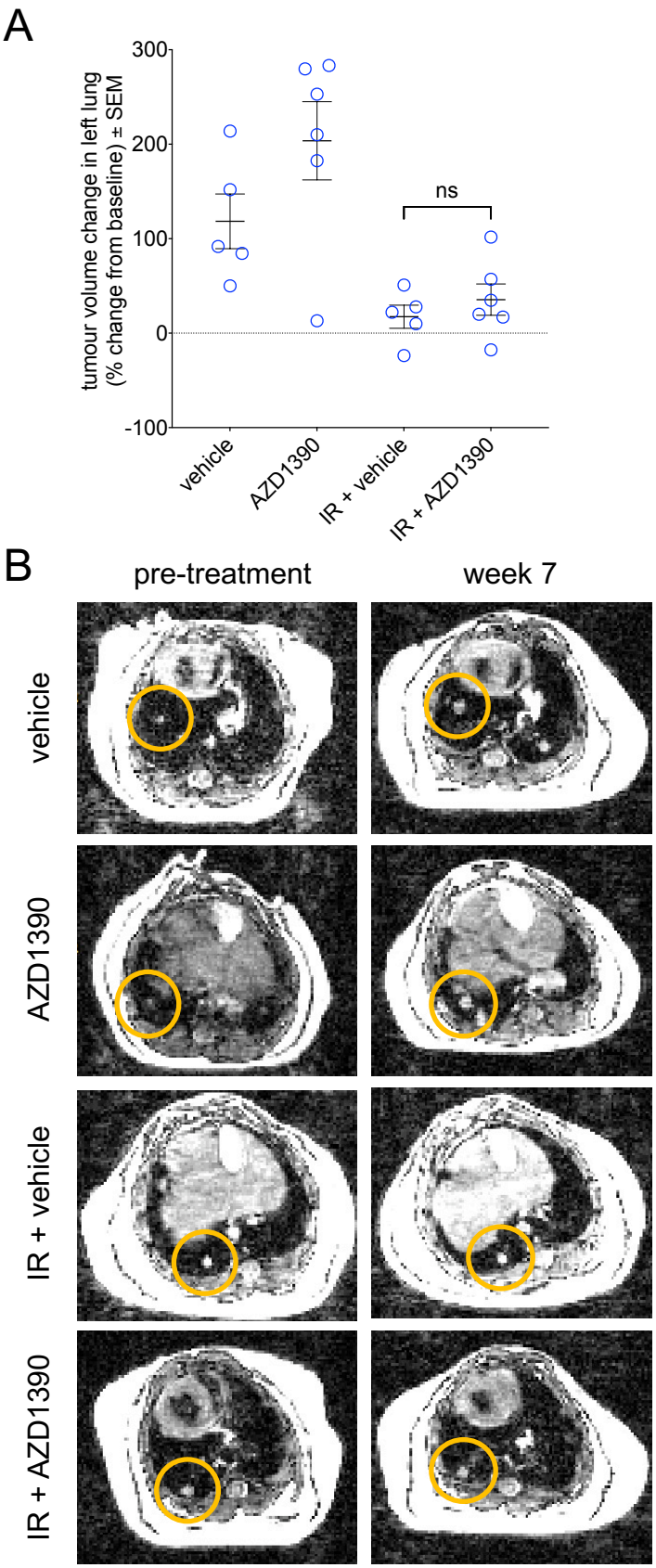

Figure 3.4.13. AZD1390 in combination with CT-guided left lung IR did not affect MRI tumour volume change compared with IR alone. Total left lung tumour volume changes of mice treated with IR + AZD1390 were similar to mice treated with IR + vehicle (A). Representative axial MR images of the mouse chest with tumours circled in yellow (B). (o) are individual left lung tumour volume changes from baseline (pre-treatment) to week 7.

Lung weights and H&E staining revealed no increase in normal lung tissue effects by gross pathology or histology (**Fig. 3.4.14 A & B**).

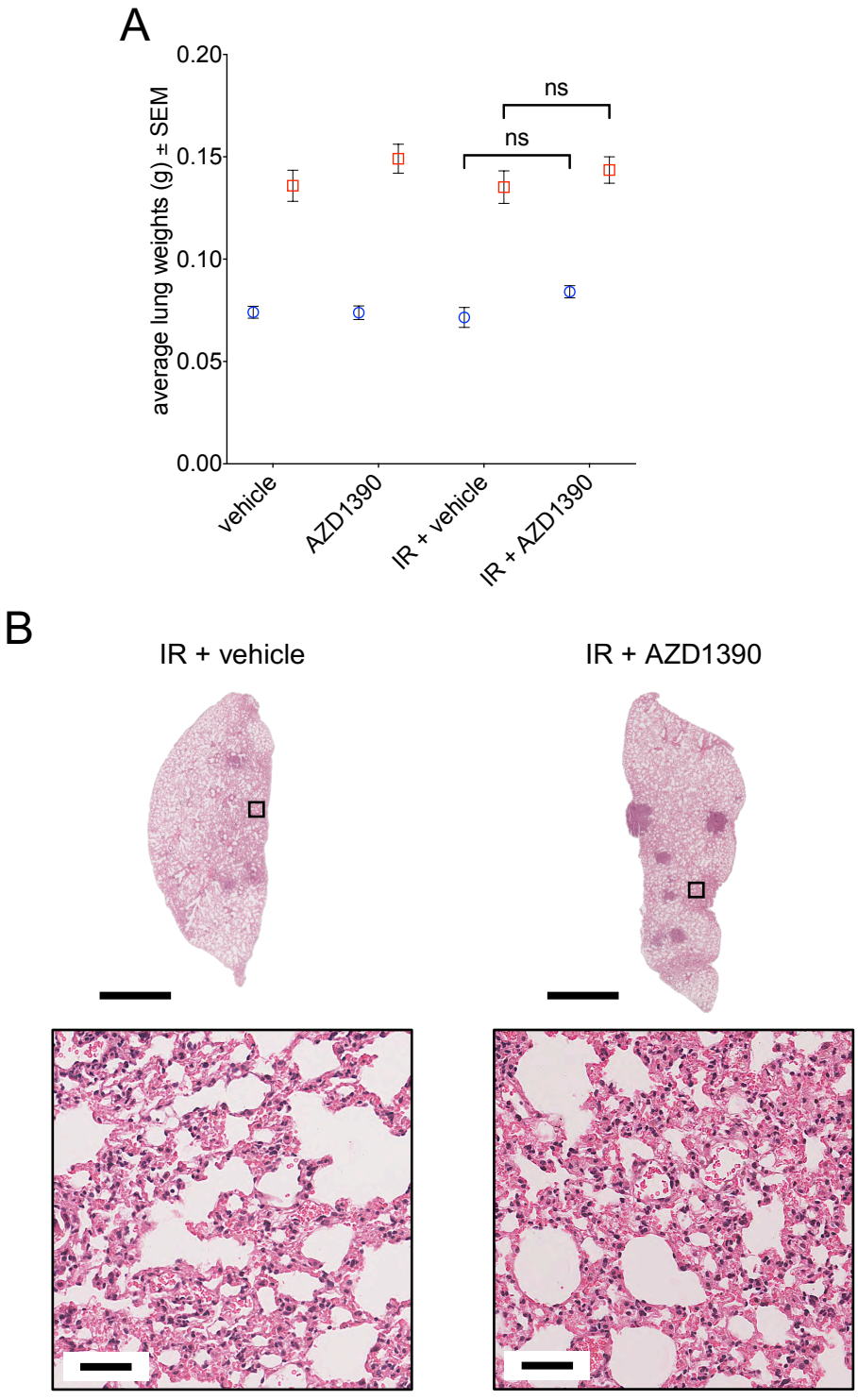

Figure 3.4.14. AZ1390 in combination with CT-guided left lung IR did not affect lung weight or histology. None of the treatment groups showed significant normal lung tissue effects as measured by lung weight (A) or by H&E staining (B). (o) are average left lungs, (□) are average right lungs. Scale bars represent 2 mm for whole lung slices and 50 μm for representative image.

Together, these results suggest that AZ1390 at 10 mg/kg is not able to modulate the effect of IR on established tumours of the A/J model in 7 weeks.

3.4.6. Pharmacodynamics of AZD1390 at 10 mg/kg combined with IR significantly decreases γH2AX levels in bronchial epithelial cells but not lung tumours or oesophageal epithelium

A PD study was also used to analyse tissue responses to the combination treatment of AZ1390 and IR in the A/J model over 24 h. A/J mice were injected with urethane to initiate tumour growth. After 18 weeks, mice were treated with AZ1390 (10 mg/kg) 1 h before IR (13 Gy) to the whole thorax (**Fig. 2.6.1.2**). Mice were euthanised at 2 and 24 h after IR (**Fig. 3.4.15 A**). IHC of γH2AX levels in cells was used to assess tumour response to IR and AZD1390. Two hours after IR, tumours in both IR + vehicle (n=5) and IR + AZD1390 (n=2) showed an increase in the percentage of γH2AX-positive cells as measured by IHC. Those treated with IR + vehicle had a higher percentage of γH2AX positive cells than the combination, but this difference was not significant (**Fig. 3.4.15 B & D**). After 24 h, the percentage of γH2AX-positive cells was lower in both IR + vehicle (n=7) and IR + AZD1390 (n=1), and there was no difference between IR treatment groups (**Fig. 3.4.15 C & D**).

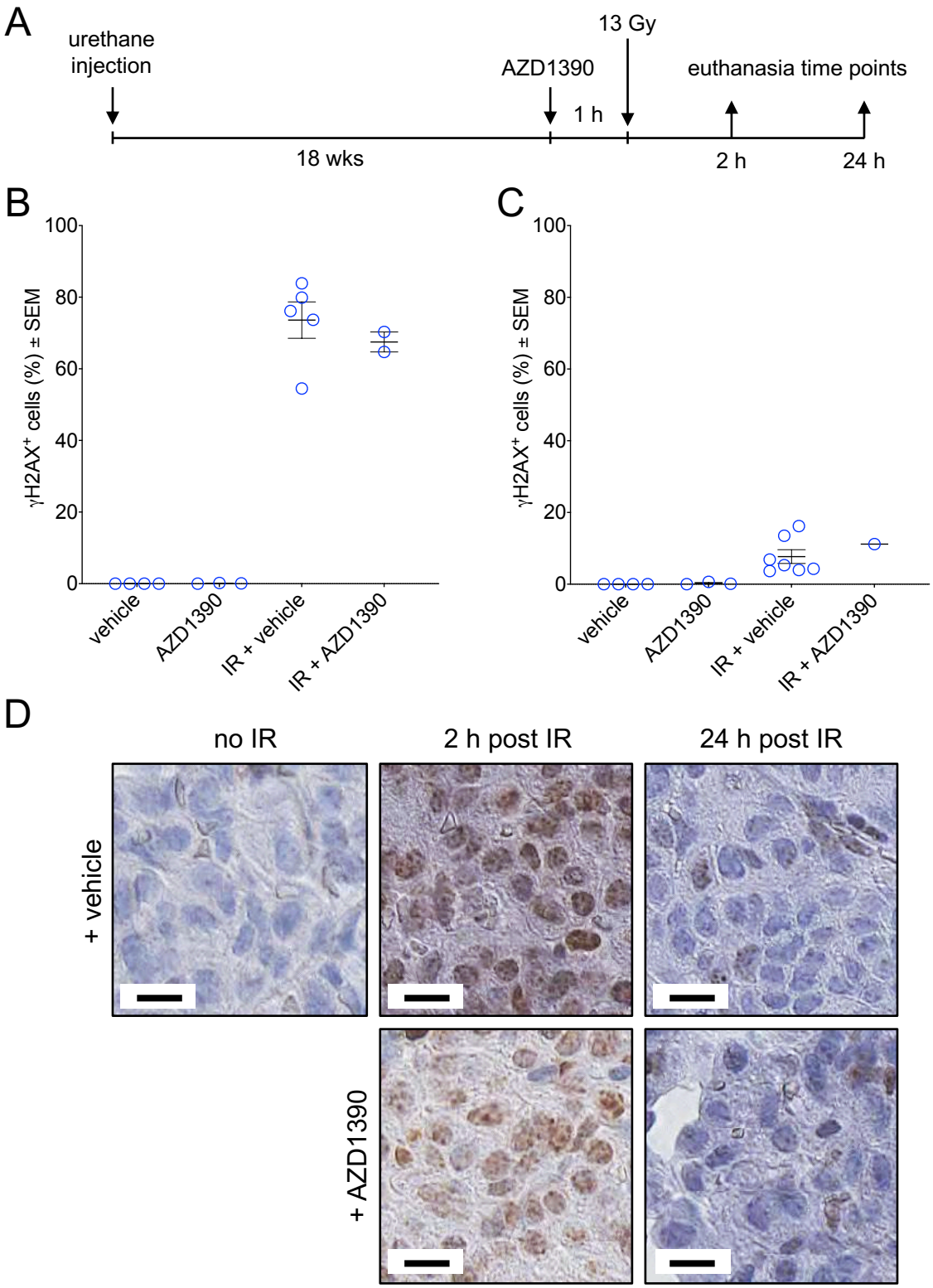

Figure 3.4.15. AZD1390 in combination with IR did not affect γH2AX levels compared with IR alone in tumours. A/J mice were injected with urethane (10 mg per 10 g body weight, i.p., A). After 18 weeks, mice were allocated into groups (n=3 for vehicle, n=6 for IR + vehicle and AZD1390, and IR + AZD1390). At week 18, mice were treated with a single dose of AZD1390 (10 mg/kg, p.o.) 1 h before whole thorax IR (13 Gy). Mice were euthanised at 2 and 24 h after IR. γH2AX levels in tumours treated with IR + AZD1390 were similar to IR + vehicle control γH2AX levels after 2 h (B) and 24 h (C). IHC of representative γH2AX levels in lung tumours (D). (o) are individual tumours. Scale bars represent 10 μm.

The effects of treatment on the percentage of γH2AX-positive cells was also measured in bronchial and oesophageal epithelial tissue. Four categories were used for counting γH2AX positive cells: (i) clear, separated foci, (ii) abundant distinct but overlapping foci, (iii) faint pan-nuclear staining, and (iv) dark pan-nuclear staining (**Fig. 2.16.1**). At 2 h after IR + vehicle treatment, the majority of bronchial epithelial cells (> 90%) displayed overlapping γH2AX foci (**Fig. 3.4.16 A & C**). Interestingly, the IR + AZD1390 treated bronchial epithelium had a lower percentage of cells with overlapping foci and a higher percentage of cells with clear, separated foci than the IR + vehicle group (**Fig. 3.4.16 A & C**). After 24 h, γH2AX levels in cells treated with IR were similar across all categories (**Fig. 3.4.16 B & C**). Neither pan-nuclear γH2AX measure was significantly increased at either time point for any treatment.

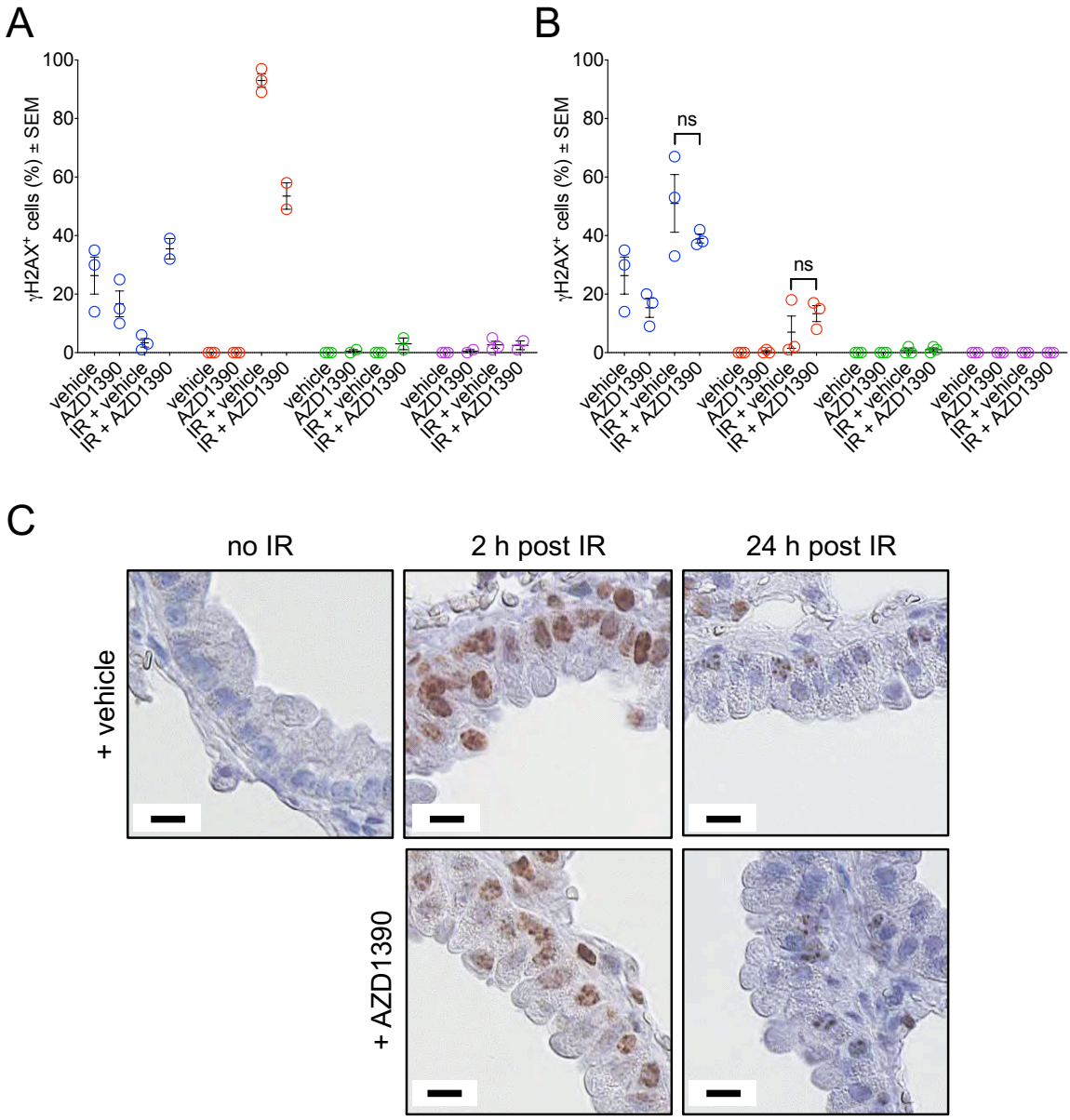

Figure 3.4.16. AZD1390 altered IR-induced γH2AX levels in bronchial epithelial cells. Bronchial epithelial cells of lungs treated with IR + vehicle showed an increase in the percentage of cells with overlapping γH2AX foci after 2 h (A). Treatment with IR + AZD1390 displayed a lower percentage of cells with overlapping γH2AX foci and a higher percentage of cells with clear, separated foci at 2 h as compared with IR + vehicle. After 24 h, both IR-treated groups had similar levels of clear, separated γH2AX foci (B). IHC of representative γH2AX staining in bronchial epithelial cells[1] (C). Circles are individual mice and (o) is clear, separated foci, (o) is abundant distinct but overlapping foci, (o) is faint pan-nuclear staining, (o) is dark pan-nuclear staining. Scale bars represent 10 μm.

In the epithelium of the oesophagus, treatment with IR + AZD1390 or IR + vehicle both resulted in a majority of cells (> 70%) with overlapping γH2AX foci at 2 h (**Fig.**

[1] One mouse treated with IR + AZD1390 at 2 h was excluded from quantitative analysis due to insufficient evaluable tissue.

3.4.17 A & C). After 24 h, both the IR + vehicle and IR + AZD1390 groups had more than 30% of cells with clear, separated γH2AX foci with no difference between the groups (**Fig. 3.4.17 B & C**). Neither pan-nuclear γH2AX measure was significantly increased at either time point for any treatment.

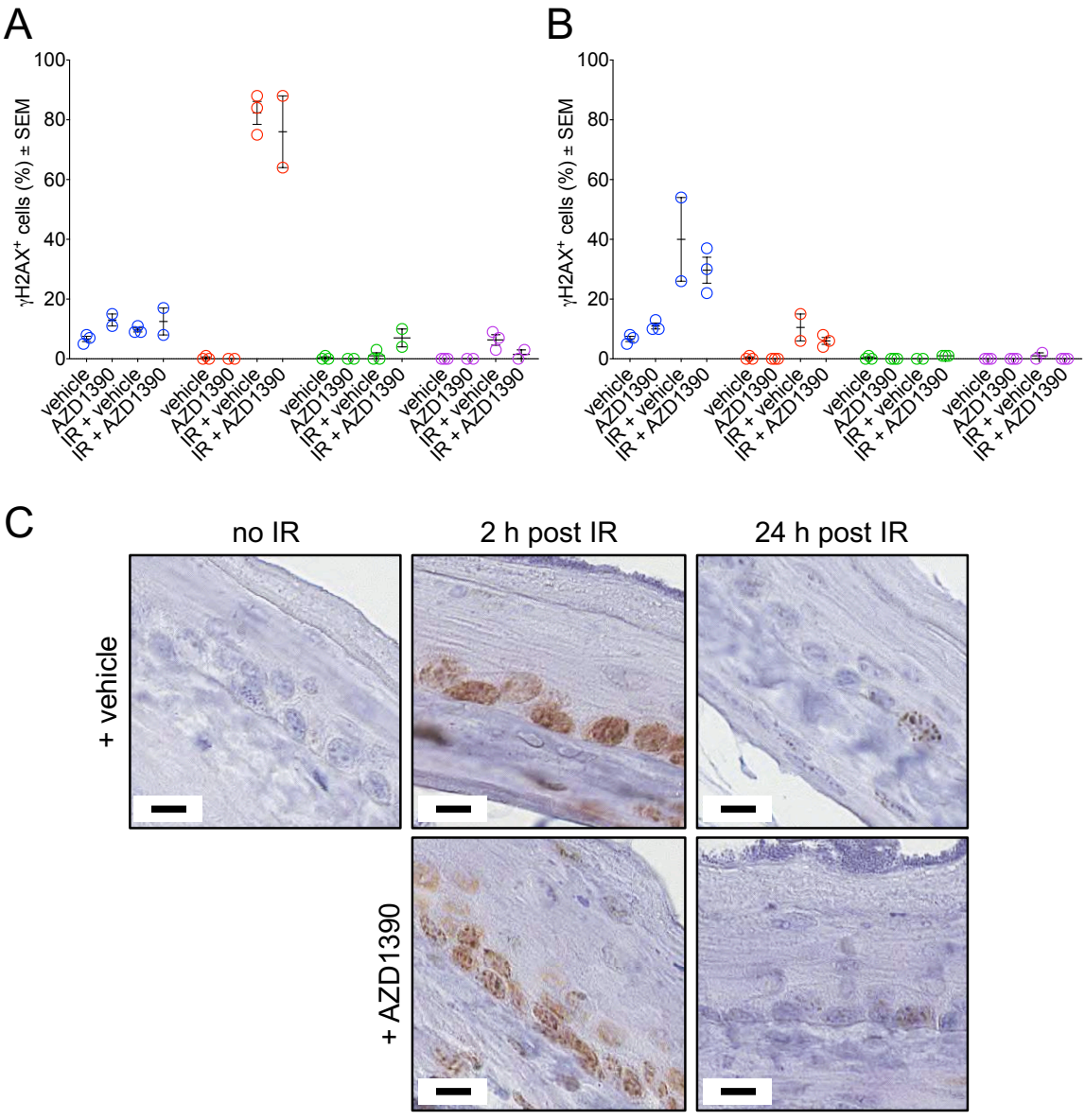

Figure 3.4.17. AZD1390 in combination with IR did not affect γH2AX levels in oesophageal epithelial cells. γH2AX levels in oesophageal epithelial cells treated with IR + AZD1390 was not significantly different when compared with IR + vehicle control after 2 h (A) or 24 h (B). IHC of representative γH2AX staining in oesophageal epithelial cells[1] (C). Circles are individual mice and (o) is clear, separated foci, (o) is abundant distinct but overlapping foci, (o) is faint pan-nuclear staining, (o) is dark pan-nuclear staining. Scale bars represent 10 μm.

[1] Mice treated with IR + AZD1390 at 2 h (1) and IR + vehicle at 24 h (1) were excluded from quantitative analysis due to insufficient evaluable tissue.

These data suggest that while AZD1390 at 10 mg/kg combined with 13 Gy does not affect the percentage of γH2AX-positive cells in tumours or the oesophageal epithelium as compared with IR alone at either time point, in A/J bronchial epithelial cells, the combination treatment does lead to a lower percentage of cells containing abundant distinct but overlapping γH2AX foci at 2 h after treatment.

3.4.7. Pharmacodynamics of AZD1390 at 10 mg/kg combined with IR decreases pKAP1 in tumours but not in bronchial or oesophageal epithelial cells

Phosphorylation of KAP1 on serine 824 was used as a second marker of tissue responses to IR and AZD1390 as measured by IHC. At 2 h after IR, tumours treated with IR + AZD1390 (n=3) had a significantly lower number of pKAP1 positive cells than those treated by IR + vehicle (n=5) (**Fig. 3.4.18 A & C**). This difference in pKAP1 between IR + AZD1390 (n=2) and IR + vehicle (n=8) was not apparent after 24 h (**Fig. 3.4.18 B & C**).

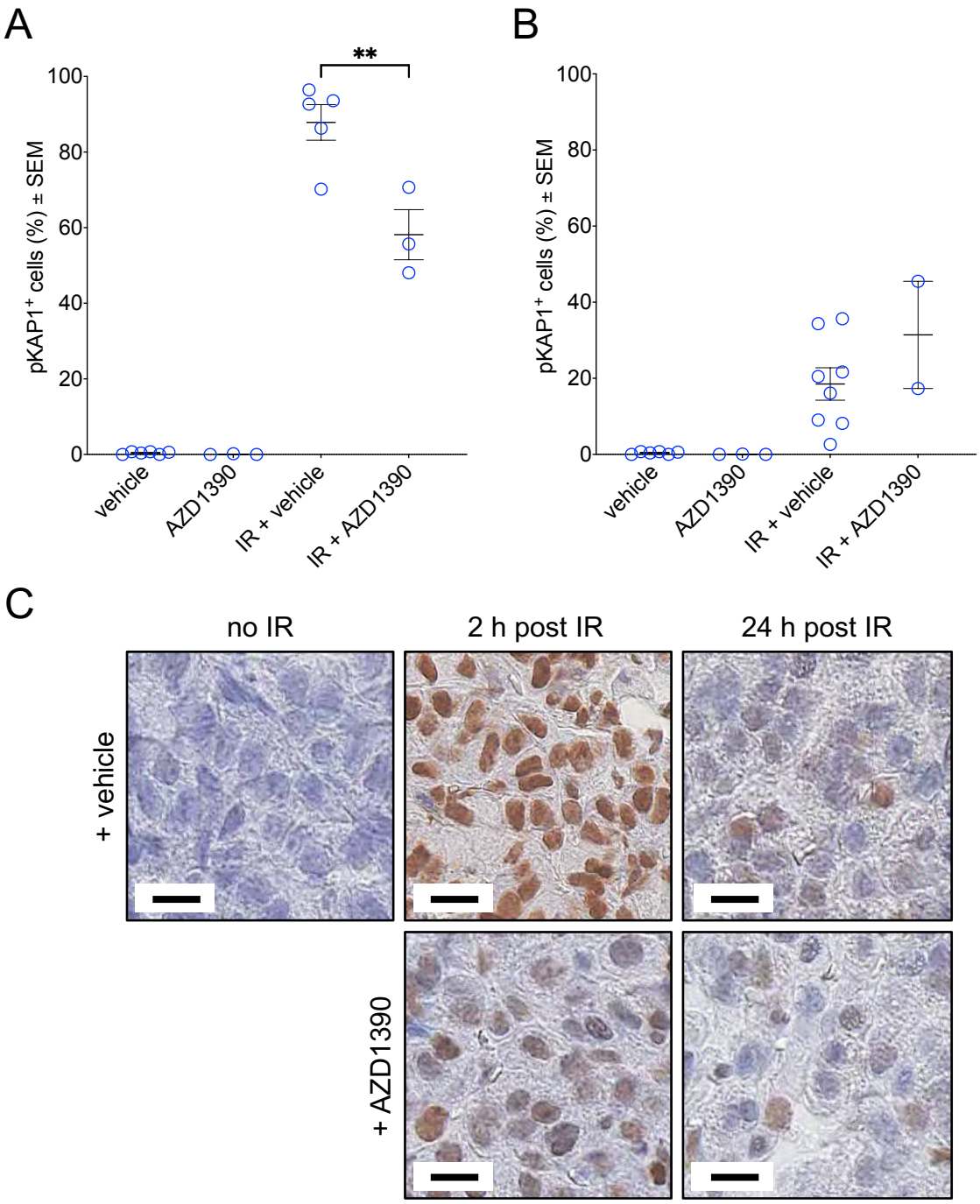

Figure 3.4.18. AZD1390 in combination with IR decreased the percentage of pKAP1-positive cells in tumours. KAP1 phosphorylation on serine 824 in tumours treated with IR + AZD1390 was significantly decreased compared with IR + vehicle control after 2 h (A). After 24 h, both IR groups showed a similar level of pKAP1 (B). IHC of representative pKAP1 ser824 levels in lung tumours (C). (o) are individual tumours. Scale bars represent 10 µm.

KAP1 phosphorylation in the bronchial and oesophageal epithelium was also examined. At both time points after IR, the percentage of pKAP1-positive cells in the bronchial epithelium treated with IR + vehicle and IR + AZD1390 were similar (**Fig. 3.4.19 A-C**).

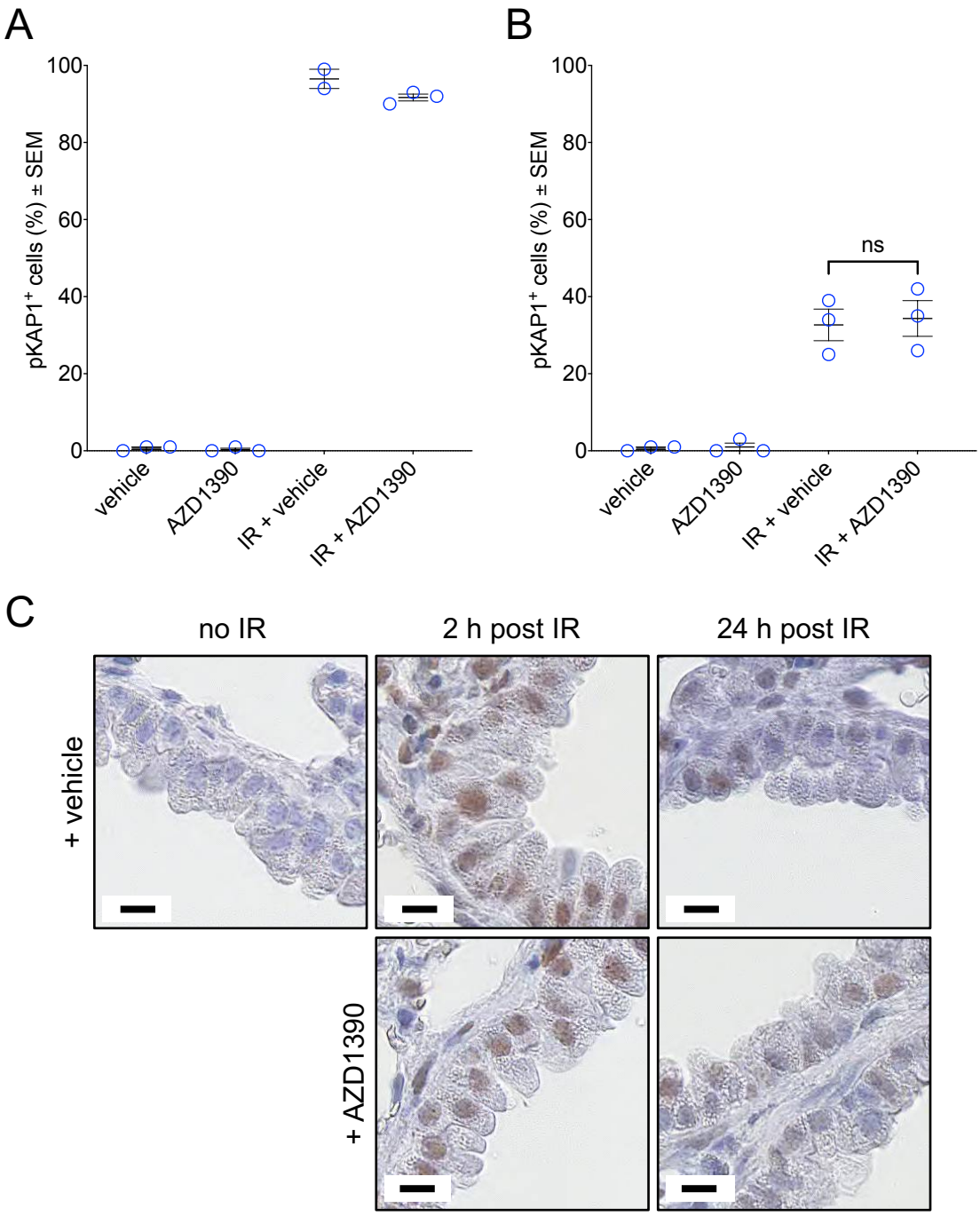

Figure 3.4.19. AZD1390 in combination with IR did not affect pKAP1 levels in bronchial epithelial cells. Levels of KAP1 ser824 phosphorylation in oesophageal epithelial cells treated with IR + AZD1390 was not significantly increased compared with IR + vehicle control after 2 h (A) or 24 h (B). IHC of representative KAP1 ser824 levels in bronchial epithelial cells[1] (C). (o) indicate individual mice. Scale bars represent 10 µm.

[1] One mouse treated with IR + vehicle at 2 h was excluded from quantitative analysis due to insufficient evaluable tissue.

In the oesophageal epithelium at 2 h and 24 h after IR, cells treated with IR + AZD1390 showed similar percentages of pKAP1-positive cells as compared with IR + vehicle (**Fig. 3.4.20 A-C**).

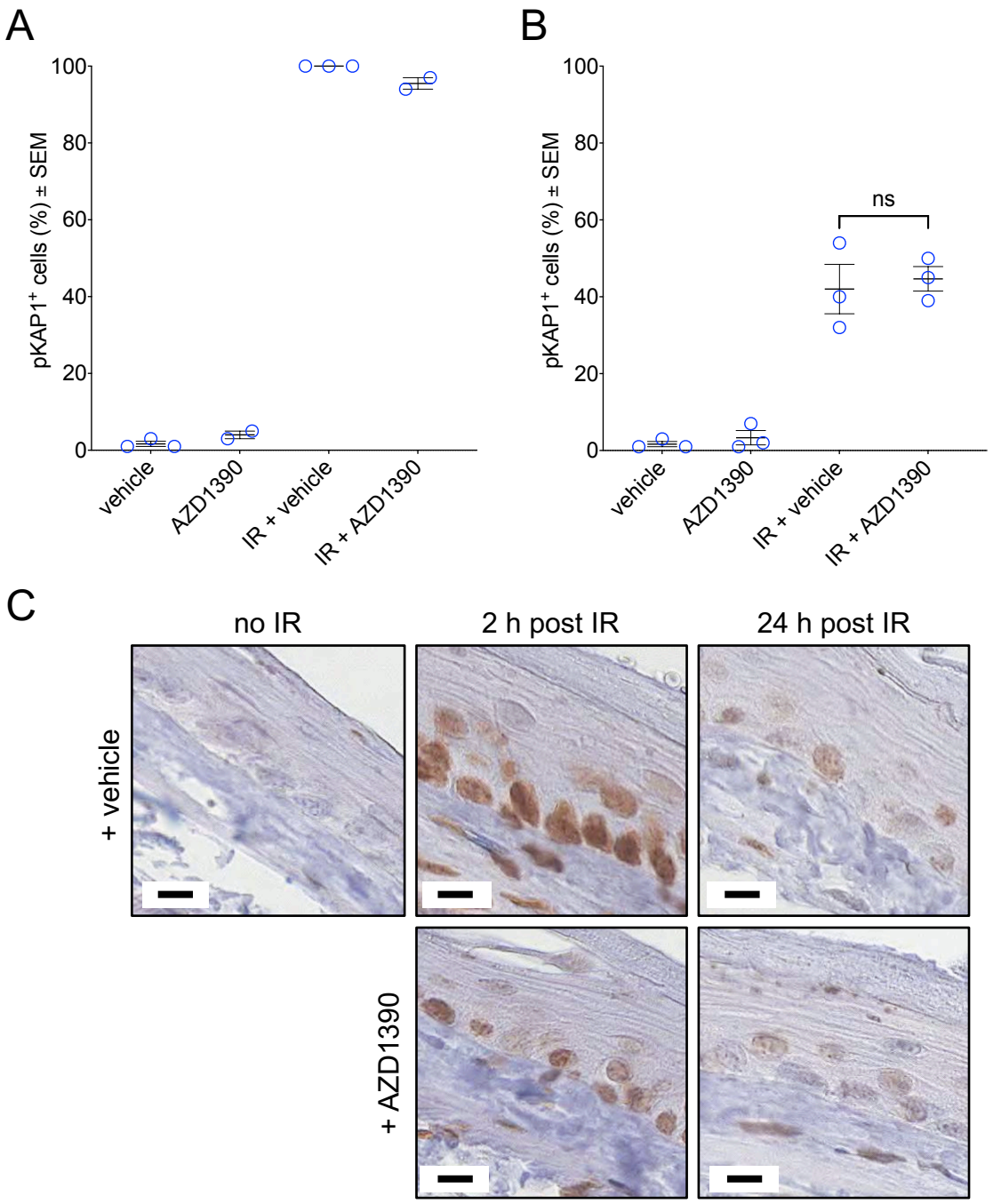

Figure 3.4.20. AZD1390 in combination with IR did not affect pKAP1 levels in oesophageal epithelial cells. Levels of pKAP1 in oesophageal epithelial cells treated with IR + AZD1390 were not significantly increased compared with IR + vehicle control after 2 h (A) or 24 h (B). IHC of representative KAP1 ser824 levels in oesophageal epithelial cells[1] (C). (o) indicate individual mice. Scale bars represent 10 µm.

[1] Mice treated with IR + AZD1390 at 2 h (1) and AZD1390 at 2 h (1) were excluded from quantitative analysis due to insufficient evaluable tissue.

These results of pKAP1 expression suggest that the addition of AZD1390 at 10 mg/kg to IR is able to decrease KAP1 phosphorylation in lung tumour cells at 2 h but not in the bronchial or oesophageal epithelium at either time point.

3.4.8. Discussion

While the treatment of xenografts with IR + AZD1390 led to significant tumour growth inhibition, this combination was not found to be efficacious in either the early or late therapeutic window studies in the A/J model. In the whole thorax tolerability study, IR + AZD1390 at 20 mg/kg was not tolerated due to weight loss from oesophagitis, a side effect also observed in A-T patients after radiotherapy treatment (Gotoff et al., 1967). By using the hemithorax rig to avoid the oesophagus and a lower dose range of AZD1390 (5 and 10 mg/kg), the efficacy and long-term toxicities of treatment could be assessed.

The final anti-tumour efficacy measurements of both IR + AZD1390 groups in the early intervention study revealed no decrease in tumour burden. However, IR + vehicle also was unable to significantly decrease tumour burden in the early intervention compared with vehicle control. This may be due to a decrease in the overall initial tumour burden of the mouse cohort in the study. The average number of tumours in the vehicle group was 5.3 while in the early intervention study of AZD6738, the average tumour number for the vehicle group was 16.7, suggesting a potential difference in urethane tumour induction between the two cohorts (**Chapter 3.2.4**). This decrease in tumour burden would lower the power of the study to detect a small effect between IR and the IR + AZD1390 groups. As discussed previously (**Chapter 3.1.3**), differences in urethane dosing results can result in different tumour numbers between experiments and batch-to-batch variability should be considered in future experiments.

Importantly, skin effects were also seen in both the early and late intervention studies. Treatment with fractionated hemithoracic IR and either AZD1390 dose

resulted in skin desquamation, and the greatest impact was on individuals in the IR + AZD1390 10 mg/kg group, 2 of which were euthanised due to weight loss. In comparison, the late intervention study using a single 13 Gy dose with AZD1390 resulted in fur loss and mild skin damage, but this was limited to the size of the treatment window (8 x 8 mm). Additionally, an increase in fibrosis score of lungs treated with IR + AZD1390 at 10 mg/kg was observed, suggesting a possible upper threshold for this compound and IR combination in the A/J model.

In the late intervention setting, there were no overall effects on tumour burden other than a significant increase in superficial tumour count ratio between the IR + vehicle and IR + AZD1390 10 mg/kg groups. There was also a trend of increasing tumour burden of those treated by IR + AZD1390 that may suggest an underlying impact of ATM inhibition on tumour growth in this model. A possible explanation for an increase in tumour growth following IR + AZD1390 treatment could involve signalling through mTOR and the complex mTORC1, of which mTOR is a component (Sabatini et al., 1994; Saxton and Sabatini, 2017). Previous work has proposed a link between ATM-CHK2-p53 deficiency and increased mTORC1 signalling, thereby suggesting that transient inhibition of ATM may prevent p53 from suppressing mTORC1 activity and lead to proliferation through the promotion of protein synthesis (Shen and Houghton, 2013; Zhou et al., 2017; Zoncu et al., 2011). However, this would need further work in A/J tumours to evaluate mTOR activity after treatment with AZD1390.

Another possible reason for increased tumour growth is based on the role that ATM plays as a tumour suppressor. Even transient ATM inhibition may be enough to facilitate tumour growth through temporarily bypassing the ATM-p53 pathway upon IR or genotoxic stress and allowing survival in p53-proficient tumours (Cremona and Behrens, 2014; Jiang et al., 2009). This is also supported by the observation of increased superficial tumour counts in both lungs of mice treated with AZD1390 as a

monotherapy (**Fig. 3.4.7 A**). Previous genotyping of urethane-induced tumours in A/J mice determined that p53 mutations may be rare events that occur at later stage of tumourigenesis (Horio et al., 1996; Ohno et al., 2001). Additionally, other studies have shown that IR and ATM inhibition as a treatment of tumours with wildtype p53 is less effective than in models that are p53-deficient (Biddlestone-Thorpe et al., 2013; Durant et al., 2018). Therefore, the p53 status of tumours in this model may be an important factor in the observed efficacy of IR + AZD1390 in both the early and late intervention studies, and further research should determine the p53 status of tumours at the time of treatment.

The PD of AZD1390 and IR treatment in the A/J model are key to understanding the therapeutic window of treatment. Importantly, treatment of A/J tumours with IR + AZD1390 10 mg/kg led to a significant decrease in pKAP1 levels after 2 h as compared with IR + vehicle, but this was no longer evident after 24 h. While γH2AX levels in tumours increased upon treatment with IR, levels were within the same range between IR + vehicle and IR + AZD1390. Although IR + AZD1390 treatment resulted in lower pKAP1 levels suggesting that ATM activity was decreased in tumours, the similarly high levels of γH2AX between both IR groups at 2 h may indicate that IR damage was detected and repaired by tumour cells at a different time post treatment. A more detailed time course of DNA damage during the first 24 h after IR should be used in future studies to determine the DNA repair kinetics after IR + AZD1390 in A/J urethane-induced tumours.

In normal bronchial epithelial cells, IR + AZD1390 treatment led to a decrease in overlapping γH2AX foci levels at 2 h compared with IR + vehicle but were similar after 24 h, suggesting that AZD1390 was initially able to reduce phosphorylation levels of H2AX. Surprisingly, there was no difference in pKAP1 levels between IR + vehicle and

IR + AZD1390 at either time point, which may be due to the tissue specific repair kinetics of bronchial epithelial cells, observed previously (Gadbois and Lehnert, 1997).

In the oesophageal epithelium, both γH2AX and pKAP1 levels were unaffected by the addition of AZD1390 to IR at 2 and 24 h. However, cells in the IR + AZD1390 group at 2 h were less intense in pKAP1 staining compared with IR + vehicle, which may suggest a different rate of repair. Oesophagitis did not manifest until days after treatment with the combination so to fully elucidate the oesophageal response to IR + AZD1390, an oesophageal tolerability study as in **Figure 3.3.6** could be used.

These data provide an expanded examination of the combination treatment of IR + AZD1390 in the A/J therapeutic window studies tumour efficacy and normal tissue damage model. Although the combination was limited in efficacy against urethane-induced tumours, understanding the potential normal tissue effects may have important implications for this treatment as it enters clinical trials.

4. General Discussion and Conclusions

Throughout this work, we have characterised and implemented the A/J model of lung cancer and thoracic IR in a series of therapeutic window studies. We have evaluated the radiosensitisation effect of three DDR inhibitor compounds *in vivo* on tumour burden in early and late development as well as their PD profile over 24 h. Importantly, we have also examined the toxicities arising from combination treatment damage to normal thoracic tissues, and the impact of treatments on bronchial and oesophageal epithelium. Finally, we have also identified a potential new study design to explore oesophageal tolerability, which may be important in the prediction and mitigation of oesophageal damage during treatment.

In **Chapter 3.1**, the A/J mouse strain was explored as a model of independently arising lung tumours using urethane as a carcinogenic agent. Tumours were shown to be slowly proliferating with limited regions of hypoxia and, importantly, the growth of each tumour was able to be tracked over several weeks using MRI, as developed previously (Gomes et al., 2019). Two different urethane dosing schedules were also evaluated in an effort to minimise the toxicities that can arise in this model, possibly caused by variations in the anaesthetic effect of urethane between cohorts of A/J mice (Field and Lang, 1988). An effective 2 dose regimen of 5 mg per 10 g body weight was developed to induce tumours and appropriate endpoint measures were identified including (i) visual superficial tumour counting, (ii) counting tumours found within a single midsection lung slice, and (iii) determining tumour area per lung slice. In addition, the use of MRI for volumetric data of detectable tumours (> 250 μm^3) provided further tumour burden information and was implemented in the late intervention studies. MRI could also be used in early intervention studies to track tumour growth inhibition or regression after treatment, although this would need to be after week 13-14 due to the detectable size limitation (Gomes et al., 2019).

The A/J strain was also used to evaluate the induction of pulmonary fibrosis, a late term normal tissue effect, by thoracic IR. IR-induced fibrosis is a critical toxicity to effectively and accurately model in order to develop potential preventative treatments and to understand the possible side effects of IR and drug combination therapies (Dabjan et al., 2016). Previous work in our laboratory revealed that a fractionated schedule of 5 treatments of 5 Gy to the whole thorax of A/J mice induced measurable pulmonary fibrosis 26 weeks after IR treatment. Additionally, this fractionated IR schedule of 5 x 5 Gy was compared with single, whole thoracic doses of 13 or 15 Gy. Both single dose regimens were able to induce fibrosis at 26 weeks after IR. However, animals treated with 15 Gy exhibited clinical signs of significant toxicity, and our results suggested a steep dose response between 13 and 15 Gy. Our report of fibrosis with both fractionated and single whole thorax IR contrasts with two previous studies that did not observe fibrosis in the A/J strain after IR (Jackson et al., 2011; Paun and Haston, 2012). Both previous studies used ^{137}Cs γ-rays at lower doses rates (0.51 Gy/min and 0.7 Gy/min) to irradiate the whole thorax (Jackson et al., 2011; Paun and Haston, 2012). The higher energy (662 KeV) and lower dose rate of ^{137}Cs γ-rays may explain the different biological response in our studies which used X-rays (**Chapter 2.6**, **Appendix Figures 6.1 & 6.2**, and **Appendix Table 6.4**), but future studies could investigate the IR differences between the methodologies. In a recent review, a compilation of whole thorax IR studies in C57BL/6 revealed significant differences in biological responses with similar whole thorax IR doses, and the authors partially attributed this to the variability in laboratory experimental conditions (Dabjan et al., 2016).

Importantly, the comparison of whole thoracic and left lung IR treatment revealed a key difference in normal tissue responses. While the delivered doses to the irradiated tissues are similar, the lower observed fibrosis scores in left lung treatment suggest an

important difference in biological response due to factors that could include targeting, organ sparing, total irradiated volume, and dose distribution across the depth of an animal, which has been observed in other mouse strains (Ghita et al., 2019). Lung tissue targeting and fibrosis has been explored using the SARRP in a few studies with non-tumour bearing mice, but optimal targeting should be examined further as a method of increasing the threshold for fibrosis induction, particularly in studies involving compounds that may modulate the effect of IR (Bazalova et al., 2014; Ghita et al., 2019).

Future work is needed to characterise the A/J model to understand the complex immune responses over time in response to both tumour induction and IR treatment. In our work, we have shown that the A/J mouse model can be used for assessment of the therapeutic window of IR combination therapies. Due to its immune competent status, this model could also be used for studies of tumour and IR immune responses as well as emerging immunotherapy or combination treatments. Early immune responses to irradiation of urethane-induced tumours in the unrelated Kunming mouse strain have been described previously (Pan et al., 2020). However, further studies with the A/J model can extend their work with a time course examining the early immune changes that affect both IR-induced fibrosis and tumour development as well as the interplay between treatment efficacy and immune responses.

From our studies, two general timelines of tumour development and treatment effects can be drawn (**Fig. 4.1.1 A & B**). Upon induction with urethane, the timeline of tumour development and growth begins, with treatment interventions possible at any point (**Fig. 4.1.1 A**). Once treated with IR in combination with a test compound (for example ATR, ATM, or DNA-PK inhibitors) a second timeline of anti-tumour effects and normal tissue effects can be initiated depending on the effect of the drug on normal tissues (**Fig. 4.1.1 B**).

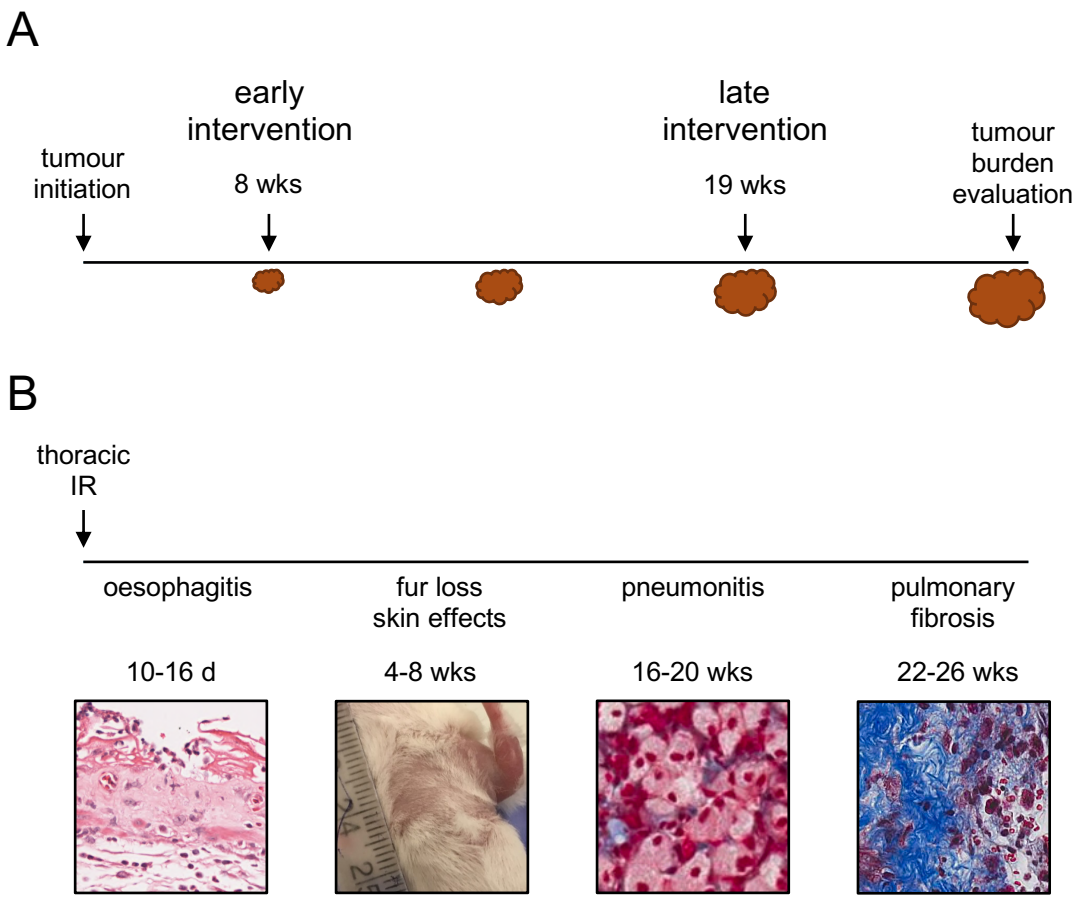

Figure 4.1.1. Timelines of therapeutic window treatments and IR-induced normal tissue effects. In the A/J model, tumours are initiated and can be treated with IR as part of either early or late intervention studies or at any point in development (A). After thoracic IR, a second timeline of normal tissue effects can be initiated, developing over days to weeks (oesophagitis and skin effects) to months (pneumonitis and pulmonary fibrosis) (B).

The DDR inhibitors examined in this work resulted in distinct findings in terms of anti-tumour effects and normal tissue damage when combined with IR (which are summarised in **Table 4.1.1**), although all three compounds induced significant oesophagitis in combination with whole thorax IR. Further work investigating the therapeutic window of each inhibitor with a variety of dosing and IR regimens is needed to understand the complex tissue and tumour responses revealed in this study.

	AZD6738 ATR inhibitor	**AZD7648** DNA-PK inhibitor	**AZD1390** ATM inhibitor
Early anti-tumour efficacy	None	Significant	Minimal
Late anti-tumour efficacy	None	Moderate	None
Whole thorax normal tissue effects	Oesophagitis	Oesophagitis	Oesophagitis
Hemithorax normal tissue effects	None	Skin effects Fur loss Fibrosis Lung shrinkage	Skin effects Fur loss Fibrosis

Table 4.1.1. Summary of anti-tumour and normal tissue effects of AZD6738, AZD7648, and AZD1390.

After avoiding the oesophagus, the combination treatment of IR and AZD6738 was well tolerated but with limited impact on tumour burden. To increase the potential drug effect on tumours, future studies should alter the treatment regimen (e.g. longer, continuous dosing periods, higher overall IR doses) or treat larger hypoxic tumours to synergise with the replication stress induced by hypoxia.

Treatment with AZD7648 in combination with IR had a significant impact on both tumour burden and normal tissues in the A/J model. While AZD7648 was able to significantly increase the efficacy of IR in both the early and late intervention studies, early and late responding normal tissues were also damaged. Future work that more directly targets tumours may be able to reduce the deleterious thoracic tissue effects of AZD7648 and IR and still maintain its anti-tumour capability, which will be essential in clinical trials.

AZD1390 in combination with IR did not reduce tumour burden in either the early or late intervention study but did result in normal tissue damage, particularly with the higher dose of 10 mg/kg. Although this combination was unable to define a therapeutic window, future studies could focus on the reported p53-deficient tumour vulnerability

to AZD1390 and IR while also reducing normal tissue effects by ensuring appropriate tumour targeting (Biddlestone-Thorpe et al., 2013; Durant et al., 2018).

The evidence in this work of the three inhibitors can inform their potential use in combination with radiotherapy in clinical trials such as CONCORDE and future phase II/III studies. While AZD7648 could be limited in its clinical application due to its safety profile, the established clinical image-guided methodology of targeting tumours to reduce normal tissue IR doses and toxicities could address this limitation as long as appropriate limits to OARs were adjusted to account for the addition of the compound to the standard radiotherapy treatment; therefore, from the evidence in this work, AZD7648 shows the most promise of the three compounds evaluated due to its radiosensitisation efficacy seen in both the early and late therapeutic window studies. However, both AZD6738 and AZD1390 in combination with radiation could also be optimised to improve the clinical relevance and application of each treatment. While this work measured limited efficacy in the A/J model overall, the value of adding AZD6738 or AZD1390 to IR has already been demonstrated in previous studies of mouse tumours with specific mutations and with daily IR and drug dosing; if the appropriate patient tumour subpopulations were selected for treatment or continuous dosing regimens were implemented, these compounds may prove efficacious in patients when added to standard radiotherapy. As with AZD7648, the normal tissue effects of AZD6738 and AZD1390 in combination with IR would need appropriately modified IR dose limits on OARs when treating patients, but current radiotherapy treatment modalities would limit the potential for toxicities with careful planning.

To further justify the clinical application of all three inhibitors, the A/J strain could be crossed with other genetic backgrounds such as ATM or p53 mutations to observe the effects of these reportedly synergistic mutations and to help identify the most relevant tumour subpopulations for treatment (Ding et al., 2008; Durant et al., 2018;

Fok et al., 2019; Min et al., 2017). Upon induction with urethane, tumours containing these mutations may have differential responses to each inhibitor and more closely match the genetic background of some human NSCLCs. This would need to include appropriate targeting to tumours as well due to the risk of increased damage to normal tissue, but the underlying mechanisms of modulating the therapeutic window of IR would be further elucidated. Additionally, increasing the IR dose to a BED for the tumour that more closely matches the potentially curative doses used in current standards of care (**Chapter 1.2**, BED of 66 Gy given as 33 x 2 Gy fractions is 79 Gy, BED of 5 x 5 Gy is 37.5 Gy) while selectively targeting tumours to limit normal tissue effects may more effectively demonstrate the clinical application of combining IR and DDR inhibitors.

Notably, each DDR inhibitor and IR combination treatment resulted in damage to normal tissues which will need to be taken into consideration as these treatments enter clinical trials and highlights the importance of preclinical testing in a relevant model. These effects will need to be confirmed in clinical trials such as the CONCORDE trial to support the clinical translatability and predictability of the A/J model using these compounds (NCT04550104). Additionally, other treatments already used in patients such as chemoradiotherapy that have established safety profiles could be used in the A/J model to assess the backwards translation of the model (Shakhnovich, 2018). If successfully demonstrated in the clinic or in a backwards translation study, the ability to detect normal tissue effects concurrently with IR combination treatment of tumours could make the A/J model an important preclinical tool for evaluating treatment therapeutic windows.

Finally, while the higher whole thorax IR dose of 15 Gy did not induce oesophageal damage, each DDR inhibitor in combination with IR did, revealing an important difference between increasing IR dose and modulating IR with drugs. This

finding also led to a new potential role for the A/J strain. Oesophagitis is a commonly seen side effect in patients treated with IR (Berkey, 2010; Fleming et al., 2016; Robinson et al., 2020). A translatable preclinical model could help predict and mitigate against oesophagitis, in particular with IR-modulating drugs that may affect the therapeutic window of treatment.

5. References

Abid, S.H., V. Malhotra, and M.C. Perry. (2001). Radiation-induced and chemotherapy-induced pulmonary injury. *Curr Opin Oncol*. 13:242-248. 10.1097/00001622-200107000-00006

Adebahr, S., T. Schimek-Jasch, U. Nestle, and T.B. Brunner. (2016). Oesophagus side effects related to the treatment of oesophageal cancer or radiotherapy of other thoracic malignancies. *Best Pract Res Clin Gastroenterol*. 30:565-580. 10.1016/j.bpg.2016.07.003

Ahnesorg, P., P. Smith, and S.P. Jackson. (2006). XLF interacts with the XRCC4-DNA ligase IV complex to promote DNA nonhomologous end-joining. *Cell*. 124:301-313. 10.1016/j.cell.2005.12.031

Amin, M.B., and American Joint Committee on Cancer. (2017). AJCC cancer staging manual. American Joint Committee on Cancer/Springer, Chicago. xvii, 1024 pages pp.

Antonia, S.J., A. Villegas, D. Daniel, D. Vicente, S. Murakami, R. Hui, T. Kurata, A. Chiappori, K.H. Lee, M. de Wit, B.C. Cho, M. Bourhaba, X. Quantin, T. Tokito, T. Mekhail, D. Planchard, Y.C. Kim, C.S. Karapetis, S. Hiret, G. Ostoros, K. Kubota, J.E. Gray, L. Paz-Ares, J. de Castro Carpeno, C. Faivre-Finn, M. Reck, J. Vansteenkiste, D.R. Spigel, C. Wadsworth, G. Melillo, M. Taboada, P.A. Dennis, M. Ozguroglu, and P. Investigators. (2018). Overall Survival with Durvalumab after Chemoradiotherapy in Stage III NSCLC. *N Engl J Med*. 379:2342-2350. 10.1056/NEJMoa1809697

Azzam, E.I., J.P. Jay-Gerin, and D. Pain. (2012). Ionizing radiation-induced metabolic oxidative stress and prolonged cell injury. *Cancer Lett*. 327:48-60. 10.1016/j.canlet.2011.12.012

Bakkenist, C.J., and M.B. Kastan. (2003). DNA damage activates ATM through intermolecular autophosphorylation and dimer dissociation. *Nature*. 421:499-506. 10.1038/nature01368

Ball, H.L., J.S. Myers, and D. Cortez. (2005). ATRIP binding to replication protein A-single-stranded DNA promotes ATR-ATRIP localization but is dispensable for Chk1 phosphorylation. *Mol Biol Cell*. 16:2372-2381. 10.1091/mbc.e04-11-1006

Bar-Ad, V., N. Ohri, and M. Werner-Wasik. (2012). Esophagitis, treatment-related toxicity in non-small cell lung cancer. *Rev Recent Clin Trials*. 7:31-35. 10.2174/157488712799363235

Bazalova, M., G. Nelson, J.M. Noll, and E.E. Graves. (2014). Modality comparison for small animal radiotherapy: a simulation study. *Med Phys*. 41:011710. 10.1118/1.4842415

Berges, A., S.Y.A. Cheung, A.J. Pierce, E. Dean, B. Felicetti, N. Standifer, S. Smith, J. Yates, A. Lau, C. Stephens, M. Krebs, K. Harrington, and S.J. Hollingsworth. (2018). Abstract CT118: PK-Biomarker-Safety modelling aids choice of recommended Phase II dose and schedule for AZD6738 (ATR inhibitor). *Cancer Research*. 78:CT118-CT118. 10.1158/1538-7445.Am2018-ct118

Berkey, F.J. (2010). Managing the adverse effects of radiation therapy. *Am Fam Physician*. 82:381-388, 394.

Biddlestone-Thorpe, L., M. Sajjad, E. Rosenberg, J.M. Beckta, N.C. Valerie, M. Tokarz, B.R. Adams, A.F. Wagner, A. Khalil, D. Gilfor, S.E. Golding, S. Deb, D.G. Temesi, A. Lau, M.J. O'Connor, K.S. Choe, L.F. Parada, S.K. Lim, N.D. Mukhopadhyay, and K. Valerie. (2013). ATM kinase inhibition preferentially sensitizes p53-mutant glioma to ionizing radiation. *Clin Cancer Res*. 19:3189-3200. 10.1158/1078-0432.CCR-12-3408

Blackford, A.N., and S.P. Jackson. (2017). ATM, ATR, and DNA-PK: The Trinity at the Heart of the DNA Damage Response. *Mol Cell*. 66:801-817. 10.1016/j.molcel.2017.05.015

Borrego, A., W.H.K. Cabrera, J.R. Jensen, M. Correa, O.G. Ribeiro, N. Starobinas, M. De Franco, A. Pettinicchio, T.A. Dragani, O.C.M. Ibanez, and G. Manenti. (2018). Germline control of somatic Kras mutations in mouse lung tumors. *Mol Carcinog*. 57:745-751. 10.1002/mc.22796

Bosma, G.C., R.P. Custer, and M.J. Bosma. (1983). A severe combined immunodeficiency mutation in the mouse. *Nature*. 301:527-530. 10.1038/301527a0

Boss, M.K., R. Bristow, and M.W. Dewhirst. (2014). Linking the history of radiation biology to the hallmarks of cancer. *Radiat Res*. 181:561-577. 10.1667/RR13675.1

Brandsma, I., and D.C. Gent. (2012). Pathway choice in DNA double strand break repair: observations of a balancing act. *Genome Integr*. 3:9. 10.1186/2041-9414-3-9

Bray, F., J. Ferlay, I. Soerjomataram, R.L. Siegel, L.A. Torre, and A. Jemal. (2018). Global cancer statistics 2018: GLOBOCAN estimates of incidence and mortality worldwide for 36 cancers in 185 countries. *CA Cancer J Clin*. 68:394-424. 10.3322/caac.21492

Brown, E.J., and D. Baltimore. (2000). ATR disruption leads to chromosomal fragmentation and early embryonic lethality. *Genes Dev*. 14:397-402.

Brown, K.F., H. Rumgay, C. Dunlop, M. Ryan, F. Quartly, A. Cox, A. Deas, L. Elliss-Brookes, A. Gavin, L. Hounsome, D. Huws, N. Ormiston-Smith, J. Shelton, C. White, and D.M. Parkin. (2018). The fraction of cancer attributable to modifiable risk factors in England, Wales, Scotland, Northern Ireland, and the United Kingdom in 2015. *Br J Cancer*. 118:1130-1141. 10.1038/s41416-018-0029-6

Buck, D., L. Malivert, R. de Chasseval, A. Barraud, M.C. Fondaneche, O. Sanal, A. Plebani, J.L. Stephan, M. Hufnagel, F. le Deist, A. Fischer, A. Durandy, J.P. de Villartay, and P. Revy. (2006). Cernunnos, a novel nonhomologous end-joining factor, is mutated in human immunodeficiency with microcephaly. *Cell*. 124:287-299. 10.1016/j.cell.2005.12.030

Burma, S., B.P. Chen, M. Murphy, A. Kurimasa, and D.J. Chen. (2001). ATM phosphorylates histone H2AX in response to DNA double-strand breaks. *J Biol Chem*. 276:42462-42467. 10.1074/jbc.C100466200

Butler, J.P., S.H. Loring, S. Patz, A. Tsuda, D.A. Yablonskiy, and S.J. Mentzer. (2012). Evidence for adult lung growth in humans. *N Engl J Med*. 367:244-247. 10.1056/NEJMoa1203983

Butterworth, K.T. (2019). Evolution of the Supermodel: Progress in Modelling Radiotherapy Response in Mice. *Clin Oncol (R Coll Radiol)*. 31:272-282. 10.1016/j.clon.2019.02.008

Caldecott, K.W. (2008). Single-strand break repair and genetic disease. *Nat Rev Genet*. 9:619-631. 10.1038/nrg2380

Cancer Research UK. (2016). Routes to diagnosis of lung cancer. Retrieved 9 September 2020, from https://www.cancerresearchuk.org/health-professional/cancer-statistics/statistics-by-cancer-type/lung-cancer/diagnosis-and-treatment#heading-Zero

Cancer Research UK. (2017). Lung cancer incidence statistics. Retrieved 10 May 2020, from http://www.cancerresearchuk.org/health-professional/cancer-statistics/statistics-by-cancer-type/lung-cancer/incidence#heading-Three

Cancer Research UK. (2019a). Lung cancer - Tests. Retrieved 14 September 2020, from https://www.cancerresearchuk.org/about-cancer/lung-cancer/getting-diagnosed/tests

Cancer Research UK. (2019b). Lung cancer survival statistics. Retrieved 10 May 2020, from http://www.cancerresearchuk.org/health-professional/cancer-statistics/statistics-by-cancer-type/lung-cancer/survival#heading-Three

Cancer Research UK. (2020). One-, five-, and ten-year survival for lung cancer. Retrieved 10 September 2020, from https://www.cancerresearchuk.org/health-professional/cancer-statistics/statistics-by-cancer-type/lung-cancer/survival#heading-Zero

Cazorla, M., L. Hernandez, P.L. Fernandez, A. Fabra, M.A. Peinado, C. Dasenbrock, T. Tillmann, K. Kamino, E. Campo, M. Kohler, G. Morawieltz, A. Cardesa, L. Tomatis, and U. Mohr. (1998). Ki-ras gene mutations and absence of p53 gene mutations in spontaneous and urethane-induced early lung lesions in CBA/J mice. *Mol Carcinog*. 21:251-260. 10.1002/(sici)1098-2744(199804)21:4<251::aid-mc4>3.0.co;2-n

Centers for Disease Control and Prevention. (2019). Who Should Be Screened for Lung Cancer? Retrieved 15 September 2020, from https://www.cdc.gov/cancer/lung/basic_info/screening.htm

Chehab, N.H., A. Malikzay, M. Appel, and T.D. Halazonetis. (2000). Chk2/hCds1 functions as a DNA damage checkpoint in G(1) by stabilizing p53. *Genes Dev*. 14:278-288.

Chen, B., L. Johanson, J.S. Wiest, M.W. Anderson, and M. You. (1994). The second intron of the K-ras gene contains regulatory elements associated with mouse lung tumor susceptibility. *Proc Natl Acad Sci U S A*. 91:1589-1593. 10.1073/pnas.91.4.1589

Cheng, M., S. Jolly, W.O. Quarshie, N. Kapadia, F.D. Vigneau, and F.M. Kong. (2019). Modern Radiation Further Improves Survival in Non-Small Cell Lung Cancer: An Analysis of 288,670 Patients. *J Cancer*. 10:168-177. 10.7150/jca.26600

Choi, M., T. Kipps, and R. Kurzrock. (2016). ATM Mutations in Cancer: Therapeutic Implications. *Mol Cancer Ther*. 15:1781-1791. 10.1158/1535-7163.MCT-15-0945

Cimprich, K.A., and D. Cortez. (2008). ATR: an essential regulator of genome integrity. *Nat Rev Mol Cell Biol*. 9:616-627. 10.1038/nrm2450

Citrin, D.E., and J.B. Mitchell. (2017). Mechanisms of Normal Tissue Injury From Irradiation. *Semin Radiat Oncol*. 27:316-324. 10.1016/j.semradonc.2017.04.001

Coleman, C.N., G.S. Higgins, J.M. Brown, M. Baumann, D.G. Kirsch, H. Willers, P.G. Prasanna, M.W. Dewhirst, E.J. Bernhard, and M.M. Ahmed. (2016). Improving the Predictive Value of Preclinical Studies in Support of Radiotherapy Clinical Trials. *Clin Cancer Res*. 22:3138-3147. 10.1158/1078-0432.CCR-16-0069

Coppe, J.P., P.Y. Desprez, A. Krtolica, and J. Campisi. (2010). The senescence-associated secretory phenotype: the dark side of tumor suppression. *Annu Rev Pathol*. 5:99-118. 10.1146/annurev-pathol-121808-102144

Cortez, D., S. Guntuku, J. Qin, and S.J. Elledge. (2001). ATR and ATRIP: partners in checkpoint signaling. *Science*. 294:1713-1716. 10.1126/science.1065521

Cortez, D., Y. Wang, J. Qin, and S.J. Elledge. (1999). Requirement of ATM-dependent phosphorylation of brca1 in the DNA damage response to double-strand breaks. *Science*. 286:1162-1166. 10.1126/science.286.5442.1162

Cotroneo, C.E., A. Dassano, F. Colombo, A. Pettinicchio, D. Lecis, M. Dugo, L. De Cecco, T.A. Dragani, and G. Manenti. (2016). Expression quantitative trait analysis reveals fine germline transcript regulation in mouse lung tumors. *Cancer Lett*. 375:221-230. 10.1016/j.canlet.2016.02.054

Cremona, C.A., and A. Behrens. (2014). ATM signalling and cancer. *Oncogene*. 33:3351-3360. 10.1038/onc.2013.275

D'Antonio, C., A. Passaro, B. Gori, E. Del Signore, M.R. Migliorino, S. Ricciardi, A. Fulvi, and F. de Marinis. (2014). Bone and brain metastasis in lung cancer: recent advances in therapeutic strategies. *Ther Adv Med Oncol*. 6:101-114. 10.1177/1758834014521110

Dabjan, M.B., C.M. Buck, I.L. Jackson, Z. Vujaskovic, B. Marples, and J.D. Down. (2016). A survey of changing trends in modelling radiation lung injury in mice: bringing out the good, the bad, and the uncertain. *Lab Invest*. 96:936-949. 10.1038/labinvest.2016.76

Dahl, G.A., J.A. Miller, and E.C. Miller. (1978). Vinyl carbamate as a promutagen and a more carcinogenic analog of ethyl carbamate. *Cancer Res*. 38:3793-3804.

Dassano, A., F. Colombo, G. Trincucci, E. Frullanti, A. Galvan, A. Pettinicchio, L. De Cecco, A. Borrego, O.C. Martinez Ibanez, T.A. Dragani, and G. Manenti. (2014). Mouse pulmonary adenoma susceptibility 1 locus is an expression QTL modulating Kras-4A. *PLoS Genet*. 10:e1004307. 10.1371/journal.pgen.1004307

De Ruysscher, D., A. Botterweck, M. Dirx, M. Pijls-Johannesma, R. Wanders, M. Hochstenbag, A.M. Dingemans, G. Bootsma, W. Geraedts, J. Simons, C. Pitz, and P. Lambin. (2009). Eligibility for concurrent chemotherapy and radiotherapy of locally advanced lung cancer patients: a prospective, population-based study. *Ann Oncol*. 20:98-102. 10.1093/annonc/mdn559

De Ruysscher, D., G. Niedermann, N.G. Burnet, S. Siva, A.W.M. Lee, and F. Hegi-Johnson. (2019). Radiotherapy toxicity. *Nat Rev Dis Primers*. 5:13. 10.1038/s41572-019-0064-5

de Seranno, S., and R. Meuwissen. (2010). Progress and applications of mouse models for human lung cancer. *Eur Respir J*. 35:426-443. 10.1183/09031936.00124709

Dehing-Oberije, C., D. De Ruysscher, A. van Baardwijk, S. Yu, B. Rao, and P. Lambin. (2009). The importance of patient characteristics for the prediction of radiation-induced lung toxicity. *Radiother Oncol*. 91:421-426. 10.1016/j.radonc.2008.12.002

Delacroix, S., J.M. Wagner, M. Kobayashi, K. Yamamoto, and L.M. Karnitz. (2007). The Rad9-Hus1-Rad1 (9-1-1) clamp activates checkpoint signaling via TopBP1. *Genes Dev*. 21:1472-1477. 10.1101/gad.1547007

Deng, H., C.W. Kennedy, E. Armour, E. Tryggestad, E. Ford, T. McNutt, L. Jiang, and J. Wong. (2007). The small-animal radiation research platform (SARRP): dosimetry of a focused lens system. *Phys Med Biol*. 52:2729-2740. 10.1088/0031-9155/52/10/007

Dillon, M.T., Z. Boylan, D. Smith, J. Guevara, K. Mohammed, C. Peckitt, M. Saunders, U. Banerji, G. Clack, S.A. Smith, J.F. Spicer, M.D. Forster, and K.J. Harrington. (2018). PATRIOT: A phase I study to assess the tolerability, safety and biological effects of a specific ataxia telangiectasia and Rad3-related (ATR) inhibitor (AZD6738) as a single agent and in combination with palliative radiation therapy in patients with solid tumours. *Clin Transl Radiat Oncol*. 12:16-20. 10.1016/j.ctro.2018.06.001

Ding, L., G. Getz, D.A. Wheeler, E.R. Mardis, M.D. McLellan, K. Cibulskis, C. Sougnez, H. Greulich, D.M. Muzny, M.B. Morgan, L. Fulton, R.S. Fulton, Q. Zhang, M.C. Wendl, M.S. Lawrence, D.E. Larson, K. Chen, D.J. Dooling, A. Sabo, A.C. Hawes, H. Shen, S.N. Jhangiani, L.R. Lewis, O. Hall, Y. Zhu, T. Mathew, Y. Ren, J. Yao, S.E. Scherer, K. Clerc, G.A. Metcalf, B. Ng, A. Milosavljevic, M.L. Gonzalez-Garay, J.R. Osborne, R. Meyer, X. Shi, Y. Tang, D.C. Koboldt, L. Lin, R. Abbott, T.L. Miner, C. Pohl, G. Fewell, C. Haipek, H. Schmidt, B.H. Dunford-Shore, A. Kraja, S.D. Crosby, C.S. Sawyer, T. Vickery, S. Sander, J. Robinson, W. Winckler, J. Baldwin, L.R. Chirieac, A. Dutt, T. Fennell, M. Hanna, B.E. Johnson, R.C. Onofrio, R.K. Thomas, G. Tonon, B.A. Weir, X. Zhao, L. Ziaugra, M.C. Zody, T. Giordano, M.B. Orringer, J.A. Roth, M.R. Spitz, Wistuba, II, B. Ozenberger, P.J. Good, A.C. Chang, D.G. Beer, M.A. Watson, M. Ladanyi, S. Broderick, A. Yoshizawa, W.D. Travis, W. Pao, M.A. Province, G.M. Weinstock, H.E. Varmus, S.B. Gabriel, E.S. Lander, R.A. Gibbs, M. Meyerson, and R.K. Wilson. (2008). Somatic mutations affect key pathways in lung adenocarcinoma. *Nature*. 455:1069-1075. 10.1038/nature07423

Doki, Y., K. Murakami, T. Yamaura, S. Sugiyama, T. Misaki, and I. Saiki. (1999). Mediastinal lymph node metastasis model by orthotopic intrapulmonary implantation of Lewis lung carcinoma cells in mice. *Br J Cancer*. 79:1121-1126. 10.1038/sj.bjc.6690178

Donzelli, M., and G.F. Draetta. (2003). Regulating mammalian checkpoints through Cdc25 inactivation. *EMBO Rep*. 4:671-677. 10.1038/sj.embor.embor887

Drouet, J., P. Frit, C. Delteil, J.P. de Villartay, B. Salles, and P. Calsou. (2006). Interplay between Ku, Artemis, and the DNA-dependent protein kinase catalytic subunit at DNA ends. *J Biol Chem*. 281:27784-27793. 10.1074/jbc.M603047200

Duncan, M., and G. Grant. (2003). Oral and intestinal mucositis - causes and possible treatments. *Aliment Pharmacol Ther*. 18:853-874. 10.1046/j.1365-2036.2003.01784.x

Dunne, V., M. Ghita, D.M. Small, C.B.M. Coffey, S. Weldon, C.C. Taggart, S.O. Osman, C.K. McGarry, K.M. Prise, G.G. Hanna, and K.T. Butterworth. (2017). Inhibition of ataxia telangiectasia related-3 (ATR) improves therapeutic index in preclinical models of non-small cell lung cancer (NSCLC) radiotherapy. *Radiother Oncol*. 124:475-481. 10.1016/j.radonc.2017.06.025

Durant, S.T., L. Zheng, Y. Wang, K. Chen, L. Zhang, T. Zhang, Z. Yang, L. Riches, A.G. Trinidad, J.H.L. Fok, T. Hunt, K.G. Pike, J. Wilson, A. Smith, N. Colclough, V.P. Reddy, A. Sykes, A. Janefeldt, P. Johnstrom, K. Varnas, A. Takano, S. Ling, J. Orme, J. Stott, C. Roberts, I. Barrett, G. Jones, M. Roudier, A. Pierce, J. Allen, J. Kahn, A. Sule, J. Karlin, A. Cronin, M. Chapman, K. Valerie, R. Illingworth, and M. Pass. (2018). The brain-penetrant clinical ATM inhibitor AZD1390 radiosensitizes and improves survival of preclinical brain tumor models. *Sci Adv*. 4:eaat1719. 10.1126/sciadv.aat1719

Eferl, R., E. Casanova, and SpringerLink (Online service). (2015). Mouse Models of Cancer : Methods and Protocols. *In* Methods in Molecular Biology,. Springer New York : Imprint: Humana Press,, New York, NY. 1 online resource (XI, 463 p. 10.1007/978-1-4939-2297-0

Eggert, J.A., M. Palavanzadeh, and A. Blanton. (2017). Screening and Early Detection of Lung Cancer. *Semin Oncol Nurs*. 33:129-140. 10.1016/j.soncn.2017.03.001

Evison, M., and U.K.L. AstraZeneca. (2020). The current treatment landscape in the UK for stage III NSCLC. *Br J Cancer*. 123:3-9. 10.1038/s41416-020-01069-z

Fabre, K.M., L. Ramaiah, R.C. Dregalla, C. Desaintes, M.M. Weil, S.M. Bailey, and R.L. Ullrich. (2011). Murine Prkdc polymorphisms impact DNA-PKcs function. *Radiat Res*. 175:493-500. 10.1667/RR2431.1

Faivre-Finn, C., S. Brown, A. Ryan, A. Greystoke, and C. Investigators. (2020). The UK at the Forefront of Innovative Drug-Radiotherapy Combination Clinical Trials: Introducing the CONCORDE Platform. *Clin Oncol (R Coll Radiol)*. 32:358-362. 10.1016/j.clon.2020.02.003

Ferguson, D.O., J.M. Sekiguchi, S. Chang, K.M. Frank, Y. Gao, R.A. DePinho, and F.W. Alt. (2000). The nonhomologous end-joining pathway of DNA repair is

required for genomic stability and the suppression of translocations. *Proc Natl Acad Sci U S A*. 97:6630-6633. 10.1073/pnas.110152897

Field, K.J., and C.M. Lang. (1988). Hazards of urethane (ethyl carbamate): a review of the literature. *Lab Anim*. 22:255-262. 10.1258/002367788780746331

Fleming, C., D.N. Cagney, S. O'Keeffe, S.M. Brennan, J.G. Armstrong, and B. McClean. (2016). Normal tissue considerations and dose-volume constraints in the moderately hypofractionated treatment of non-small cell lung cancer. *Radiother Oncol*. 119:423-431. 10.1016/j.radonc.2016.03.013

Fok, J.H.L., A. Ramos-Montoya, M. Vazquez-Chantada, P.W.G. Wijnhoven, V. Follia, N. James, P.M. Farrington, A. Karmokar, S.E. Willis, J. Cairns, J. Nikkila, D. Beattie, G.M. Lamont, M.R.V. Finlay, J. Wilson, A. Smith, L.O. O'Connor, S. Ling, S.E. Fawell, M.J. O'Connor, S.J. Hollingsworth, E. Dean, F.W. Goldberg, B.R. Davies, and E.B. Cadogan. (2019). AZD7648 is a potent and selective DNA-PK inhibitor that enhances radiation, chemotherapy and olaparib activity. *Nat Commun*. 10:5065. 10.1038/s41467-019-12836-9

Fokas, E., R. Prevo, E.M. Hammond, T.B. Brunner, W.G. McKenna, and R.J. Muschel. (2014). Targeting ATR in DNA damage response and cancer therapeutics. *Cancer Treat Rev*. 40:109-117. 10.1016/j.ctrv.2013.03.002

Foote, K.M., J.W.M. Nissink, T. McGuire, P. Turner, S. Guichard, J.W.T. Yates, A. Lau, K. Blades, D. Heathcote, R. Odedra, G. Wilkinson, Z. Wilson, C.M. Wood, and P.J. Jewsbury. (2018). Discovery and Characterization of AZD6738, a Potent Inhibitor of Ataxia Telangiectasia Mutated and Rad3 Related (ATR) Kinase with Application as an Anticancer Agent. *J Med Chem*. 61:9889-9907. 10.1021/acs.jmedchem.8b01187

Forkert, P.G. (2010). Mechanisms of lung tumorigenesis by ethyl carbamate and vinyl carbamate. *Drug Metab Rev*. 42:355-378. 10.3109/03602531003611915

Gadbois, D.M., and B.E. Lehnert. (1997). Cell cycle response to DNA damage differs in bronchial epithelial cells and lung fibroblasts. *Cancer Res*. 57:3174-3179.

Gaillard, H., T. Garcia-Muse, and A. Aguilera. (2015). Replication stress and cancer. *Nat Rev Cancer*. 15:276-289. 10.1038/nrc3916

Gandhi, L., D. Rodriguez-Abreu, S. Gadgeel, E. Esteban, E. Felip, F. De Angelis, M. Domine, P. Clingan, M.J. Hochmair, S.F. Powell, S.Y. Cheng, H.G. Bischoff, N. Peled, F. Grossi, R.R. Jennens, M. Reck, R. Hui, E.B. Garon, M. Boyer, B. Rubio-Viqueira, S. Novello, T. Kurata, J.E. Gray, J. Vida, Z. Wei, J. Yang, H. Raftopoulos, M.C. Pietanza, M.C. Garassino, and K.-. Investigators. (2018). Pembrolizumab plus Chemotherapy in Metastatic Non-Small-Cell Lung Cancer. *N Engl J Med*. 378:2078-2092. 10.1056/NEJMoa1801005

Gariboldi, M., G. Manenti, F. Canzian, F.S. Falvella, M.T. Radice, M.A. Pierotti, G. Della Porta, G. Binelli, and T.A. Dragani. (1993). A major susceptibility locus to murine lung carcinogenesis maps on chromosome 6. *Nat Genet*. 3:132-136. 10.1038/ng0293-132

Ghita, M., V. Dunne, G.G. Hanna, K.M. Prise, J.P. Williams, and K.T. Butterworth. (2019). Preclinical models of radiation-induced lung damage: challenges and

opportunities for small animal radiotherapy. *Br J Radiol*. 92:20180473. 10.1259/bjr.20180473

Ghita, M., S.J. McMahon, H.F. Thompson, C.K. McGarry, R. King, S.O.S. Osman, J.L. Kane, A. Tulk, G. Schettino, K.T. Butterworth, A.R. Hounsell, and K.M. Prise. (2017). Small field dosimetry for the small animal radiotherapy research platform (SARRP). *Radiat Oncol*. 12:204. 10.1186/s13014-017-0936-3

Ghobadi, G., S. van der Veen, B. Bartelds, R.A. de Boer, M.G. Dickinson, J.R. de Jong, H. Faber, M. Niemantsverdriet, S. Brandenburg, R.M. Berger, J.A. Langendijk, R.P. Coppes, and P. van Luijk. (2012). Physiological interaction of heart and lung in thoracic irradiation. *Int J Radiat Oncol Biol Phys*. 84:e639-646. 10.1016/j.ijrobp.2012.07.2362

Gilad, O., B.Y. Nabet, R.L. Ragland, D.W. Schoppy, K.D. Smith, A.C. Durham, and E.J. Brown. (2010). Combining ATR suppression with oncogenic Ras synergistically increases genomic instability, causing synthetic lethality or tumorigenesis in a dosage-dependent manner. *Cancer Res*. 70:9693-9702. 10.1158/0008-5472.CAN-10-2286

Giuranno, L., J. Ient, D. De Ruysscher, and M.A. Vooijs. (2019). Radiation-Induced Lung Injury (RILI). *Front Oncol*. 9:877. 10.3389/fonc.2019.00877

Goldstraw, P., J. Crowley, K. Chansky, D.J. Giroux, P.A. Groome, R. Rami-Porta, P.E. Postmus, V. Rusch, L. Sobin, C. International Association for the Study of Lung Cancer International Staging, and I. Participating. (2007). The IASLC Lung Cancer Staging Project: proposals for the revision of the TNM stage groupings in the forthcoming (seventh) edition of the TNM Classification of malignant tumours. *J Thorac Oncol*. 2:706-714. 10.1097/JTO.0b013e31812f3c1a

Gomes, A.L., P. Kinchesh, S. Gilchrist, P.D. Allen, L.M. Lourenco, A.J. Ryan, and S.C. Smart. (2019). Cardio-Respiratory synchronized bSSFP MRI for high throughput in vivo lung tumour quantification. *PLoS One*. 14:e0212172. 10.1371/journal.pone.0212172

Gomez, D.R., G.R. Blumenschein, Jr., J.J. Lee, M. Hernandez, R. Ye, D.R. Camidge, R.C. Doebele, F. Skoulidis, L.E. Gaspar, D.L. Gibbons, J.A. Karam, B.D. Kavanagh, C. Tang, R. Komaki, A.V. Louie, D.A. Palma, A.S. Tsao, B. Sepesi, W.N. William, J. Zhang, Q. Shi, X.S. Wang, S.G. Swisher, and J.V. Heymach. (2016). Local consolidative therapy versus maintenance therapy or observation for patients with oligometastatic non-small-cell lung cancer without progression after first-line systemic therapy: a multicentre, randomised, controlled, phase 2 study. *Lancet Oncol*. 17:1672-1682. 10.1016/S1470-2045(16)30532-0

Good, J.S., and K.J. Harrington. (2013). The hallmarks of cancer and the radiation oncologist: updating the 5Rs of radiobiology. *Clin Oncol (R Coll Radiol)*. 25:569-577. 10.1016/j.clon.2013.06.009

Gotoff, S.P., E. Amirmokri, and E.J. Liebner. (1967). Ataxia telangiectasia. Neoplasia, untoward response to x-irradiation, and tuberous sclerosis. *Am J Dis Child*. 114:617-625. 10.1001/archpedi.1967.02090270073006

Gottlieb, T.M., and S.P. Jackson. (1993). The DNA-dependent protein kinase: requirement for DNA ends and association with Ku antigen. *Cell*. 72:131-142. 10.1016/0092-8674(93)90057-w

Graves, P.R., F. Siddiqui, M.S. Anscher, and B. Movsas. (2010). Radiation pulmonary toxicity: from mechanisms to management. *Semin Radiat Oncol*. 20:201-207. 10.1016/j.semradonc.2010.01.010

Grawunder, U., D. Zimmer, S. Fugmann, K. Schwarz, and M.R. Lieber. (1998). DNA ligase IV is essential for V(D)J recombination and DNA double-strand break repair in human precursor lymphocytes. *Mol Cell*. 2:477-484. 10.1016/s1097-2765(00)80147-1

Gray, J.E., A. Villegas, D. Daniel, D. Vicente, S. Murakami, R. Hui, T. Kurata, A. Chiappori, K.H. Lee, B.C. Cho, D. Planchard, L. Paz-Ares, C. Faivre-Finn, J.F. Vansteenkiste, D.R. Spigel, C. Wadsworth, M. Taboada, P.A. Dennis, M. Ozguroglu, and S.J. Antonia. (2020). Three-Year Overall Survival with Durvalumab after Chemoradiotherapy in Stage III NSCLC-Update from PACIFIC. *J Thorac Oncol*. 15:288-293. 10.1016/j.jtho.2019.10.002

Gross, T.J., and G.W. Hunninghake. (2001). Idiopathic pulmonary fibrosis. *N Engl J Med*. 345:517-525. 10.1056/NEJMra003200

Gu, Y., K.J. Seidl, G.A. Rathbun, C. Zhu, J.P. Manis, N. van der Stoep, L. Davidson, H.L. Cheng, J.M. Sekiguchi, K. Frank, P. Stanhope-Baker, M.S. Schlissel, D.B. Roth, and F.W. Alt. (1997). Growth retardation and leaky SCID phenotype of Ku70-deficient mice. *Immunity*. 7:653-665. 10.1016/s1074-7613(00)80386-6

Gunning, W.T., A. Castonguay, P.J. Goldblatt, and G.D. Stoner. (1991). Strain A/J mouse lung adenoma growth patterns vary when induced by different carcinogens. *Toxicol Pathol*. 19:168-175. 10.1177/019262339101900212

Gurley, K.E., R.D. Moser, and C.J. Kemp. (2015). Induction of Lung Tumors in Mice with Urethane. *Cold Spring Harb Protoc*. 2015:pdb prot077446. 10.1101/pdb.prot077446

Haahr, P., S. Hoffmann, M.A. Tollenaere, T. Ho, L.I. Toledo, M. Mann, S. Bekker-Jensen, M. Raschle, and N. Mailand. (2016). Activation of the ATR kinase by the RPA-binding protein ETAA1. *Nat Cell Biol*. 18:1196-1207. 10.1038/ncb3422

Hall, E.J., and A.J. Giaccia. (2012). Radiobiology for the radiologist. Wolters Kluwer Health/Lippincott Williams & Wilkins, Philadelphia. ix, 546 p. pp.

Hammond, E.M., M.J. Dorie, and A.J. Giaccia. (2004). Inhibition of ATR leads to increased sensitivity to hypoxia/reoxygenation. *Cancer Res*. 64:6556-6562. 10.1158/0008-5472.CAN-04-1520

Hanahan, D., and R.A. Weinberg. (2000). The hallmarks of cancer. *Cell*. 100:57-70.

Hanahan, D., and R.A. Weinberg. (2011). Hallmarks of cancer: the next generation. *Cell*. 144:646-674. 10.1016/j.cell.2011.02.013

Hernandez, L.G., and P.G. Forkert. (2007). In vivo mutagenicity of vinyl carbamate and ethyl carbamate in lung and small intestine of F1 (Big Blue x A/J) transgenic mice. *Int J Cancer*. 120:1426-1433. 10.1002/ijc.22502

Hirao, A., Y.Y. Kong, S. Matsuoka, A. Wakeham, J. Ruland, H. Yoshida, D. Liu, S.J. Elledge, and T.W. Mak. (2000). DNA damage-induced activation of p53 by the checkpoint kinase Chk2. *Science*. 287:1824-1827. 10.1126/science.287.5459.1824

Hirsch, F.R., G.V. Scagliotti, J.L. Mulshine, R. Kwon, W.J. Curran, Jr., Y.L. Wu, and L. Paz-Ares. (2017). Lung cancer: current therapies and new targeted treatments. *Lancet*. 389:299-311. 10.1016/S0140-6736(16)30958-8

Hoffman, R.M., and R. Sanchez. (2017). Lung Cancer Screening. *Med Clin North Am*. 101:769-785. 10.1016/j.mcna.2017.03.008

Horio, Y., A. Chen, P. Rice, J.A. Roth, A.M. Malkinson, and D.S. Schrump. (1996). Ki-ras and p53 mutations are early and late events, respectively, in urethane-induced pulmonary carcinogenesis in A/J mice. *Mol Carcinog*. 17:217-223. 10.1002/(SICI)1098-2744(199612)17:4<217::AID-MC5>3.0.CO;2-A

Hosoya, N., and K. Miyagawa. (2014). Targeting DNA damage response in cancer therapy. *Cancer Sci*. 105:370-388. 10.1111/cas.12366

Hubner, R.H., W. Gitter, N.E. El Mokhtari, M. Mathiak, M. Both, H. Bolte, S. Freitag-Wolf, and B. Bewig. (2008). Standardized quantification of pulmonary fibrosis in histological samples. *Biotechniques*. 44:507-511, 514-507. 10.2144/000112729

Huhn, D., H.A. Bolck, and A.A. Sartori. (2013). Targeting DNA double-strand break signalling and repair: recent advances in cancer therapy. *Swiss Med Wkly*. 143:w13837. 10.4414/smw.2013.13837

U.S. Department of Health and Human Services. (2017). Common Terminology Criteria for Adverse Events (CTCAE). Retrieved 5 October 2020, from https://ctep.cancer.gov/protocolDevelopment/electronic_applications/docs/CTCAE_v5_Quick_Reference_8.5x11.pdf

Ishikawa, Y., T. Kozakai, H. Morita, K. Saida, S. Oka, and Y. Masuo. (2006). Rapid detection of mycoplasma contamination in cell cultures using SYBR Green-based real-time polymerase chain reaction. *In Vitro Cell Dev Biol Anim*. 42:63-69. 10.1290/0505035.1

Jackson, I.L., Z. Vujaskovic, and J.D. Down. (2010). Revisiting strain-related differences in radiation sensitivity of the mouse lung: recognizing and avoiding the confounding effects of pleural effusions. *Radiat Res*. 173:10-20. 10.1667/RR1911.1

Jackson, I.L., Z. Vujaskovic, and J.D. Down. (2011). A further comparison of pathologies after thoracic irradiation among different mouse strains: finding the best preclinical model for evaluating therapies directed against radiation-induced lung damage. *Radiat Res*. 175:510-518. 10.1667/RR2421.1

Jackson, S.P., and J. Bartek. (2009). The DNA-damage response in human biology and disease. *Nature*. 461:1071-1078. 10.1038/nature08467

Jain, V., and A.T. Berman. (2018). Radiation Pneumonitis: Old Problem, New Tricks. *Cancers (Basel)*. 10. 10.3390/cancers10070222

Janker, F., W. Weder, J.H. Jang, and W. Jungraithmayr. (2018). Preclinical, non-genetic models of lung adenocarcinoma: a comparative survey. *Oncotarget*. 9:30527-30538. 10.18632/oncotarget.25668

Jeremic, B., Y. Shibamoto, B. Milicic, A. Dagovic, N. Nikolic, J. Aleksandrovic, L. Acimovic, and S. Milisavljevic. (2003). Impact of treatment interruptions due to toxicity on outcome of patients with early stage (I/II) non-small-cell lung cancer (NSCLC) treated with hyperfractionated radiation therapy alone. *Lung Cancer*. 40:317-323. 10.1016/s0169-5002(03)00078-3

Jerzak, K.J., T. Mancuso, and A. Eisen. (2018). Ataxia-telangiectasia gene (ATM) mutation heterozygosity in breast cancer: a narrative review. *Curr Oncol*. 25:e176-e180. 10.3747/co.25.3707

Jiang, H., H.C. Reinhardt, J. Bartkova, J. Tommiska, C. Blomqvist, H. Nevanlinna, J. Bartek, M.B. Yaffe, and M.T. Hemann. (2009). The combined status of ATM and p53 link tumor development with therapeutic response. *Genes Dev*. 23:1895-1909. 10.1101/gad.1815309

Jiang, W., V.M. Estes, X.S. Wang, Z. Shao, B.J. Lee, X. Lin, J.L. Crowe, and S. Zha. (2019). Phosphorylation at S2053 in Murine (S2056 in Human) DNA-PKcs Is Dispensable for Lymphocyte Development and Class Switch Recombination. *J Immunol*. 203:178-187. 10.4049/jimmunol.1801657

Jiang, Y., J. Martin, M. Alkadhimi, K. Shigemori, P. Kinchesh, S. Gilchrist, V. Kersemans, S. Smart, J.M. Thompson, M.A. Hill, M.J. O'Connor, B.R. Davies, and A.J. Ryan. (2021). Olaparib increases the therapeutic index of hemithoracic irradiation compared with hemithoracic irradiation alone in a mouse lung cancer model. *Br J Cancer*. 10.1038/s41416-021-01296-y

Jin, H., Y. Yoo, Y. Kim, Y. Kim, J. Cho, and Y.S. Lee. (2020). Radiation-Induced Lung Fibrosis: Preclinical Animal Models and Therapeutic Strategies. *Cancers (Basel)*. 12. 10.3390/cancers12061561

Jin, M.H., and D.Y. Oh. (2019). ATM in DNA repair in cancer. *Pharmacol Ther*. 203:107391. 10.1016/j.pharmthera.2019.07.002

Jucaite, A., P. Stenkrona, Z. Cselenyi, S. De Vita, N. Buil-Bruna, K. Varnas, A. Savage, A. Varrone, P. Johnstrom, M. Schou, C. Davison, A. Sykes, V.P. Reddy, M. Hoch, A. Vazquez-Romero, M.M. Moein, C. Halldin, M.S. Merchant, M. Pass, and L. Farde. (2020). Brain exposure of the ATM inhibitor AZD1390 in humans - a positron emission tomography (PET) study. *Neuro Oncol*. 10.1093/neuonc/noaa238

Karnitz, L.M., and L. Zou. (2015). Molecular Pathways: Targeting ATR in Cancer Therapy. *Clin Cancer Res*. 21:4780-4785. 10.1158/1078-0432.CCR-15-0479

Kasmann, L., A. Dietrich, C.A. Staab-Weijnitz, F. Manapov, J. Behr, A. Rimner, B. Jeremic, S. Senan, D. De Ruysscher, K. Lauber, and C. Belka. (2020). Radiation-induced lung toxicity - cellular and molecular mechanisms of pathogenesis,

management, and literature review. *Radiat Oncol*. 15:214. 10.1186/s13014-020-01654-9

Katsuno, Y., A. Suzuki, K. Sugimura, K. Okumura, D.H. Zineldeen, M. Shimada, H. Niida, T. Mizuno, F. Hanaoka, and M. Nakanishi. (2009). Cyclin A-Cdk1 regulates the origin firing program in mammalian cells. *Proc Natl Acad Sci U S A*. 106:3184-3189. 10.1073/pnas.0809350106

Kellar, A., C. Egan, and D. Morris. (2015). Preclinical Murine Models for Lung Cancer: Clinical Trial Applications. *Biomed Res Int*. 2015:621324. 10.1155/2015/621324

Kim, C.F., E.L. Jackson, D.G. Kirsch, J. Grimm, A.T. Shaw, K. Lane, J. Kissil, K.P. Olive, A. Sweet-Cordero, R. Weissleder, and T. Jacks. (2005a). Mouse models of human non-small-cell lung cancer: raising the bar. *Cold Spring Harb Symp Quant Biol*. 70:241-250. 10.1101/sqb.2005.70.037

Kim, C.F., E.L. Jackson, A.E. Woolfenden, S. Lawrence, I. Babar, S. Vogel, D. Crowley, R.T. Bronson, and T. Jacks. (2005b). Identification of bronchioalveolar stem cells in normal lung and lung cancer. *Cell*. 121:823-835. 10.1016/j.cell.2005.03.032

Kim, K.S., S.U. Jeon, C.J. Lee, Y.E. Kim, S. Bok, B.J. Hong, D.Y. Park, G.O. Ahn, and H.J. Kim. (2016). Radiation-Induced Esophagitis In Vivo and In Vitro Reveals That Epidermal Growth Factor Is a Potential Candidate for Therapeutic Intervention Strategy. *Int J Radiat Oncol Biol Phys*. 95:1032-1041. 10.1016/j.ijrobp.2016.02.051

Kim, K.S., S. Song, Y.E. Kim, S.U. Jeon, S. Bok, B.J. Hong, C.J. Lee, G.O. Ahn, and H.J. Kim. (2015). Establishing a mouse model for radiation-induced esophagitis. *European Journal of Cancer*. 51:S119-S120. Doi 10.1016/S0959-8049(16)30347-1

Ko, E.C., D. Raben, and S.C. Formenti. (2018). The Integration of Radiotherapy with Immunotherapy for the Treatment of Non-Small Cell Lung Cancer. *Clin Cancer Res*. 24:5792-5806. 10.1158/1078-0432.CCR-17-3620

Kong, F.M., T. Ritter, D.J. Quint, S. Senan, L.E. Gaspar, R.U. Komaki, C.W. Hurkmans, R. Timmerman, A. Bezjak, J.D. Bradley, B. Movsas, L. Marsh, P. Okunieff, H. Choy, and W.J. Curran, Jr. (2011). Consideration of dose limits for organs at risk of thoracic radiotherapy: atlas for lung, proximal bronchial tree, esophagus, spinal cord, ribs, and brachial plexus. *Int J Radiat Oncol Biol Phys*. 81:1442-1457. 10.1016/j.ijrobp.2010.07.1977

Kumagai, A., J. Lee, H.Y. Yoo, and W.G. Dunphy. (2006). TopBP1 activates the ATR-ATRIP complex. *Cell*. 124:943-955. 10.1016/j.cell.2005.12.041

Kwok, M., N. Davies, A. Agathanggelou, E. Smith, C. Oldreive, E. Petermann, G. Stewart, J. Brown, A. Lau, G. Pratt, H. Parry, M. Taylor, P. Moss, P. Hillmen, and T. Stankovic. (2016). ATR inhibition induces synthetic lethality and overcomes chemoresistance in TP53- or ATM-defective chronic lymphocytic leukemia cells. *Blood*. 127:582-595. 10.1182/blood-2015-05-644872

Kwon, M.C., and A. Berns. (2013). Mouse models for lung cancer. *Mol Oncol*. 7:165-177. 10.1016/j.molonc.2013.02.010

Landau, D.A., S.L. Carter, P. Stojanov, A. McKenna, K. Stevenson, M.S. Lawrence, C. Sougnez, C. Stewart, A. Sivachenko, L. Wang, Y. Wan, W. Zhang, S.A. Shukla, A. Vartanov, S.M. Fernandes, G. Saksena, K. Cibulskis, B. Tesar, S. Gabriel, N. Hacohen, M. Meyerson, E.S. Lander, D. Neuberg, J.R. Brown, G. Getz, and C.J. Wu. (2013). Evolution and impact of subclonal mutations in chronic lymphocytic leukemia. *Cell*. 152:714-726. 10.1016/j.cell.2013.01.019

Lee, J., A. Kumagai, and W.G. Dunphy. (2007). The Rad9-Hus1-Rad1 checkpoint clamp regulates interaction of TopBP1 with ATR. *J Biol Chem*. 282:28036-28044. 10.1074/jbc.M704635200

Lee, Y.C., Q. Zhou, J. Chen, and J. Yuan. (2016). RPA-Binding Protein ETAA1 Is an ATR Activator Involved in DNA Replication Stress Response. *Curr Biol*. 26:3257-3268. 10.1016/j.cub.2016.10.030

Lin, L., M.F. Festing, T.R. Devereux, K.A. Crist, S.C. Christiansen, Y. Wang, A. Yang, K. Svenson, B. Paigen, A.M. Malkinson, and M. You. (1998). Additional evidence that the K-ras protooncogene is a candidate for the major mouse pulmonary adenoma susceptibility (Pas-1) gene. *Exp Lung Res*. 24:481-497. 10.3109/01902149809087382

Liu, Q., S. Guntuku, X.S. Cui, S. Matsuoka, D. Cortez, K. Tamai, G. Luo, S. Carattini-Rivera, F. DeMayo, A. Bradley, L.A. Donehower, and S.J. Elledge. (2000). Chk1 is an essential kinase that is regulated by Atr and required for the G(2)/M DNA damage checkpoint. *Genes Dev*. 14:1448-1459.

Lloyd, R.L., P.W.G. Wijnhoven, A. Ramos-Montoya, Z. Wilson, G. Illuzzi, K. Falenta, G.N. Jones, N. James, C.D. Chabbert, J. Stott, E. Dean, A. Lau, and L.A. Young. (2020). Combined PARP and ATR inhibition potentiates genome instability and cell death in ATM-deficient cancer cells. *Oncogene*. 39:4869-4883. 10.1038/s41388-020-1328-y

Lomax, M.E., L.K. Folkes, and P. O'Neill. (2013). Biological consequences of radiation-induced DNA damage: relevance to radiotherapy. *Clin Oncol (R Coll Radiol)*. 25:578-585. 10.1016/j.clon.2013.06.007

Lopes, M., C. Cotta-Ramusino, A. Pellicioli, G. Liberi, P. Plevani, M. Muzi-Falconi, C.S. Newlon, and M. Foiani. (2001). The DNA replication checkpoint response stabilizes stalled replication forks. *Nature*. 412:557-561. 10.1038/35087613

Lord, C.J., and A. Ashworth. (2012). The DNA damage response and cancer therapy. *Nature*. 481:287-294. 10.1038/nature10760

Ma, J., J. Setton, L. Morris, P.B. Albornoz, C. Barker, B.H. Lok, E. Sherman, N. Katabi, K. Beal, I. Ganly, S.N. Powell, N. Lee, T.A. Chan, and N. Riaz. (2017). Genomic analysis of exceptional responders to radiotherapy reveals somatic mutations in ATM. *Oncotarget*. 8:10312-10323. 10.18632/oncotarget.14400

Malkinson, A.M. (1992). Primary lung tumors in mice: an experimentally manipulable model of human adenocarcinoma. *Cancer Res*. 52:2670s-2676s.

Matsuoka, S., B.A. Ballif, A. Smogorzewska, E.R. McDonald, 3rd, K.E. Hurov, J. Luo, C.E. Bakalarski, Z. Zhao, N. Solimini, Y. Lerenthal, Y. Shiloh, S.P. Gygi, and S.J. Elledge. (2007). ATM and ATR substrate analysis reveals extensive protein

networks responsive to DNA damage. *Science*. 316:1160-1166. 10.1126/science.1140321

Matsuoka, S., M. Huang, and S.J. Elledge. (1998). Linkage of ATM to cell cycle regulation by the Chk2 protein kinase. *Science*. 282:1893-1897. 10.1126/science.282.5395.1893

Mazzone, P.J., G.A. Silvestri, S. Patel, J.P. Kanne, L.S. Kinsinger, R.S. Wiener, G. Soo Hoo, and F.C. Detterbeck. (2018). Screening for Lung Cancer: CHEST Guideline and Expert Panel Report. *Chest*. 153:954-985. 10.1016/j.chest.2018.01.016

McBride, W.H., and D. Schaue. (2020). Radiation-induced tissue damage and response. *J Pathol*. 250:647-655. 10.1002/path.5389

McDonald, S., P. Rubin, T.L. Phillips, and L.B. Marks. (1995). Injury to the lung from cancer therapy: clinical syndromes, measurable endpoints, and potential scoring systems. *Int J Radiat Oncol Biol Phys*. 31:1187-1203. 10.1016/0360-3016(94)00429-O

Medova, M., M. Medo, L. Hovhannisyan, C. Munoz-Maldonado, D.M. Aebersold, and Y. Zimmer. (2020). DNA-PK in human malignant disorders: Mechanisms and implications for pharmacological interventions. *Pharmacol Ther*. 215:107617. 10.1016/j.pharmthera.2020.107617

Mei, L., J. Zhang, K. He, and J. Zhang. (2019). Ataxia telangiectasia and Rad3-related inhibitors and cancer therapy: where we stand. *J Hematol Oncol*. 12:43. 10.1186/s13045-019-0733-6

Mentzer, S.J. (2018). The puzzling mechanism of compensatory lung growth. *Stem Cell Investig*. 5:8. 10.21037/sci.2018.03.01

Meuwissen, R., and A. Berns. (2005). Mouse models for human lung cancer. *Genes Dev*. 19:643-664. 10.1101/gad.1284505

Meuwissen, R., S.C. Linn, M. van der Valk, W.J. Mooi, and A. Berns. (2001). Mouse model for lung tumorigenesis through Cre/lox controlled sporadic activation of the K-Ras oncogene. *Oncogene*. 20:6551-6558. 10.1038/sj.onc.1204837

Middleton, F.K., J.R. Pollard, and N.J. Curtin. (2018). The Impact of p53 Dysfunction in ATR Inhibitor Cytotoxicity and Chemo- and Radiosensitisation. *Cancers (Basel)*. 10. 10.3390/cancers10080275

Miller, Y.E., L.D. Dwyer-Nield, R.L. Keith, M. Le, W.A. Franklin, and A.M. Malkinson. (2003). Induction of a high incidence of lung tumors in C57BL/6 mice with multiple ethyl carbamate injections. *Cancer Lett*. 198:139-144. 10.1016/s0304-3835(03)00309-4

Min, A., S.A. Im, H. Jang, S. Kim, M. Lee, D.K. Kim, Y. Yang, H.J. Kim, K.H. Lee, J.W. Kim, T.Y. Kim, D.Y. Oh, J. Brown, A. Lau, M.J. O'Connor, and Y.J. Bang. (2017). AZD6738, A Novel Oral Inhibitor of ATR, Induces Synthetic Lethality with ATM Deficiency in Gastric Cancer Cells. *Mol Cancer Ther*. 16:566-577. 10.1158/1535-7163.MCT-16-0378

Ming, X., Y. Feng, C. Yang, W. Wang, P. Wang, and J. Deng. (2016). Radiation-induced heart disease in lung cancer radiotherapy: A dosimetric update. *Medicine (Baltimore)*. 95:e5051. 10.1097/MD.0000000000005051

Mohiuddin, I.S., and M.H. Kang. (2019). DNA-PK as an Emerging Therapeutic Target in Cancer. *Front Oncol*. 9:635. 10.3389/fonc.2019.00635

Moolenbeek, C., and E.J. Ruitenberg. (1981). The "Swiss roll": a simple technique for histological studies of the rodent intestine. *Lab Anim*. 15:57-59.

Moro, M., G. Bertolini, M. Tortoreto, U. Pastorino, G. Sozzi, and L. Roz. (2012). Patient-derived xenografts of non small cell lung cancer: resurgence of an old model for investigation of modern concepts of tailored therapy and cancer stem cells. *J Biomed Biotechnol*. 2012:568567. 10.1155/2012/568567

Mostofi, F.K., and C.D. Larsen. (1951). Carcinogenic and toxic effects of urethane in animals. *Am J Clin Pathol*. 21:342-348.

Murro, D., and S. Jakate. (2015). Radiation esophagitis. *Arch Pathol Lab Med*. 139:827-830. 10.5858/arpa.2014-0111-RS

National Lung Screening Trial Research Team, D.R. Aberle, A.M. Adams, C.D. Berg, W.C. Black, J.D. Clapp, R.M. Fagerstrom, I.F. Gareen, C. Gatsonis, P.M. Marcus, and J.D. Sicks. (2011). Reduced lung-cancer mortality with low-dose computed tomographic screening. *N Engl J Med*. 365:395-409. 10.1056/NEJMoa1102873

National Cancer Registration and Analysis Service. (2015). Chemotherapy, Radiotherapy and Tumour Resection by Tumour & Patient Characteristics in England, 2013 – 2015. Retrieved from http://www.ncin.org.uk/view?rid=3681

Ng, N., K. Purshouse, I.P. Foskolou, M.M. Olcina, and E.M. Hammond. (2018). Challenges to DNA replication in hypoxic conditions. *FEBS J*. 285:1563-1571. 10.1111/febs.14377

National Health Service. (2019). Diagnosis - Lung Cancer. Retrieved 14 September 2020, from https://www.nhs.uk/conditions/lung-cancer/diagnosis/

National Institute for Health and Care Excellence. (2020). 2020 Surveillance of suspected cancer: recognition and referral (NICE guideline NG12). Retrieved from https://www.ncbi.nlm.nih.gov/pubmed/32040285

Nussenzweig, A., K. Sokol, P. Burgman, L. Li, and G.C. Li. (1997). Hypersensitivity of Ku80-deficient cell lines and mice to DNA damage: the effects of ionizing radiation on growth, survival, and development. *Proc Natl Acad Sci U S A*. 94:13588-13593. 10.1073/pnas.94.25.13588

Nyman, J., A. Hallqvist, J.A. Lund, O.T. Brustugun, B. Bergman, P. Bergstrom, S. Friesland, R. Lewensohn, E. Holmberg, and I. Lax. (2016). SPACE - A randomized study of SBRT vs conventional fractionated radiotherapy in medically inoperable stage I NSCLC. *Radiother Oncol*. 121:1-8. 10.1016/j.radonc.2016.08.015

O'Connor, M.J. (2015). Targeting the DNA Damage Response in Cancer. *Mol Cell*. 60:547-560. 10.1016/j.molcel.2015.10.040

Ochi, T., A.N. Blackford, J. Coates, S. Jhujh, S. Mehmood, N. Tamura, J. Travers, Q. Wu, V.M. Draviam, C.V. Robinson, T.L. Blundell, and S.P. Jackson. (2015). DNA repair. PAXX, a paralog of XRCC4 and XLF, interacts with Ku to promote DNA double-strand break repair. *Science*. 347:185-188. 10.1126/science.1261971

Ohno, J., Y. Horio, Y. Sekido, Y. Hasegawa, M. Takahashi, J. Nishizawa, H. Saito, F. Ishikawa, and K. Shimokata. (2001). Telomerase activation and p53 mutations in urethane-induced A/J mouse lung tumor development. *Carcinogenesis*. 22:751-756.

Okayasu, R., K. Suetomi, Y. Yu, A. Silver, J.S. Bedford, R. Cox, and R.L. Ullrich. (2000). A deficiency in DNA repair and DNA-PKcs expression in the radiosensitive BALB/c mouse. *Cancer Res*. 60:4342-4345.

Pan, S., J. Wang, A. Wu, Z. Guo, Z. Wang, L. Zheng, Y. Dai, L. Zhu, J. Nie, T.K. Hei, G. Zhou, Y. Li, B. Li, and W. Hu. (2020). Radiation Exposure-Induced Changes in the Immune Cells and Immune Factors of Mice With or Without Primary Lung Tumor. *Dose Response*. 18:1559325820926744. 10.1177/1559325820926744

Patel, A., E. Seraia, D. Ebner, and A.J. Ryan. (2020). Adefovir dipivoxil induces DNA replication stress and augments ATR inhibitor-related cytotoxicity. *Int J Cancer*. 147:1474-1484. 10.1002/ijc.32966

Paun, A., and C.K. Haston. (2012). Genomic and genome-wide association of susceptibility to radiation-induced fibrotic lung disease in mice. *Radiother Oncol*. 105:350-357. 10.1016/j.radonc.2012.08.004

PDQ® Adult Treatment Editorial Board. PDQ Non-Small Cell Lung Cancer Treatment. Bethesda, MD:National Cancer Institute. Updated 19 November 2020. Available at: https://www.cancer.gov/types/lung/hp/non-small-cell-lung-treatment-pdq. Accessed 14 December 2020. [PMID: 26389304]

Peterson, S.R., A. Kurimasa, M. Oshimura, W.S. Dynan, E.M. Bradbury, and D.J. Chen. (1995). Loss of the catalytic subunit of the DNA-dependent protein kinase in DNA double-strand-break-repair mutant mammalian cells. *Proc Natl Acad Sci U S A*. 92:3171-3174. 10.1073/pnas.92.8.3171

Pilie, P.G., C. Tang, G.B. Mills, and T.A. Yap. (2019). State-of-the-art strategies for targeting the DNA damage response in cancer. *Nat Rev Clin Oncol*. 16:81-104. 10.1038/s41571-018-0114-z

Pires, I.M., M.M. Olcina, S. Anbalagan, J.R. Pollard, P.M. Reaper, P.A. Charlton, W.G. McKenna, and E.M. Hammond. (2012). Targeting radiation-resistant hypoxic tumour cells through ATR inhibition. *Br J Cancer*. 107:291-299. 10.1038/bjc.2012.265

Prewett, S.L., S. Aslam, M.V. Williams, and D. Gilligan. (2012). The management of lung cancer: a UK survey of oncologists. *Clin Oncol (R Coll Radiol)*. 24:402-409. 10.1016/j.clon.2012.03.005

The Royal College of Radiologists. (2019). Lung Cancer. *In* Radiology dose fractionation, third edition. The Royal College of Radiologists, London.

Ramroth, J., D.J. Cutter, S.C. Darby, G.S. Higgins, P. McGale, M. Partridge, and C.W. Taylor. (2016). Dose and Fractionation in Radiation Therapy of Curative Intent for Non-Small Cell Lung Cancer: Meta-Analysis of Randomized Trials. *Int J Radiat Oncol Biol Phys*. 96:736-747. 10.1016/j.ijrobp.2016.07.022

Richards, T.B., M.C. White, and R.S. Caraballo. (2014). Lung cancer screening with low-dose computed tomography for primary care providers. *Prim Care*. 41:307-330. 10.1016/j.pop.2014.02.007

Robinson, S.D., B.A. Tahir, K.A.R. Absalom, A. Lankathilake, T. Das, C. Lee, P.M. Fisher, E. Bates, and M.Q.F. Hatton. (2020). Radical accelerated radiotherapy for non-small cell lung cancer (NSCLC): A 5-year retrospective review of two dose fractionation schedules. *Radiother Oncol*. 143:37-43. 10.1016/j.radonc.2019.08.025

Rogakou, E.P., D.R. Pilch, A.H. Orr, V.S. Ivanova, and W.M. Bonner. (1998). DNA double-stranded breaks induce histone H2AX phosphorylation on serine 139. *J Biol Chem*. 273:5858-5868. 10.1074/jbc.273.10.5858

Rose, M., J.T. Burgess, K. O'Byrne, D.J. Richard, and E. Bolderson. (2020). PARP Inhibitors: Clinical Relevance, Mechanisms of Action and Tumor Resistance. *Front Cell Dev Biol*. 8:564601. 10.3389/fcell.2020.564601

Rundle, S., A. Bradbury, Y. Drew, and N.J. Curtin. (2017). Targeting the ATR-CHK1 Axis in Cancer Therapy. *Cancers (Basel)*. 9. 10.3390/cancers9050041

Sabatini, D.M., H. Erdjument-Bromage, M. Lui, P. Tempst, and S.H. Snyder. (1994). RAFT1: a mammalian protein that binds to FKBP12 in a rapamycin-dependent fashion and is homologous to yeast TORs. *Cell*. 78:35-43. 10.1016/0092-8674(94)90570-3

Saldivar, J.C., D. Cortez, and K.A. Cimprich. (2017). The essential kinase ATR: ensuring faithful duplication of a challenging genome. *Nat Rev Mol Cell Biol*. 18:622-636. 10.1038/nrm.2017.67

Santivasi, W.L., and F. Xia. (2014). Ionizing radiation-induced DNA damage, response, and repair. *Antioxid Redox Signal*. 21:251-259. 10.1089/ars.2013.5668

Sasso, F.S., G. Sasso, H.R. Marsiglia, G. de Palma, C. Schiavone, A. Barone, A. Polo, and R. Orecchia. (2001). Pharmacological and dietary prophylaxis and treatment of acute actinic esophagitis during mediastinal radiotherapy. *Dig Dis Sci*. 46:746-749. 10.1023/a:1010735914163

Savic, V., B. Yin, N.L. Maas, A.L. Bredemeyer, A.C. Carpenter, B.A. Helmink, K.S. Yang-Iott, B.P. Sleckman, and C.H. Bassing. (2009). Formation of dynamic gamma-H2AX domains along broken DNA strands is distinctly regulated by ATM and MDC1 and dependent upon H2AX densities in chromatin. *Mol Cell*. 34:298-310. 10.1016/j.molcel.2009.04.012

Savitsky, K., A. Bar-Shira, S. Gilad, G. Rotman, Y. Ziv, L. Vanagaite, D.A. Tagle, S. Smith, T. Uziel, S. Sfez, M. Ashkenazi, I. Pecker, M. Frydman, R. Harnik, S.R. Patanjali, A. Simmons, G.A. Clines, A. Sartiel, R.A. Gatti, L. Chessa, O. Sanal, M.F. Lavin, N.G. Jaspers, A.M. Taylor, C.F. Arlett, T. Miki, S.M. Weissman, M. Lovett, F.S. Collins, and Y. Shiloh. (1995). A single ataxia telangiectasia gene

with a product similar to PI-3 kinase. *Science*. 268:1749-1753. 10.1126/science.7792600

Saxton, R.A., and D.M. Sabatini. (2017). mTOR Signaling in Growth, Metabolism, and Disease. *Cell*. 168:960-976. 10.1016/j.cell.2017.02.004

Scheenstra, A.E., M.M. Rossi, J.S. Belderbos, E.M. Damen, J.V. Lebesque, and J.J. Sonke. (2014). Alpha/beta ratio for normal lung tissue as estimated from lung cancer patients treated with stereotactic body and conventionally fractionated radiation therapy. *Int J Radiat Oncol Biol Phys*. 88:224-228. 10.1016/j.ijrobp.2013.10.015

Schoppy, D.W., R.L. Ragland, O. Gilad, N. Shastri, A.A. Peters, M. Murga, O. Fernandez-Capetillo, J.A. Diehl, and E.J. Brown. (2012). Oncogenic stress sensitizes murine cancers to hypomorphic suppression of ATR. *J Clin Invest*. 122:241-252. 10.1172/JCI58928

Senan, S., D. De Ruysscher, P. Giraud, R. Mirimanoff, V. Budach, R. Radiotherapy Group of European Organization for, and C. Treatment of. (2004). Literature-based recommendations for treatment planning and execution in high-dose radiotherapy for lung cancer. *Radiother Oncol*. 71:139-146. 10.1016/j.radonc.2003.09.007

Shadad, A.K., F.J. Sullivan, J.D. Martin, and L.J. Egan. (2013). Gastrointestinal radiation injury: symptoms, risk factors and mechanisms. *World J Gastroenterol*. 19:185-198. 10.3748/wjg.v19.i2.185

Shakhnovich, V. (2018). It's Time to Reverse our Thinking: The Reverse Translation Research Paradigm. *Clin Transl Sci*. 11:98-99. 10.1111/cts.12538

Sharma, R.A., R. Plummer, J.K. Stock, T.A. Greenhalgh, O. Ataman, S. Kelly, R. Clay, R.A. Adams, R.D. Baird, L. Billingham, S.R. Brown, S. Buckland, H. Bulbeck, A.J. Chalmers, G. Clack, A.N. Cranston, L. Damstrup, R. Ferraldeschi, M.D. Forster, J. Golec, R.M. Hagan, E. Hall, A.R. Hanauske, K.J. Harrington, T. Haswell, M.A. Hawkins, T. Illidge, H. Jones, A.S. Kennedy, F. McDonald, T. Melcher, J.P. O'Connor, J.R. Pollard, M.P. Saunders, D. Sebag-Montefiore, M. Smitt, J. Staffurth, I.J. Stratford, S.R. Wedge, and N.C.A.-P.J.W. Group. (2016). Clinical development of new drug-radiotherapy combinations. *Nat Rev Clin Oncol*. 13:627-642. 10.1038/nrclinonc.2016.79

Shechter, D., V. Costanzo, and J. Gautier. (2004). ATR and ATM regulate the timing of DNA replication origin firing. *Nat Cell Biol*. 6:648-655. 10.1038/ncb1145

Shen, C., and P.J. Houghton. (2013). The mTOR pathway negatively controls ATM by up-regulating miRNAs. *Proc Natl Acad Sci U S A*. 110:11869-11874. 10.1073/pnas.1220898110

Shiloh, Y. (2006). The ATM-mediated DNA-damage response: taking shape. *Trends Biochem Sci*. 31:402-410. 10.1016/j.tibs.2006.05.004

Shiloh, Y., and Y. Ziv. (2013). The ATM protein kinase: regulating the cellular response to genotoxic stress, and more. *Nat Rev Mol Cell Biol*. 14:197-210. 10.1038/nrm3546

Singh, M., C.L. Murriel, and L. Johnson. (2012). Genetically engineered mouse models: closing the gap between preclinical data and trial outcomes. *Cancer Res*. 72:2695-2700. 10.1158/0008-5472.CAN-11-2786

Sonis, S.T. (1998). Mucositis as a biological process: a new hypothesis for the development of chemotherapy-induced stomatotoxicity. *Oral Oncol*. 34:39-43. 10.1016/s1368-8375(97)00053-5

Spella, M., I. Lilis, M.A. Pepe, Y. Chen, M. Armaka, A.S. Lamort, D.E. Zazara, F. Roumelioti, M. Vreka, N.I. Kanellakis, D.E. Wagner, A.D. Giannou, V. Armenis, K.A. Arendt, L.V. Klotz, D. Toumpanakis, V. Karavana, S.G. Zakynthinos, I. Giopanou, A. Marazioti, V. Aidinis, R. Sotillo, and G.T. Stathopoulos. (2019). Club cells form lung adenocarcinomas and maintain the alveoli of adult mice. *Elife*. 8. 10.7554/eLife.45571

Steel, G.G., T.J. McMillan, and J.H. Peacock. (1989). The 5Rs of radiobiology. *Int J Radiat Biol*. 56:1045-1048. 10.1080/09553008914552491

Stone, H.B., E.J. Bernhard, C.N. Coleman, J. Deye, J. Capala, J.B. Mitchell, and J.M. Brown. (2016). Preclinical Data on Efficacy of 10 Drug-Radiation Combinations: Evaluations, Concerns, and Recommendations. *Transl Oncol*. 9:46-56. 10.1016/j.tranon.2016.01.002

Sundberg, J.P., C.A. Hanson, D.R. Roop, K.S. Brown, and H.G. Bedigian. (1991). Myoepitheliomas in inbred laboratory mice. *Vet Pathol*. 28:313-323. 10.1177/030098589102800408

Takizawa, C.G., and D.O. Morgan. (2000). Control of mitosis by changes in the subcellular location of cyclin-B1-Cdk1 and Cdc25C. *Curr Opin Cell Biol*. 12:658-665. 10.1016/s0955-0674(00)00149-6

Tekatli, H., N. Haasbeek, M. Dahele, P. De Haan, W. Verbakel, E. Bongers, S. Hashemi, E. Nossent, F. Spoelstra, A.J. de Langen, B. Slotman, and S. Senan. (2016). Outcomes of Hypofractionated High-Dose Radiotherapy in Poor-Risk Patients with "Ultracentral" Non-Small Cell Lung Cancer. *J Thorac Oncol*. 11:1081-1089. 10.1016/j.jtho.2016.03.008

Tibbetts, R.S., K.M. Brumbaugh, J.M. Williams, J.N. Sarkaria, W.A. Cliby, S.Y. Shieh, Y. Taya, C. Prives, and R.T. Abraham. (1999). A role for ATR in the DNA damage-induced phosphorylation of p53. *Genes Dev*. 13:152-157. 10.1101/gad.13.2.152

Tibbetts, R.S., D. Cortez, K.M. Brumbaugh, R. Scully, D. Livingston, S.J. Elledge, and R.T. Abraham. (2000). Functional interactions between BRCA1 and the checkpoint kinase ATR during genotoxic stress. *Genes Dev*. 14:2989-3002. 10.1101/gad.851000

Timmerman, R., R. McGarry, C. Yiannoutsos, L. Papiez, K. Tudor, J. DeLuca, M. Ewing, R. Abdulrahman, C. DesRosiers, M. Williams, and J. Fletcher. (2006). Excessive toxicity when treating central tumors in a phase II study of stereotactic body radiation therapy for medically inoperable early-stage lung cancer. *Journal of Clinical Oncology*. 24:4833-4839. 10.1200/Jco.2006.07.5937

Titis, A.P., and P.G. Forkert. (2001). Strain-related differences in bioactivation of vinyl carbamate and formation of DNA adducts in lungs of A/J, CD-1, and C57BL/6 mice. *Toxicol Sci*. 59:82-91. 10.1093/toxsci/59.1.82

To, M.D., J. Perez-Losada, J.H. Mao, J. Hsu, T. Jacks, and A. Balmain. (2006). A functional switch from lung cancer resistance to susceptibility at the Pas1 locus in Kras2LA2 mice. *Nat Genet*. 38:926-930. 10.1038/ng1836

To, M.D., C.E. Wong, A.N. Karnezis, R. Del Rosario, R. Di Lauro, and A. Balmain. (2008). Kras regulatory elements and exon 4A determine mutation specificity in lung cancer. *Nat Genet*. 40:1240-1244. 10.1038/ng.211

Toledo, L.I., M. Murga, and O. Fernandez-Capetillo. (2011a). Targeting ATR and Chk1 kinases for cancer treatment: a new model for new (and old) drugs. *Mol Oncol*. 5:368-373. 10.1016/j.molonc.2011.07.002

Toledo, L.I., M. Murga, R. Zur, R. Soria, A. Rodriguez, S. Martinez, J. Oyarzabal, J. Pastor, J.R. Bischoff, and O. Fernandez-Capetillo. (2011b). A cell-based screen identifies ATR inhibitors with synthetic lethal properties for cancer-associated mutations. *Nat Struct Mol Biol*. 18:721-727. 10.1038/nsmb.2076

Topatana, W., S. Juengpanich, S. Li, J. Cao, J. Hu, J. Lee, K. Suliyanto, D. Ma, B. Zhang, M. Chen, and X. Cai. (2020). Advances in synthetic lethality for cancer therapy: cellular mechanism and clinical translation. *J Hematol Oncol*. 13:118. 10.1186/s13045-020-00956-5

Tran Chau, V., W. Liu, M. Gerbe de Thore, L. Meziani, M. Mondini, M.J. O'Connor, E. Deutsch, and C. Clemenson. (2020). Differential therapeutic effects of PARP and ATR inhibition combined with radiotherapy in the treatment of subcutaneous versus orthotopic lung tumour models. *Br J Cancer*. 123:762-771. 10.1038/s41416-020-0931-6

Trenz, K., E. Smith, S. Smith, and V. Costanzo. (2006). ATM and ATR promote Mre11 dependent restart of collapsed replication forks and prevent accumulation of DNA breaks. *EMBO J*. 25:1764-1774. 10.1038/sj.emboj.7601045

Tsoutsou, P.G., and M.I. Koukourakis. (2006). Radiation pneumonitis and fibrosis: mechanisms underlying its pathogenesis and implications for future research. *Int J Radiat Oncol Biol Phys*. 66:1281-1293. 10.1016/j.ijrobp.2006.08.058

Tsujino, K., S. Hirota, M. Endo, K. Obayashi, Y. Kotani, M. Satouchi, T. Kado, and Y. Takada. (2003). Predictive value of dose-volume histogram parameters for predicting radiation pneumonitis after concurrent chemoradiation for lung cancer. *Int J Radiat Oncol Biol Phys*. 55:110-115. 10.1016/s0360-3016(02)03807-5

Tyldesley, S., C. Boyd, K. Schulze, H. Walker, and W.J. Mackillop. (2001). Estimating the need for radiotherapy for lung cancer: An evidence-based, epidemiologic approach. *Int J Radiat Oncol*. 49:973-985. Doi 10.1016/S0360-3016(00)01401-2

U.S. Food & Drug Administration. (2012). Harmful and Potentially Harmful Constituents in Tobacco Products and Tobacco Smoke: Established List. Retrieved 13 November 2020, from https://www.fda.gov/tobacco-products/rules-regulations-and-guidance/harmful-and-potentially-harmful-constituents-tobacco-products-and-tobacco-smoke-established-list

U.S. Preventive Services Task Force. (2013). Final Recommendation Statement Lung Cancer: Screening. Retrieved 15 September 2020, from https://www.uspreventiveservicestaskforce.org/uspstf/recommendation/lung-cancer-screening

Uto, K., D. Inoue, K. Shimuta, N. Nakajo, and N. Sagata. (2004). Chk1, but not Chk2, inhibits Cdc25 phosphatases by a novel common mechanism. *EMBO J*. 23:3386-3396. 10.1038/sj.emboj.7600328

Valdiglesias, V., S. Giunta, M. Fenech, M. Neri, and S. Bonassi. (2013). gammaH2AX as a marker of DNA double strand breaks and genomic instability in human population studies. *Mutat Res*. 753:24-40. 10.1016/j.mrrev.2013.02.001

van Luijk, P., H. Faber, H. Meertens, J.M. Schippers, J.A. Langendijk, S. Brandenburg, H.H. Kampinga, and R.P. Coppes. (2007). The impact of heart irradiation on dose-volume effects in the rat lung. *Int J Radiat Oncol Biol Phys*. 69:552-559. 10.1016/j.ijrobp.2007.05.065

van Luijk, P., A. Novakova-Jiresova, H. Faber, J.M. Schippers, H.H. Kampinga, H. Meertens, and R.P. Coppes. (2005). Radiation damage to the heart enhances early radiation-induced lung function loss. *Cancer Res*. 65:6509-6511. 10.1158/0008-5472.CAN-05-0786

Vendetti, F.P., A. Lau, S. Schamus, T.P. Conrads, M.J. O'Connor, and C.J. Bakkenist. (2015). The orally active and bioavailable ATR kinase inhibitor AZD6738 potentiates the anti-tumor effects of cisplatin to resolve ATM-deficient non-small cell lung cancer in vivo. *Oncotarget*. 6:44289-44305. 10.18632/oncotarget.6247

Vogelius, I.R., and S.M. Bentzen. (2012). A literature-based meta-analysis of clinical risk factors for development of radiation induced pneumonitis. *Acta Oncol*. 51:975-983. 10.3109/0284186X.2012.718093

Walls, G.M., J.B. Oughton, A.J. Chalmers, S. Brown, F. Collinson, M.D. Forster, K.N. Franks, A. Gilbert, G.G. Hanna, N. Hannaway, S. Harrow, T. Haswell, C.T. Hiley, S. Hinsley, M. Krebs, G. Murden, R. Phillip, A.J. Ryan, A. Salem, D. Sebag-Montefoire, P. Shaw, C.J. Twelves, K. Walker, R.J. Young, C. Faivre-Finn, and A. Greystoke. (2020). CONCORDE: A phase I platform study of novel agents in combination with conventional radiotherapy in non-small-cell lung cancer. *Clin Transl Radiat Oncol*. 25:61-66. 10.1016/j.ctro.2020.09.006

Weber, A.M., and A.J. Ryan. (2015). ATM and ATR as therapeutic targets in cancer. *Pharmacol Ther*. 149:124-138. 10.1016/j.pharmthera.2014.12.001

Westcott, P.M., K.D. Halliwill, M.D. To, M. Rashid, A.G. Rust, T.M. Keane, R. Delrosario, K.Y. Jen, K.E. Gurley, C.J. Kemp, E. Fredlund, D.A. Quigley, D.J. Adams, and A. Balmain. (2015). The mutational landscapes of genetic and chemical models of Kras-driven lung cancer. *Nature*. 517:489-492. 10.1038/nature13898

White, D.E., D. Negorev, H. Peng, A.V. Ivanov, G.G. Maul, and F.J. Rauscher, 3rd. (2006). KAP1, a novel substrate for PIKK family members, colocalizes with numerous damage response factors at DNA lesions. *Cancer Res*. 66:11594-11599. 10.1158/0008-5472.CAN-06-4138

White, M.R., A. Grendon, and H.B. Jones. (1970). Tumor incidence and cellularity in lungs of mice given various dose schedules of urethan. *Cancer Res*. 30:1030-1036.

Williams, M.V., J. Denekamp, and J.F. Fowler. (1985). A review of alpha/beta ratios for experimental tumors: implications for clinical studies of altered fractionation. *Int J Radiat Oncol Biol Phys*. 11:87-96. 10.1016/0360-3016(85)90366-9

Willoughby, C.E., Y. Jiang, H.D. Thomas, E. Willmore, S. Kyle, A. Wittner, N. Phillips, Y. Zhao, S.J. Tudhope, L. Prendergast, G. Junge, L.M. Lourenco, M.R.V. Finlay, P. Turner, J.M. Munck, R.J. Griffin, T. Rennison, J. Pickles, C. Cano, D.R. Newell, H.L. Reeves, A.J. Ryan, and S.R. Wedge. (2020). Selective DNA-PKcs inhibition extends the therapeutic index of localized radiotherapy and chemotherapy. *J Clin Invest*. 130:258-271. 10.1172/JCI127483

Wold, M.S., and T. Kelly. (1988). Purification and characterization of replication protein A, a cellular protein required for in vitro replication of simian virus 40 DNA. *Proc Natl Acad Sci U S A*. 85:2523-2527. 10.1073/pnas.85.8.2523

Wood, S.L., M. Pernemalm, P.A. Crosbie, and A.D. Whetton. (2015). Molecular histology of lung cancer: from targets to treatments. *Cancer Treat Rev*. 41:361-375. 10.1016/j.ctrv.2015.02.008

Xu, C., L. Zhou, L. Lu, T. Chen, S. Wei, X. Lin, and X. Lian. (2016). Inflammation has a role in urethaneinduced lung cancer in C57BL/6J mice. *Mol Med Rep*. 14:3323-3328. 10.3892/mmr.2016.5661

Yazbeck, V.Y., L. Villaruz, M. Haley, and M.A. Socinski. (2013). Management of normal tissue toxicity associated with chemoradiation (primary skin, esophagus, and lung). *Cancer J*. 19:231-237. 10.1097/PPO.0b013e31829453fb

Yu, Y., R. Okayasu, M.M. Weil, A. Silver, M. McCarthy, R. Zabriskie, S. Long, R. Cox, and R.L. Ullrich. (2001). Elevated breast cancer risk in irradiated BALB/c mice associates with unique functional polymorphism of the Prkdc (DNA-dependent protein kinase catalytic subunit) gene. *Cancer Res*. 61:1820-1824.

Yushkevich, P.A., J. Piven, H.C. Hazlett, R.G. Smith, S. Ho, J.C. Gee, and G. Gerig. (2006). User-guided 3D active contour segmentation of anatomical structures: significantly improved efficiency and reliability. *Neuroimage*. 31:1116-1128. 10.1016/j.neuroimage.2006.01.015

Zhou, B.B., and S.J. Elledge. (2000). The DNA damage response: putting checkpoints in perspective. *Nature*. 408:433-439. 10.1038/35044005

Zhou, X., W. Liu, X. Hu, A. Dorrance, R. Garzon, P.J. Houghton, and C. Shen. (2017). Regulation of CHK1 by mTOR contributes to the evasion of DNA damage barrier of cancer cells. *Sci Rep*. 7:1535. 10.1038/s41598-017-01729-w

Ziv, Y., D. Bielopolski, Y. Galanty, C. Lukas, Y. Taya, D.C. Schultz, J. Lukas, S. Bekker-Jensen, J. Bartek, and Y. Shiloh. (2006). Chromatin relaxation in response to DNA double-strand breaks is modulated by a novel ATM- and KAP-1 dependent pathway. *Nat Cell Biol*. 8:870-876. 10.1038/ncb1446

Zoncu, R., A. Efeyan, and D.M. Sabatini. (2011). mTOR: from growth signal integration to cancer, diabetes and ageing. *Nat Rev Mol Cell Biol*. 12:21-35. 10.1038/nrm3025

Zou, L., and S.J. Elledge. (2003). Sensing DNA damage through ATRIP recognition of RPA-ssDNA complexes. *Science*. 300:1542-1548. 10.1126/science.1083430

6. Appendix

Primary tumour	
TX	Primary tumour cannot be assessed, or tumour proven by the presence of malignant cells in sputum or bronchial washings but not visualised by imaging or bronchoscopy
T0	No evidence of primary tumour
Tis	Carcinoma in situ
T1	Tumour 3 cm or less in greatest dimension, surrounded by lung or visceral pleura, without bronchoscopic evidence of invasion more proximal than the lobar bronchus (i.e., not in the main bronchus)
T1mi	Minimally invasive adenocarcinoma: adenocarcinoma (≤ 3 cm in greatest dimension) with a predominantly lepidic pattern and ≤ 5 mm invasion in greatest dimension
T1a	Tumour ≤ 1 cm in greatest dimension. A superficial, spreading tumour of any size whose invasive components is limited to the bronchial wall and may extend proximal to the main bronchus also is classified as T1a, but these tumours are uncommon
T1b	Tumour > 1 cm but ≤ 2 cm in greatest dimension
T1c	Tumour > 2 cm but ≤ 3 cm in greatest dimension
T2	Tumour > 3 cm but ≤ 5 cm or having any of the following features: • Involves the main bronchus regardless of distance to the carina, but without involvement of the carina • Invades visceral pleura • Associated with atelectasis or obstructive pneumonitis that extends to the hilar region, involving part or all of the lung
T2a	Tumour > 3 cm but ≤ 4 cm in greatest dimension
T2b	Tumour > 4 cm but ≤ 5 cm in greatest dimension
T3	Tumour > 5 cm but ≤ 7 cm in greatest dimension or directly invading any of the following: parietal pleural, chest wall (including superior sulcus tumours), phrenic nerve, parietal pericardium; or separate tumour nodule(s) in the same lobe as the primary
T4	Tumour > 7 cm or tumour of any size invading one of more of the following: diaphragm, mediastinum, heart, great vessels, trachea, recurrent laryngeal nerve, oesophagus, vertebral body, or carina; separate tumour nodule(s) in an ipsilateral lobe different from that of the primary

Regional lymph node	
NX	Regional lymph nodes cannot be assessed
N0	No regional lymph node metastases
N1	Metastasis in ipsilateral peribronchial and/or ipsilateral hilar lymph nodes and intrapulmonary nodes, including involvement by direct extension
N2	Metastasis in ipsilateral mediastinal and/or subcarinal lymph node(s)
N3	Metastasis in contralateral mediastinal, contralateral hilar, ipsilateral or contralateral scalene, or supraclavicular lymph node(s)

Distant metastasis	
M0	No distant metastasis
M1	Distant metastasis
M1a	Separate tumour nodule(s) in a contralateral lobe; tumour with pleural or pericardial nodules or malignant pleural or pericardial effusion. Most pleural (pericardial) effusions with lung cancer are a result of the tumour. In a few patients, however, multiple microscopic examinations of pleural (pericardial) fluid are negative for tumour, and the fluid is nonbloody and not an exudate. If these elements and clinical judgment dictate that the effusion is not related to the tumour, the effusion should be excluded as a staging descriptor.
M1b	Single extrathoracic metastasis in a single organ (including involvement of a single nonregional node)
M1c	Multiple extrathoracic metastases in a single organ or multiple organs

Appendix Table 6.1. Definitions of TNM staging. (Amin and American Joint Committee on Cancer., 2017; Goldstraw et al., 2007).
Each category within Distant Metastasis is assigned a further subcategory of either c (clinical classification used for all patients with cancer identified before treatment) or p (pathological classification used for patients if surgery is the first definitive therapy and the category is confirmed microscopically).

Stage	Primary Tumour (T)	Regional lymph node (N)	Distant metastasis (M)
Occult carcinoma	TX	N0	M0
Stage 0	Tis	N0	M0
Stage IA1	T1mi/a	N0	M0
Stage IA2	T1b	N0	M0
Stage IA3	T1c	N0	M0
Stage IB	T2a	N0	M0
Stage IIA	T2b	N0	M0
Stage IIB	T1a/b/c	N1	M0
	T2a	N1	M0
	T2b	N1	M0
	T3	N0	M0
Stage IIIA	T1a/b/c	N2	M0
	T2a/b	N2	M0
	T3	N1	M0
	T4	N0/1	M0
Stage IIIB	T1a/b/c	N3	M0
	T2a/b	N3	M0
	T3	N2	M0
	T4	N2	M0
Stage IIIC	T3	N3	M0
	T4	N3	M0
Stage IV	Any T	Any N	M1
Stage IVA	Any T	Any N	M1a/b
Stage IVB	Any T	Any N	M1c

Appendix Table 6.2. TNM Staging within each prognostic stage. (Amin and American Joint Committee on Cancer., 2017; Goldstraw et al., 2007).

Reagent	Company (country)	Catalogue number
Acetic acid (glacial)	BDH Chemicals (UAE)	100012K
Antibody diluent	Abcam (UK)	ab64211
Aquatex®	Sigma-Aldrich (USA)	108562
Bouin's solution	Sigma-Aldrich	HT10132
5-Bromo-2′-deoxyuridine (BrdU)	Sigma-Aldrich	B9285
Citrate Buffer, pH 6.0, 10X	Sigma-Aldrich	C9999
Citroclear	TCS Biosciences (UK)	HC5005
Dako Dual Endogenous Enzyme Block	Agilent (USA)	S2003
Dako EnVision+ System-HRP Labelled Polymer Anti-Rabbit	Agilent	K4003
Dako EnVision+ System-HRP Labelled Polymer Anti-mouse	Agilent	K4000
Dako Liquid DAB+ Substrate Chromogen System	Agilent	K3468
Dimethyl sulfoxide (DMSO)	Thermo Fisher Scientific (USA)	85190
DPX mountant	Merck (Germany)	44581
Dulbecco's Modified Eagle Medium/Ham's F-12	Thermo Fisher Scientific	12634-010
Ethylenediaminetetraacetic acid (EDTA)	BDH Chemicals	4438882G
Elite ABC Rat IgG	Vector Laboratories (UK)	PK-6104
Ethanol	Thermo Fisher Scientific	E/0665DF/17
Eosin	Sigma-Aldrich	HT110132
Foetal bovine serum	Sigma-Aldrich	F7524
Formalin (10% neutral buffered)	Sigma-Aldrich	HT501128
GlutaMAX	Thermo Fisher Scientific	35050-038
Haematoxylin (Harris's)	Sigma-Aldrich	351945S
Haematoxylin (Gill's)	Sigma-Aldrich	GHS132
Hydrochloric acid	Sigma-Aldrich	320331
Hydrogen peroxide 30%	Thermo Fisher Scientific	H/1750/15
Hydroxypropyl methyl cellulose	Merck	9004-65-3
Isaderm	Dechra Pharmaceuticals PLC (UK)	-
Isoflurane (IsoFlo)	Zoetis Inc. (USA)	NDC 0044-5260-05
Lithium carbonate	Scientific Laboratory Supplies (UK)	CHE2354
Magnesium Sulfate	Sigma-Aldrich	M7506
Matrigel	Corning (USA)	356234
Mouse on Mouse Blocking Reagent	Vector Laboratories	MKB-2213-1
Paraffin (Histoplast)	Thermo Scientific	6774060
Pentobarbitone sodium (Pentoject®)	Animalcare Ltd. (UK)	-
Penicillin-Streptomycin (5,000 U/mL)	Thermo Fisher Scientific	15070063
Phosphate-buffered saline (PBS)	Sigma-Aldrich	94417
Pimonidazole HCl	Hypoxyprobe, Inc. (USA)	HP1-1000Kit
Poly(ethylene glycol)	Sigma-Aldrich	91893
Sodium bicarbonate	Corning	61-065-RO
Trizma® base (Tris Base)	Sigma-Aldrich	T1503
TWEEN 20	Sigma-Aldrich	P1379
TWEEN 80	Merck	8.17061.1000
Urethane	Sigma-Aldrich	U2857
Weigert's iron hematoxylin	Sigma-Aldrich	HT1079
Xylene	Sigma-Aldrich	534056

Appendix Table 6.3. Reagents.

Variation with Position		Variation with Depth	
A	101.1%	0 mm	112.4%
B	99.8%	7.5 mm	100%
C	99.1%	15 mm	84.9%

Appendix Table 6.4. Dosimetry variation of whole thorax and hemithorax lung rig at each position and depth into phantom mouse.

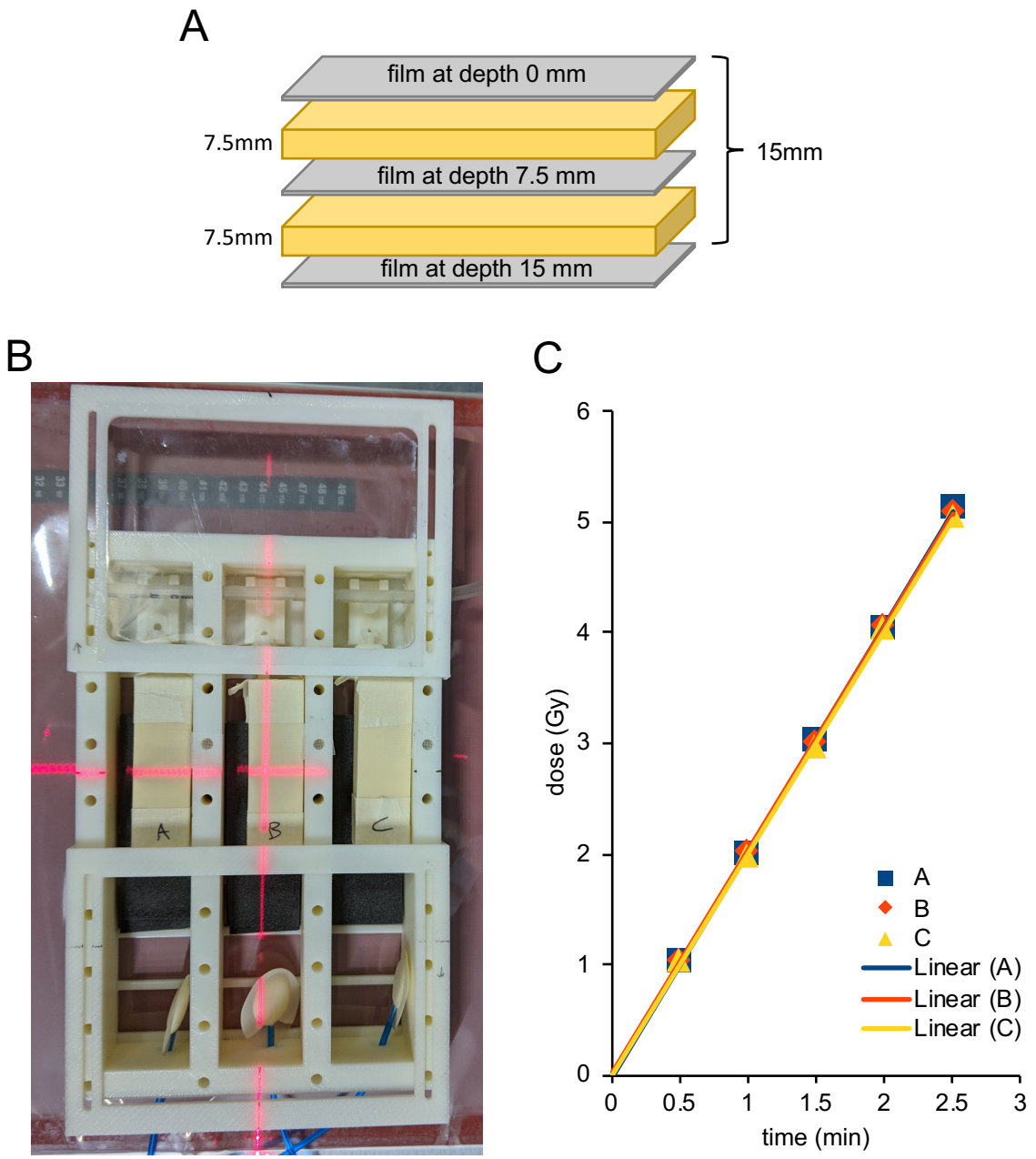

Appendix Figure 6.1. Experimental design of Gulmay 320 dosimetry using mouse phantoms in whole thorax and hemithorax lung irradiation rig. Mouse phantoms were created with Gafchromic EBT3 films stacked with 7.5 mm thick solid water slabs (A). Dosimetry was performed at 3 depths at 3 positions labelled A, B, and C with the beam centred on the middle position (B). Dose rates at each position at a depth of 7.5 mm (considered lung depth) were similar, and the average dose rate was 2.02 Gy/min (C).

A B

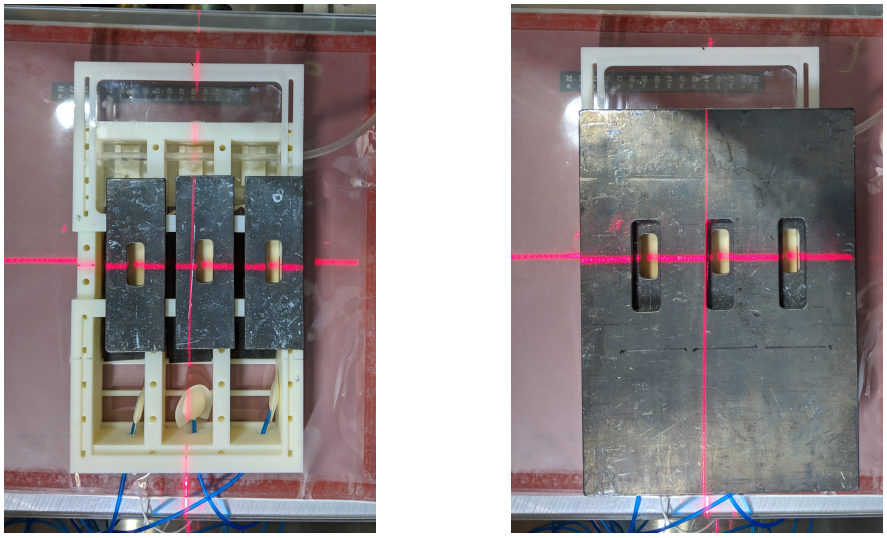

Appendix Figure 6.2. Hemithorax irradiation rig led placement. Individual lead windows were placed over each position (A) and a larger lead shield was placed over all three positions (B).

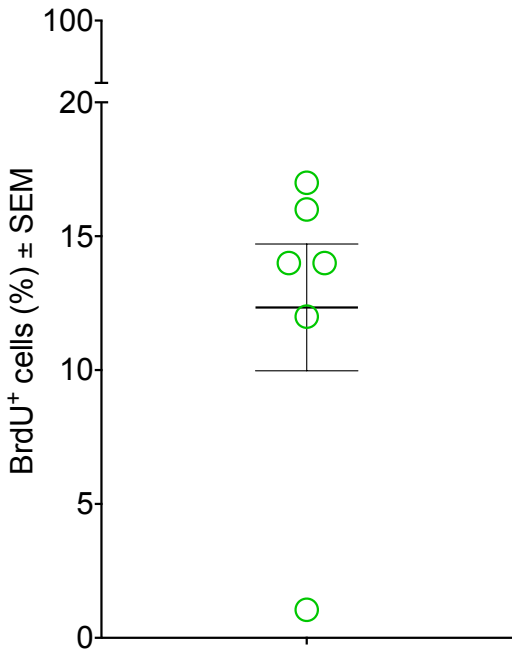

Appendix Figure 6.3. A/J oesophageal epithelial cells are BrdU-positive. BrdU quantitation of oesophageal epithelial IHC. (o) are individual oesophagi.

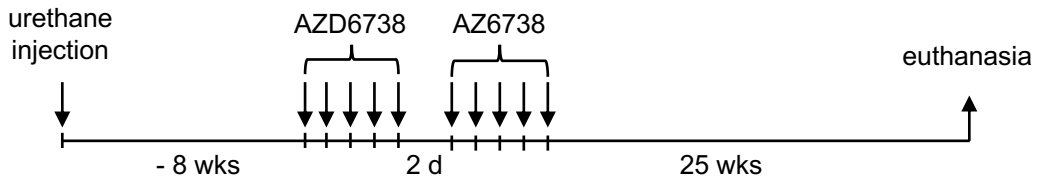

Appendix Figure 6.4. Early intervention schedule for A/J treated with AZD6738. A/J mice were injected with urethane (2 x 5 mg per 10 g body weight, i.p.). After 8 weeks, mice were allocated into groups (n=6 for vehicle treated and n=6 for AZD6738) and treated with AZD6738 (50 mg/kg, p.o.) for 10 days total, with 2 days between 2 sets of 5 days. Euthanasia was planned for 25 weeks after the first dose (unpublished data, Steve Stribbling).

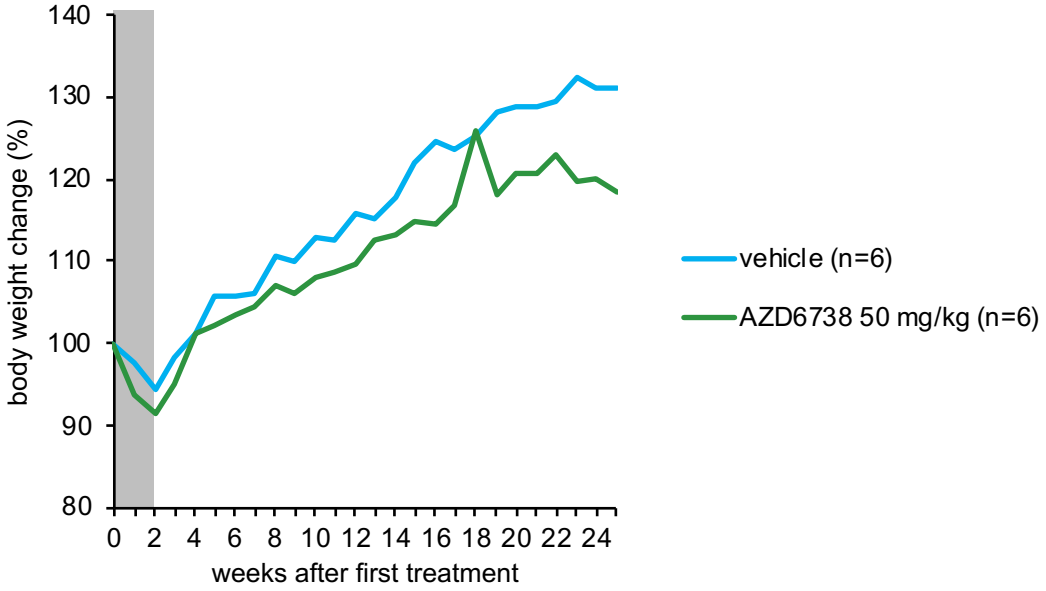

Appendix Figure 6.5. AZD6738 did not induce body weight loss. During treatment, both groups showed mild (< 10%) weight loss but recovered within 2-3 weeks. Both groups showed no significant weight loss during the study and were euthanised 25 weeks after treatment. Grey bar indicates 2 weeks of treatment (unpublished data, Steve Stribbling).

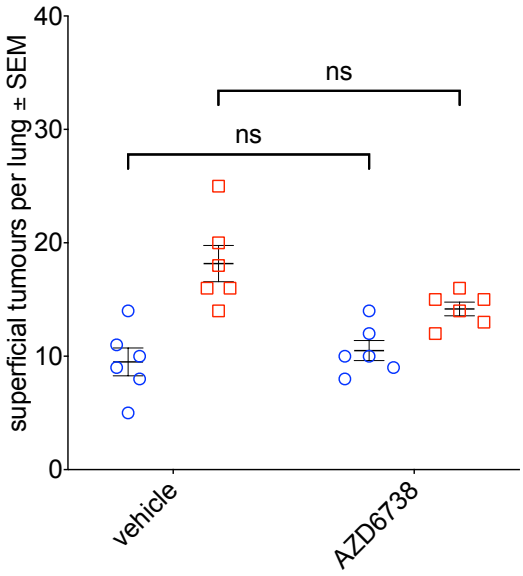

Appendix Figure 6.6. AZD6738 treatment did not reduce superficial tumour counts. Both left and right lungs of mice treated with AZD6738 did not show a significant change in tumour counts as compared with vehicle control. (o) are individual left lungs and (□) are individual right lungs (unpublished data, Steve Stribbling).

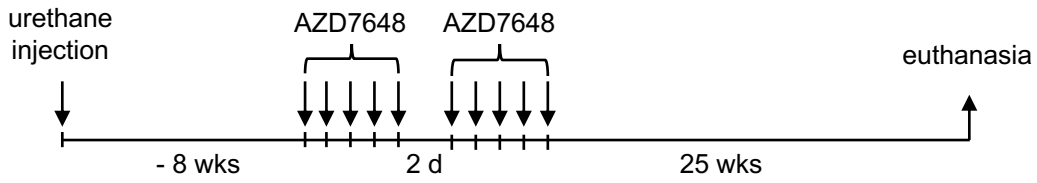

Appendix Figure 6.7. Early intervention schedule for A/J treated with AZD7648. A/J mice were injected with urethane (2 x 5 mg per 10 g body weight, i.p.). After 8 weeks, mice were allocated into groups (n=6 for vehicle treated and n=6 for AZD7648) and treated with AZD7648 (50 mg/kg, p.o.) for 10 days total, with 2 days between 2 sets of 5 days. Euthanasia was planned for 25 weeks after the first dose (unpublished data, Steve Stribbling).

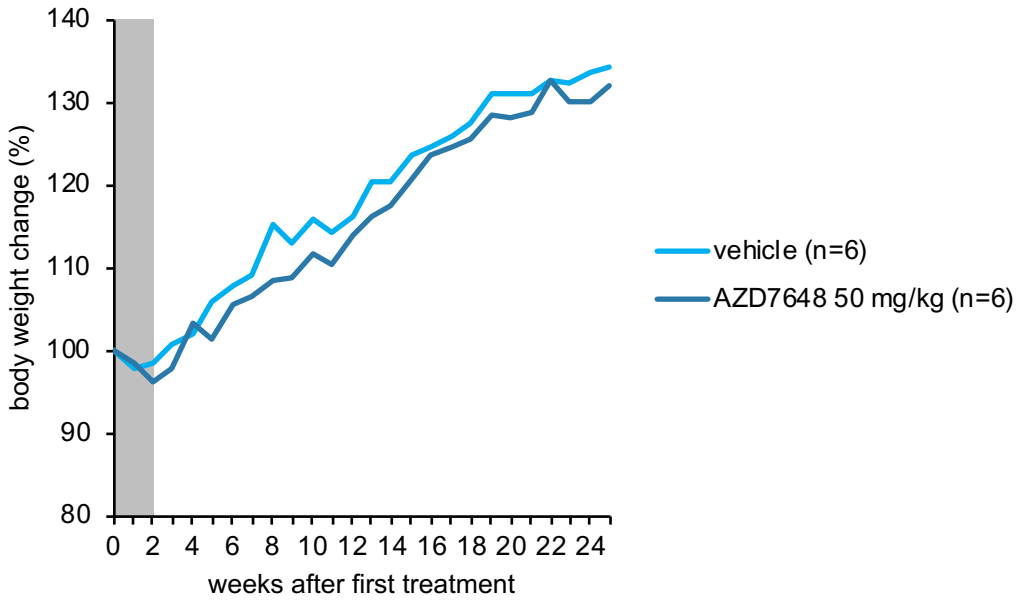

Appendix Figure 6.8. AZD7648 did not induce body weight loss. During treatment, both groups showed mild (< 5%) weight loss but recovered within 2-3 weeks. Both groups showed no significant weight loss during the study and were euthanised 25 weeks after treatment. Grey bar indicates 2 weeks of treatment (unpublished data, Steve Stribbling).

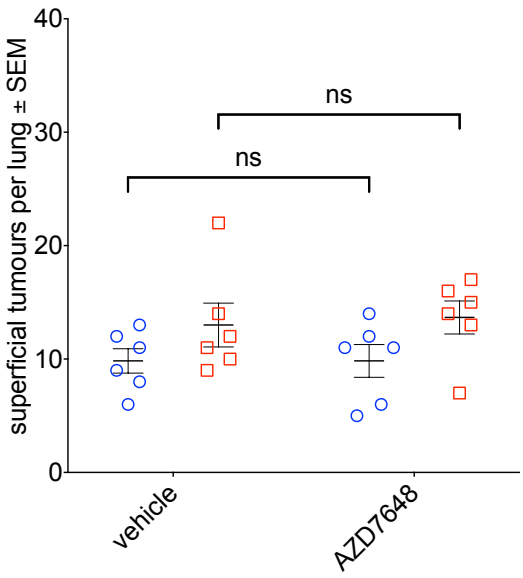

Appendix Figure 6.9. AZD7648 treatment did not reduce superficial tumour counts. Both left and right lungs of mice treated with AZD7648 did not show a significant change in tumour counts as compared with vehicle control. (o) are individual left lungs and (□) are individual right lungs (unpublished data, Steve Stribbling).